



UNIVERSITÉ PARIS XIII - SORBONNE PARIS NORD
École Doctorale Sciences, Technologies, Santé Galilée

Développement de photocatalyseurs à base de TiO_2 pour réacteur pilot solaire. Application au traitement de l'eau contaminée par Cefixime pharmaceutique.

Development of TiO_2 based photocatalysts for sunlight pilot reactor.
Application to treatment of contaminated water with pharmaceutical
Cefixime.

THÈSE DE DOCTORAT
présentée par

Fatemehsadat MOOSAVI

Laboratoire des Sciences des Procédés et des Matériaux CNRS UPR 3407

Pour l'obtention du grade de
DOCTEUR EN Génie des Procédés
soutenue le 31/05/2023 devant le jury d'examen composé de:

AREFI Farzaneh, Professeur, Sorbonne Université (SU). Présidente / Président du jury
COLBEAU JUSTIN Christophe, Professeur, Université Paris-Saclay. . . Rapporteur / Rapportrice
ROUSSEAU Frédéric, MCF-HDR, ParisTech ENSCP Rapporteur / Rapportrice
KANAIEV Andrei, DR émérite, CNRS USPN Examineur/Examinatrice
TRAORÉ Mamadou, MCF-HDR, USPN. Examineur/Examinatrice
LEMARCHAND Alex, MCF, USPN. Examineur/Examinatrice
HADDAD Oriana, MCF, USPN. Examineur/Examinatrice
NIKRAVECH Mehrdad, Professeur, USPN Directeur de thèse
TAVAKOLI GHEINANI Touraj, Professeur, Université Isfahan Co-directeur de thèse

Acknowledgments

This doctoral thesis is the result of four-year research work which was performed in Laboratoire des Sciences des Procédés et des Matériaux of CNRS (LSPM UPR 3407) at the University of Sorbonne Paris Nord in collaboration with the Chemical Engineering Department of the University of Isfahan. Funding for this work was provided by the Cultural Service of the Embassy of France in Iran, and the complementing financial support of the University of Sorbonne Paris North (USPN) and the Deputy of Research and Technology of the University of Isfahan. Thanks to the financial support of the Center for International Scientific Studies and Collaboration of Iran that permitted the start of this collaboration between USPN and the University of Isfahan.

First and foremost, I would like to express my special thanks and gratitude to my supervisor professor Mehrdad NIKRAVECH. He was a great and kind supervisor for giving the main lines and ideas in my research and sincerely teaching me his knowledge, especially for his encouragement and support during my stay in France.

I would like to deeply thank my co-supervisor professor Touraj TAVAKOLI GHEINANI at the University of Isfahan for helping and advising me with his expert knowledge during all these years.

I also would like to thank M. Khaled HASSOUNI and M. Dominique VREL, directors of LSPM, for permission to perform this thesis in the laboratory. I thank M. Amir Hossein NAVARCHIAN, head of the chemical engineering department, and all his colleagues for their help and support to use Chemical Engineering laboratory facilities. Additionally, thanks to the International and Scientific Cooperation office at the University of Isfahan and the International Relations services of the University of Sorbonne Paris Nord. My sincere thank goes to M. Andrei KANAIEV for his help and advice, especially in editing the scientific papers relative to this work.

I would like to thank Mrs. Farzaneh AREFI-KHONSARI, M. Christophe COLBEAU JUSTIN, and M. Frédéric ROUSSEAU for the acceptance to participate in my doctoral defense and to evaluate this thesis. I also want to thank M. Mamadou TRAORÉ and M. Alex LEMARCHAND for their acceptance to be the referee of this thesis and for their kind support during this work.

Thanks to Mrs. Maria KONSTANTAKOPOULOU and M. Ovidui BRINZA for their help in scanning electron microscopy and transmission electron microscopy measurements, and all members of LSPM.

Special thanks go to Institut Lavoisier de Versailles at Université de Versailles Saint-Quentin-en-Yvelines for the X-ray photoelectron spectroscopy analysis of our samples.

Thanks to Mrs. Claude JOLLIVALT, M. Jean Philippe PASSARELLO, and M. Michaël REDOLFI for their participation to “Comité de suivi de l’Ecole doctorale de Galilée”.

My deeply special thanks to my spouse Pedram DANESHFAR, these four years really were hard to bear sometimes without him. Thanks for the support, love, understanding, and freedom he gave me to finish this work.

Thanks to my father who supported me in my decisions during all the years when I decide to go to Europe for a doctorate. I surely don’t believe that I can reach as far as this educational stage without his encouragement and support.

Thanks to my friends, I found in France and Iran, thanks for all the funny, patient, laughs, and help. Thanks to Ms. Marjan for her deep friendship who talked to me in difficult times and offered advice.

Finally, thanks and appreciation go out to various people who helped and supported me to do this work.

CONTENTS

Part 1: General introduction	14
Notations.....	18
Part 2: Literature review	19
Chapter 1. Water resource and pharmaceutical water pollutants.....	20
1.1. Cefixime as a pollutant model	22
Chapter 2. Water and wastewater treatment methods for antibiotic removal.....	23
2.1. Advanced oxidation processes (AOPs).....	24
2.1.1. Semiconductor photocatalysis	27
2.1.1.1. Properties of TiO ₂ semiconductor	30
Chapter 3. Generalities of plasma-enhanced chemical vapor deposition (PECVD).....	34
3.1. Plasma parameters effect on films deposition	35
3.1.1. Modification of TiO ₂ photocatalytic activity by doping.....	40
3.1.1.1. Mn doping in TiO ₂ structure	41
Chapter 4. Solar photochemical process	45
4.1. Solar energy	45
4.2. Solar photo-reactors	48
4.2.1. Solar collectors	49
4.2.1.1. Non-concentrating	49
4.2.1.2. Concentrating collector	50
4.2.1.2.1. Parabolic Trough Collector (PTC)	50
4.2.1.2.2. Compound Parabolic Collector (CPC).....	51
4.2.1.2.3. Parabolic Dish Concentrator (PDC)	53
4.2.1.2.4. Fresnel concentrator	53
4.2.1.2.5. Optical fiber photoreactors.....	54
4.2.2. Solar photoreactor's tube (absorber).....	54
4.2.3. Reflecting material of solar collectors.....	55
4.3. Solar photodegradation studies	55
Chapter 5. Regeneration of TiO ₂ photocatalyst.....	59
Conclusions	61
Notations.....	63
Part 3: Elaboration and characterization of nano-photocatalysts	66
Chapter 1. Elaboration methods and experimental setups	67
1.1. Elaboration of photocatalysts.....	67
1.1.1. The low-pressure fluidized bed plasma setup.....	68
1.1.1.1. Plasma process for deposition of TiO ₂ films on glass beads.....	69
1.1.1.2. Deposition of manganese doping in the TiO ₂ structure	71
1.1.1.2.1. Inductively coupled plasma-optical emission spectroscopy (ICP-OES)	72
1.1.2. Crystallization of deposited films by post annealing.....	73
1.2. Sol-Gel method in a micro-mixing reactor.....	73
1.2.1. Synthesize of TiO ₂ and doped-TiO ₂ nano-particles coated on glass beads	73
Chapter 2: Characterization of physicochemical properties of photocatalysts.....	75
2.1. X-ray diffraction	75
2.2. Raman spectroscopy.....	77
2.3. X-ray photoelectron spectroscopy.....	77

2.4.	Scanning electron microscopy.....	78
2.5.	Transmission electron microscopy	80
2.6.	Atomic force microscopy	81
2.7.	Inductively coupled plasma-optical emission spectroscopy (ICP-OES).....	82
Chapter 3: Results and discussion.....		83
3.1.	Effect of oxygen flux in plasma gas on the structure of TiO ₂ films	83
3.1.1.	Raman spectroscopy	85
3.1.2.	X-ray diffraction (XRD).....	86
3.1.3.	X-ray photoelectron microscopy (XPS).....	88
3.1.4.	Scanning electron microscopy (SEM)	93
3.1.5.	Transmission electron microscopy (TEM)	96
3.1.6.	Atomic force microscopy.....	99
3.2.	Characterization of deposited Mn _x Ti _{1-x} O ₂ films on glass beads	106
3.2.1.	Raman spectroscopy	108
3.2.2.	X-ray diffraction (XRD).....	109
3.2.3.	Transmission electron microscopy (TEM)	111
Conclusion.....		112
Notations.....		113
Part 4. Photocatalytic activity of TiO ₂ films		115
Chapter 1. Experimental setups.....		116
1.1.	The solar photo-reactor	116
1.1.1.	Photocatalysis experiments by natural irradiation in the CPC solar photo-reactor	117
1.2.	The lab scale photo-reactor	118
1.2.1.	Photocatalysis experiments by an artificial irradiation in the lab-scale photo-reactor	119
1.3.	Characterization methods	120
1.3.1.	UV-Visible spectrophotometric technique	120
1.3.1.1.	Calibration curve	120
1.3.2.	Liquid chromatography–mass spectrometry	122
1.3.3.	Solar energy measurements.....	123
1.3.3.1.	Cefixime degradation kinetic study	125
Chapter 2. Experimental results of cefixime degradation		125
2.1.	Photocatalysis study of plasma deposited TiO ₂ catalysts under natural and artificial light	125
2.1.1.	Photocatalytic activity of TiO ₂ samples deposited with different oxygen flux in plasma gas under solar irradiation.....	126
2.1.2.	Photocatalytic activity of TiO ₂ samples deposited with different oxygen flux in plasma gas under artificial irradiation	132
2.1.3.	Reproducibility of TiO ₂ deposited films on glass beads with fluidized bed plasma device	136
2.1.4.	Photocatalytic activity, under solar irradiation, of TiO ₂ samples deposited with two deposition times in plasma gas influencing the quantity of coating on beads surface	139
2.1.5.	Effect of net weight of coated glass beads.....	141
2.2.	Influence of doping in TiO ₂ photocatalytic activity.....	142
2.2.1.	Photocatalytic activity of Mn-doped TiO ₂ samples deposited with the plasma method under solar irradiation.....	143
2.3.	Photocatalytic activity of TiO ₂ coatings on glass beads prepared with sol-gel method	145
Chapter 3. Regeneration of photocatalysts		148
3.1.	Regeneration of photocatalysts.....	148
3.2.	Reusability of plasma deposited TiO ₂ and MnTiO ₂ films on glass beads	149
3.3.	Photocatalysts regeneration methods	151
3.3.1.	Hot water regeneration method	151

3.3.1.1.	Study the cefixime degradation under longer solar irradiation time.....	154
3.3.2.	Heat treatment regeneration method	155
3.3.3.	Alkaline solution regeneration	156
3.3.4.	Regeneration stability of plasma deposited photocatalysts	158
3.3.5.	Regeneration of sol-gel prepared photocatalysts	159
3.3.5.1.	Regeneration of the fresh TiO ₂ and VTiO ₂ (3 mol%) prepared with sol-gel method.....	160
Chapter 4. Mechanism of cefixime photocatalytic degradation under solar irradiation		161
4.1.	Analysis of treated cefixime solution by LC-MS technique	161
Conclusions		165
Notations.....		167
Part 5. Multiphysics modeling by COMSOL		169
Chapter 1. Introduction		170
Chapter 2. Multiphysics modeling		172
2.1.	Geometry of the solar photoreactor.....	172
2.2.	Optical modeling.....	173
2.2.1.	Results of optical modeling	177
2.3.	Thermal modeling	179
2.3.1.	Multiphysics coupling of optical and thermal modeling	180
2.3.2.	Results of thermal modeling	181
2.4.	Fluid flow modeling	182
2.4.1.	Multiphysics coupling of fluid flow and thermal modeling	183
2.4.2.	Results of fluid flow modeling.....	183
2.5.	Transport modeling	185
2.5.1.	Kinetic study of photodegradation process	186
2.5.2.	Results of transport modeling.....	190
Notations.....		192
Part 6. General conclusions and perspectives		194
General conclusions		195
Perspectives		197
Publications and conferences		198
Annex		199
References		208

Figure index

Figure 1. Regional patterns of pharmaceutical therapeutic groups analyzed in each United Nations region. MEC = measured environmental concentration; EEG = Eastern Europe Group; GRULAC = Latin American and Caribbean States; WEOG = Western Europe and Others Group (10).	21
Figure 2. Pathway of pharmaceuticals and personal care products in water and soil (16).	22
Figure 3. Overview of Advanced Oxidation Processes (AOPs) applied for pollutants removal (7, 37).	25
Figure 4. Schematic of the typical semiconductor excitation by band gap illumination (46).	28
Figure 5. Schematic of semiconductor excitation by band gap illumination leading to the creation of “electrons” in the conduction band and “holes” in the valance band (48).	29
Figure 6. TiO ₂ crystalline structures: (a) anatase, (b) rutile, and (c) brookite (60).	31
Figure 7. (a) Effect of argon flux and plasma distance on thickness of TiO ₂ thin films (b) SEM images of TiO ₂ thin film on silicon substrate prepared with $P_{(Ar + TTIP)} = 22.5 \text{ Pa}$ and $d_p = 3.0 \text{ cm}$ (96).	36
Figure 8. SEM images of the TiO ₂ films deposited by RF PECVD with the glow discharge power of (a) 100 W, (b) 200 W, and (c) 300 W (97).	36
Figure 9. Raman spectrum of TiO ₂ film deposited at 200 W: (A) before and (B) after thermal annealing at 450 °C for 1 h (83).	37
Figure 10. PECVD deposition rate as a function of equivalence ratio at 5 W (squares) and 20 W (circles) (93).	38
Figure 11. Deposition rate as a function of O ₂ flow rate in PECVD with different radio frequency power (94).	38
Figure 12. SEM micrographs of anatase titania synthesized by PECVD at room temperature: (a) clusters of nanocrystals at 30 Pa (0.3 mbar), (b) nanorods at 50 Pa (0.5 mbar), (c) nanoparticles at 80 Pa (0.8 mbar), (d) comb-like structure at 100 Pa (1 mbar) (95).	39
Figure 13. XRD patterns of a TiO ₂ thin film deposited under Ar/O ₂ = 30:0 and Ar/O ₂ = 30:0 sccm flow rate (56).	40
Figure 14. X-ray diffraction patterns of TiO ₂ , Mn-TiO ₂ , Co-TiO ₂ and Mn-Co-TiO ₂ (109).	42
Figure 15. XRD pattern of Mn ²⁺ /TiO ₂ samples (111).	42
Figure 16. Variation of optical band gap with Mn atomic concentration and the energy level diagram of undoped TiO ₂ and (5 at. %) Mn doped TiO ₂ (104).	44
Figure 17. Raman spectroscopy shift of pure and Mn-doped TiO ₂ nanomaterials: (a) TiO ₂ , (b) 1% Mn- TiO ₂ , (c) 2% Mn- TiO ₂ , (d) 4% Mn- TiO ₂ , and (e) 8% Mn- TiO ₂ (117).	45
Figure 18. Properties of the sun (119).	46
Figure 19. Global Horizontal Irradiation (120).	47
Figure 20. The TiO ₂ photocatalyst adsorption spectrum in comparison with Solar spectrum (55).	48
Figure 21. Example of non-concentrating photoreactor (130, 131).	49
Figure 22. Global solar radiation include direct and diffuse (127).	50
Figure 23. Schematic of a PTC photoreactor with one-axis tracking motor(135).	51
Figure 24. The geometry of CPC configuration (135).	52
Figure 25. Schematic and photo of PDC at University of Isfahan (139).	53
Figure 26. Schematic of Fresnel lens receiver(70).	53
Figure 27. The transmittance of different materials suitable for solar photoreactor’s tube (42).	55

Figure 28. Cross-section of solar reactors: (a) compound parabolic, (b) parabolic and (c) V-groove (42).....	56
Figure 29. Photocatalytic degradation of moxifloxacin solution under sunlight and UV- A lamp (UV-A_5.5 and UV-A_6.3) shown as function of accumulated energy (kJ/L) (147).....	57
Figure 30. The set-up of the compound parabolic concentrator reactor packed with supported TiO ₂ beads (148).....	58
Figure 31. Metronidazole removal with different AOP processes versus the accumulated energy (C ₀ = 25 mg/L)(148).	58
Figure 32. Comparison of the results obtained for the different regeneration processes for pharmaceuticals, respect to the used photocatalyst (5th cycle) (152).	60
Figure 33. Schematic of the low-pressure fluidized bed plasma reactor for TiO ₂ depositions.	69
Figure 34. Photo of the fluidized bed plasma reactor installed at LSPM, France.....	70
Figure 35. Schematic of the fluidized bed plasma device for Mn-doped TiO ₂ depositions. ...	72
Figure 36. Schematic of sol-gel micro-mixing reactor with T-mixer used in photocatalyst preparation (170).....	74
Figure 37. X-ray diffraction from two planes of atoms in a crystal.	76
Figure 38. XPS analysis technique on the surface of a glass bead.....	78
Figure 39. Electron beam interaction with the sample in SEM and TEM techniques.	79
Figure 40. A schematic diagram of the pathway of an electron beam within a TEM technique (172) (left), a TEM image of a sample in the present study (right).	80
Figure 41. Schematic procedure of AFM technique.	81
Figure 42. Schematic diagram of an ICP-OES analysis method (170).....	82
Figure 43. Photos of deposited TiO ₂ films on glass beads with different oxygen flux in plasma gas (a) before annealing and (b) after annealing at T = 450 °C in 4 h.	84
Figure 44. Raman spectroscopy of unannealed TiO ₂ film revealed the presence of graphene and graphite in deposited films before annealing.....	85
Figure 45. Raman spectra of TiO ₂ deposited films on glass beads with different oxygen flux in plasma gas during 60 min.	86
Figure 46. XRD patterns of TiO ₂ deposited films on glass beads with a) 0 ml/min, b) 2 ml/min, and c) 10 ml/min oxygen flow in plasma gas.....	87
Figure 47. XPS analysis of TiO ₂ film coated with 0 ml/min oxygen flux in plasma gas during 60 min.	91
Figure 48. SEM images and histogram graphs of TiO ₂ films on glass beads with (a) 0 ml/min, (b) 2 ml/min, (c) 10 ml/min, and (d) 25 ml/min oxygen flux in plasma gas during 60 min.....	95
Figure 49. TEM images of TiO ₂ films deposited on glass beads with 0 ml/min O ₂ in plasma gas during 60 min. The photo on the right represents the profile of light intensity that permitted to measure the inter-reticular distance with a high accuracy (Image J free software (209)).	96
Figure 50. TEM images of TiO ₂ films deposited on glass beads with (a) 2 ml/min, and (b) 10 ml/min O ₂ in plasma gas during 60 min.....	98
Figure 51. TEM images of TiO ₂ films deposited on glass beads with 25 ml/min O ₂ in plasma gas during 60 min (left) and analysis of interplane distances of anatase and rutile phases by Image J (right).	99
Figure 52. AFM images, depth histogram and the value of root mean square roughness (RMS) of TiO ₂ films on glass beads with 0 ml/min oxygen flux in plasma gas during 60 min.....	100
Figure 53. AFM images, depth histogram and the value of root mean square roughness (RMS) of TiO ₂ films on glass beads with 10 ml/min oxygen flux in plasma gas during 60 min.....	101

Figure 54. AFM images, depth histogram and the value of root mean square roughness (RMS) of TiO ₂ films on glass beads with 25 ml/min oxygen flux in plasma gas during 60 min.....	102
Figure 55. AFM image, developed length and height distribution of TiO ₂ films on glass beads with 2 ml/min oxygen flux in plasma gas during 45 min.	103
Figure 56. AFM image, developed length and height distribution of TiO ₂ films on glass beads with 10 ml/min oxygen flux in plasma gas during 45 min.	104
Figure 57. AFM image, developed length and height distribution of TiO ₂ films on glass beads with 25 ml/min oxygen flux in plasma gas during 45 min.	105
Figure 58. Photos of deposited TiO ₂ and Mn _x Ti _{1-x} O ₂ (x = 0.01 and x = 0.02) films on glass beads with 10 ml/min oxygen flux in plasma gas (a) before annealing and (b) after annealing at T = 450 °C in 4 h.	107
Figure 59. Raman spectra of TiO ₂ and Mn _x Ti _{1-x} O ₂ (x = 0.003, 0.01, and 0.02) deposited films on glass beads with 10 and 25 ml/min oxygen flux in plasma gas during 35 min.....	108
Figure 60. XRD patterns of TiO ₂ and Mn _x Ti _{1-x} O ₂ (x = 0.01 and x = 0.02) deposited films on glass beads with 10 ml/min oxygen flux in plasma gas during 45 min.	109
Figure 61. TEM images of Mn _x Ti _{1-x} O ₂ (x = 0.1) films deposited on glass beads with 10 ml/min oxygen flux in plasma gas during 45 min.	111
Figure 62. Schematic of the CPC photo-reactor installed at the University of Isfahan, Iran.	117
Figure 63. Photos of the CPC solar photo-reactor with its measurement equipment installed at the University of Isfahan, Iran.	118
Figure 64. Schematic of the lab-scale photo-reactor using UV lamp.	119
Figure 65. Photos of the lab-scale photoreactor with an artificial light installed at LSPM, France.....	120
Figure 66. Cefixime trihydrate chemical structure and characteristics.....	121
Figure 67. a) Absorbance graphs of different cefixime concentrations, and b) calibration graph and equation of cefixime.	122
Figure 68. Schematic of a LC-MS analytical device.....	122
Figure 69. UV light meter (left) and solar power meter (right) devices.	124
Figure 70. Typical UV radiation (wave length) during a day in summer at the University of Isfahan, Iran.	124
Figure 71. Blank experiment of cefixime with TiO ₂ films deposited with different oxygen flux in plasma gas during 60 min.	127
Figure 72. Cefixime degradation with TiO ₂ films deposited with different oxygen flux in plasma gas during 60 min. The graph inset depicts the efficiency of TiO ₂ catalysts elaborated in plasma vs rutile fraction.	128
Figure 73. a) Evolution of the species fluxes as a function of O ₂ fraction at 30 mTorr. c) Evolution of the ratio of the O flux and the total positive ion flux as a function of O ₂ fraction at 30 mTorr. The power is 400 W (227).....	130
Figure 74. Kinetic plots of cefixime degradation with TiO ₂ films deposited with different oxygen flux in plasma gas during 60 min.	131
Figure 75. Schematic of the lab-scale photo-reactor.	132
Figure 76. Cefixime degradation with TiO ₂ films deposited with different oxygen flux in plasma gas (deposition time 60 min) under UV 370 nm irradiation.....	133
Figure 77. Cefixime degradation with TiO ₂ films deposited with different oxygen flux in plasma gas (deposition time 60 min) versus accumulated energy of UV lamp irradiation.....	134
Figure 78. Cefixime adsorption on TiO ₂ films coated on glass beads with different oxygen flow rates (from 0 to 10 ml/min) during 45 min.....	137

Figure 79. Cefixime degradation with TiO ₂ films deposited with different oxygen flux in plasma gas during 45 min.....	138
Figure 80. Rate constant comparison of cefixime degradation with TiO ₂ films deposited under 30 and 50% of TTIP precursor concentration during 45 and 60 min with different oxygen flux in plasma gas.....	139
Figure 81. Photo-degradation (left) and rate constant (right) of cefixime with TiO ₂ films deposited with 10 ml/min oxygen flux in plasma gas during 30 and 60 min.....	140
Figure 82. Cefixime degradation with TiO ₂ photocatalyst (2 ml/min O ₂ , 45 min) with different net weight of coated glass beads under solar light.	141
Figure 83. Linear regression between rate constant of cefixime degradation and net weight of TiO ₂ (2 ml/min O ₂ , 45 min) coated glass beads.	142
Figure 84. Cefixime degradation of TiO ₂ and Mn _x Ti _{1-x} O ₂ (x = 0.003, 0.01, and 0.02 at mol% Mn) deposited films on glass beads with 10 ml/min oxygen flow in plasma gas during 35 min..	144
Figure 85. Cefixime degradation with used TiO ₂ , V _x Ti _{1-x} O ₂ (x = 2, 3, 5, 10 and 20 mol% V) and Zr _x Ti _{1-x} O ₂ (x = 5 mol%) nano-powder coated on glass beads with sol-gel method. MB refers to methylene blue, ANT refers to amoxicillin antibiotic, and Deg refers to degradation.	146
Figure 86. Hot water regeneration process.....	148
Figure 87. Comparison of cefixime degradation's reaction rate constant with different plasma deposited TiO ₂ films on glass beads in solar photo-reactor.....	150
Figure 88. Raman spectra of TiO ₂ films deposited on glass beads before and after photocatalysis experiment.	151
Figure 89. Cefixime concentration reduction after hot water regenerated TiO ₂ (2 and 25 ml/min O ₂ in plasma gas at 60 min of deposition time) photocatalysts.	153
Figure 90. Cefixime concentration reduction after hot water regenerated TiO ₂ (2 ml/min O ₂ in plasma gas at 60 min of deposition time) during four consecutive cycles.....	153
Figure 91. Rate constant of cefixime degradation with TiO ₂ (C _{Ti} = 1.002 mol/L, 45 min) films in first usage and after hot water regenerated photocatalyst usage.....	154
Figure 92. Cefixime degradation of two TiO ₂ films (2 and 25 ml/min O ₂ flux, 60 min) at loner time of solar irradiation.	155
Figure 93. Rate constant comparison of Mn _x Ti _{1-x} O ₂ (x = 0.01 and 0.02 mol% Mn, 10 ml/min O ₂) films regenerated with hot water and heat treatment (annealed at 450 °C, 4 h) methods.	156
Figure 94. Comparison of different regeneration methods used for Mn _x Ti _{1-x} O ₂ (x = 0.01 mol%, 10 ml/min O ₂) photocatalyst coated on glass beads.	157
Figure 95. Regeneration stability of hot water regenerated TiO ₂ (25 ml/min O ₂ , 60 min) sample coated on glass beads.....	159
Figure 96. The rate constant of cefixime degradation with used TiO ₂ , VTiO ₂ (2, 3, 5, 10 and 20 mol% V) and ZrTiO ₂ (5 mol%) beads before and after two regeneration methods.	160
Figure 97. Rate constant comparison of the fresh and regenerated TiO ₂ and VTiO ₂ (3%) beads prepared by sol-gel, with hot water and heat treatment regeneration methods.	161
Figure 98. Proposed pathway for degradation of Cefixime antibiotic by the sono-electro-Fenton process (12).	163
Figure 99. Schematic and geometry of photocatalytic reactor with fixed TiO ₂ beds on mesh layers (250).....	171
Figure 100. Dimensions of the CPC photoreactor contained coated glass beads.....	172
Figure 101. Three main optical parts in the system, (a) CPC, (b) Pyrex tube, and (c) reactive surfaces.	175

Figure 102. The coordinate preview of the simulated solar radiation with Release from Grids node.	176
Figure 103. Schematic of ray trajectory on the CPC photoreactor.....	177
Figure 104. The distribution of solar flux on the surface of a) CPC, b) exterior wall of Pyrex tube, and c) coated glass beads with TiO ₂ photocatalyst.....	178
Figure 105. The temperature profiles of the feed at various times during an experiment. .	182
Figure 106. The variation of the average water temperature inside the CPC solar photoreactor during an experiment.	182
Figure 107. The slice velocity distribution in 3D domain of feed.	184
Figure 108. Velocity profile variations at the first plane (left legend column) and the second plane (right legend column) in the solar pilot with an initial flow rate of 20 ml/s.	184
Figure 109. The contour plots of Reynolds number distribution along the tube at a flow rate of 20 ml/s in inlet.	185
Figure 110. Relation between $1/k_{app}$ and initial cefixime concentration (C_0).	190
Figure 111. Comparison of experimental data and model prediction of concentration of cefixime at the outlet of solar reactor as a function of time ($C_0 = 10$ mg/L) for three photocatalysis experiments.	191
Figure 112. XPS analysis of TiO ₂ film coated with 0 ml/min oxygen flux in plasma gas during 60 min.	199
Figure 113. XPS analysis of TiO ₂ film coated with 10 ml/min oxygen flux in plasma gas during 60 min.	200
Figure 114. XPS analysis of TiO ₂ film coated with 10 ml/min oxygen flux in plasma gas during 45 min.	201
Figure 115. XPS analysis of TiO ₂ film coated with 10 ml/min oxygen flux in plasma gas during 60 min.	203
Figure 116. Mass spectra and chromatograms of treated cefixime solution sample with the degradation efficiency of 85%.	205
Figure 117. Mass spectra and chromatograms of treated cefixime solution sample with the degradation efficiency of 45%.	206
Figure 118. Rate constant comparison of TiO ₂ ($C_{Ti} = 1.002$ mol/L, 0 and 1 ml/min O ₂ , 45 min) films regenerated with hot water and heat treatment methods.....	207

Table index

Table 1. Cefixime degradation with various photocatalysts in literature.	33
Table 2. Advantages and disadvantages of various photoreactor tube (42, 132).....	54
Table 3. Plasma deposition conditions of TiO ₂ photocatalysts prepared with the fluidized bed plasma method.	71
Table 4. Deposition conditions of Mn _x Ti _{1-x} O ₂ photocatalysts prepared with the fluidized bed plasma method.	72
Table 5. The final composition of TiO ₂ layers doped with Mn measured with ICP-OES.	73
Table 6. Plasma deposition conditions of TiO ₂ layers coated on glass beads with different oxygen flow rates.....	83
Table 7. Nano particles' size measurement with Scherrer equation and XRD patterns.	88
Table 8. Properties of XPS analysis samples.	90
Table 9. XPS analysis of TiO ₂ films deposited with 0 ml/min O ₂ in plasma gas.....	92
Table 10. XPS analysis of TiO ₂ films deposited with 10 ml/min O ₂ in plasma gas.....	92
Table 11. Roughness parameters of TiO ₂ films deposited with 0, 10, and 25 ml/min O ₂ in plasma gas during 60 min.	102
Table 12. Roughness parameters of TiO ₂ films deposited with 2, 10, and 25 ml/min O ₂ in plasma gas during 45 min.	105
Table 13. Plasma deposition conditions of Mn _x Ti _{1-x} O ₂ layers coated on glass beads with different deposition times.	106
Table 14. Nano particles' size measurement with Scherrer equation and XRD patterns.	110
Table 15. Cefixime degradation efficiency with TiO ₂ samples deposited under various oxygen flux in plasma gas during 60 min.	128
Table 16. The rate constant of cefixime degradation with TiO ₂ films deposited with different O ₂ in plasma gas during 60 min under solar irradiation.	131
Table 17. The rate constant of cefixime degradation with TiO ₂ films deposited with different O ₂ in plasma gas during 60 min under artificial irradiation.....	135
Table 18. The rate constant of cefixime degradation efficiency after 240 min with TiO ₂ films deposited with different oxygen flux in plasma gas during 45 min.	138
Table 19. The rate constant of cefixime degradation with TiO ₂ and Mn _x Ti _{1-x} O ₂ (x = 0.01, 0.003, and 0.02 mol% Mn) deposited films on glass beads with 10 ml/min oxygen flow in plasma gas for 35 min.....	145
Table 20. The rate constant of cefixime degradation with TiO ₂ , Zr _{0.05} Ti _{0.95} O ₂ and V _x Ti _{1-x} O ₂ (x = 2, 3, 5, 10, and 20 mol% V) nanoparticles coated on glass beads used in CPC photo-reactor. MB refers to methylene blue, AMX refers to amoxicillin, and Deg refers to degradation. ..	147
Table 21. Identified products of cefixime degradation by solar photocatalytic process (Experimental conditions: initial cefixime concentration = 10 mg/L, reaction time = 240 min, catalyst = TiO ₂)	162
Table 22. Optical and thermal parameters values and ranges in the experimental setup ...	181
Table 23. XPS analysis of TiO ₂ films deposited with 0 ml/min O ₂ in plasma gas during 60 min.	199
Table 24. XPS analysis of TiO ₂ films deposited with 10 ml/min O ₂ in plasma gas during 60 min.	200
Table 25. XPS analysis of TiO ₂ films deposited with 10 ml/min O ₂ in plasma gas during 45 min.	201

Table 26. XPS analysis of TiO ₂ film coated with 10 ml/min oxygen flux in plasma gas during 60 min.	203
---	-----

PART 1: GENERAL INTRODUCTION

Water is a crucial resource for humanity and water pollution is one of the biggest challenges in developed and developing countries worldwide. Pharmaceutical contamination has been detected in the aquatic environment at various concentrations. Cefixime as one of the β -lactam antibiotics was observed in different water supplies. Conventional treatment is typically based on biological technology that cannot effectively remove antibiotics such as cefixime due to its complex structure.

The common types of energy production make environmental problems that put in danger the quality of life and natural ecosystems. Sun is a suitable alternative energy source for helping to solve environmental problems. Iran is located in the Middle East and is in a favorable position for solar energy reception because of the vast deserts and high altitudes. The number of sunny days in two-thirds of Iran is more than 300 per year. The estimated energy potential of total solar radiation is about 1800-2200 kWh/m² per year. The annual average of sunshine in Iran is 3200 h and it differs in the wide latitudinal range. The highest solar radiation value is in central Iran which can be well recommended as having large potential for solar applications.

Several advanced techniques were used for wastewater treatment containing antibiotics like adsorption, membrane filtration, flocculation, and Advanced Oxidation Processes (AOPs). Among different AOPs, solar photocatalysis has raised great attention during the last decades due to the effective utilization of abundant and free natural solar radiation as the source of photons. Solar photocatalysis using wide-gap semiconductors (TiO₂, ZnO, etc.) is based on the collection of high energy short wavelength photons (UV radiation) to promote photoreactions. Photocatalyzed AOP is a good alternative method for pharmaceutical treatment that involves the generation of hydroxyl radical (*OH). The most known catalysts for this application with commercially available, photochemically stable, high chemical stability, mineralization of hazardous contaminants, the capability of using natural solar UV energy, and superior redox ability is titanium dioxide. The powder form of TiO₂ in the photocatalytic process requires a filtration step. However, nowadays it is forbidden for example by European Union directives to add to the surface waters the nanoparticles that constitute by themselves a new category of pollutant. A solution to this problem is to produce nanostructured photocatalysts stabilized on the surface of immobile surfaces permitting the recovery of the photocatalysts after use and preventing their diffusion in the water. Therefore, an immobilized catalyst on a substrate can eliminate the costly separation section.

Plasma-enhanced chemical vapor deposition (PECVD) can facilitate the deposition of TiO₂ films on a substrate in one step by controlling photocatalyst composition and structure by plasma deposition parameters. The capability of using natural solar UV energy in photocatalysis can reduce the cost associated with UV radiation production. The usage of solar radiation can be interesting as the source of UV radiation due to the high electricity demand for UV lamps.

The objective of the thesis was to investigate the application of the solar photocatalysis process for the degradation of cefixime as pharmaceutical contamination in water by employing TiO_2 plasma deposited films. The films of TiO_2 were deposited on glass beads with the fluidized bed plasma-enhanced chemical vapor deposition method. The effect of plasma operating parameters including oxygen flow rate, deposition time, and Ti concentration in precursor solution on physicochemical properties of coated TiO_2 films have been studied. Crystalline phase and size, TiO_2 composition, surface morphology, and roughness can be reflected from X-ray diffraction, Raman spectroscopy, X-ray photoelectron spectroscopy, scanning electron microscopy, transmission electron microscopy, and atomic force microscopy measurement. The photocatalyst coatings on glass beads were prepared in the fluidized bed plasma process from working gases of argon/oxygen, followed by a post-annealing step for crystallization. Another part of this work was manganese doping in the TiO_2 structure with the fluidized bed plasma device. The $\text{Mn}_x\text{Ti}_{1-x}\text{O}_2$ films were deposited in the range of 1-10 mol% concentrations. At the same time TiO_2 and $\text{V}_x\text{Ti}_{1-x}\text{O}_2$ ($0.02 \leq x \leq 0.2$) were synthesized by using the sol-gel method in a micro-mixing reactor. The photodegradation efficiency of the cefixime solution was examined on the lab scale and CPC solar photo-reactors were built at the University of Sorbonne Paris North (LSPM, France) and the University of Isfahan (Iran) in partnership with the doctoral project. In the continuous work regeneration study deactivated photocatalysts in the liquid phase were investigated.

This Ph.D. thesis contains six parts each containing several chapters.

The Part 1 describes the general introduction.

The Part 2 is focused on the literature review concerning water pollution, AOP and TiO_2 photocatalysis process, plasma-enhanced chemical vapor deposition for photocatalyst elaboration, solar photo-reactor, and photocatalysts regeneration methods.

The elaboration methods and characterization of photocatalysts are described in Part 3. The applied low-pressure fluidized bed plasma and sol-gel techniques to produce supported TiO_2 layers followed by characterization techniques employed in this study will be presented. The characterization techniques XRD, Raman spectroscopy, XPS, SEM, TEM, AFM, and ICP-OES used were described. Afterward, results of the effects of plasma deposition parameters on the physicochemical properties of coated TiO_2 annealed films, including nanocrystal structure, crystalline phase, chemical states, and surface morphology are presented in the last chapter of this part.

The Part 4 explains the photocatalytic activity of all TiO_2 -based samples under natural and artificial irradiation. It contains four chapters, the first chapter presents the solar pilot, the lab-scale photoreactor, and other characterization techniques such as UV-vis spectrophotometer, liquid chromatography-mass spectroscopy, and solar energy measurements. The photodegradation studies on cefixime are connected to the preparation conditions in the fluidized bed plasma and sol-gel reactors. The recovery of the deactivated photocatalysts is explained in chapter 3 of part 4. Three regeneration methods are discussed

for the recovery of TiO_2 -coated samples that have begun to lose their photoactivity. The last chapter of part 4 presents the results of the LC-MS analytical technique.

Lastly, the part 5 describes the mathematical modeling of the CPC solar photo-reactor with the COMSOL Multiphysics software.

A general conclusion of the Ph.D. thesis and perspectives for future research are given at the end of the manuscript in part 6.

Notations

AOPs	Advanced Oxidation Processes
$\cdot\text{OH}$	Hydroxyl Radical
UV	Ultraviolet
TiO_2	Titanium Dioxide
PECVD	Plasma-Enhanced Chemical Vapor Deposition
Mn	Manganese
V	Vanadium
CPC	Compound Parabolic Concentrator
XRD	X-ray Diffractometer
XPS	X-ray Photoelectron Spectroscopy
SEM	Scanning Electron Microscopy
TEM	Transmission Electron Microscopy
AFM	Atomic Force Microscopy
ICP-OES	Inductively Coupled Plasma Optical Emission Spectroscopy
UV-vis	Ultraviolet visible
LC-MS	Liquid Chromatography-Mass Spectroscopy

PART 2: LITERATURE REVIEW

Chapter 1. Water resource and pharmaceutical water pollutants

Water is a key resource of humanity, however, 97.5% is salty, and the remaining (2.5%) is drinking water. Also, less than 1% of it is available for domestic, agricultural and industrial uses, but this quantity is not enough to cover all of the humanity needs. Furthermore, adverse health and other potential effects of any substances present in water are harmful. Increasing knowledge to protect and develop the quality of water resources is fundamental to public health (1).

Modern life in industrialized society increases pharmaceutical consumption in the healthcare sector. For example, China is one of the largest pharmaceutical providers and consumers counties in the world (2). Pharmaceutical contamination of water resources is already an environmental issue because of its potential effects on natural ecosystems (3).

Many researchers from France, Italy, Sweden, Greece (4), China (5), and others countries have reported numerous pharmaceutical and personal care products (PPCPs), as emerging contaminants in surface waters, ground waters, and soils (6). Pharmaceuticals encompass antibiotics, analgesics, steroids, anti-depressants, antipyretics, stimulants, antimicrobials, painkillers, hormones, anti-inflammatory, beta-blockers, lipid regulators, and impotence drugs (7).

A lot has been written about the source, fate, and behavior of pharmaceutical substances in the natural environment (8, 9). Antibiotics in Asia, estrogens in Africa and analgesics in eastern Europe, and different types of compounds in other groups were identified and analyzed as the highest maximum concentration according to studies (see figure 1) (10).

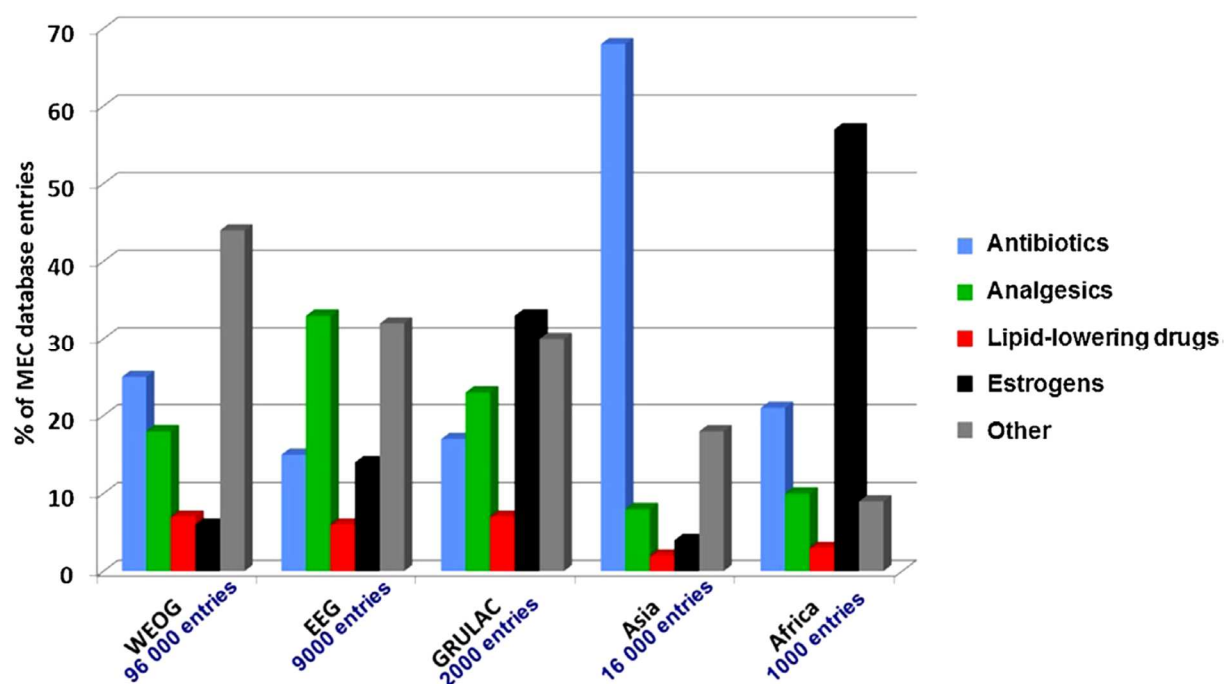


Figure 1. Regional patterns of pharmaceutical therapeutic groups analyzed in each United Nations region. MEC = measured environmental concentration; EEG = Eastern Europe Group; GRULAC = Latin American and Caribbean States; WEOG = Western Europe and Others Group (10).

As shown in figure 2, municipal landfills are the main source of a wide range of compounds like heavy metals, pesticides, pharmaceuticals, and dyes. Incomplete human metabolism and excretion into the water stream and industrial wastewaters are other sources of drugs that entering to the environment (11). Hospitals are one of the main sites of pharmaceutical effluents due to the high consumption of antibiotics (12).

The possible reuse of treated municipal wastewater from treatment plants for agricultural and industrial activities may be a solution in water management (13). The irrigation of agricultural lands with waste water discharge leads to the existence of pharmaceuticals into solid sewage sludge (14). In addition, animal farming releases veterinary pharmaceuticals to the environment directly from fields. Disposal of drugs by the consumer is the other channel of pharmaceutical residuals to be discharged into the inland waters (15).

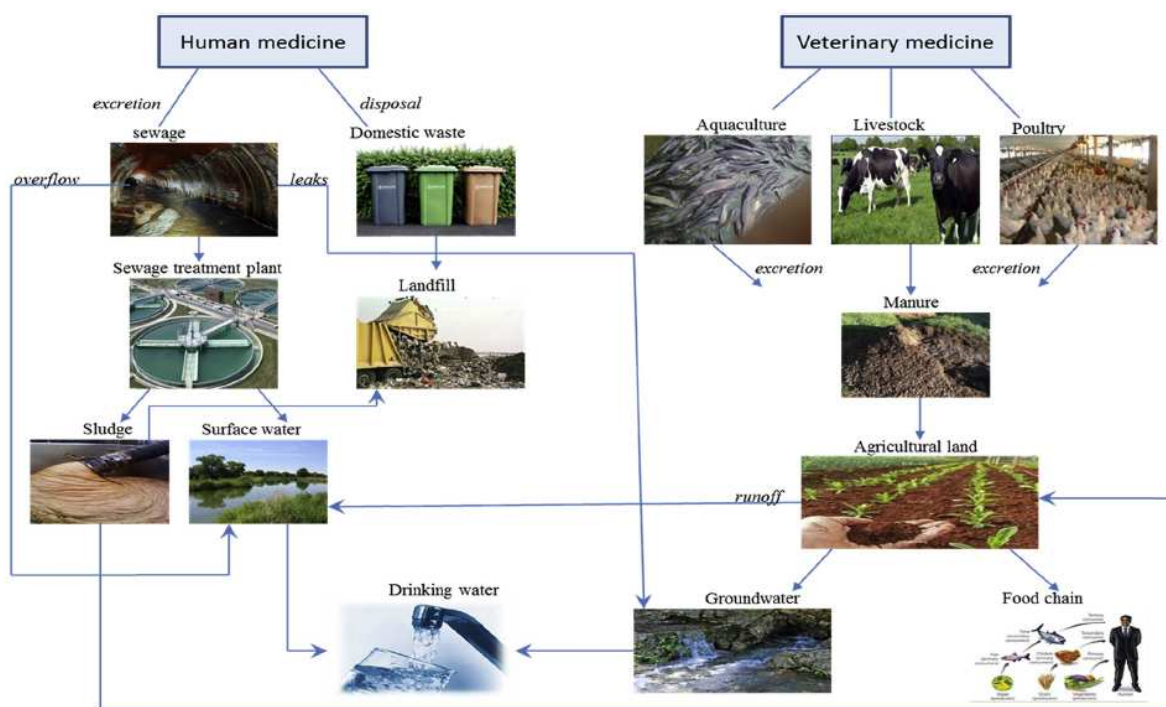


Figure 2. Pathway of pharmaceuticals and personal care products in water and soil (16).

Pharmaceutical wastes release has short and long-term effects on micro-organisms in the aquatic environment (15). The release of antimicrobials in the aquatic environment causes serious problems like toxicity effects on organisms, antibiotic resistance bacteria, and genes. Due to this, infection treatment with antibiotics becomes less effective (17). In addition, the standard environmental regulation only permits a maximum total pharmaceutical waste concentration of 0.05 µg/L in discharge water (18).

1.1. Cefixime as a pollutant model

Amongst pharmaceuticals, nearly 250 different antibiotics are recorded and used in human and veterinary medicine. 0.1 to 0.2 million tons per annum of antibiotics have been utilized all around the world (7, 19). Antibiotics are categorized based on their chemical structure or mechanism of action. They are divided into different classes e.g., tetracycline, macrolides, β -lactams, fluoroquinolones, and sulfonamides. The β -lactams antibiotics are the most popular antimicrobials in European countries. Based on the literature (7, 19), it has been identified that the β -lactams are detected at high concentrations (12680 ng/L) in WWTP effluent in India. Saeid et al. (20) reported a drug has been detected in a broad range of concentrations from 0.35 µg/L to 20 µg/L in rivers of Europe. A study (3) reported amoxicillin has the highest concentration among 38 detected pharmaceuticals in the Eastern Mediterranean Sea and it found about 127.8 ng/L. In Japan, a study reported (21) that six anti-cancer compounds were detected in the sewage treatment plant. Or in china, the mean concentration of twenty-four pharmaceuticals was detected ranging from 2.3 to 840 ng/L under the influent of the wastewater treatment plant (21).

A variety of antibiotics have been detected in many ground waters and surface water sources. One of the most important antibiotics utilized to treat infection is cefixime trihydrate (22, 23). Cefixime is a semi-synthetic antibiotic from the third generation of cephalosporins consumed against a variety of bacterial organisms (24, 25). About 40-50% of the oral dose of cefixime is excreted from the human body in wastewater (26). A study (22) indicated cefixime antibiotic recognized with a concentration between 278.65 and 422.1 ng/L in the aquatic environment. For example, cefixime concentration ranging from 19.24 to 43.33 µg/L in effluent samples of pharmaceutical factories in Vietnam (27).

Mirzaei et al. (28) have found amoxicillin, penicillin, ciprofloxacin, azithromycin, erythromycin, and cefixime antibiotics in the wastewater treatment plants, rivers, groundwater resources, and water treatment plants in Tehran, Iran, with concentrations up to 800 ng/L. The cefixime concentration was quantified in influent samples of Ekbatan and Teheran southern WWTPs in the range of 278-422 ng/L and 272-777 ng/L, respectively (28-30). The treatment configuration of the two WWTPs can remove cefixime from the aqueous phase ranging from 36-43% (28, 30).

Chapter 2. Water and wastewater treatment methods for antibiotic removal

Conventional biological water treatment plants including sedimentation, filtration, flocculation and physical and photochemical processes play a minor role in micropollutants removal (14). The studies (21, 31) that have investigated sewage treatment plans could not remove them completely. Or removal efficiency of pharmaceuticals with biological processes was low. In general, biological degradation of these compounds was related to the treatment process, physicochemical properties of compounds, microbial population, operational parameters, and so on. Biological treatment has a low price and simple mechanism but it brings problems such as time-consuming and low efficiency.

Several promising applications have been employed for antibiotic removal including physical, chemical, and oxidation processes (32).

The various type of absorbents like powder-activated carbon, granular carbon, zeolite (33), activated carbon nano-tubes, clay, graphene oxide (32), ion-exchange resins and other bio-based or non-bio-based materials have been widely used for antibiotic removal as physical absorption. Cigeroglu et al. (34) studied cefixime removal with the magnetic nanoparticles rGO-chitosan (reduced graphene oxide) composite beads as absorbent. They reported 30.63 mg/g of antibiotic absorbed onto the surface of the composite beads in the optimal conditions. In the study (26) adsorption of cefixime was studied by activated carbon driven from date press cake. With this method adsorption capacity between 557.9 and 571.5 mg/g has been obtained. Absorption process is effective with simple and low-cost design and operation (34). But the high material cost, limited adsorption capacity (31, 32), and high regeneration cost are major obstacles for absorbents (31).

The other antibiotic removal technology is the use of membrane filtration. This method is a mechanical process and is classified by the nominal pore size as microfiltration, nanofiltration, and reverse osmosis. In membrane filtration methods physicochemical properties of the pollutant (32), size and molecular weight of pollutants are considered as the main parameter (31). Clogging of membranes (12), susceptibility to chemical properties and organic materials salinity of the solution (31) are disadvantages of membrane technologies.

Flocculation is an interesting method in environmental engineering due to its high efficiency and simple operation. However, it is not practical for complex pollutants (31). Coagulation is a low-cost method that involves the destabilization, agglomeration, and settling of stable soluble molecules, ions, or particles. Surface charge, coagulant dosage, and operating factors are the main elements in this process (32). Coagulation-filtration is the most prominent chemical process applied in pharmaceutical water treatment. Wetlands are another artificial method that combined soil, plants, and microorganisms to treat contaminated water (33).

Adsorption, filtration, flocculation, and coagulation water treatment technologies exclusively concentrate the pollutions and transfer them to their phases without destroying or eliminating them (12, 13). So effective alternative methods like Advanced Oxidation Processes (AOPs) are required to improve water treated quality.

2.1. Advanced oxidation processes (AOPs)

Advanced oxidation processes (AOPs) are a good alternative for pharmaceutical treatment methods that are based on physicochemical processes which involve the generation of highly reactive oxygen species or free radical species with low selectivity (21). The chemical oxidant generally used in AOP technologies include hydrogen peroxide (H_2O_2 ; $E^\circ = 1.8 \text{ V}$), persulfate ($\text{S}_2\text{O}_8^{2-}$; $E^\circ = 2.01 \text{ V}$), permanganate (MnO_4^- ; $E^\circ = 1.68 \text{ V}$), ozone (O_3 ; $E^\circ = 2.07 \text{ V}$), hydroxyl radical (OH^\bullet ; $E^\circ = 2.8 \text{ V}$), superoxide anion radicals ($\text{O}_2^{\bullet-}$), O^\bullet ($E^\circ = 2.42 \text{ V}$), hydroperoxyl radicals ($\text{H}_2\text{O}^\bullet$; $E^\circ = 1.7 \text{ V}$), Cl_2 ($E^\circ = 1.36 \text{ V}$) and alkoxyl radicals (RO^\bullet) (15, 21, 35, 36). The common AOP technologies applied for pharmaceutical removal are categorized into ozonation, Fenton, sonolysis, radiation (UV and UV/peroxide oxidation), electrochemical oxidation, radiation, and photocatalysis (21) which are summarized in figure 3 (37).

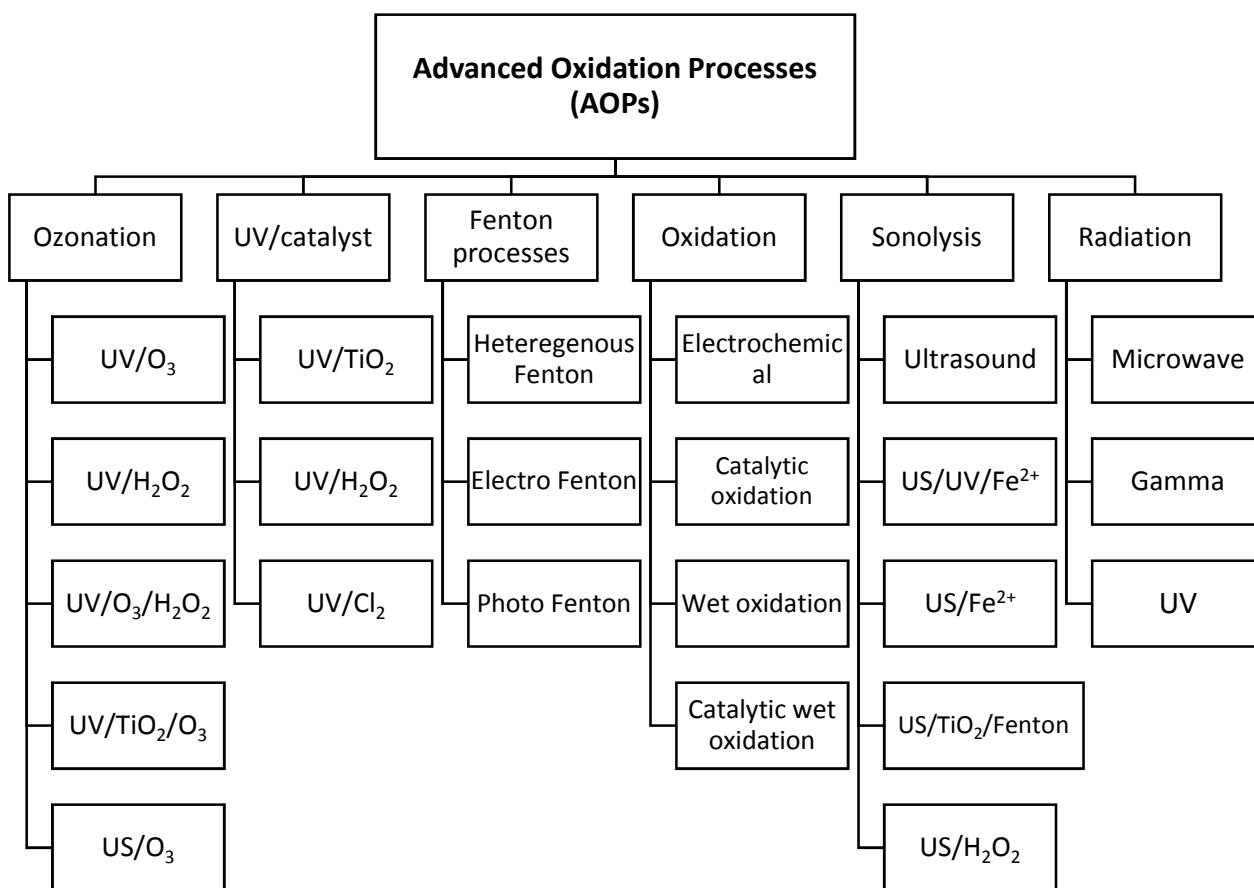
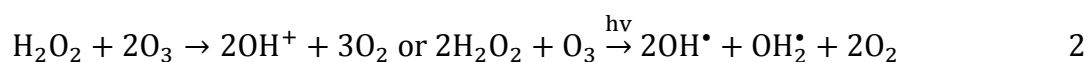
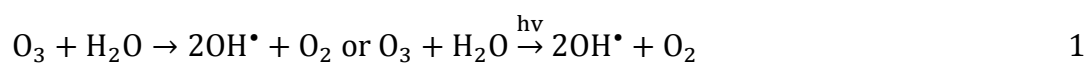


Figure 3. Overview of Advanced Oxidation Processes (AOPs) applied for pollutants removal (7, 37).

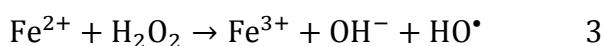
Ozon: ozone has strong power to generate hydroxyl radicals and is usually performed at high pH values ($\text{pH} > 8$) (7). Different reagents can be used in ozonation to boost oxidation reactions, for instance, $\text{O}_3/\text{H}_2\text{O}_2$, also called the peroxin process, O_3/UV , $\text{O}_3/\text{catalyst}$ (38), and the $\text{UV}/\text{H}_2\text{O}_2/\text{O}_3$. In comparison, $\text{UV}/\text{H}_2\text{O}_2/\text{O}_3$ process was the most powerful ozone oxidation method (15).

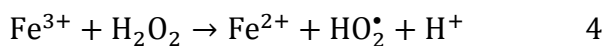
The reactions of O_3 with and without H_2O_2 are given in the following equations (eq. 1-2) (1, 7):



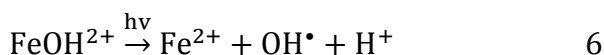
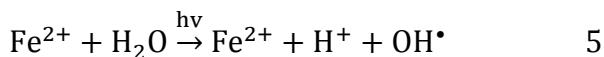
This application has disadvantages like high energy demand and high cost due to the short lifetime of ozone (21).

Fenton: this reaction is based on the use of iron salts, the reactivity of Fenton increased with the mixture of H_2O_2 as oxidant (7). Reactions are shown in the following reactions (eq. 3-4) (21):



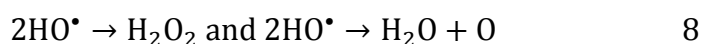


The Fenton process can be performed under artificial and solar UV-vis radiation (21) to enhance additional OH^\bullet (7). Iron salts act as photocatalysts and H_2O_2 as an oxidizing agent. The reactions (eq. 5-6) are presented below (7):



The efficiency of Fenton-based methods were greatly affected by water matrix, concentration of iron salt, acidic pH, H_2O_2 concentration, and source of iron species (21).

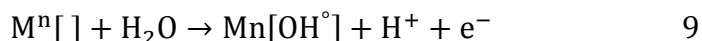
Sonolysis: another AOP technology is ultrasound irradiation also known as sonolysis. This method is based on the production of hydroxy radicals from pyrolysis of water as shown in the equations 7 and 8 (21):



Degradation of pharmaceuticals related to the power and frequency of ultrasound. Demanding high energy and low mineralization keep this technique on the lab scale and it may be combined with other AOPs to decrease costs (21).

The combined use of the electro-Fenton process with the ultrasonic process or also called sono-electro-Fenton led to better performance. These hybrid methods rise the hydroxyl radicals and hydron radicals. As a consequence of this method, at acidic pH, 94.5% of cefixime molecules break down due to higher ferrous ions and adding H_2O_2 in the experiment (12, 39).

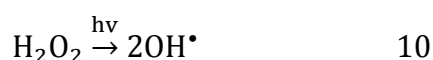
Electrochemical: in the electrochemical method, reactive species generate electricity without any chemicals. Direct oxidation at the anode surface and indirect oxidation on the surface of electrode are mechanisms in this oxidation process. Conventional anodes like Pt, IrO_2 , PbO_2 , RuO_2 , SnO_2 , (38), and boron-doped diamond (BDD) are used in electrochemical oxidation for pharmaceutical compounds (21). BDD is the most applied electrode because of its low cost and high stability (38). The key reaction is (eq. 9) (15):



In a study (40), the electrochemical (EC) technique was used for antibiotic degradation, this reactor was made with aluminum/aluminum electrodes and applied to study four operating parameters effects. The results of EC process indicated cefixime removal efficiency increased at these conditions: pH = 7.5, retention time = 72.5 min, current intensity = 6.0 amperes, and primary concentration of cefixime = 5.75 mg/L. Or in another published paper (41), electrochemical was combined with H_2O_2 to increase the degradation efficiency.

Radiation: in UV and UV/peroxide process, UV absorption of a compound is the main parameter. UV combined with peroxide usually showed better degradation performance in pharmaceutical treatment (21). UV-based processes usually consist of low pressure or medium pressure mercury lamps and UV-light emitting diode (LED) (38). Belghadr et al. (39) used the UV/H₂O₂ process to cefixime degradation, they concluded that 9 mg/L can be degraded completely in 180 min.

Besides UV-based AOPs, gamma irradiation also has been used for hydroxy radicals or hydrated electrons formation to degrade pharmaceuticals. There is no requirement for additional chemicals (21). Microwave radiation in the range of 300 MHz-300 GHz has been used for water treatment in combination with H₂O₂ or TiO₂. Unfortunately, most of the applied microwave energy was converted to heat so a cooling device was required for the system (38). UV (photolysis) and UV/peroxide mechanisms depend on the light intensity, peroxide type and concentration, water matrix and chemical structure of pollutants (21). UV light radiation consists of wavelengths from 200 to 400 nm was traditionally used for photolysis. The mechanism of H₂O₂ cleavage into OH[•] presents in the following reaction (eq. 10) (15):



With increasing irradiation time, the organic pollutants are degraded into their intermediate and finally mineralized to CO₂, water, and inorganic compounds (13).

AOP hybrid techniques: hybrid AOP techniques increased removal efficiency due to the synergistic effect which enhances the concentration of reactive species. Many studies have examined coupling AOPs in pharmaceutical degradation (21). A review paper has been written on the integration of AOPs with membrane filtration. They reported a combination of these methods increased AOP efficiency. However, these hybrid membranes required high cost (15).

It is evident that using various AOPs is more efficient while increasing method's costs. To overcome this disadvantage coupling AOPs technology with conventional wastewater treatment plants can be suggested to enhance the degradation efficiency (21).

The UV radiation generation by lamps or ozone production costs are high, so the future application of AOPs must improve through the use of sunlight (42). Solar energy as an alternative source of irradiation can be applied for OH[•] generation (15). Several processes such as photo-Fenton, heterogenous photocatalysis, or modified photocatalysis used sunlight use up to 600 nm. The sunlight at wavelengths over 600 nm is not useful for these AOPs (42).

2.1.1. Semiconductor photocatalysis

The slight difference between photolysis (radiation) and photocatalysis is the presence of a photocatalyst. Photocatalysis is one of the most promising technology for the destruction of

pharmaceutical compounds in the aquatic environment, it is based on semiconductors in the presence of artificial or solar irradiation (43, 44). In semiconductor structures, the conduction band and valence band are formed by the lowest unoccupied and the highest occupied molecular orbitals, respectively. The separation between these states is known as the band gap or energy gap that has any electron inside. In photocatalysis, photons can be seen as a reactant and have a critical role (45). As illustrated in figure 4, with sufficient photon energy, electrons in the valence band exited to conduction band as well as positively charge holes create in the valence band (46):

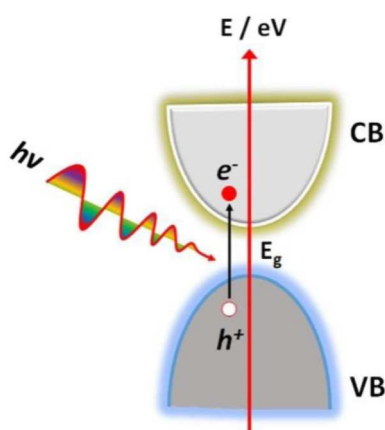


Figure 4. Schematic of the typical semiconductor excitation by band gap illumination (46).

In semiconductor photocatalysis, schematically is presented in figure 5, the photocatalytic activity is explained as follows: initially, an electron-hole (e^-/h^+) pair is generated in the semiconductor particles when radiation of energy greater than or equal to the band gap is arrived on the surface. Electrons are excited from the valence band (VB) to the conduction band (CB) of the semiconductor, thus creating an electronic vacancy at the valence band edge. The valence band hole is strongly oxidizing, whereas the conduction band electron is strongly reducing. A hole can migrate to the surface and oxidize an electron donor; in turn, while at the surface, the semiconductor can donate electrons to reduce an electron acceptor. Consequently, the semiconductor particle can act as either an electron donor or an electron acceptor for molecules in the surrounding medium, depending on the charge transfer to the adsorbed species (19, 21, 47).

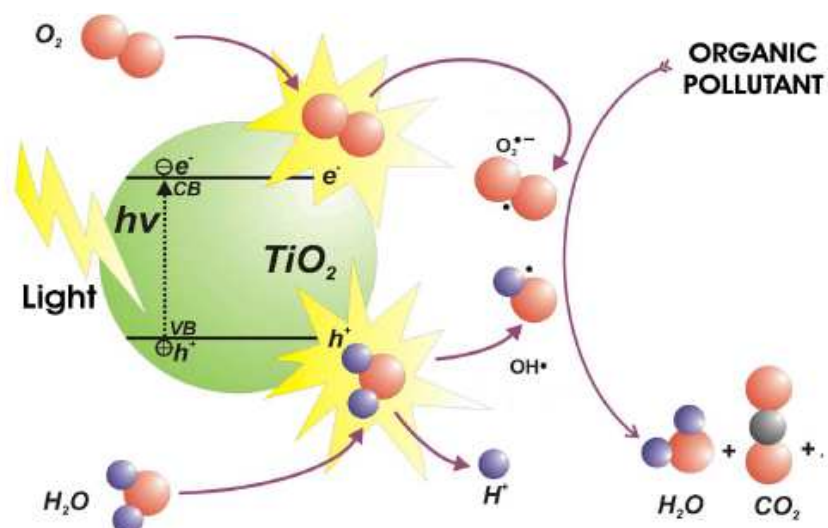


Figure 5. Schematic of semiconductor excitation by band gap illumination leading to the creation of “electrons” in the conduction band and “holes” in the valence band (48).

There are three possible paths for photo-excited electrons: 1) be captured and trapped by defect sites, 2) recombine and release energy to heat or light, and 3) migrate to the surface and generate radicals. The third path plays important role in the photocatalysis process and it should be enhanced for increasing efficiency (46).

A vast number of works studied different semiconductor photocatalytic activity by their structure modification. For example, Nano-diamonds (NDs)- TiO_2 composites synthesized by oxidation, hydrogenation, and amination to investigate the role of porosity, nitrogen, and oxygen functionalities on TiO_2 -based photocatalytic performance under near-UV/vis irradiation ($\lambda = 366, 436, \text{ and } 546 \text{ nm}$). High degradation efficiency for amoxicillin was achieved because of surface functionalities incorporated on the ND materials (oxygen = 6.3%, nitrogen = 2.1%) and their porosity ($\sim 0.37 \text{ cm}^3/\text{g}$). The rate constant for antibiotic removal varied from 25.6×10^{-3} to 0.0833 1/min . The stability of the catalyst samples demonstrated that a decrease of the rate constant could be described by alteration of surface chemistry and the presence of adsorbed intermediates via strong interaction with the carbon network of the ND (49).

Boussatha et al. (50) reported the performance of the thin nanogranular ZnO layer which was synthesized by the sol-gel method for pharmaceutical removal under UV irradiation. The thickness of the films decreased for various ammonium acetate (NAC) incorporation between 10% and 100%. Grains varied from 50 nm to 25 nm for the low NAC contents ($\leq 10\%$) and high NAC contents ($\geq 100\%$), respectively. The degradation efficiency ranged between 45% and 65% for all samples and thickness did not influence the photocatalytic performance. In addition, the top layers support the degradation reaction, so very thick layers use a low amount of material.

The NiO ($E_g = 3.6\text{--}4\text{ eV}$) was loaded on nano-clinoptilolite (NCP) particles by ion-exchange method at different concentrations. The XRD results confirmed that ion exchange did not damage the structure of NCP and the particle size was estimated at 30 nm. The red shift was observed in the band gap of the photocatalyst. Photolysis of cefixime under Hg-lamp irradiation was 8% after 2 h which confirmed UV radiation could break some bonds of cefixime molecules and produce chemical structures that needed more powerful radicals. Results confirmed that supported NiO on nanoparticles of clinoptilolite increased photocatalytic activity due to super adsorption capacity in gathering organic pollutants near NiO particles. In addition, ion exchange of NiO on NCP sites prevented the aggregation of NiO particles and also prevented e^-/h^+ recombination as an electron acceptor. After 300 min irradiation suspension, maximum efficiency was 80% at optimal parameters (51).

BiOBr is another semiconductor, its band gap is $E_g = 2.85\text{ eV}$ with visible light absorption at 435 nm. The 3D flower-like BiOBr catalyst was prepared by precipitation method. Cefixime removal efficiency obtained 86.78% after 120 min visible light irradiation (52).

Despite the existence of various semiconductors photocatalyst (oxides or sulfides) such as ZnO ($E_g = 2.8\text{ eV}$), ZnS ($E_g = 3.7\text{ eV}$), Fe_2O_3 , CdS ($E_g = 2.5\text{ eV}$), BiOBr, NiO, WO_3 ($E_g = 2.8\text{ eV}$), SO_2 , Fe_3O_4 , Mn_2O_3 , CeO_2 (53) and TiO_2 , they don't contain all properties of ideal photocatalyst (53-55).

2.1.1.1. Properties of TiO_2 semiconductor

TiO_2 has been widely used in a variety of applications like anti-fogging plants, photovoltaics (solar cells), as a coating for self-cleaning surface (56, 57), sensing applications and photocatalysis of organic pollutants (58, 59). The TiO_2 photocatalyst is available at three crystalline phases: anatase, rutile, and brookite. All TiO_2 phases are TiO_6 octahedra but defer in both the distortion of their octahedra units and the manner in which they share edges and corners. As shown in figure 6, the different structural arrangements result in different space group (46).

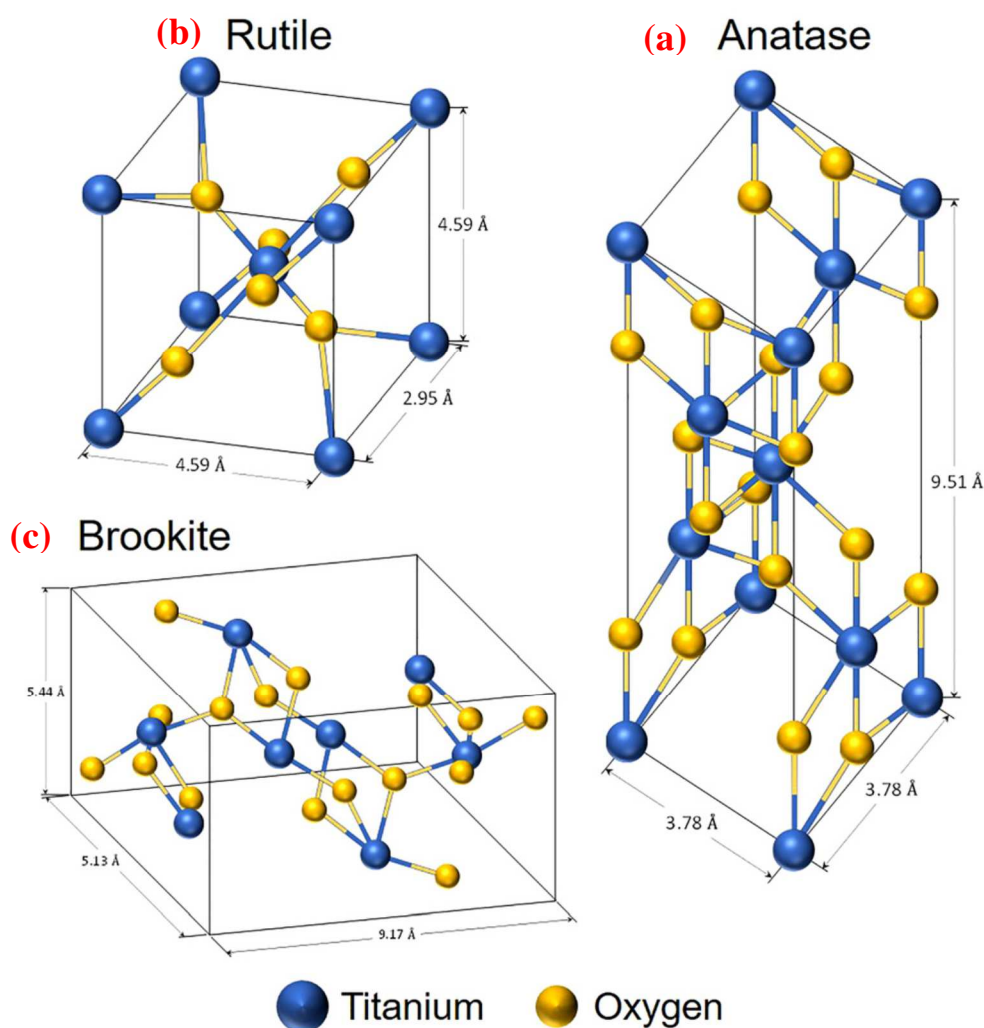
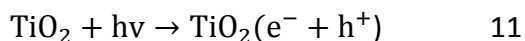
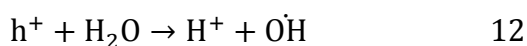


Figure 6. TiO_2 crystalline structures: (a) anatase, (b) rutile, and (c) brookite (60).

Anatase possesses an energy band gap of 3.2 eV with an absorption edge at 386 nm which lies in the near UV range. Rutile has a narrower energy band gap of 3.02 eV with an absorption edge in the visible range at 416 nm (61). The anatase phase has a notable photocatalytic activity due to its thermal stability and adsorption power (62). Brookite is stable at very low temperatures and thus is not suitable for photocatalysis application (63).

Semiconductor photocatalysis especially TiO_2 has been accorded great significance in recent times due to its potential to mineralize a wide range of organic pollutants at ambient pressure and temperature under artificial and solar radiation (43, 64, 65). In fact, the catalyst is commercially available at various crystalline phases, biologically inert (54), water insolubility, acid resistance, superior redox ability, hydrophilicity (66), corrosion resistance (58), and physical and chemical stability (21, 47). In this process, TiO_2 photocatalyst can be used as commercial or synthetic in suspension or fixed mode. The TiO_2 photocatalysis involves some reaction mechanisms (eq. 11-15), which have been discussed in the literature (55, 67-69).





In a study (21), eight commercial TiO₂ photocatalysts were investigated for amoxicillin degradation, P25 Degussa resulted in maximum efficiency due to its lower e⁻/h⁺ recombination ratio. The TiO₂ P25 Degussa has higher photocatalytic activity than other available commercial TiO₂ due to its structure of mixture anatase: rutile phase (70).

In another study (69), amoxicillin photocatalytic degradation was investigated with commercial TiO₂ (Aldrich, purity 99%) in a solar pilot plant with compound parabolic collectors (CPCs). The results showed that amoxicillin antibiotic degradation efficiency was affected by TiO₂ dosage, pH, and initial concentration of pollutant. The optimum conditions found were TiO₂ dosage = 1.5 g/L, initial concentration = 17 mg/L and pH=9.5 for amoxicillin degradation under 240 min solar irradiation.

There were several studies related to optimizing the synthesis of different types of TiO₂ materials like core-shell nanoparticles (71), nanotubes (59, 72), nanofilms on substrates (73-76), and nanoparticles (77). Titanium dioxide can be deposited by various techniques, including sol-gel (78), hydrothermal (61, 79), solvothermal (80), physical vapor deposition (PVD) (81), chemical vapor deposition (CVD) (82), and plasma enhanced chemical vapor deposition (PECVD) (57, 83).

The TiO₂ nano-powder was synthesized by the sol-gel method and was crystallized at different temperatures from 100 to 800 °C. The increase in temperature induced the anatase to rutile phase transformation. The rutile phase was started at a temperature higher than 600 °C. The position shift in Raman spectra depended on the O/Ti stoichiometric ratio. Photocatalytic activity of nano-powder in the anatase phase was better than pure rutile due to faster e⁻/h⁺ recombination in the rutile phase (78). Low cost is the most advantage of the sol-gel method (63).

The hollow TiO₂ microspheres were prepared via facile solvothermal technique with various organic solvents. Catalyst structure and morphology were affected by moderate polarity, boiling point, and viscosity of the solvent. Under Hg lamp radiation, 0.5 mg/L of TiO₂ powder could be removed completely Rhodamine B after 120 min (80). The hydrothermal method is generally executed in steel pressure vessels called autoclaves with/or without Teflon liners under controlled temperature and pressure in an aqueous solution (58).

Table 1 presents the comparison between synthesized photocatalysts in other published results based on TiO₂ photocatalyst for removal of cefixime.

Table 1. Cefixime degradation with various photocatalysts in literature.

Catalyst	Deposition technique	Cefixime concentration	Catalyst concentration	Irradiation source	Degradation efficiency	Irradiation time (min)	Ref.
TiO ₂	Hydrothermal	10 mg/L	0.2 g/L	Natural	85%	120	(84)
Fe/TiO ₂	Solvothermal			solar light	90%		
TiO ₂ /GO/chitosan	Chemical method	20.29 mg/L	0.327 g/L	Artificial light	95.34%	60	(25)
Bi ₁₂ TiO ₂	Sol-Gel	10 mg/L	1.5 g/L	Artificial light	94.9%	180	(24)
TiO ₂	Commercial	20 mg/L	0.001 g/L	Artificial light	94.5%	90	(85)
N-TiO ₂ /GO	Electrophoretic	5 mg/L	Fixed on sheet	Artificial light	29%	120	(86)

In water photocatalytic processes, TiO₂ catalysts were generally used in the form of powder. The main trouble in this approach at an industrial scale is the catalyst recovery step. This method has its benefits and defects, slurry systems have high efficiency due to excellent mass transfer between catalyst and fluid (55). Smaller TiO₂ particles which have a high surface-to-volume ratio, have great specific areas (58). In slurry-type systems illumination of all catalyst particles were difficult because the light penetration was limited, and further away particles from the light source (13).

Studies in wastewater treatment by TiO₂ photocatalysis remained on the laboratory scale due to some technical obstacles. Nano powder has a more specific surface area while they may agglomerate in slurry form as well as they need filtration (58). Small particle sizes lead to high filtration costs. Difficulty in the recovery of nanosized particles is one of the limitations in the application of TiO₂-based photocatalytic degradation of pollutants. One approach is fixing them into a support structure such as glass beads, fiberglass, glass sheets, stainless steel, quartz beads, and polymeric films (13).

Support materials have to satisfy several features like strong adherence between catalyst and support, non-degradable or reactivity with catalysts, sustainable in high calcination temperature, cheap, and mechanical stable (63). To this end, many excellent studies have been published on the immobilized photocatalysts onto a variety of surfaces. Numerous techniques were reported for preparing supported titania, for instance, sol-gel (spread coating and dip coating) (63), PECVD, and which aid to make the photocatalysis method an environment-friendly process in large-scale water treatment industries. TiO₂ film has its own advantages and disadvantages, when TiO₂ nanoparticles were immobilized on supporting materials or membranes, the material loss decreased during water treatment. In addition, the

TiO₂ film could be connected to an external electric power source to reduce the e⁻/h⁺ pairs recombining (58).

Chapter 3. Generalities of plasma-enhanced chemical vapor deposition (PECVD)

In general, plasma is an ionized gas that can be generated by several methods, including electric discharges (glow, microwave, plasma jet, radio frequency, and so on) (87, 88). Plasma known as the fourth state of matter is derived from gas through ionization dissociation and excitation of atoms or molecules. Plasma induced reactive particles such as electrons, ions, and free radicals (89). Depending on their energy level, temperature, and ionic density, plasmas are usually classified as high-temperature plasmas (for nuclear applications) and low-temperature plasmas (including thermal and non-thermal plasmas) (76, 90, 91).

The low-temperature plasmas have been used in catalyst preparation (76, 90, 91). Thermal plasma is an electrical discharge process and the electron temperature is equal to gas temperature and ions ($T_e \approx T_i \approx T_g \approx 1500\text{-}10^6$ K, 10-15 eV) that takes advantage of highly energized electrons. Thermal plasmas are also named equilibrium plasmas. Thermal plasma can be used for solid and liquid waste recovery, hydrogen production, CO₂ conversion, etc. But at the industrial level, it can be costly (76, 89-91).

Non-thermal (cold) plasma occurs in the temperature range of 300-50000 K and the electron temperature is greater than the gas temperature and ions ($T_e \gg T_i \approx T_g \approx 10000\text{-}50000$ K, 1-10 eV). On the other hand, the bulk temperature in cold plasmas can be as low as room temperature, while the electron temperature can reach as high as 10,000-100,000 K. Thus, the cold plasmas are so-called non-equilibrium plasmas (76, 90, 91).

Chemical vapor deposition (CVD) refers to methods in which material precursors are condensed from a vapor state to form a solid-phase material (58). This is a good method for TiO₂ films in a short period of time. Various CVD processes differ in reaction conditions. Atmospheric pressure CVD (57), plasma enhanced chemical vapor deposition (PECVD), metal-organic CVD, and physical CVD are the subscribe of CVD (63, 92). Usually, these methods used to fabricate different nano-materials in different forms. CVD methods could take place in a vacuum condition and they make a facile approach to covering supports surface in comparison with other technologies (58). On other hand, these methods indicated a strong interaction between surface and photocatalyst (63).

PECVD uses electric power as an activation source for producing ionized species and radicals from gasses or vapors (i.e. Argon). The recombination of radicals of the plasma phase leads to the formation of a thin film in one step on any substrate, whatever its nature and size may be. In the case of TiO₂ as plasma-deposited material, PECVD enables to control of the size of TiO₂ nanoparticles and also the thickness and microstructure of the thin film (76, 90, 91). This

is a promising strategy for preparing a mixed crystalline phase of TiO_2 like P25 Degussa (46). The anatase thin film can be obtained without post-annealing if the substrate temperature is above 450 °C or a bias voltage is applied. Most of the time PECVD was carried out at low pressure where the reactions and the coating characteristics were well-controlled (89). PECVD has advantages as follows:

- Significant reduction in substrate temperature relative to CVD.
- High deposition rate.
- Excellent mechanical properties.
- Suitable for the fabrication of functionally graded films.
- Wide-ranging control of plasma reactions and plasma-surface interactions to optimize the film composition (93).
- High purity.
- Good step coverage.
- Easy control parameters (94, 95).

In addition, PECVD makes possible the doping of TiO_2 deposits (adding Co, Fe) to shift the band gap energy to a lower value and, as a consequence, to improve the solar light efficiency (76, 90, 91).

3.1. Plasma parameters effect on films deposition

The TiO_2 deposited films have been affected by operational parameters of plasma enhanced chemical vapor deposition process. In the following text, different studies are presented that investigated TiO_2 preparation with plasma techniques under various operation conditions.

In a published paper (96), TiO_2 deposition was investigated with the PECVD technique. As figure 7 presented, the thickness of TiO_2 film was increased by higher argon flux and shorter plasma distance because of an increasing number of TTIP vapor molecules. But in the lowest Argon flux, the TiO_2 growth slightly depended on plasma volume. The higher Ti–O abundance at higher pressure (22.5 Pa) and 3 cm distance can be explained by a larger amount of precursor vapor molecules in the gaseous phase and having more time for TTIP decomposition, respectively.

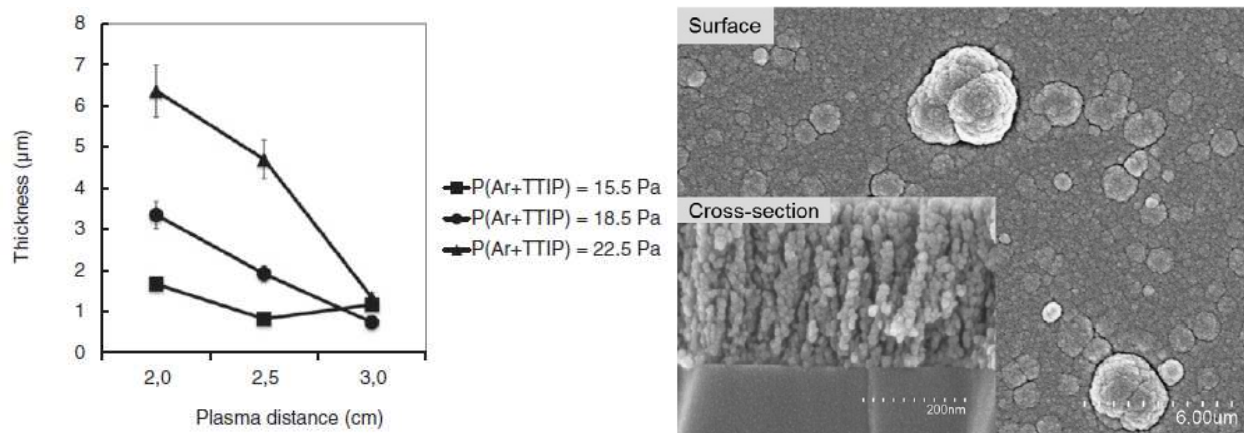


Figure 7. (a) Effect of argon flux and plasma distance on thickness of TiO₂ thin films (b) SEM images of TiO₂ thin film on silicon substrate prepared with $P(\text{Ar} + \text{TTIP}) = 22.5 \text{ Pa}$ and $d_p = 3.0 \text{ cm}$ (96).

The TiO₂ films on substrates were prepared by sol-gel and PECVD methods. The films with the sol-gel method were continuous, pinhole-free, and smooth. The films with the PECVD method showed that aggregates were increased by increasing discharge power from 100 to 300 W. The film thickness in sol-gel method decreased from 120 to 80 nm by increasing annealing temperature from 300 to 500 °C. But in the PECVD method particles size were increased (85, 150, and 525 nm for 100, 200, and 300 W) by increasing power (see figure 8). Granulate structures were observed for both methods and the distribution of spheres was uniform. The XRD analysis for sol-gel films showed the anatase phase but RF PECVD confirmed the amorphous structure. In the photocatalysis process, the rate of bacterial death increased with increasing annealing temperature due to the crystalline structure of the anatase. The photocatalyst efficiency was about 98% with PECVD TiO₂ films (97).

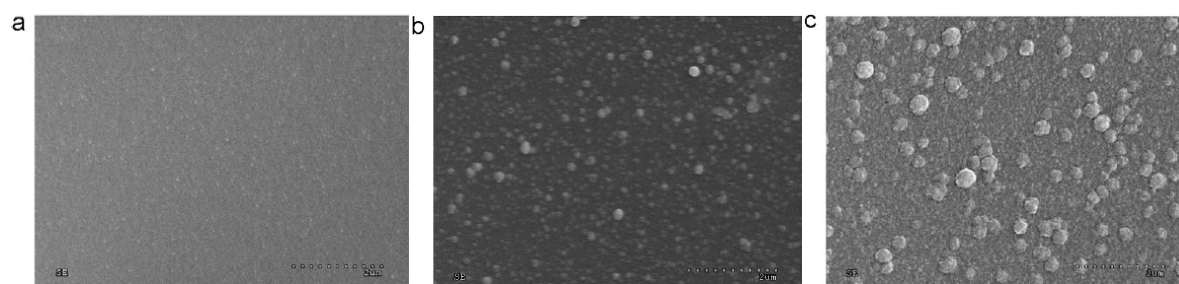


Figure 8. SEM images of the TiO₂ films deposited by RF PECVD with the glow discharge power of (a) 100 W, (b) 200 W, and (c) 300 W (97).

Szymanowski et al. (98) concluded the thickness of films increased by increasing radio frequency power and there was not any saturation when power was changed from 20 to 300 W. The results of UV transmittance analysis demonstrated that transmittance increased by power increasing, and optical gap (E_g) was increased.

A large diameter of particles could obtain by high power discharge and small particles tend to agglomerate. The roughness parameters increased by increasing power and annealing slightly increased the values (99).

Kim et al. reported (100) the thickness of TiO₂ films coated on glass beads decreased by increasing power from 5 to 30 W due to increased plasma and glass temperature but the uniformity of film was increased. The film thickness increased by increasing reactor pressure and TTIP flow rate, but in reactor pressure, the growth was not proportional.

In another study, optical gap and thickness increased with increasing radio frequency power. After calcination at 450 °C, the anatase phase was begun to appear in Raman spectra (see figure 9). High roughness was achieved for 200 and 300 W power and was about 6.4 and 11.6 nm, respectively (83).

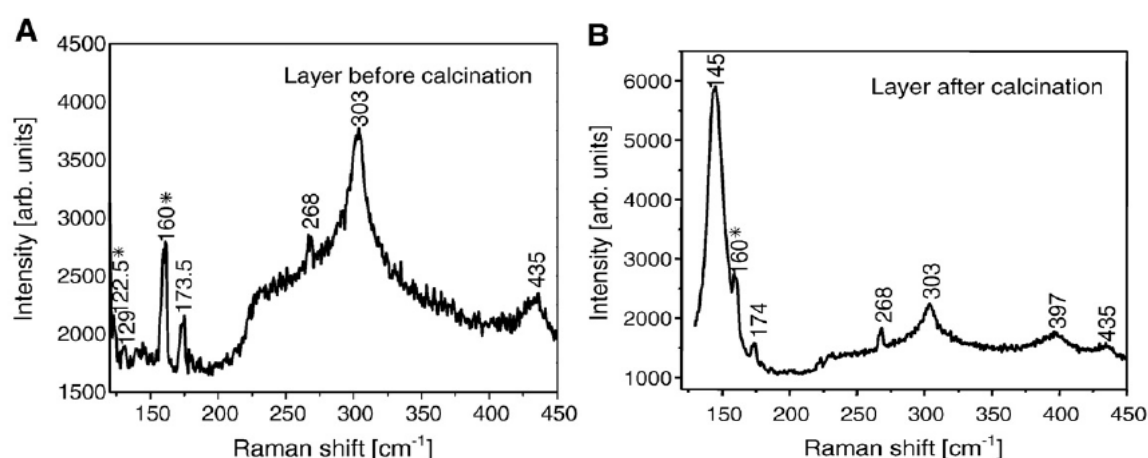


Figure 9. Raman spectrum of TiO₂ film deposited at 200 W: (A) before and (B) after thermal annealing at 450 °C for 1 h (83).

TiO₂ film was deposited by plasma-assisted CVD and remote plasma CVD on some substrates and was annealed from 500 to 900 °C for 4 h. Increasing oxygen partial pressure from 5 to 10 sccm could increase the oxygen content and decrease the carbon content on the films. The type of precursor did not have any effect on oxygen content. In remote plasma CVD, the anatase phase was achieved at 400 °C deposition temperature (82).

Yang and Wolden (93) examined the growth of TiO₂ thin film with PECVD and thermal CVD methods with different oxygen ratios. Deposition rate varied from 3 to 30 nm/min as a function of oxygen ratio (see figure 10). The equivalence ratio was used to explain the combustion content of hydrocarbon for obtaining the deposition rate. The deposition ratio decreased by increasing oxygen concentration and radio frequency power. The anatase phase was observed at 450 °C deposition temperature.

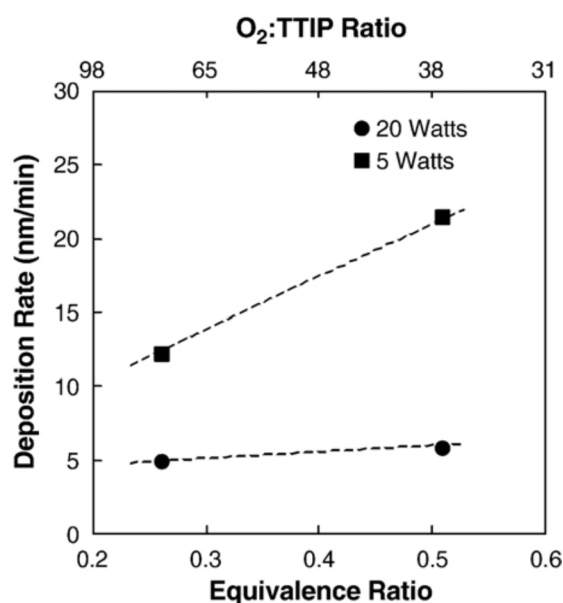


Figure 10. PECVD deposition rate as a function of equivalence ratio at 5 W (squares) and 20 W (circles) (93).

As figure 11 presents, by increasing radio frequency power, the deposition rate increased due to an increase in activated reactive species. The oxygen flow rate had an optimum deposition rate and the best one was obtained at 100 sccm in all radio frequency power ranges. The reason for oxygen flow could be explained by the reduction of adsorption sites for TTIP because oxygen gas was predominantly adsorbed. In conclusion, deposition with the PECVD process was controlled by surface reaction of the Langmuir-Hinshelwood type. The XRD analysis showed anatase construction after 600 °C annealing at optimum condition and changed from anatase to rutile in 900 °C annealing temperature (94).

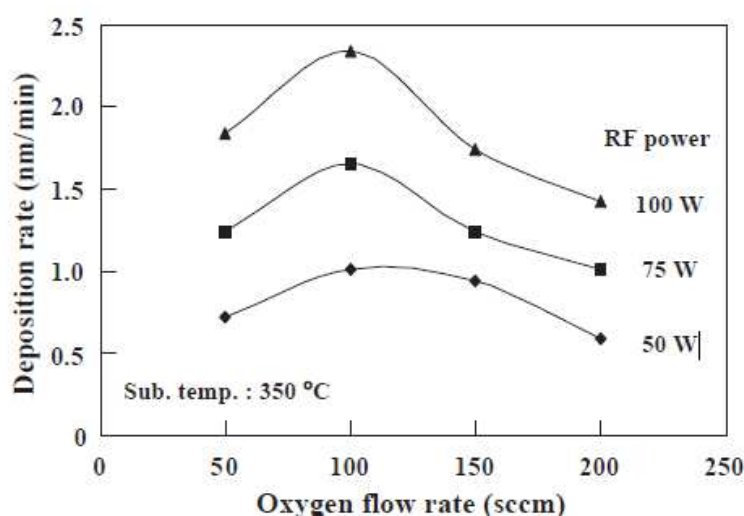


Figure 11. Deposition rate as a function of O₂ flow rate in PECVD with different radio frequency power (94).

Srivatsa et al. (95) investigated the influence of deposition pressure (30-100 Pa) on TiO_2 films. Based on their results, the average crystalline size was about 58 nm. SEM images of these films are displayed in figure 12, these indicated the morphology of anatase structure was changed by various deposition pressures. At 50 Pa, the films formed as nanorods but at 80 Pa the forms were nanoparticles. The growth mechanism of titania nanostructure at a pressure above 30 Pa was related to the bombardment of energetic ions and supersaturation of the feedstock vapors and gasses.

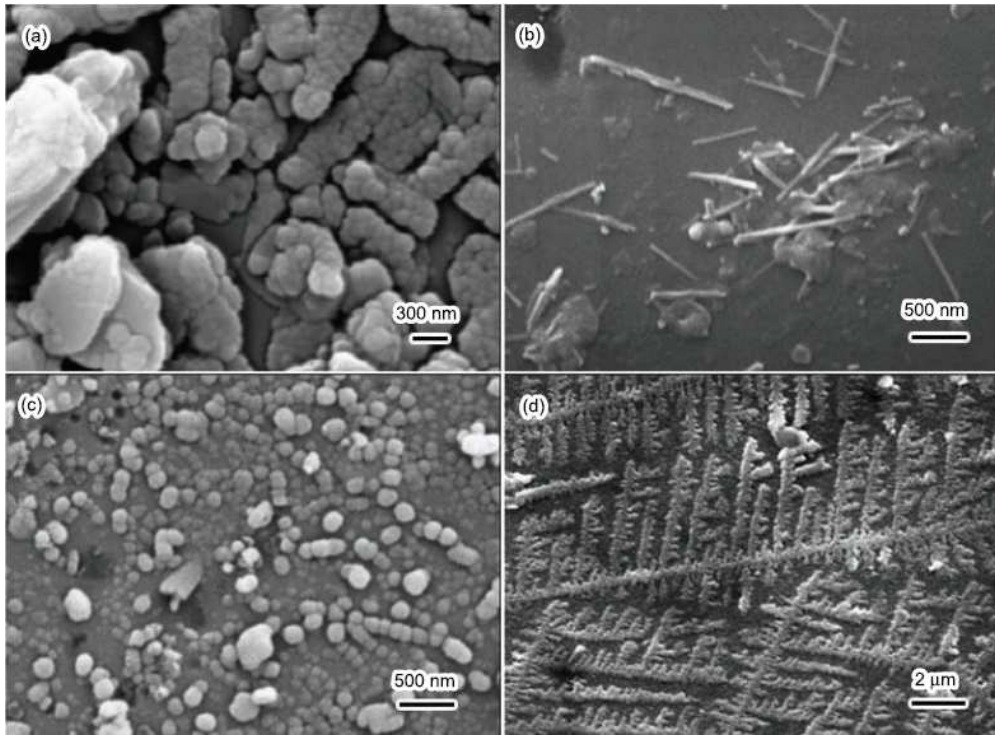


Figure 12. SEM micrographs of anatase titania synthesized by PECVD at room temperature: (a) clusters of nanocrystals at 30 Pa (0.3 mbar), (b) nanorods at 50 Pa (0.5 mbar), (c) nanoparticles at 80 Pa (0.8 mbar), (d) comb-like structure at 100 Pa (1 mbar) (95).

Simionescu et al. (56) studied the Ar/O_2 ratio effect on the structural parameter of TiO_2 . They reported, the lattice strain increased significantly when oxygen flux varied between 0 and 2 sccm. On the other hand, the average crystallite size decreased strongly for different Ar/O_2 flow rates. The XRD results display in figure 13, the rutile phase appeared as the oxygen flux increased from 0 to 0.5 sccm. The roughness was the same for all samples with a continuous thin film. The band gap increased with decreasing oxygen flux from 3.31 eV to 3.9 eV due to oxygen vacancies in the TiO_2 lattice.

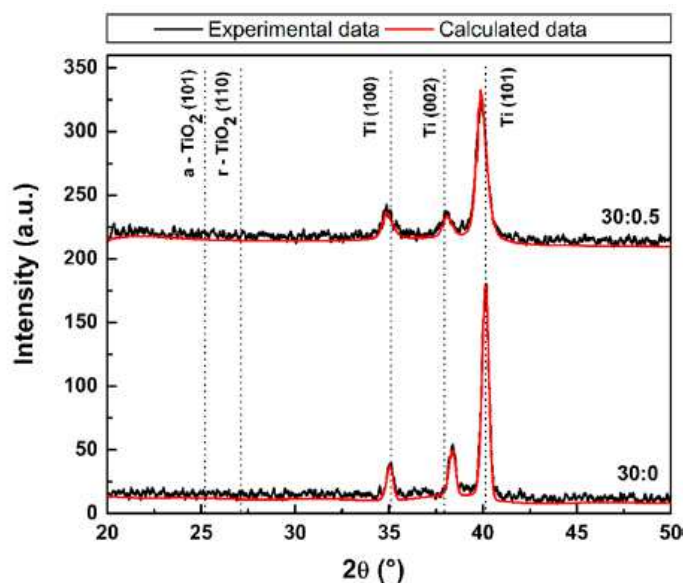


Figure 13. XRD patterns of a TiO₂ thin film deposited under Ar/O₂ = 30:0 and Ar/O₂ = 30:0 sccm flow rate (56).

3.1.1. Modification of TiO₂ photocatalytic activity by doping

Structure, surface morphology, and electronics of TiO₂ have an important role in photocatalytic activity (21, 101). The major limitations in TiO₂ photocatalytic activity are: 1) large band gap and using UV region, and 2) fast recombination of electron/hole pairs during the photogenerated process. Therefore, it is essential to modify TiO₂ properties to shift its absorption threshold from the UV region to the visible region and reduce the rate of e⁻/h⁺ pairs recombination (58, 102).

Based on the literature, doping materials in TiO₂ lattice could modify its photocatalytic activity by decreasing the band gap. Several approaches have been applied including metal doping (e.g. Ag, Cu, Ce, Fe, Al) (57), non-metal doping (e.g. C, B, F, N) (103), co-doping with metals/non-metals, dye sensitization, coupling with carbonaceous materials (e.g. graphene) and metal oxides and coupling two semiconductors (58). Cation doping can replace Ti with cations and produce an intermediate impurity level in the energy band that acts as an electron donor or acceptor. Anion doping replaces the O in the TiO₂ structure and consequently decreases the band gap by shifting it upward (46). These materials enhanced the photocatalytic efficiency by modifying the band gap, surface area, or particles size (104).

Aba-Guevara et al. (105) investigated Fe, N-co-doped TiO₂ materials with sol-gel (SG) and microwave (MW) methods. The band gaps of co-doped TiO₂ obtained ~2.53 eV (SG) and ~3.00 eV (MW), the difference for E_g values was due to the amount of incorporated carbon into the materials.

The iron-doped ZnO-SWCNT-COOH nanomaterials were synthesized for antibiotic degradation under UV-A irradiation. The optical band gap of the photocatalyst was decreased from 3.2 to 3.08 eV compared with pure ZnO. The performance of the ZnO photocatalyst increased with metal doping and the cefixime molecule was degraded at about 94.19% (106).

In other research (107), photo activities of SrTiO_3 and $\text{TiO}_2/\text{SrTiO}_3$ microspheres which prepared by hydrothermal method and decorated with Pt, Rh, and Ru nanoparticles by the photo-deposition method. The SrTiO_3/Ru catalyst exhibited a higher phenol degradation rate than non-modified SrTiO_3 and $\text{TiO}_2/\text{SrTiO}_3$ under UV-Vis and visible light.

Graphene- TiO_2 nanotubes (GN-TNT) were prepared by hydrothermal method and used for pharmaceutical degradation under UV-A light radiation. The crystalline size of GN-TNT was less than 20 nm and had optical adsorption at 360-800 nm. Band gap energy for 15% GN was measured at 2.66 eV. The GN addition can effectively improve the photocatalytic properties and the optimum was 10% because increasing amount gives black color so light shielding increased (108).

3.1.1.1. Mn doping in TiO_2 structure

The doping of metals in the TiO_2 structure affects the crystallization process, photocatalytic activity, and extension of the adsorption spectrum into the visible light range. Among these dopants, Mn is attractive because of its variable valence states, as well as its significant influence on particle size. Doping Mn in TiO_2 created intermediate energy states within the band gap. Mn^{4+} ions could easily replace Ti^{4+} ions in the lattice of TiO_2 . Moreover, doping of Mn with TiO_2 made a magnetic photocatalyst with recyclable properties, it aided in magnetic separation from aqueous solution after wastewater treatment. High photodegradation efficiency needed two conditions: firstly, higher crystallinity to decrease electron/hole recombination rate, second was a large surface area (104).

Synthesis of Mn and Co co-doped TiO_2 for antibiotic degradation was prepared by the sol-gel method. No impurity peaks in XRD patterns indicated Mn^{2+} and Co^{2+} ions were substituted in the TiO_2 lattice. As shown in figure 14, slight shifting and widening could explain by the strain that was induced with Mn or Co and the reduction of crystallite size. Increasing the lattice parameter "a" ($\text{TiO}_2 = 3.78 \text{ \AA}$, $\text{Mn-TiO}_2 = 3.81 \text{ \AA}$, $\text{Co-TiO}_2 = 3.83 \text{ \AA}$, $\text{Mn-Co-TiO}_2 = 3.84 \text{ \AA}$) could be attributed to the large radii of Mn^{2+} (0.66 \AA) and Co^{2+} (0.65 \AA) in comparison with Ti^{4+} (0.61 \AA) (109).

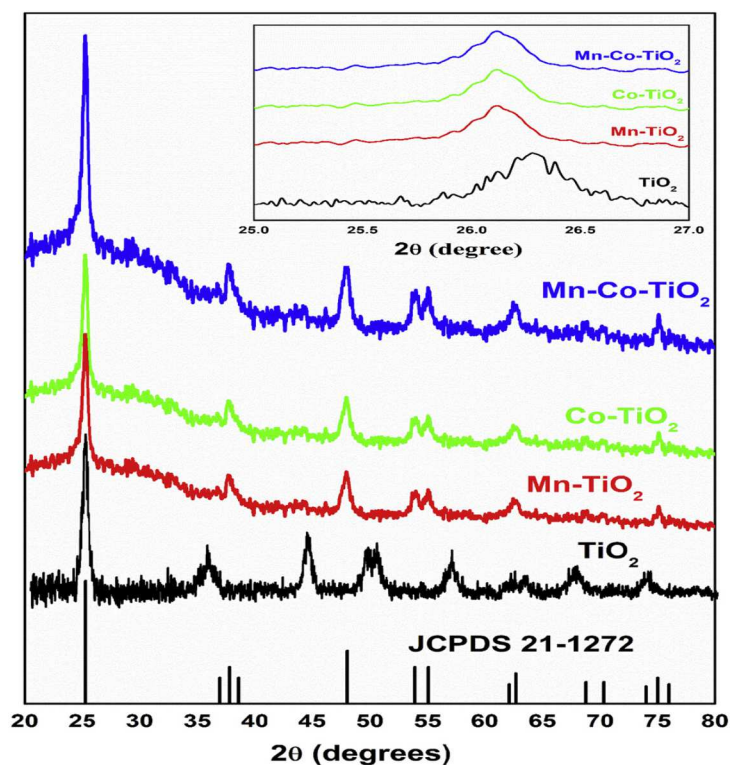


Figure 14. X-ray diffraction patterns of TiO_2 , Mn-TiO_2 , Co-TiO_2 and Mn-Co-TiO_2 (109).

Devi et al. (110) studied the effect of Mn, Ni, and Zn doping in TiO_2 nanoparticles for aniline blue removal under UV/solar irradiation. Ni-TiO_2 and Zn-TiO_2 had anatase phase but Mn-TiO_2 had both anatase and rutile phase due to its charge and ionic radius (see figure 15).

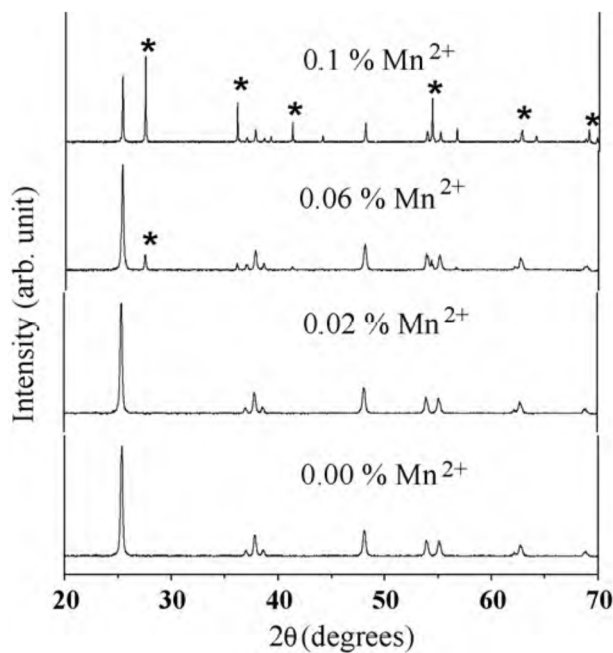


Figure 15. XRD pattern of $\text{Mn}^{2+}/\text{TiO}_2$ samples (111).

In photocatalytic degradation, dopant ions (Mn, Co, and Zr) had an impact to generate more e^-/h^+ which increased the efficiency. Maximum yield was achieved for both methyl blue and methyl orange dyes by Mn-TiO₂ after 240 min irradiation under visible light. The large surface area confirmed the synergetic effect between TiO₂ and metal ions (Mn, Co, Zr), so the photocatalytic performance enhanced by the surface modification (62).

According to published paper (110), the higher Mn content generated a high rutile fraction in the Mn-doped TiO₂ sample because the density of surface defects at the anatase phase increased. Thus, anatase to rutile transformation took place in defect sites due to their high energy. Catalyst with 1 wt.% Mn showed both anatase and rutile phase (111). On other hand, high content of Mn increased the crystallite size of TiO₂ and decrease surface area and agglomeration increased, so the optimum contents were required (112, 113). In pure TiO₂, the oxygen vacancies acted as luminescence enhancers then increase emission intensity but Mn disturbed the TiO₂ crystal lattice and broke the Ti–O bonds, and increased oxygen vacancies, so the photo excited electrons were trapped and localized in oxygen vacancies thereby decreasing the recombination of e^-/h^+ . Also decreasing particles size resulted in an increased number of defects (104).

High activity of Mn-TiO₂ was obtained because the TiO₂ polycrystalline network could effectively reduce the recombination of charge carriers. The small crystalline size decreased the diffusion path length for the charge carriers from production place to reaction place, so a reduction in this pathway reduced the recombination resulting in an enhanced interfacial charge transfer process (110, 114).

Mn doping on the Ti lattice sites acted as an intermediate band in the forbidden gap of anatase TiO₂ and was attributed to charge transfer transitions between Mn ion and conduction band or valence band of TiO₂. As shown in figure 16, it is observed that the band gap was 3.26 eV for pure anatase TiO₂, and for the Mn-doped (5%) sample, the band gap was reduced to 2.88 eV, Thus, tuning the optical band gap of TiO₂ by doping manganese leads to enhanced photocatalytic efficiency in the visible region. The degradation efficiency of Rhodamine B was 86% for Mn-doped TiO₂ under the visible light (at 5%) due to the decrease in particle size which resulted in higher specific areas. Also, Mn doping created intermediate bands that could help induce electrons and holes under various light wavelengths (104).

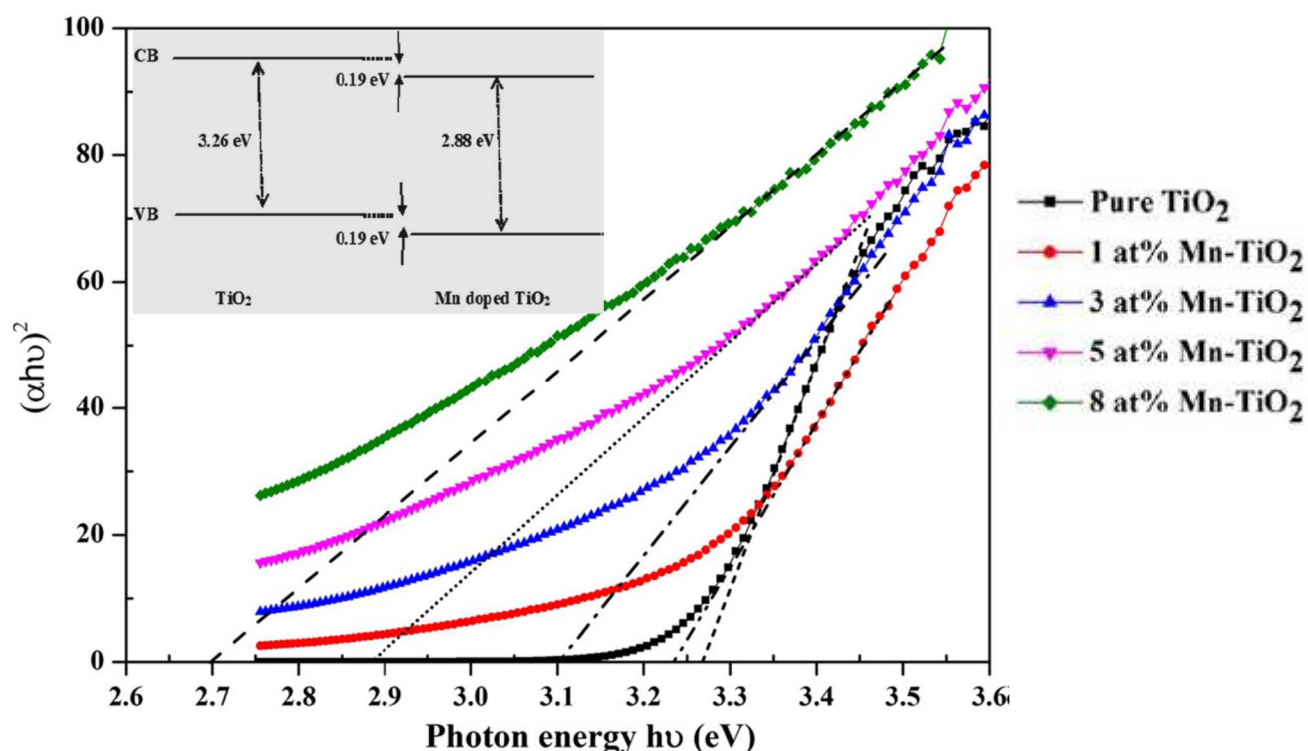


Figure 16. Variation of optical band gap with Mn atomic concentration and the energy level diagram of undoped TiO_2 and (5 at. %) Mn doped TiO_2 (104).

Mn doping introduced a new energy level in the band gap of TiO_2 that decreased the band gap energy. It also might be due to the overlapping of the d-orbital with the conduction band of TiO_2 that helped the absorption of visible light (115).

The lower band gap energy of Mn- TiO_2 can be attributed to the charge transfer transition between the Mn ion electrons and the TiO_2 conduction or valence band (116).

To this end, Mn-doped TiO_2 nanoparticles were obtained by the microwave-assisted hydrothermal method. Raman active modes for anatase were confirmed at 144, 197, 399, 516, and 639 cm^{-1} . The highest mode (144 cm^{-1}) corresponded to the symmetrical stretching of the O-Ti-O bonds. According to figure 17, as the amount of Mn in the samples was increased, a decrease in vibration frequency was observed comparing pure TiO_2 . These results confirmed the symmetry change in TiO_2 crystal structure, reinforcing the proposal that Ti^{4+} ions were replaced by the dopant. Also, Raman vibrational mode did not reveal Mn-oxide-associated absorption (77, 117).

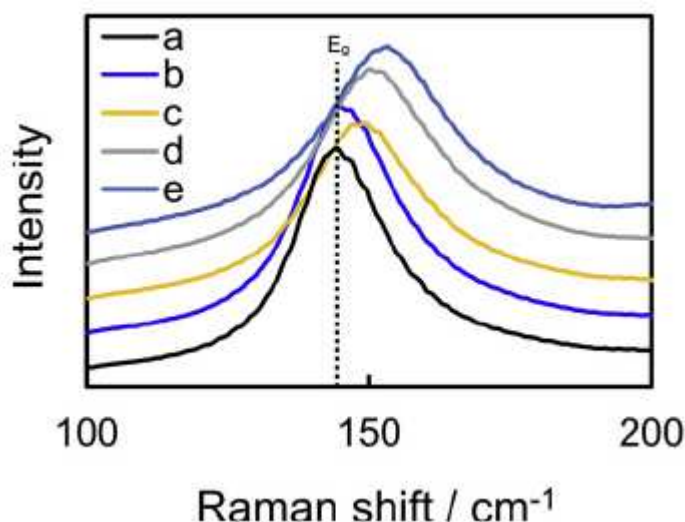


Figure 17. Raman spectroscopy shift of pure and Mn-doped TiO₂ nanomaterials: (a) TiO₂, (b) 1% Mn- TiO₂, (c) 2% Mn- TiO₂, (d) 4% Mn- TiO₂, and (e) 8% Mn- TiO₂ (117).

Chapter 4. Solar photochemical process

4.1. Solar energy

Population growth and demand for energy in the various regions of the world, especially in developing countries increase because all persons require modern energy services for their basic needs (118). The common types of energy production make environmental problems that put in danger the quality of life and natural ecosystems. The large majority of greenhouse gas emissions and climate change is the result of conventional fossil fuel sources like oil, coal, gas, biomass, etc. There is an increased recognition that will replace fossil fuels as the main future energy. Many alternative energy sources can be used instead of fossil fuels. The energy source should be utilized in each case and must be made on the basis of economic, environmental, and safety considerations. The most important benefit of renewable energy systems is the decrease in environmental pollution. Renewable energy technologies produce energy by converting natural phenomena into useful forms of energy. These technologies are solar energy, wind energy, biomass, geothermal energy, hydrogen, and ocean energy (119). Sun is suitable alternative energy for helping to solve environmental problems, also is a non-selective process, and is environmentally friendly (1). Solar plays an important role in providing pollution-free energy services and reduction of CO₂ emissions in the future (120).

The sun is a major source of renewable energy that can be utilized for light and/or heat sources. As observed in figure 18, the sun is a sphere of intensely hot gaseous matter 1.5×10⁸ km away from earth, so thermal radiation travels with the speed of light in a vacuum (300,000 km/s), after leaving the sun solar energy reaches our planet in 8 min and 20 s. The sun has an effective black-body temperature of 5760 K. The temperature in the central region is much higher. The sun's total energy output is 3.8×10²⁰ MW, which is equal to 63 MW/m² of the

sun's surface. This energy radiates outward in all directions. The earth receives only a tiny fraction of the total radiation emitted, equal to 1.7×10^{14} kW; however, even with this small fraction, it is estimated that 84 min of solar radiation falling on the earth is equal to the world energy demand for one year (about 900 EJ).

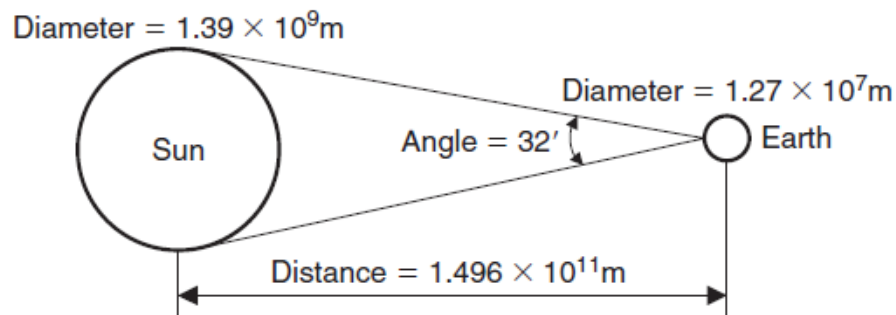


Figure 18. Properties of the sun (119).

Knowledge of the variation of solar incidence angle is necessary to calculate the amount of solar energy radiation received on a surface of a location (119).

In general, solar thermal technology is the most well-known application in drying, heating, cooking, cooling, etc. Classification of solar technologies is arranged into three common applications, 1) thermal technology, 2) photovoltaic technology (121), 3) solar fuels (119, 122).

As figure 19 shows, the large amount of sunlight receives in the regions of Africa, China, southern Europe, southern USA, Australia, and the middle east (120).

GLOBAL HORIZONTAL IRRADIATION

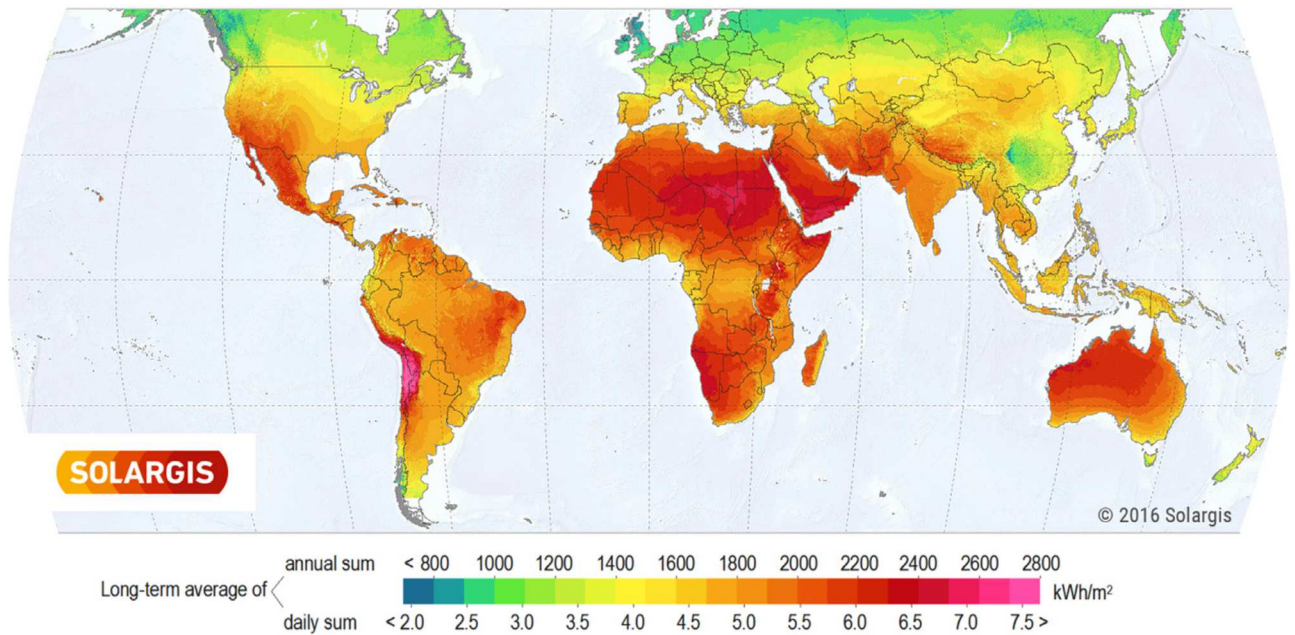


Figure 19. Global Horizontal Irradiation (120).

Various areas receive different amount of solar radiation annually. The earth's surface receives about 1000 W/m^2 at sea level on a clear day (123). The UV flux on the earth's surface is near $20\text{-}30 \text{ W/m}^2$ in the range of $300\text{-}400 \text{ nm}$ and puts $0.2\text{-}0.3 \text{ mol photons per m}^2 \times \text{h}$ (55).

Iran is located in the Middle East and is in a favorable position for the solar energy reception. It has suitable geographical locations for solar energy technologies because of the vast deserts (124). The number of sunny days in two-thirds of Iran is more than 300 per year (124). The estimated energy potential of total solar radiation is about $1800\text{-}2200 \text{ kWh/m}^2$ per year (125, 126). The annual mean daily of global solar radiation was 19.6 MJ/m^2 with the highest and lowest values being 21.6 and 14.11 MJ/m^2 respectively (125, 126). The sum of direct and diffuse components of solar radiation has been known as global radiation (127). Direct radiation is the portion of solar radiation that reaches the ground without being absorbed or scattered and radiation that is dispersed before arriving ground is diffuse (42). The diffusion fraction of total solar radiation was measured at about $7\text{-}12.5 \text{ MJ/m}^2$ during a year in different areas of Iran (124). As previously reported (125, 126), the annual average of sunshine in Iran is 3200 h and it differs in the wide latitudinal range. The recorded data for five cities in Iran showed that the monthly mean daily sunshine duration varied between 5 and 12 h (124), smaller values corresponded to the January and December of the year and it is larger in June and July (124). The highest solar radiation value is in central Iran which can be well recommended as having large potential for solar farms and other solar applications and facilities (125, 126). Therefore, appropriate utilization of this massive source of a freely accessible energy requires development of suitable technologies.

4.2. Solar photo-reactors

The most important difference between thermal and photochemical processes is the temperature role which means the temperature is not a significant element in the photocatalytic process (128).

Solar photocatalysis is based on the collection of high energy short wavelength photons (UV radiation) to promote photoreactions. The mechanism of solar photocatalysis has five steps: (1) transfer of reactants in the fluid phase to the surface of the catalyst; (2) adsorption of the reactants on the surface; (3) reaction in the adsorbed phase with the energy of a photon that activates photocatalyst; (4) desorption of the products; and (5) removal of products from the interface region (13, 19, 48, 58). Figure 20 presents the TiO_2 photocatalyst adsorption spectrum in comparison with the solar spectrum. This semiconductor can use natural (solar) UV because it has an appropriate energetic separation between its valence and conduction bands (55).

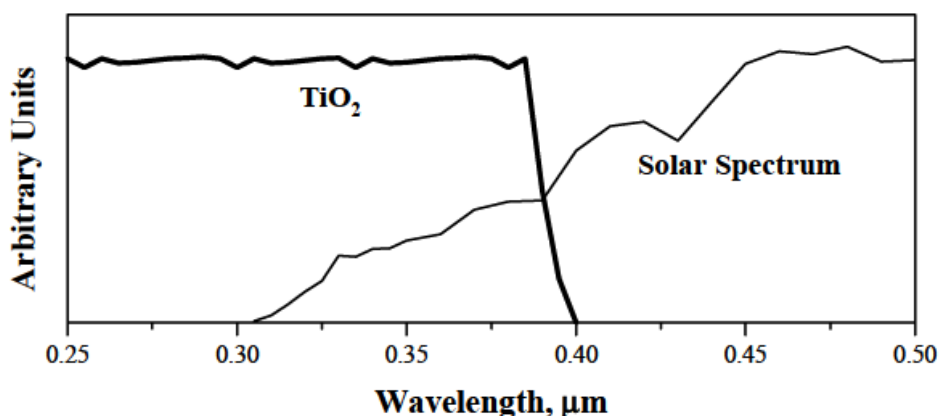


Figure 20. The TiO_2 photocatalyst adsorption spectrum in comparison with Solar spectrum (55).

Solar photocatalysis reactors require specific features to absorb and transmit solar radiation efficiently. Solar photoreactors efficiently should collect and reflect solar photons to promote catalyst reactions. The equipment that does this function is a collector. Solar collectors are mainly classified into concentrating and non-concentrating systems. The first model focuses solar light through a reflecting surface. Generally, non-concentrating designs have the potential for lower costs when compared to concentrating ones. There are five types of concentrating systems for water treatment methods. 1) parabolic trough concentrator (PTC), 2) compound parabolic concentrator (CPC), 3) parabolic dish concentrator (PDC) 4) Fresnel concentrator 5) optical fiber photoreactors (70).

4.2.1. Solar collectors

4.2.1.1. Non-concentrating

Non-concentrating collectors do not concentrate radiation and they have no tracking systems but these collectors are cheaper due to their low-cost manufactory. They use diffuse and direct solar radiations (55, 129). These collectors usually are in flat mode and facing the sun depending on the place's latitude. The main applications of non-concentrating collectors are inclined plate collectors as known thin film fixed bed reactors and water bell photoreactors (70). Two examples of these photoreactors are presented in figure 21.

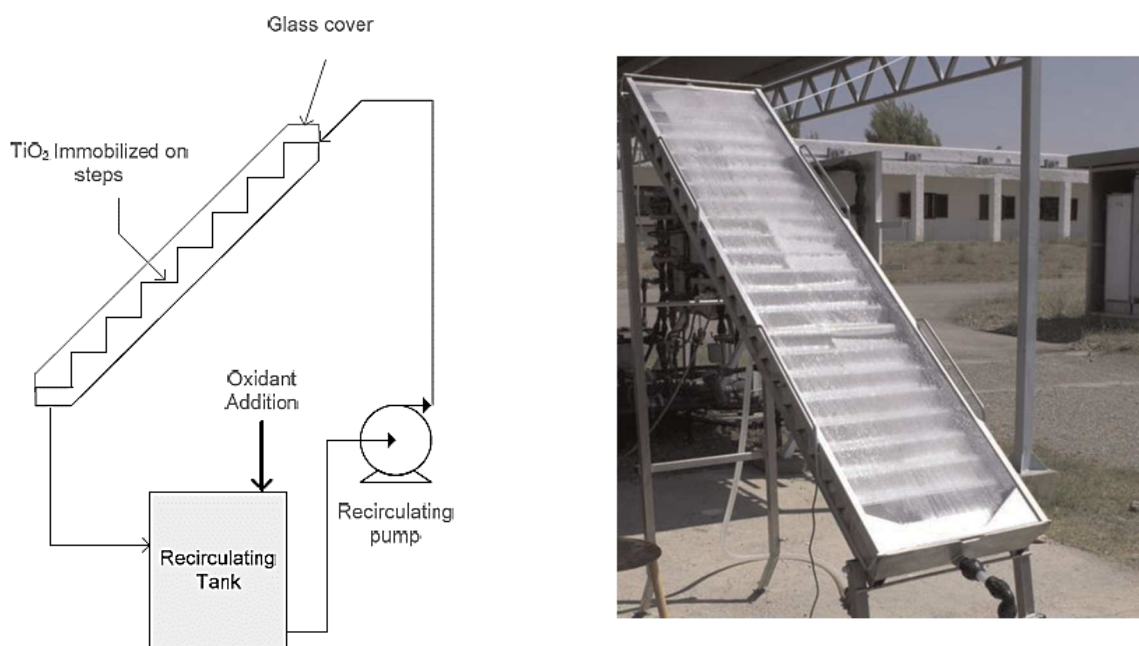


Figure 21. Example of non-concentrating photoreactor (130, 131).

The non-concentrating solar reactor systems have main features like simplicity and low-cost manufacturing and less surface is required for installation (their support structure). Their design and fabrication costs are low and work with both direct and diffuse solar radiations (70). But they can use in small-scale situations (129). The main drawback may be water losses because of interference with the atmosphere (132).

Several designs of non-concentrating reactors have been established and tested, in general, they can be classified as follows:

- Trickle-down flat plate, a fixed plate facing the sun that water and wastewater fall, a catalyst is normally fixed on the plate (133).
- Free-falling film is similar to Trickle-down flat plate and open to atmosphere, but with a higher flow rate.
- Pressurized flat plate, consisting of two plates between that fluid circulates using a separating wall (133).

- Tubular, consisting of many small tubes connected in parallel.
- Shallow solar ponds, small pond reactors having little depth.

A tubular reactor is more effective because of its structure; tubing is available in a large variety of materials and sizes, also its construction is economical (129, 134). In these reactors usually flow is laminar which produces mass transfer limitation and fluid evaporation (129).

4.2.1.2. Concentrating collector

4.2.1.2.1. Parabolic Trough Collector (PTC)

Parabolic Trough Collectors (PTC) is the original solar photoreactor that was designed for photochemical applications. The parabolic trough collector has one or two motors to trace solar radiation on one or two axes (east-west movement around a north-south oriented axis and north-south movement around an east-west oriented axis) (128) that keeps the collector aperture always perpendicular to solar rays (129). This structure aids to collect all the solar radiations on the collector aperture and reflects to absorber tube at the focal line where the wastewater flows. Using only direct solar radiation, low optical and quantum efficiencies due to higher e^-/h^+ recombination (128), and expensive design are its main drawbacks (55, 132).

As illustrated in figure 22, direct radiation is the portion of solar radiation that reaches the ground without being absorbed or scattered and radiation that is dispersed before arriving ground is diffuse.

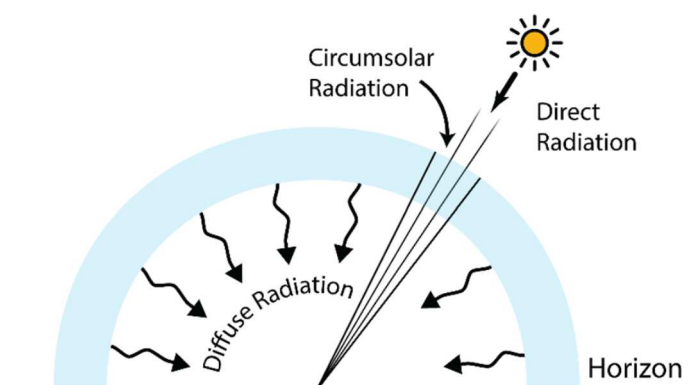


Figure 22. Global solar radiation include direct and diffuse (127).

The direct and diffuse radiation of sunlight is equal on the surface of the earth (42). The sum of direct and diffuse components of solar radiation has been known as global radiation (127). On other hand, fifty percent of the UV radiation for 4-6% of total solar radiation is in the diffuse part so PTCs do not have efficient performance on cloudy days (131). Figure 23 shows the schematic of the PTC system, the PTC application can be used for water heating, desalination, and water disinfection. The first outdoor engineering-scale of PTC reactor was designed and built at the National Solar Thermal Test Facility at the Sandia Laboratories in Albuquerque, New Mexico (USA), in 1989. In 1990, a similar plant was built at the Plataforma Solar de Almeria for water detoxification in Europe (42).

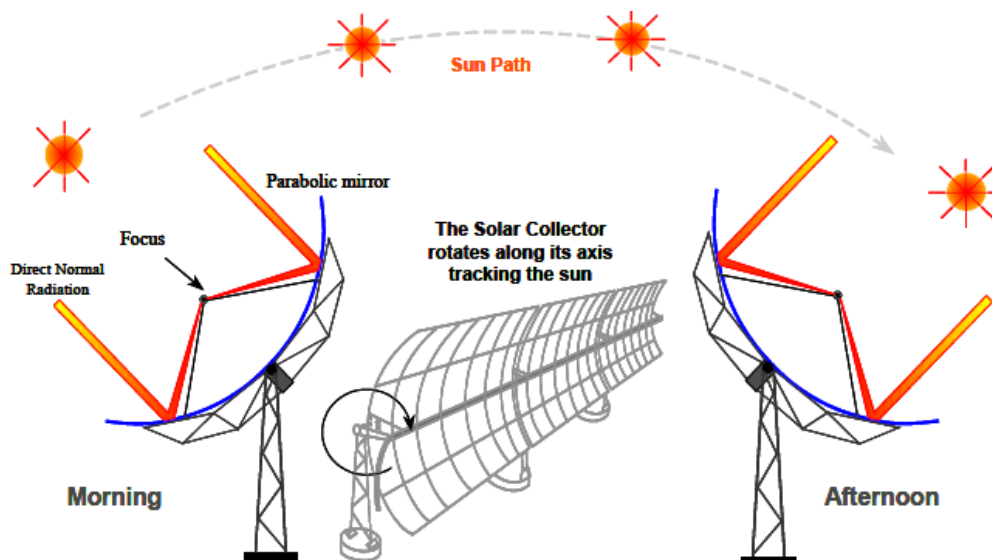


Figure 23. Schematic of a PTC photoreactor with one-axis tracking motor(135).

For the PTC reactor, the parabola equation is given by equation 16:

$$y = \frac{x^2}{4f} \quad 16$$

and C is the geographic concentration of the collector (eq. 17):

$$C = \frac{D}{\pi d} \quad 17$$

f is the focal length, D is the aperture width, and d is the reactor tube diameter (129, 136, 137). The concentration ratio of PTC systems is 5 and 20 (131).

4.2.1.2.2. Compound Parabolic Collector (CPC)

The collector for the photocatalytic purpose must be economical and efficient, CPC combines the characteristic of both technologies (PTC and non-concentration) and has none of their disadvantages of them. The CPC is a variant of a PTC concentrator under the category of concentrating solar reactor. They are static and collect all radiations (diffuse and direct) that reach the aperture area (45, 55) and then reflect around the back of the tubular reactor. So, they have higher optical and quantum efficiencies due to lower e^-/h^+ recombination (45, 128, 132).

The design of the CPC collector-based reactor with a tubular reactor presents in figure 24. A generic reflector point S can be described in terms of two parameters, angle θ , subtended by lines originating at O (center of the reactor tube) to A and R, and distance p, given by segment RS (eq. 18-19):

$$\theta = \overline{OA} \supset \overline{OR} \quad 18$$

$$\rho = \overline{RS} \quad 19$$

RS being tangent to the reactor tube at R. One important parameter for CPC definition is the angle of acceptance $2\theta_a$, which is the angular range over which all or almost all rays are accepted without moving the collector.

The solution is given in two separate portions, an ordinary involute for A to B (eq. 20) and an outer portion from B to C (eq. 21):

$$\rho = r\theta \quad 20 \quad |\theta| \leq \theta_a + \frac{\pi}{2} \quad \text{part AB of the curve}$$

$$\rho = r \frac{\theta + \theta_a + \frac{\pi}{2} - \cos(\theta - \theta_a)}{1 + \sin(\theta - \theta_a)} \quad 21 \quad \theta_a + \frac{\pi}{2} \leq |\theta| \leq \frac{3\pi}{2} - \theta_a \quad \text{part BC of the curve}$$

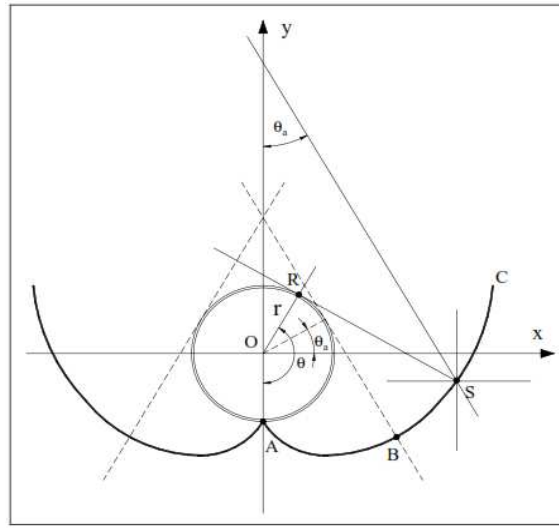


Figure 24. The geometry of CPC configuration (135).

The concentration ratio (CR) is the ratio of the collector aperture area to the reactor area. The concentration factor of a CPC is related to the acceptance angle, as per the equation 22 (70, 132):

$$CR = \frac{1}{\sin \theta_a} = \frac{A}{2\pi r} \quad 22$$

A is the aperture of the photoreactor, and θ_a is the semi-angle of acceptance. For photocatalytic application half of the acceptance, the angle is between 60 and 90, in this range, the absorber can collect both direct and diffuse rays. In the case of 90 where $CR = 1$ all UV radiations that receive on the aperture area can redirect to the tube (132). CPCs have high efficiency because of using both radiations without the need for a tracking system (55, 128, 137, 138).

4.2.1.2.3. Parabolic Dish Concentrator (PDC)

PDC systems are widely used for electrical and chemical energy from solar radiation and they reflect the sunlight on a spot-like focus. A PDC has a support frame with a sun tracking motor and works with direct radiation (70). A schematic drawing of PDC indicates in figure 25 and an image of a parabolic module was used at the University of Isfahan. The typical concentration ratio is in the range of 100-10,000 (128).

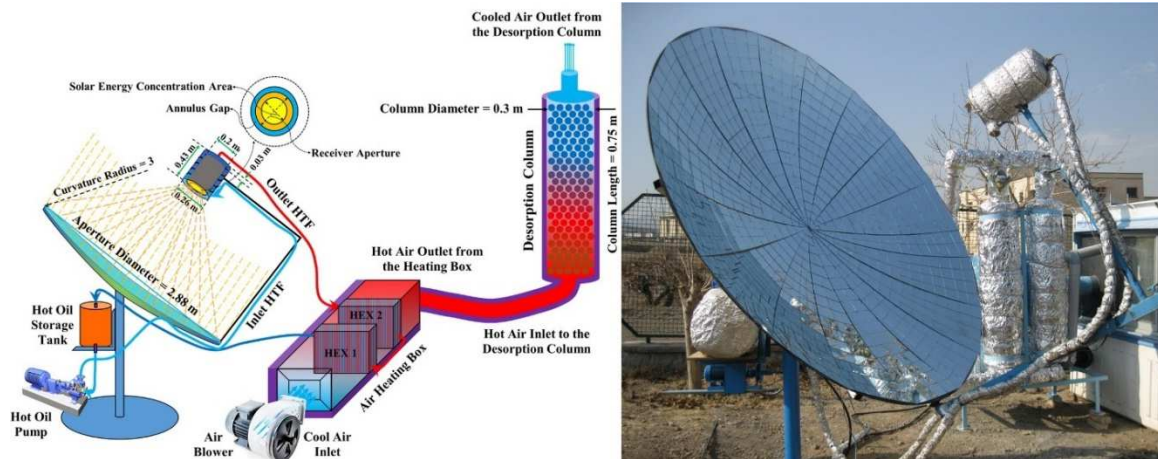


Figure 25. Schematic and photo of PDC at University of Isfahan (139).

4.2.1.2.4. Fresnel concentrator

Fresnel collector applied for solar energy production in a line or spot focus design. They use mirrors and lenses with a flat surface to track the sun's rays and concentrate onto a focal receiver which has usually a tubular design. Fresnel configuration has two advantages such as fixed and simple design and cheaper fabrication in comparison with PTCs. Figure 26 shows the common mode of Fresnel collectors (70). Fresnel lenses and PTC models concentrate solar light between 5 and 50 times (128).

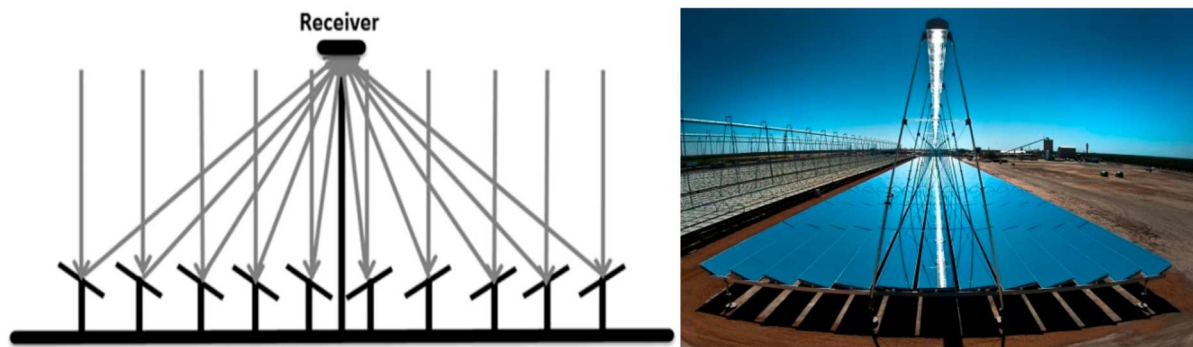


Figure 26. Schematic of Fresnel lens receiver(70).

4.2.1.2.5. Optical fiber photoreactors

In this model, the photocatalyst was directly fixed on the waveguides like optical fibers, and sunlight was used as a light source. To date, its complexity and low efficiency make it impractical for wastewater treatment (70).

4.2.2. Solar photoreactor's tube (absorber)

The requirements for the solar photocatalytic reactor are similar to other advanced oxidation processes. The reactor tube must be transmitted solar UV radiation and withstand summer temperature without no damage (55). It should be providing good mass transfer of the contaminant to the photocatalyst surface with the minimum pressure drop. In addition, it must not react with either the catalyst or the pollutants to be treated or their products. Photoreactor materials must be stable with regard to chemicals and low pH resistance (134, 140).

There are some choices of materials for photoreactors. Their advantages and disadvantages can be classified as follows in table 2 (55, 129).

Table 2. Advantages and disadvantages of various photoreactor tube (42, 132).

Type	Advantages	Disadvantages
Quartz	<ul style="list-style-type: none">• Excellent UV transmittance• Thermal and chemical resistance	<ul style="list-style-type: none">• High cost
Fluoropolymer	<ul style="list-style-type: none">• Good UV transmission• Chemical stability	<ul style="list-style-type: none">• Lower UV transmittance due to wall thickness• Lack of rigidity• High pressure drops
Commercial glass	<ul style="list-style-type: none">• Cheap• Thermal and chemical resistance	<ul style="list-style-type: none">• Absorbing UV radiation
Borosilicate glass (Pyrex)	<ul style="list-style-type: none">• Good UV transmission• Reasonable cost• Thermal and chemical resistance	

Therefore, Pyrex has the best choice of materials with a combination of cost and UV transmittance in large volumes (55). The transmittance of several types of glass and fluoropolymers like ethylene-tetrafluoroethylene (ETF) presents in figure 27 (42).

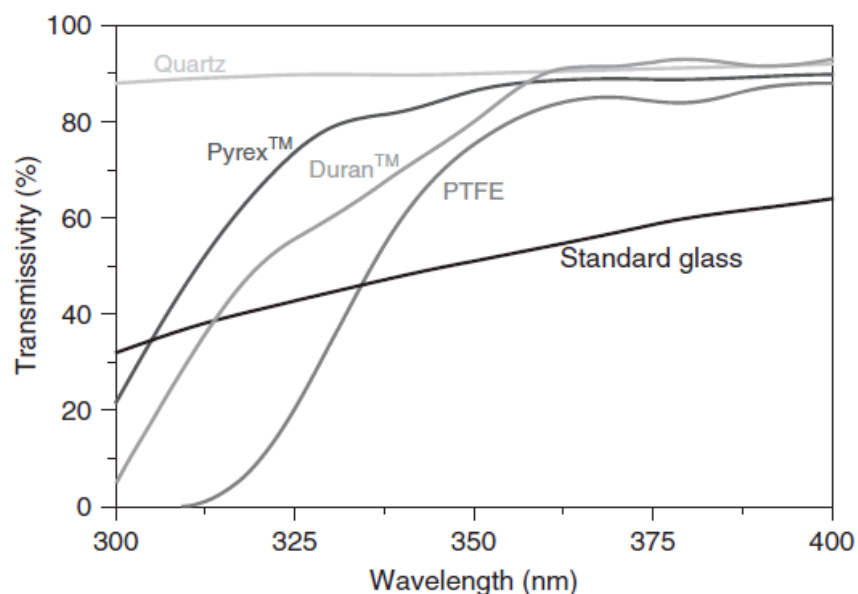


Figure 27. The transmittance of different materials suitable for solar photoreactor's tube (42).

One important factor is the photoreactor's diameter because uniform flow must be maintained. In a heterogeneous photocatalysis system, turbulent flow requires avoiding the sedimentation of catalyst particles. On the other hand, turbulent flow makes higher pressure drop, especially in the case of industrial-scale plants. For these reasons, the diameters of the photoreactor should be between 25 and 50 mm (128). It must be a guarantee that all arriving photons are kept inside the reactor. Very small diameters cause high-pressure drop and very high diameters make a dark zone, thus overall system efficiency decrease (42).

4.2.3. Reflecting material of solar collectors

The most important hardware in the solar photoreactor is the reflective surface. Reflecting materials should be reasonably cheap, have high reflectivity and weather resistance (70, 132). Since in photocatalytic application reflection of wavelength in the range of 300-400 nm is interesting, mirrors fabricated with aluminum covering, silver mirrors, and aluminum-coated plastic film are not suitable due to UV light filtering (128, 134) and their lack of rigidity. Aluminum is the best option and its reflection values are 92.3 and 92.5% at 280 and 385 nm, respectively. Comparable values for silver are 25.2 and 92.8% (42).

Other additional parts are the recirculation pump and tank. The pipes and connections must be made of materials which commercially available and resistant to oxidant conditions of the process. Another important issue is the reactivity of materials with catalysts or pollutants.

4.3. Solar photodegradation studies

When solar energy is used as a light source in the photocatalyst process, two parameters are important: 1) variety of solar radiation during a day, season, and year, 2) experiments' time, so it needs to normalize solar intensity for experiments due to yield comparison. The

photocatalytic destruction of pharmaceuticals usually was first order based on literature reviews and related to the accumulated solar energy (141, 142).

In kinetic of pharmaceutical degradation reaction rate, accumulated UV energy was used instead of reaction time and it can be calculate by equation 23 (143):

$$\ln \frac{C}{C_0} = -kQ_{UV} \quad 23$$

C_0 is the cefixime initial concentration and C is the concentration at the time of with drawl, k is the rate constant (L/kJ). The accumulated solar UV energy (Q_{UV}) received in the solar reactor per unit of treated solution volume was calculated using equation 24 (144):

$$Q_{UV,n} = Q_{UV,n-1} + \Delta t_n \overline{UV_{G,n}} \frac{A_r}{1000 \times V_t}: \quad \Delta t_n = t_n - t_{n-1} \quad 24$$

t_n is the experimental time for each sample (S), V_t is the total volume of wastewater at n water sample (L), A_r is illuminated collector surface area (m^2), $Q_{UV,n}$ is the accumulated energy (per unit of volume in kJ/L), and $UV_{G,n}$ is the average solar UV radiation during Δt_n (W/m^2).

McLoughlin et al. (42) improved the performance of the parabolic, CPC, and V-groove profile (see figure 28) in solar photoreactor using Pyrex tube to optimize the inactivation of *E. coli*. The performance of the compound parabolic profile demonstrated a clear advantage in terms of disinfection efficiency over the V-groove and parabolic profiles which performed comparably. Compared the Inactivation rate constant of experimental values were obtained which indicated high efficiency belonged to the CPC profile.

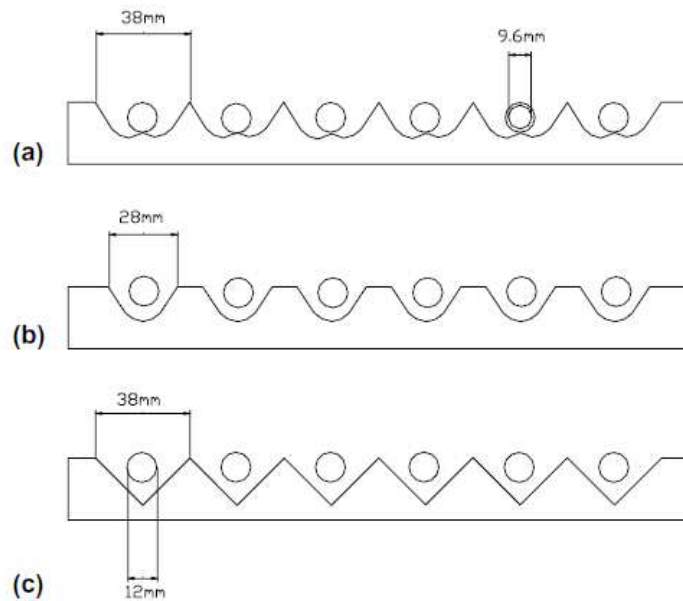


Figure 28. Cross-section of solar reactors: (a) compound parabolic, (b) parabolic and (c) V-groove (42).

Ajona and Vidal (145) studied the collector aperture tilt and the orientation of the reactor. Two tilts were considered: an all-the-year fixed tilt and everyday adjustment. In addition, two different reactor orientations have been studied: East-West and North-South. They summarized their results: the difference between both orientations was quite small (1 %), the East-West orientation had some advantages such as lower construction costs, the length of the CPC can be as long as required, and reducing the number of passive areas.

CPC photoreactor was used in Spain for treating water contaminated with trimethoprim and levofloxacin pharmaceuticals. This reactor was manufactured with aluminum foil mirrors having borosilicate glass pipe of 50 mm in diameter. The reactor worked in two trials (a) continuous (once-through experiment), and (b) batch (recirculation during 300 min). Using P25 $\text{TiO}_2/\text{TiO}_2/\text{SiO}_2$ supported on an inner glass pipe. Fifty percent destruction of trimethoprim was obtained in continuous mode and 95% of levofloxacin degraded in batch mode (146).

Moxifloxacin solution was treated using immobilized $\text{Ti}/\text{Ru}_{30\%}/\text{Ti}_{70\%}\text{O}_2$ catalyst with 220 cm^2 of surface area under solar and artificial radiation. The results are presented in figure 29, that 65% of moxifloxacin degradation was achieved in 24 h under the average of 45 kJ/L accumulated energy while under artificial light with similar conditions had a degradation efficiency of around 23%. The kinetic reaction rate of different light radiations can be seen in the figure (147).

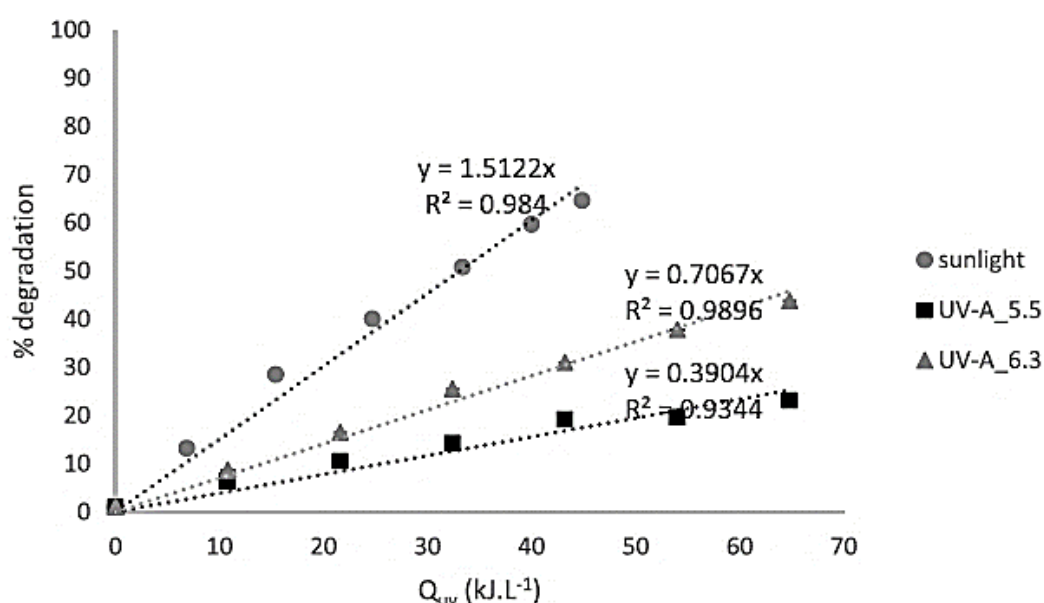


Figure 29. Photocatalytic degradation of moxifloxacin solution under sunlight and UV- A lamp (UV- A_5.5 and UV-A_6.3) shown as function of accumulated energy (kJ/L) (147).

Talwar et al. (148) studied the breakdown of metronidazole using a plug flow CPC reactor with supported catalyst on spherical-shaped beads (diameter = 12.50 mm). As shown in figure 32, TiO_2 coated beads were loaded inside the Pyrex tubes. They used two AOP processes, photo-

Fenton and photocatalysis experiments were applied for antibiotic degradation under natural solar light.

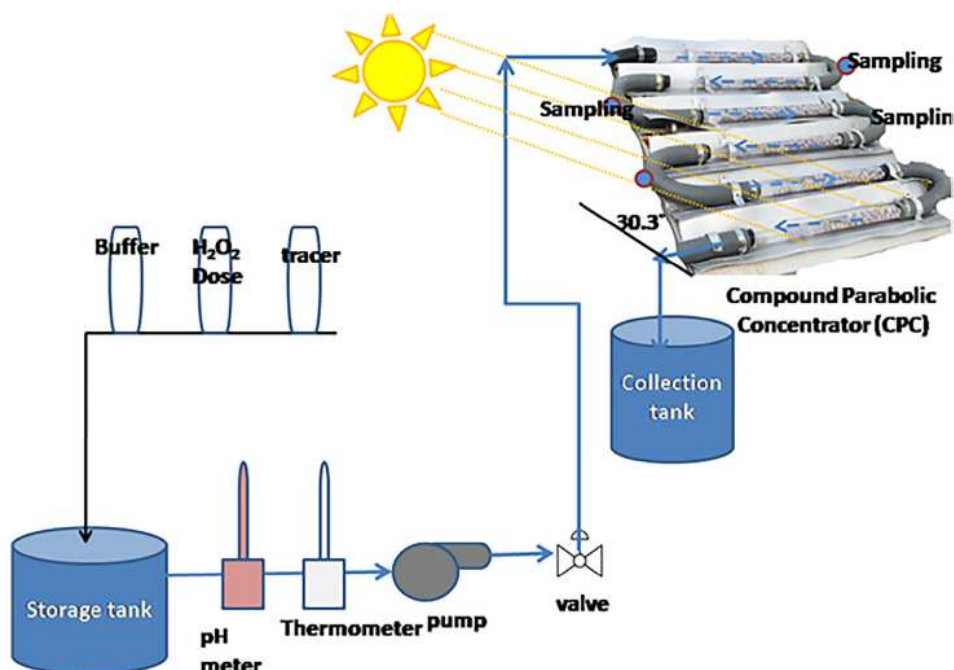


Figure 30. The set-up of the compound parabolic concentrator reactor packed with supported TiO_2 beads (148).

The metronidazole removal efficiencies for photolysis, photo-Fenton, photocatalysis, and adsorption (dark test) are depicted in figure 31. They obtained only 6% and 9% degradation efficiency for metronidazole in an exposure time of 60 min in photocatalysis and photo-Fenton processes, respectively. In addition, the degradation efficiency with different oxidations processes was in the order of Dual > Photocatalysis > photo-Fenton > photolysis > adsorption (148).

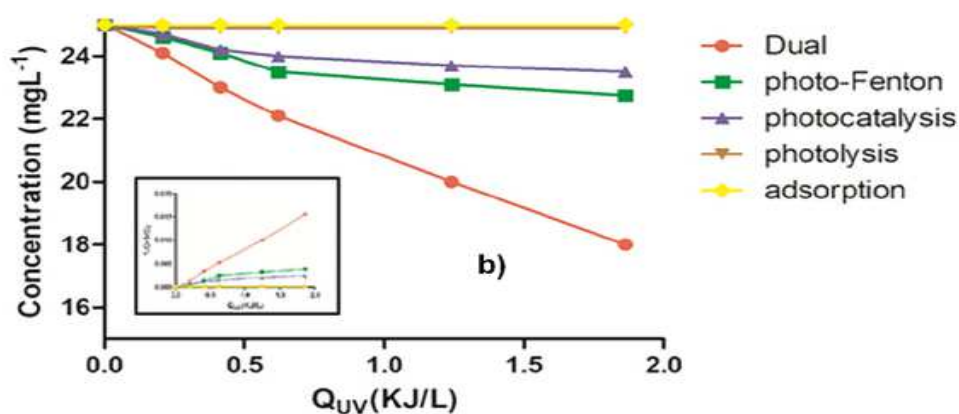


Figure 31. Metronidazole removal with different AOP processes versus the accumulated energy ($C_0 = 25 \text{ mg/L}$)(148).

Chapter 5. Regeneration of TiO₂ photocatalyst

Instead of discarding the deactivated photocatalyst, regeneration is a desirable and cost-effective method with environment-friendly benefits (149). A major interest in the photocatalysis process is the deactivation and regeneration of catalysts. Regeneration also is important because in real wastewater there are lots of organic and inorganic particles which cause the deactivation of the photocatalysts.

Adsorbed species including carbonaceous (150), polymeric substance, chloride, nitrate, and sulfate (149, 151, 152) were responsible for the deactivation of the TiO₂ surface (153, 154). This deactivation would be related to the change of surface properties. Blocking the adsorption of target contamination on the catalyst surface decreases the number of active sites which means accumulation on the TiO₂ surface that is hard to be degraded under photocatalytic conditions.

Different types of regeneration methods have been examined to recover deactivated photocatalysts, for instance, water washing (151), sonicating with water or alcohol (155), thermal process (156), using chemical solution (NaOH, H₂SO₄, NaOH, NH₃) (151, 157), and hot water method (149). Most research worked on the regeneration of photocatalyst mainly deals with gas phase photocatalytic reaction systems (149, 158, 159) and in liquid phase systems, the studies were less due to the presence of water as a solvent which could remove by-products of degradation mechanisms (160).

Shang et al. (153) studied photocatalytic oxidation of three organic pollutants with TiO₂ in the gas phase. They reported that adsorbed by-product species blocked the active sites of the catalyst. The deactivated photocatalyst was regenerated by sonicating in water and methanol which could recover the TiO₂ activity. Moreover, washing and drying techniques showed promising prospects to recover the activity of deactivated photocatalysts used in the degradation of air pollutants (155). In another work (157), the SiO_x pollutants have been easily removed by treatment in an alkaline solution without destroying the TiO₂ structure, also photocatalytic activity was restored completely.

Garcia et al. (152) studied pharmaceutical contaminants using TiO₂ photocatalysts immobilized on glass spheres in a solar pilot. As shown in figure 32, the photoactivity decreased after five cycles, and degradation efficiency was remarkably reduced. In order to recover the photocatalysts, different regeneration strategies such as oxidation treatment (H₂O₂ with UV and calcination) and chemical solution. Treatment with an alkaline solution partially removed the TiO₂ layer according to the XPS analysis. They found calcination was the most technique to remove nitrogen-containing species.

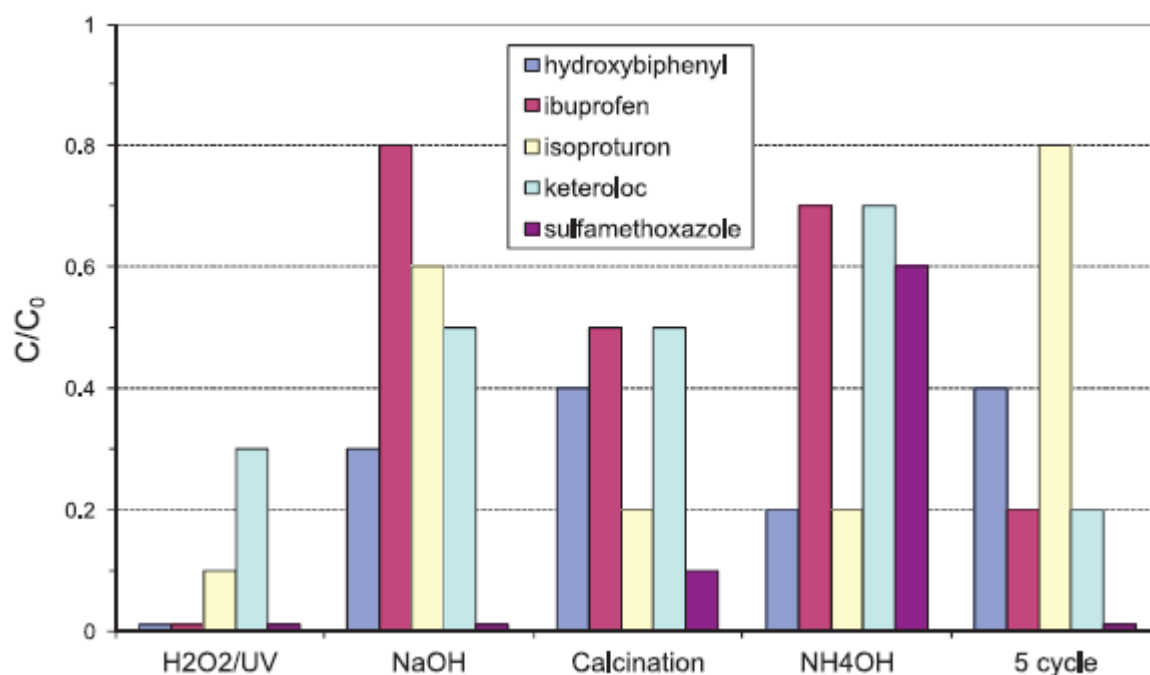


Figure 32. Comparison of the results obtained for the different regeneration processes for pharmaceuticals, respect to the used photocatalyst (5th cycle) (152).

In liquid solution, reuse and regeneration of TiO₂ coating on glass beads were studied for methylene blue degradation under solar radiation in a CPC reactor. Results confirmed the effective method for recovering TiO₂ coating was water washing under UV-vis irradiation (156).

Conclusions

Water is a key resource of humanity and developing the quality of water resources is fundamental to public health. Pharmaceutical wastes as emerging contaminants release in surface waters, groundwaters, and soils. One of the most important pharmaceuticals recognized in the aquatic environment is cefixime trihydrate with a concentration ranging from 278-777 ng/L.

Conventional biological water treatment plants could not remove pharmaceuticals completely. Advanced oxidation processes (AOPs) are a good alternative to pharmaceutical treatment methods which involve the generation of highly reactive oxygen species or free radical species. Photocatalysis is based on semiconductors in the presence of artificial or solar irradiation. Semiconductor especially TiO_2 has been accorded great significance in recent times due to their potential to mineralize a wide range of organic pollutants at ambient pressure and temperature. It has advantages commercially available at various crystalline phases, biologically inert, water insolubility, acid resistance, superior redox ability, hydrophilicity, corrosion resistance, and physical and chemical stability. Difficulty in the recovery of catalyst particles in slurry mode is one of the limitations in the application of TiO_2 -based photocatalytic degradation of pollutants. One approach is immobilized photocatalysts onto a variety of surfaces. Numerous techniques were reported for preparing supported TiO_2 , for instance, sol-gel, plasma-enhanced chemical vapor deposition, chemical vapor deposition, hydrothermal, etc.

In the case of TiO_2 films, the plasma-deposited method enables control of the size of TiO_2 nanoparticles, the thickness, and the microstructure of the thin film. This is a promising strategy for preparing a mixed crystalline phase of TiO_2 like P25 Degussa with a high deposition rate and good substrate coverage.

Doping materials in TiO_2 lattice could modify their photocatalytic activity by modifying the band gap, surface area, or particle size. Among these dopants, Mn is attractive because of its variable valence states, as well as its significant influence on particle size.

Solar photocatalysis is based on the collection of high energy short wavelength photons (UV radiation) to promote photoreactions. Solar photocatalysis reactors require specific features to absorb and transmit solar photons efficiently to promote catalyst reactions. There are five types of concentrating systems for water treatment methods like parabolic trough concentrator (PTC), compound parabolic concentrator (CPC), parabolic dish concentrator (PDC), Fresnel concentrator, and optical fiber photoreactors.

The collector for the photocatalytic purpose must be economical and efficient, CPC combines the characteristic of both technologies (PTC and non-concentration) and has none of their disadvantages of them. The CPC is static and collects all radiations (diffuse and direct) and then reflects around the back of the tubular reactor. So, they have higher optical and quantum efficiencies due to lower e^-/h^+ recombination

In the solar photocatalysis process, the kinetic of the pharmaceutical degradation reaction rate was determined by the accumulated UV energy used instead of reaction time. The accumulated solar UV energy (Q_{UV}) received in the solar reactor per unit of treated solution volume was calculated using an expression.

Regeneration is a desirable and cost-effective method instead of discarding the deactivated photocatalyst. Adsorbed species on the catalyst surface decrease the number of active sites. Different types of regeneration methods have been examined to recover deactivated photocatalysts, for instance, water washing, sonicating with water or alcohol, thermal process, using a chemical solution, and hot water method.

Notations

PPCPs	Pharmaceutical and Personal Care Products
WWTP	Waste Water Treatment Plant
ng/L	Nano gram per liter
µg/L	Micro gram per liter
rGO	Reduced Graphene Oxide
mg/g	Milli gram per gram
AOPs	Advanced Oxidation Processes
E_g	Band gap (eV)
eV	Electron Volt
H ₂ O ₂	Hydrogen Peroxide
S ₂ O ₈ ²⁻	Persulfate
MnO ₄ ⁻	Permanganate
O ₃	Ozone
OH [•]	Hydroxyl radical
O ₂ ^{•-} , O [•]	Superoxide anion radicals
H ₂ O [•]	Hydroperoxyl radicals
Cl ₂	Chlorine
RO [•]	Alkoxy radicals
UV	Ultraviolet
US	Ultra-sonic
TiO ₂	Titanium dioxide
Fe	Ferrous
Pt	Platinum
IrO ₂	Iridium oxide,
PbO ₂	Plumbic oxide
RuO ₂	Ruthenium oxide
SnO ₂	Stannic oxide
BDD	Boron-Doped Diamond
EC	Electrochemical
CO ₂	Carbon dioxide
nm	Nano meter
VB	Valence Band
CB	Conduction Band
λ	Wavelength (nm)
cm ³ /g	Cubic centimeter per gram
min	Minute
ND	Nano-Diamonds
ZnO	Zinc oxide
NAC	Nanogranular ammonium acetate
NiO	Nickle oxide

NCP	Nano-Clinoptilolite
BiOBr	Bismuth bromide oxide
ZnS	Zinc sulfide
Fe ₂ O ₃	Ferric oxide
CdS	Cadmium sulfide
WO ₃	Tungsten trioxide
SO ₂	Sulfur dioxide
Fe ₃ O ₄	Ferrous ferric oxide
Mn ₂ O ₃	Di-manganese trioxide
CeO ₂	Ceric dioxide
g/L	Gram per liter
PVD	Physical Vapor Deposition
CVD	Chemical Vapor Deposition
PECVD	Plasma Enhanced Chemical Vapor Deposition
Hg lamp	Hydrargyrum lamp
mg/L	Milli gram per liter
T	Temperature (°C or K)
T _e	Electron temperature (°C or K)
T _i	Ion temperature (°C or K)
T _g	Gas temperature (°C or K)
W	Watt
XRD	X-ray diffraction
RF	Radio Frequency
SEM	Scanning Electron Microscopy
TTIP	Titanium tetraisopropoxide
h	Hour
sccm	Standard cubic centimeters per minute
nm/min	Nano meter per minute
Pa	Pascal (unit of pressure)
mbar	Milli bar (unit of pressure)
Ar/O ₂	Argon per oxygen
h	Planck's constant ($j \times s$, $6.626 \cdot 10^{-34}$)
ν	Light frequency (Hz)
SG	Sol-gel
MW	Microwave
SrTiO ₃	Strontium titanium oxide
GN-TNT	Graphene-TiO ₂ nanotubes
km	Kilometer
km/s	Kilometer per second
MW/m ²	Megawatt per square meter
kW	Kilowatt

EJ	Exajoule
W/m ²	Watt per square meter
PTC	Parabolic Trough Concentrator
CPC	Compound Parabolic Concentrator
PDC	Parabolic Dish Concentrator
α	Absorption coefficient
h ν	Photon energy (eV)
C	Geographic concentration of the PTC collector
f	Focal length
D	Aperture width of PTC
D	Diameter
θ	Angle (°)
CR	Concentration Ratio
A	Surface (m ²)
C ₀	Initial concentration (mol/L)
C	Concentration
K	Rate constant (L/kJ)
Q _{UV}	Accumulated solar UV energy (kJ/L)
t _n	Time for each sample (s)
V _t	Total volume (L)
A _r	Illuminated collector surface area (m ²)
UV _{G,n}	Average solar UV radiation (W/m ²)
NaOH	Sodium hydroxide
H ₂ SO ₄	Sulfuric acid
NH ₃	Hydrogen nitride (ammonia)
XPS	X-ray photoelectron spectroscopy

PART 3: ELABORATION AND CHARACTERIZATION OF NANO-PHOTOCATALYSTS

This part contains three chapters. In the first chapter, the elaboration methods of TiO₂-based photocatalysts will be presented. In the following, we will describe the general techniques and principles of the characterization methods including, inductively coupled plasma-optical emission spectroscopy (ICP-OES), Raman spectroscopy, X-ray diffraction (XRD), X-ray photoelectron spectroscopy (XPS), scanning electron microscopy (SEM), transmission electron microscopy (TEM), and atomic force microscopy (AFM). In chapter 3, we will describe the physicochemical characterization of the pure and Mn-doped TiO₂ photocatalysts that were prepared by the fluidized bed plasma device. Results of ICP, Raman, XRD, XPS, SEM, TEM, and AFM analytical methods will be discussed.

Chapter 1. Elaboration methods and experimental setups

1.1. Elaboration of photocatalysts

The elaboration of nanostructured layers by plasma has been known promising development for decades. The fluidized bed plasma technique used in this work was inspired by the Low-pressure plasma used by A. Rahmani (9-10) to deposit CuO, Zn-CuO catalysts on the surface of alumina beads (161, 162) in a fluidized bed plasma reactor. The plasma technique used in these works showed high performances in terms of the doping rate, the crystallinity, and the control of oxidation rate due to the reactive species of plasma such as energetic electrons, oxidant species OH and O radicals. In these works, the role of plasma parameters on the properties of the final deposited layers has been emphasized.

On the other hand, there are intense research efforts around the world to develop photocatalysts for pollutant abatement in aqueous solutions. In this way, TiO₂ nanoparticles have shown promising behavior. However, nowadays it is forbidden for example by European Union directives to add to the surface waters the nanoparticles that constitute by themselves a new category of pollutant. A solution to this problem is to produce nanostructured photocatalysts stabilized on the surface of immobile surfaces permitting the recovery of the photocatalysts after use and preventing their diffusion in the water. In connection with the effects of the elaboration method on the properties of TiO₂ layers Sobczyk-Guzenda et al. (99) confirmed the good hardness and adhesion of TiO₂ films obtained by plasma enhanced chemical vapor (PECVD) deposition technique. Kim et al. (100) used a rotational cylindrical plasma reactor to deposit uniform TiO₂ layers on glass beads surfaces while in our work we used a fluidized bed fluidized bed plasma reactor to obtain thin TiO₂ films fixed on the surface of glass beads.

The aim of this work is to produce nanostructured TiO₂ layers on the surface of glass beads in order to develop stabilized photocatalysts layers for pharmaceutical pollutants removal in surface waters.

The effects of the experimental parameters on the properties of TiO₂ thin layers are presented and compared with those of the layers obtained by the conventional sol-gel method.

Thus, the TiO_2 and metal-doped TiO_2 films were coated on glass beads through a fluidized bed plasma and T-mixer sol-gel reactor. The pure TiO_2 and Mn-doped were deposited with the fluidized bed plasma device under different operating conditions. The sol-gel method with a micro-mixing reactor was used to synthesize TiO_2 , ZrTiO_2 , and VTiO_2 nanoparticles fixed on the glass beads. The immobilized catalyst was chosen to prevent the loss of catalyst material and to avoid the posterior filtration step, related to the recovery of the catalyst. Titanium oxide layers were always coated on the surface of glass beads 4 mm in diameter.

1.1.1. The low-pressure fluidized bed plasma setup

The titanium dioxide coatings were prepared by the fluidized bed low-pressure fluidized bed plasma reactor. A schematic representation of the fluidized bed plasma device is depicted in figure 33 which has been explained in the previous publication (163). It consisted of a quartz tube, a vacuum equipment, an inductive coil, a radio frequency generator with a matching box, a solution container, an electro valve, plasma gases, and measurement devices. The inner diameter and the length of the cylindrical quartz tube were 50 mm and 600 mm, respectively. The quartz tube was equipped with a quartz mesh in its center to hold the glass beads substrates. The inductive coil was rounded at the center of the quartz tube for producing the plasma discharge. The radio frequency power generator coupled with the matching box was connected to the inductive coil for producing the plasma discharge in the presence of argon or argon/oxygen flows. The gas flow rates of argon and oxygen were controlled with the mass flowmeters (Bronkhorst, MFC). Before deposition, the vacuum in the chamber was maintained in the order of 20 Pa by pumping. The precursor solution was injected into the plasma chamber through the electro valve which fluidized the substrates with pressure differences before and after opening the valve.

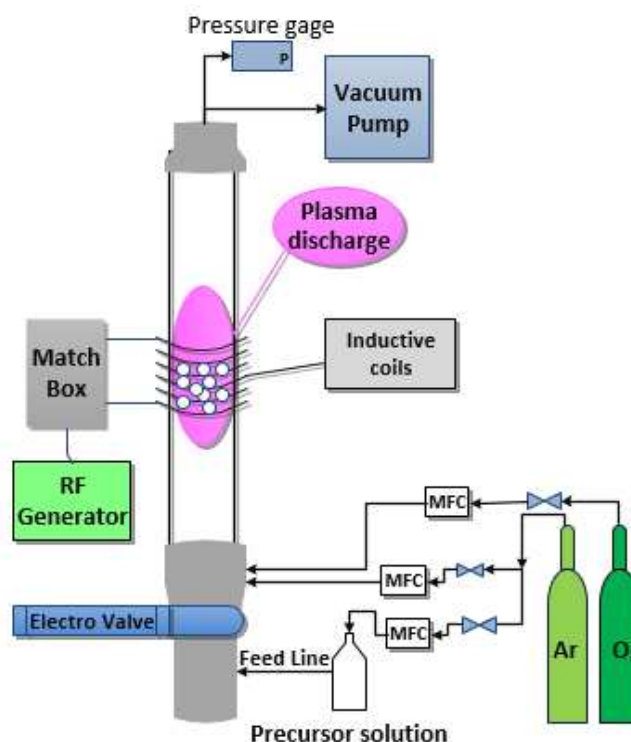


Figure 33. Schematic of the low-pressure fluidized bed plasma reactor for TiO_2 depositions.

1.1.1.1. Plasma process for deposition of TiO_2 films on glass beads

Prior to deposition, the glass beads were cleaned in sulfuric acid and distilled water before loading into the reactor chamber. First, pollutants on the surface of glass beads were removed by immersion in a sulfuric acid (H_2SO_4 , 98%, Sigma-Aldrich) solution overnight. Then rinsed and washed with distilled water more than fifteen times. Finally, they were dried in an oven at 80 °C during the night.

In each deposition batch, 100 g of glass beads (diameter = 4 mm) were coated with the fluidized bed plasma chemical vapor deposition method. The titanium tetra isopropoxide (TTIP, $\text{C}_{12}\text{H}_{28}\text{O}_4\text{Ti}$, 284.219 g/mol, 98%), from Sigma-Aldrich, was utilized as the primary titanium precursors for the deposition of TiO_2 films. The TTIP has several benefits: volatile at ambient temperature, non-dangerous (164), high reactivity, and weak saturation vapor pressure (27 Pa) (165). The liquid precursor TTIP was solved in the isopropanol ($\text{C}_3\text{H}_8\text{O}$, 60.1 g/mol, Aldrich) at the ambient temperature, under an argon atmosphere. In a typical procedure, 50 ml of precursor solution was prepared with two concentrations: $C_{\text{Ti}} = 1.67$ mol/L and 1.002 mol/L in isopropanol.

Before opening the precursor valve to insert the droplets inside the reactor, the glass beads were subjected to pure argon plasma discharge at the following parameters: flow rate of argon $\text{Ar} = 90$ ml/min, discharge power $P = 250$ W, and duration of $t = 10$ min before the deposition.

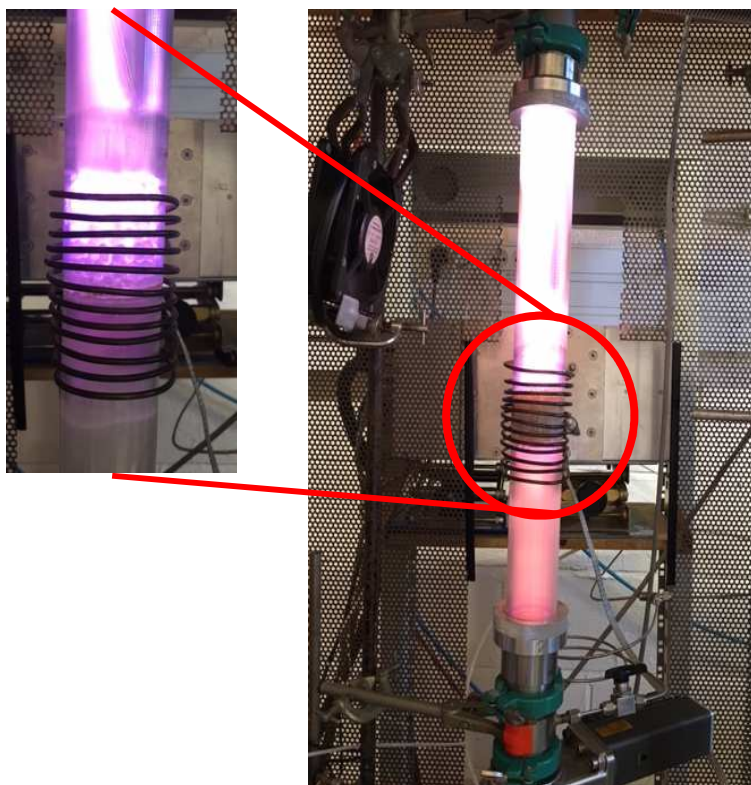


Figure 34. Photo of the fluidized bed plasma reactor installed at LSPM, France.

The plasma gases were oxygen and argon. The argon gas as the carrier gas was applied in the precursor solution at the fixed flow rate of 300 ml/min. The oxygen gas was employed as a reactant gas and injected into the reactor chamber separately. The argon was used as a vector gas to transport the (TTIP + isopropanol) droplets inside the plasma discharge. The reactive species of plasma (electrons, OH and O radicals) reacting with TTIP and isopropanol molecules led to form the TiO_2 films on the surface of glass beads (figure 34). The feed line of TTIP was heated at $T = 140^\circ\text{C}$ to help the evaporation of TTIP droplets and to avoid condensation of TTIP.

To calculate the flow rate of precursor consumption, the volume difference in precursor solution was measured before and after each deposition. The average flow rate of precursor consumption was 0.33 ml/min (20 ml of precursor mixture injected during 60 minutes of deposition). The pressure in the fluidized bed plasma reactor ranged between 5 and 20 Pa.

In these deposition experiments, the effect of several plasma parameters on the TiO_2 film formation and composition has been studied. The oxygen flow rate, the deposition time, and the precursor concentration were changed to study their effect on the structural properties of TiO_2 films coated on glass beads. These parameters might influence the density of gaseous molecules and distribution of ion energy, and consequently the thickness and physicochemical properties of samples. Oxygen content was changed from 0 to 25 ml/min, and TiO_2 deposition times were between 30 and 60 min. Other plasma parameters in the

deposition conditions were kept constant such as the weight of glass beads, feed line temperature, and vector gas flux. The TiO₂ layers were successfully deposited on the surface of glass beads. Experimental variables and ranges for photocatalyst depositions are listed in table 3.

Table 3. Plasma deposition conditions of TiO₂ photocatalysts prepared with the fluidized bed plasma method.

Catalyst	C _{Ti} (mol/L)	O ₂ flux (ml/min)	Deposition time (min)	Plasma power (W)
TiO ₂	1.67	0	60	250
TiO ₂	1.67	2	60	250
TiO ₂	1.67	10	60	250
TiO ₂	1.67	25	60	250
TiO ₂	1.67	10	30	250
TiO ₂	1.002	0	45	300
TiO ₂	1.002	1	45	300
TiO ₂	1.002	2	45	300
TiO ₂	1.002	3	45	300
TiO ₂	1.002	4	45	300
TiO ₂	1.002	10	45	300

1.1.1.2. Deposition of manganese doping in the TiO₂ structure

In this work, the Mn-doped titanium dioxide films were deposited by a similar procedure via the fluidized bed plasma technique. In brief, plasma discharge was created for the TiO₂ layers previously described. During the preparative steps, we observed that the manganese precursor (manganese acetate) could not be mixed with TTIP as they react together and form a solid precipitate in the mixing vessel before injection in the fluidized bed plasma reactor. Thus, for Mn-doped TiO₂ samples, another liquid precursor was prepared in a separate container. Manganese acetate (C₄H₆MnO₄, 173.027 g/mol) from Sigma-Aldrich chemical company was used as precursor material.

Different amounts of manganese acetate (0.128, 0.313, and 1.284 g) were solved in the 40 ml of methanol (CH₃OH, 32.04 g/mol, Sigma-Aldrich) as a solvent in the ratio of 1, 3, and 10 mol%. The plasma power was adjusted at 300 W and the net weight of glass beads was 100 g. The TTIP concentration was fixed at C_{Ti} = 1.67 M in isopropanol for all Mn-doped TiO₂ catalysts. Both liquid precursors, i.e. TTIP in isopropanol and Mn acetate in methanol, were injected into the reactor. As shown in figure 35, two precursor droplets were separately injected inside the reactor and photocatalyst films were generated on the surface of the glass beads by reaction with plasma. The argon flux as the carrier gas for TTIP and Mn solutions was adjusted

at 300 and 150 ml/min, respectively. It is noteworthy that in our experimental conditions the exact amount of Mn in TiO₂ deposits should be determined by ICP analysis.

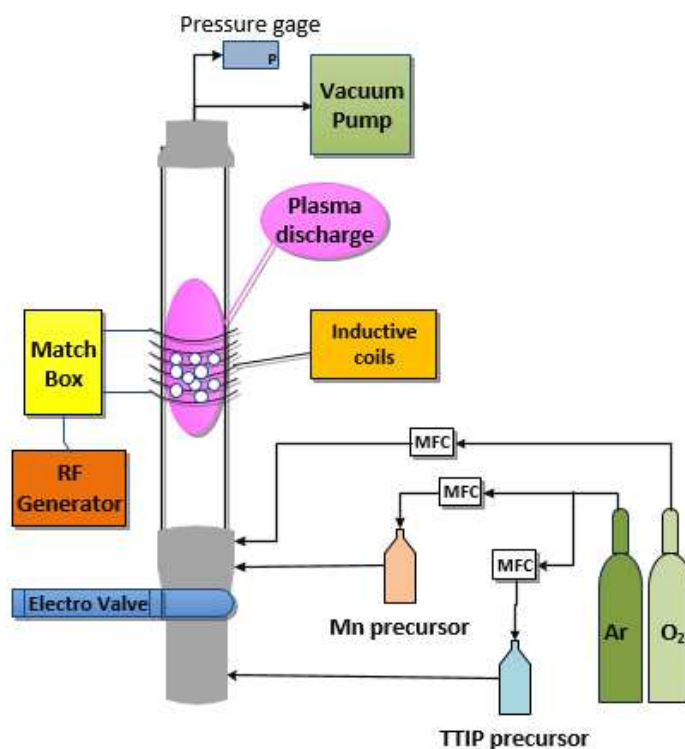


Figure 35. Schematic of the fluidized bed plasma device for Mn-doped TiO₂ depositions.

The Mn_xTi_{1-x}O₂ layers were coated on glass beads. The operational parameters of all Mn-doped TiO₂ films are presented in table 4.

Table 4. Deposition conditions of Mn_xTi_{1-x}O₂ photocatalysts prepared with the fluidized bed plasma method.

Catalyst	x (%)	C _{Ti} (mol/L)	O ₂ flux (ml/min)	Deposition time (min)
Mn _x Ti _{1-x} O ₂	1	1.67	10	35
Mn _x Ti _{1-x} O ₂	3	1.67	10	35
Mn _x Ti _{1-x} O ₂	10	1.67	10	35
Mn _x Ti _{1-x} O ₂	3	1.67	25	35

1.1.1.2.1. Inductively coupled plasma-optical emission spectroscopy (ICP-OES)

The ICP-OES analysis was used to quantitatively determine the Mn content in our composites. For the quantification of Mn loading in TiO₂ photocatalyst, the coated films on the substrate were introduced in the concentrated nitric acid for several days ensuring the total dissolution of the deposit ready for ICP analysis. Then 0.5 ml of the resulting solution was finally diluted with deionized water up to a final volume of 8 ml.

The final values of Mn and Ti percentages on the MnTiO₂ deposits were characterized by the ICP analysis technique. The ICP-OES measurements of Mn doping are summarized in table 5. The exact Mn/Ti ratio that was obtained with the ICP method for three kinds of MnTiO₂.

Table 5. The final composition of TiO₂ layers doped with Mn measured with ICP-OES.

Mn acetate in precursor (g)	Photocatalyst	Ti (ppm)	Mn (ppm)	Ti (mmol/l)	Mn (mmol/l)	Mn/(Mn+Ti)
0.128	Mn _{0.01} Ti _{0.99} O ₂	23.13	0.2896	0.48308271	0.00527216	0.01079577
0.313	Mn _{0.003} Ti _{0.997} O ₂	0.3963	0.0014	0.00827694	2.5487E-05	0.00306982
1.284	Mn _{0.02} Ti _{0.98} O ₂	13.3	0.369	0.2777777	0.00671764	0.02361247

The results of the analysis displayed that the mass ratio of $(x = N_{Mn}/N_{Ti} + N_{Mn})$ in Mn_xTi_{1-x}O₂ were 0.01, 0.003, and 0.02 respectively which were significantly lower than the desired values.

1.1.2. Crystallization of deposited films by post annealing

Preliminary characterization showed that our TiO₂ and Mn_xTi_{1-x}O₂ deposits were found in the amorphous phase. To get crystallized films, annealing was applied to the as-deposited samples in a furnace (RHTC-80230115, Nobertherm) with a heating rate of 8 °C/min from the room temperature to 450 °C then during for 4 h at 450 °C. The cooling was done naturally. The amorphous form of titanium dioxide was known to have low photocatalytic activity, while the crystalline form of titanium dioxide was photoactive. Thermal annealing of all films was carried out under atmospheric pressure and the annealing time always was four hours.

1.2. Sol-Gel method in a micro-mixing reactor

The preparation of the photocatalysts in a sol-gel micro-mixing reactor was performed following the procedure described in the previous papers (166-168). The vanadium-doped TiO₂ particles coated on the surface of glass beads were obtained as described in the Ph.D. thesis of M. Miguel Sanchez (169), and the Zirconia-doped glass beads were obtained in the frame of M. Cheng's Ph.D. thesis (170). In this work, we verified the photocatalytic activity of these particles in the solar reactor for the destruction of cefixime molecules in water.

1.2.1. Synthesize of TiO₂ and doped-TiO₂ nano-particles coated on glass beads

Pure and doped titanium dioxide nanoparticles were prepared in a sol-gel T-mixer reactor, shown in figure 36, and coated on 4 mm diameter borosilicate glass beads. The solutions of precursor and water to synthesize colloidal solution of titanium oxide were prepared in a LABstar glove box workstation (MBraun) for avoiding any contamination from atmospheric humidity (the vapor of H₂O was kept at below 0.5 ppm). The mixed oxide V-TiO₂ nanoparticles with different vanadium content V/(V+Ti) between 0 and 20 mol% were prepared in a laboratory chemical reactor with ultra-rapid micro-mixing of the titanium and vanadium

precursors. Two stock solutions of precursors were prepared: (A) mixed vanadium oxytriisopropoxide (98%, Sigma Aldrich) and titanium tetraisopropoxide (TTIP, 98%, Sigma-Aldrich) precursors in n-propanol (99.5%, Sigma Aldrich); (B) bi-distilled filtered water in n-propanol (99.5%, Sigma-Aldrich) used as a solvent. The titanium precursor concentration in the reaction volume was $C_{Ti}=0.3$ mol/l and water concentration C_w was adjusted to maintain the hydrolysis ratio $H=C_w/(C_{Ti}+C_v) = 1.5$, which according to our previous results assures the particle's nucleation but prohibits their mutual aggregation and growth. The total titanium precursor concentrations were kept at 0.292 M and hydrolysis ratio according to Cheng et al. (171).

These solutions were transferred and injected into tanks (A) and (B) of the micro-mixing reactor. The nitrogen pressure of 4 bar was used for applying to mix (A) and (B) solutions at T-mixer to reach Reynold's number $Re \approx 6000$. The micro-mixing reactor was made up of a metal tube having an inner diameter of 1 mm for the input arms joining the tanks (A) and (B) to an output metal tube of 2 mm in diameter. This permitted to development vortex when the two liquids met together fast and thus leading to produce nano-metric TiO_2 particles. The mixed fluid flow rate was about 10 m/s, which was believed faster than the nucleation and growing phenomena, with a controlled temperature at 20 °C by a thermo-cryostat Haake, DC10K15.

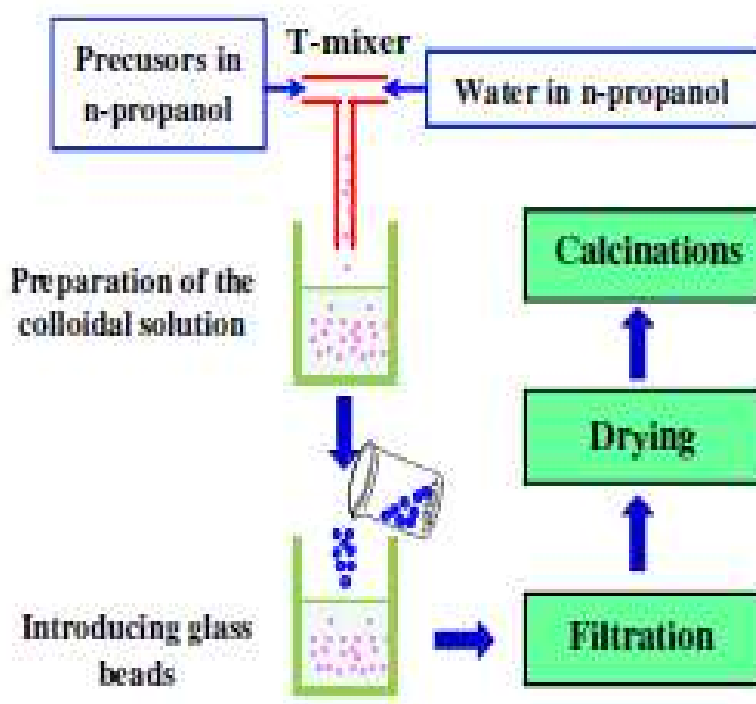


Figure 36. Schematic of sol-gel micro-mixing reactor with T-mixer used in photocatalyst preparation (170).

The borosilicate glass beads with 4 mm diameter were put and kept in concentrated sulfuric acid (95-98%) overnight and then well cleaned with distilled water until 10 times. Then they were dried in the oven (at 80 °C around overnight). After the obtained colloidal solutions had been mixed by a micro-mixing reactor and transferred into the glove box, these dried borosilicate glass beads were coated for 10 min with these nanoparticles. The coated beads were filtered with filter papers and dried at a temperature of around 70 °C.

The film-coated pure TiO₂ and V-doped TiO₂ on borosilicate beads were treated at 450 °C for 4 hours.

Chapter 2: Characterization of physicochemical properties of photocatalysts

Several physicochemical characterization techniques were applied to study the structure and morphology of photocatalysts. These methods gave us information about the crystallite, morphology, and chemical properties of coated films on glass beads. The aim of analyzing the film's structure and morphonology was to identify similarities and differences in their phase composition and to assess the influence of deposition parameters. For structure examination, we used Raman, XRD, and XPS techniques while SEM, TEM, and AFM were used to determine the morphology of deposited layers.

2.1. X-ray diffraction

X-ray diffraction (XRD) is a rapid analytical technique for the identification of different crystalline phases of materials, determination of unit cell dimensions, and structural parameters such as the size of crystallite, and the percentage of each phase. The monochromatic X-rays which are generated in a cathode ray tube by heating a filament, are directed toward the sample and the diffracted rays are collected. As shown in figure 37, the key component of all diffraction is the angle between the incident and diffracted when conditions satisfy Bragg's equation that presents in the following equation 25:

$$n\lambda = 2d \sin \theta \quad 25$$

Which λ is the wavelength of incident radiation, d is the interplanar distance between planes, θ is Bragg angle, and n is the integer characterizing the diffraction order. This law relates the wavelength of electromagnetic radiation to the diffraction angle and the lattice spacing in a crystalline sample. A detector records and processes this X-ray signal and converts the signal to a count rate by scanning the sample through a range of 2θ angles which is then output to a device such as a printer or a computer monitor. The d -spacings aid to identify the material because each material has a set of unique d -spacings. In XRD analysis a standard reference requires for the identification of unknown samples (172).

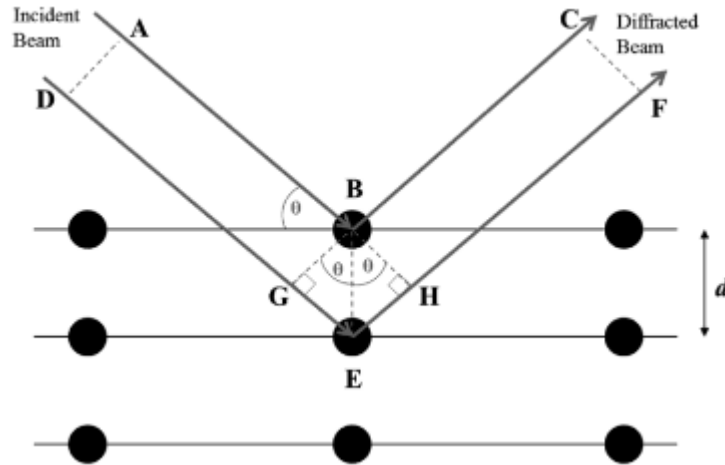


Figure 37. X-ray diffraction from two planes of atoms in a crystal.

In the present work, the x-ray diffraction (XRD) patterns were collected at a grazing incidence using Panalytical Empyrean diffractometer equipped with a Cu-K α source ($\lambda=1.541 \text{ \AA}$). The x-ray incident beam was collimated with $1/16^\circ$ slits coupled with a 5 mm mask to ensure that the beam footprint did not exceed the sample surface. The diffractometer was equipped with a PIXcel1D 255-channels detector operating in scanning line mode coupled with a parallel plate collimator (acceptance angle of 0.18°). The patterns were collected with an incident angle of 0.5° in the range from 15° to 70° (2θ) with a step of 0.03° and counting time per step of 75 s.

The crystalline size of deposited films can be calculated from the XRD patterns and Scherrer equation. Scherrer equation was used to measure the crystallite size of photocatalyst films deposited by plasma method on glass beads. The value of D can be calculated using the following expression (eq. 26):

$$D = K\lambda / \beta \cos(\theta) \quad 26$$

where D is the crystallite size, λ is the wavelength of X-ray, β is the full width at half maximum, θ is diffraction angle, K is the shape factor, a constant between 0.8 and 1.39 (173).

During our experiments, we observed by TEM and XRD the presence of both phases rutile and anatase in the same deposited layer. The phase quantification was estimated from the Grazing Incidence XRD (GIXRD) patterns with rutile/anatase ratio calculated from the respective (110) and (101) peak intensities via the equation 27 suggested in references (174, 175):

$$f = \left(1 + 1.265 \frac{I_R}{I_A}\right)^{-1} \quad 27$$

where I_A and I_R are the X-ray intensities of peaks corresponding to anatase and rutile phases.

2.2. Raman spectroscopy

The general Raman spectrum (the intensity and wavelength position) is a distinct chemical fingerprint for a particular molecule or material, each peak corresponds to a specific molecular bond vibration and can be used to very quickly identify the material. A Raman microscope couples a Raman spectrometer to a standard optical microscope, allowing high magnification visualization of a sample and Raman analysis with a microscopic laser spot. Raman micro-analysis is easy: simply place the sample under the microscope, focus, and make a measurement. A Jobin-Yvon HR800 equipped with a motorized X-Y stage that allowed to do the imaging and an adjustable aperture confocal slit system was used to measure Raman spectra of nano TiO₂ films deposited on glass beads. The excitation wavelengths that can be used are 632.8 nm thanks to a laser He/Ne incorporated into the equipment and where the wavelengths go from the visible (514 and 448 nm) up to the ultra-visible (363.8 nm) using high power ionized Argon laser (30 mW).

2.3. X-ray photoelectron spectroscopy

X-ray photoelectron spectroscopy (XPS) is the most widely used surface analysis technique because it can be applied to a broad range of materials. The information XPS provides valuable quantitative and chemical state information from the surface of the material to characterize thin film structures. Thin film composition plays a critical role in the performance of catalysis nanomaterials

XPS is typically accomplished by exciting the surface of a sample with mono-energetic Al K α x-rays causing photoelectrons to be emitted from the sample surface. An electron energy analyzer is used to measure the energy of the emitted photoelectrons. From the binding energy and intensity of a photoelectron peak, the elemental identity, chemical state, and quantity of a detected element can be determined.

The XPS analysis technique used in the present study is illustrated in figure 38. The XPS analysis was realized on Thermofisher Scientific Escalab 250xi equipment with a spot size of 650 μ m and flood gun assistance (Al-K α , λ =1486.6 eV, Pass Energy (survey/HR) 100 eV / 20 eV, dwell time 100 ms, step (survey/HR) 1 eV / 0.1 eV). Spectra were then charge corrected by shifting all peaks to the adventitious C1s spectral component (C-C, C-H) binding energy set to 284.8 eV. Quantification is performed based on the photopeak areas after a Shirley type background subtraction using the Thermofisher Scientific Advantage© software and its "ALTHERMO1" library as sensitivity factor collection.



Figure 38. XPS analysis technique on the surface of a glass bead.

2.4. Scanning electron microscopy

Scanning electron microscope (SEM) gives information about the sample morphology, chemical composition (using EDS), the orientation of particles, and crystalline structure by giving a two-dimensional image. A SEM produces images by scanning the surface of a sample with interactions of the electron beam and atoms and producing different signals that contain information about the surface topography and composition.

As shown in figure 39, produced signals of electron-sample interactions are classified into secondary electrons (SE), reflected or back-scattered electrons (BSE that are used to determine crystal structures and orientations of minerals), characteristic X-rays (photons, used for elemental analysis and light (cathodoluminescence), absorbed, transmitted electrons and heat which carry significant amounts of kinetic energy. In the common SEM method, secondary electrons and backscattered electrons detectors are standard equipment for showing morphology and topography and rapid discrimination of phases in multiphase

samples, respectively. Additional detectors are critically dependent on which detectors it accommodates.

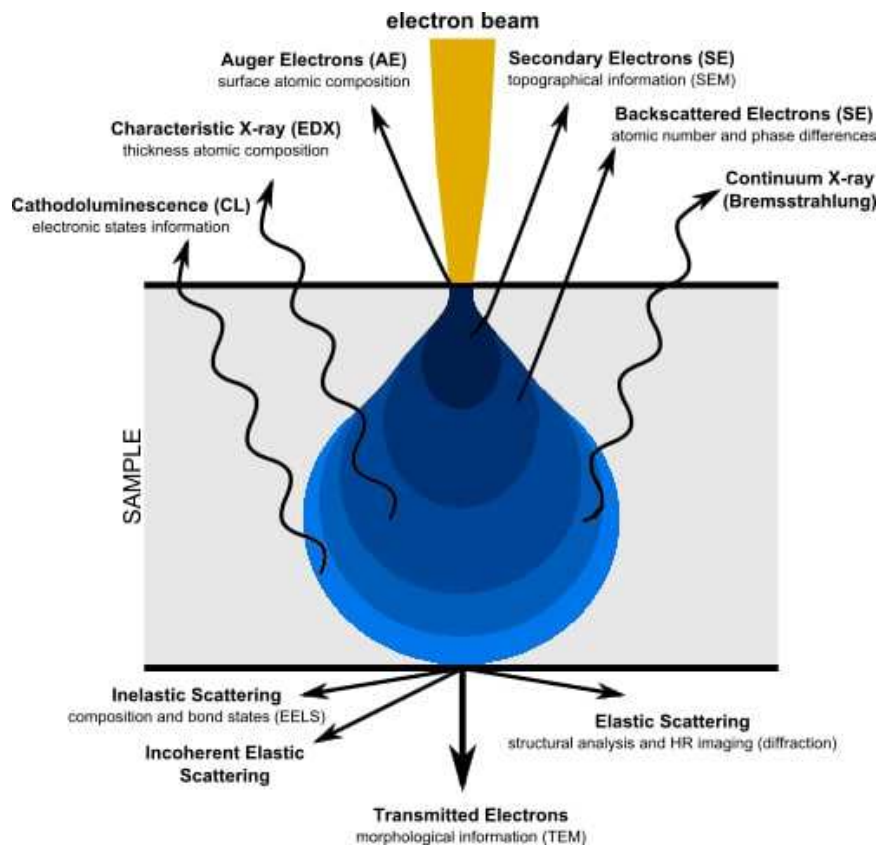


Figure 39. Electron beam interaction with the sample in SEM and TEM techniques.

For conventional imaging in the SEM technique, a sample has to fit on the specimen which must be electrically conductive and electrically grounded to prevent the accumulation of electrostatic charge. A Special treatment for non-conducting materials is used, that consists usually on coating the sample with an ultrathin film of gold, gold/palladium alloy, platinum, iridium, tungsten, chromium, osmium, or graphite by low-vacuum sputter coating or by high-vacuum evaporation.

All SEM devices include electron source "Gun", electron lenses, sample stage, detectors for all signals of interest, display/data output devices, and infrastructure requirements.

An electron beam, which typically has an energy ranging from 0.2 keV to 40 keV, is emitted from a field emission gun (FEG) or thermionic electron gun fitted with a tungsten or lanthanum hexaboride (LaB₆) filament cathode.

Then electron beam is focused by one or two condenser lenses to a spot about 0.4 nm to 5 nm in diameter. The beam passes through pairs of scanning coils or pairs of deflector plates in the electron column, typically in the final lens, which deflects the beam in the x and y axes so that it scans in a raster fashion over a rectangular area of the sample surface. Samples must

be solid in specific dimensions and be stable in a vacuum on the order of 10^{-5} - 10^{-6} torr. Generally, SEMs use a solid state x-ray detector (EDS), and these detectors are very fast and easy to utilize.

The SEM images in the present study were obtained using a ZEISS Supra 40VP device.

2.5. Transmission electron microscopy

The transmission electron microscope is a very powerful tool to observe features such as the crystal structure and features in the structure, and chemical analysis. And high resolution can be used to analyze the quality, shape, size, and density of quantum wells, wires, and dots.

An electron gun, an objective lens, a movable stage holding the specimen, intermediate and projector lenses, and a florescent screen are the main parts of a TEM device as illustrated in figure 40 (left). A high-energy beam of electrons from the electron gun is focused through a very thin sample. The condenser lens system works to converge the beam of electrons to the specimen. The first lens which has strong magnification, produces a smaller image of the specimen, to the second condenser lens, directing the image to the objectives. The beam is restricted by the condenser aperture, which excludes high-angle electrons.

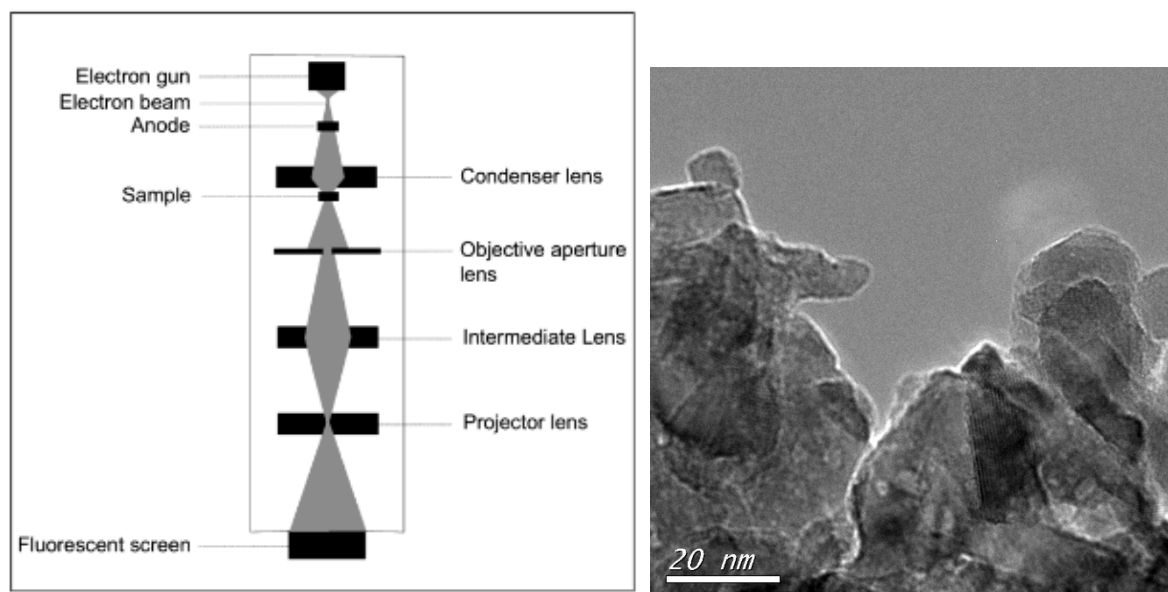


Figure 40. A schematic diagram of the pathway of an electron beam within a TEM technique (172) (left), a TEM image of a sample in the present study (right).

The beam then strikes the specimen and parts of it are transmitted depending upon the thickness and electron transparency of the specimen. This transmitted portion is focused by the objective lens into an image on a phosphor screen or charge-coupled device camera. The image is then passed down the column through the intermediate and projector lenses and is enlarged all the way. The intermediate lens allows great magnification of the image and the projector lens which gives a generally greater magnification over the intermediate lens. The

image strikes the phosphor screen and light is generated, allowing the user to see the image. The electrons are allowed to pass through a fluorescent screen fixed at the base of the microscope.

The image that is formed is called a monochromatic image, which is greyish or black and white (see figure 43, right).

In this work, the transmission electron microscopy (TEM) was performed using JEOL 2011 equipment operating at 200 kV with a LaB₆ electron emission source (Japan). The images were recorded using a Gatan MultiScan CCD camera positioned at the output of the Gatan Imaging Filter system. Samples were prepared by tearing off some pieces of the thin film and depositing them on holey carbon film-supported 400 mesh copper grids. The interplanar lattice spacing of TEM patterns was analyzed with ImageJ.

2.6. Atomic force microscopy

The atomic force microscopy (AFM) technique was applied to observe surface morphology and roughness. An AFM operates by scanning the surface of a sample with a sharp tip equipped at the end of a small lever. It can be used to measure the force between tip and sample by a laser beam deflection which impacts the AFM imaging mechanism. A schematic procedure of the AFM technique is shown in figure 41.

This force does not measure directly but is measured by a laser reflection from the back of a lever. As the tip interacts with the surface, changing the laser position affects the amount of laser light reflected on the photodiode and converts it into an electrical signal, so AFM images generate. Bending and height changing of the lever result in a feedback loop to form an image of the three-dimensional shape of a sample surface. The intensity of this signal will be proportional to the displacement of the cantilever. AFM tips generally fabricate from Si or Si₃N₄ with a radius under 10s nm.

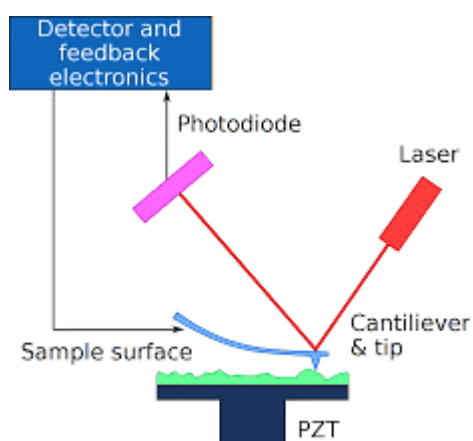


Figure 41. Schematic procedure of AFM technique.

Based on the nature of the tip motion, three modes use in function; static or contact mode (dynamic mode), a vibrating mode, and tapping mode. AFM provides a three-dimensional surface profile; it does not need lenses or beam irradiation. In addition, AFM does not require a vacuum environment like an electron microscope and sample preparation or treatment. Scanning speed and low area of scanning are its main disadvantages (176).

For AFM analysis of the films, tapping mode AFM studies were performed by a Veeco Dimension V (Veeco Metrology Group) device.

2.7. Inductively coupled plasma-optical emission spectroscopy (ICP-OES)

Inductively coupled plasma optical emission spectrometry (ICP-OES) is a powerful tool for the determination of many elements in a variety of different samples. With this method, as shown in figure 42, liquid samples are injected into an argon plasma using a nebulizer and the sample mist reaching the plasma is quickly dried, vaporized, and energized through collisional excitation at high temperature. The atoms and ions can absorb energy to move electrons from the ground state to an excited state. The excited atoms return to low energy position, emission rays (spectrum rays) are released and the emission rays that correspond to the photon wavelength are measured. The element type and the content of each element is determined based on the position of the photon rays, intensity, respectively.

To generate plasma, first, argon gas is supplied to torch coil, and high frequency electric current is applied to the work coil at the tip of the torch tube. Using the electromagnetic field created in the torch tube by the high frequency current, argon gas is ionized and plasma is generated. This plasma has high electron density and temperature (10000 K).

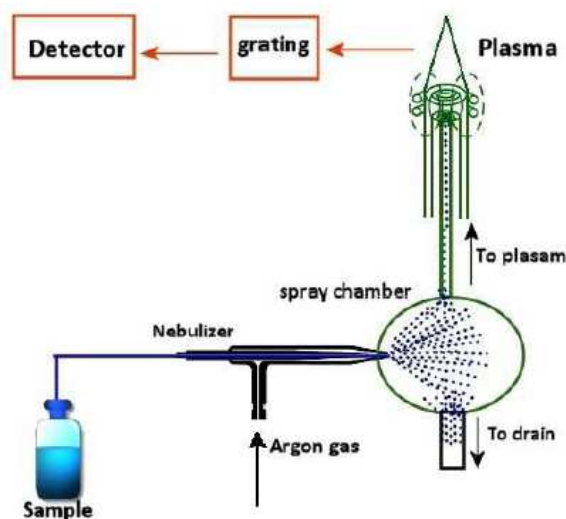


Figure 42. Schematic diagram of an ICP-OES analysis method (170).

In the present work, the ICP-OES analysis was performed on an iCAP 6000 that has an optical resolution < 0.02 nm. The spectrometer is equipped with a polychromator and an optical assembly thermostated at 38°C . The spectral range is between 193 and 900 nm. The detector

RACIDTM is of type Charge Injection Device (CID) and the generator is RF 27, 12 MHz. The iCAP 6000 provides direct control via the iTEVATM software.

Chapter 3: Results and discussion

3.1. Effect of oxygen flux in plasma gas on the structure of TiO₂ films

The TiO₂ films were coated on glass beads by fluidized bed plasma method with various oxygen flows. In these depositions 20 ml of precursor solution was used for the duration of 60 min. The titanium (TTIP, 98% purity, Sigma-Aldrich) precursor concentration in the isopropanol (99%, Sigma-Aldrich) was $C_{Ti} = 1.67$ mol/L. The droplets of TTIP solution were injected inside the plasma chamber by argon gas, TiO₂ films were deposited on glass beads 4 mm in diameter in plasma discharge. The concentration of TTIP in precursor solution, the flow rate of argon, the deposition time, the plasma power, and the weight of glass beads in the deposition experiments were kept constant. We changed the flow rate of oxygen in plasma gas between zero and 25 ml/min. Typically, each deposition was done under the following conditions that are presented in table 6:

Table 6. Plasma deposition conditions of TiO₂ layers coated on glass beads with different oxygen flow rates.

Deposition conditions	Value
Oxygen plasma gas	0 to 25 ml/min
Precursor TTIP carrier gas	300 ml/min
Concentration of TTIP in solution	1.67 mol/L (50:50 V% TTIP: isopropanol)
Duration of each experiment	60 min
Quantity of glass beads 4 mm in diameter	90-100 g

Photographs of the glass beads coated as a function of oxygen flow in the plasma gas are presented in Figure 43. It can be seen that there was a vivid color change of TiO₂ films from black to white after deposition with various oxygen flux in plasma gas. Figure 43 (a) shows coated layers on glass beads before annealing, without any oxygen in plasma gas the color of the layers was black while it changed to brown and white with increasing oxygen concentration from 2 to 25 ml/min in the plasma discharge. The appearance of the samples presented that the increase of oxygen content in the plasma gas was probably linked to the carbon content of films.

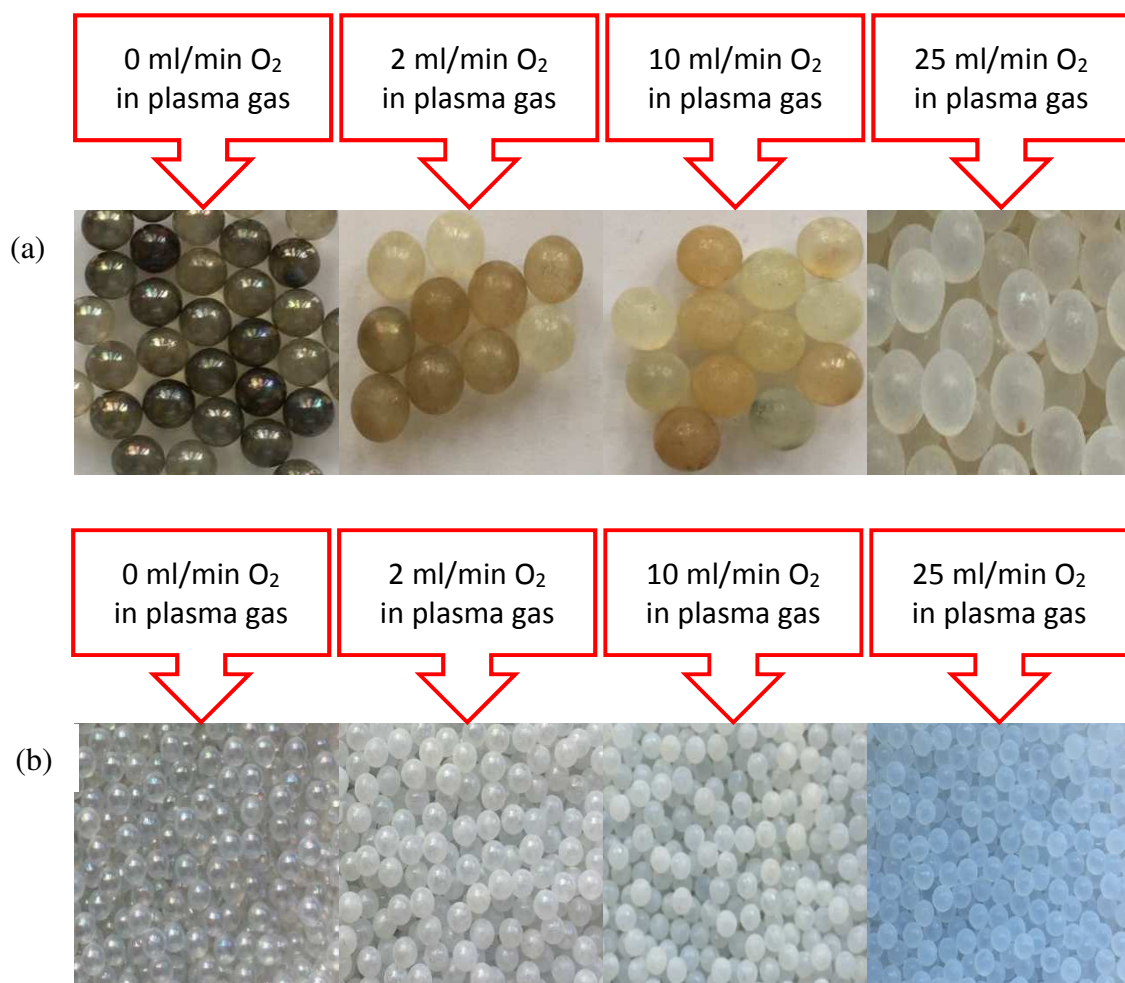


Figure 43. Photos of deposited TiO₂ films on glass beads with different oxygen flux in plasma gas (a) before annealing and (b) after annealing at T = 450 °C in 4 h.

As shown in figure 43 (b), after annealing at 450 °C for 240 min, the color of the layers changed from transparent to white and then to light blue due to the combustion of carbon on the surface of the samples. It appears that oxygen affects the appearance of the layers coated on glass beads. On other hand, the carbon content was evidenced by the Raman spectroscopy analysis presented in figure 44. This figure shows when the unannealed film was analyzed by Raman technique two peaks were observed. Based on previous studies (177, 178) reported that the Raman modes at 1350 and 1582 cm⁻¹ correspond to the graphene-based materials like graphene and graphite. The peak at waveband 1350 cm⁻¹ related to the graphene and the peak at waveband 1582 cm⁻¹ corresponded to the graphite structure.

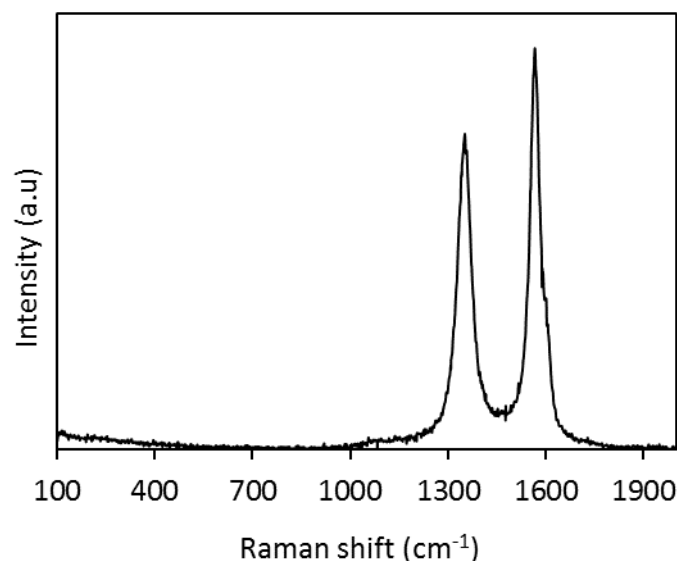


Figure 44. Raman spectroscopy of unannealed TiO₂ film revealed the presence of graphene and graphite in deposited films before annealing.

3.1.1. Raman spectroscopy

All deposited films on glass beads were subjected to Raman Spectroscopy analysis. Figure 45 shows the Raman spectra of TiO₂ nanofilms grown on glass beads before and after annealing. As seen in the figure, none of the wavebands, typical for crystalline forms of TiO₂, were presented for the sample before annealing. However, two distinct broad bands of low intensity at about 460 cm⁻¹ and 640 cm⁻¹ seemingly indicate the appearance of rutile phase (179) in course of the plasma processing along. The Raman tests of the deposits before annealing indicated the amorphous nature of TiO₂ films as prepared in the fluidized bed plasma reactor. This was in agreement with previous studies (96, 180, 181) focusing on the TiO₂ deposited by PECVD where the films were found amorphous. They concluded post-annealing process was required to turn or convert TiO₂ films from amorphous to crystallite structures. For crystal growth of TiO₂ films, a substrate temperature of 450 °C was essential in the their PECVD reactors. Therefore, those TiO₂ films deposited without this temperature all were amorphous (96, 181). Unlike these studies, Kim et al. (182) have prepared the TiO₂ films on silica gel powder by PECVD in a recirculation fluidized bed reactor, at T = 250 °C, and crystallization into the anatase phase has been obtained without any post-treatment.

The Raman spectra of post-annealed (at T = 450 °C, t = 4 h) TiO₂ samples attested to the crystallization of amorphous into the anatase phase. These Raman modes evidenced a crystalline anatase phase. According to previously reported data, the anatase phase of TiO₂ had six Raman bands at 144, 197, 399, 513, and 639 cm⁻¹ and the rutile phase had four Raman bands at 143, 447, 612 and 826 cm⁻¹ (76).

On 0, 2, 10, and 25 ml/min oxygen flow five Raman active modes were observed with anatase structure. All Raman spectra presented in this work had a strong peak at 144 cm^{-1} . For the TiO_2 films grown with the fluidized bed plasma technique five peaks exhibited at 144, 198, 395, 516, and 640 cm^{-1} that correspond to E_g , B_{1g} , A_{1g} , and E_g modes (183-185).

Our result indicating the rutile phase preformation in the original plasma process seem appealing and require further investigations. The expected rutile Raman bands were not identified in the measured spectra, probably because of the screening effect by more intense anatase bands. According to previous studies (185), more annealing temperature required obtaining rutile phase, especially at temperatures more than $500\text{ }^\circ\text{C}$. Despite these results as we will see later the presence of the rutile phase has been detected by XRD together with the anatase phase in our deposits.

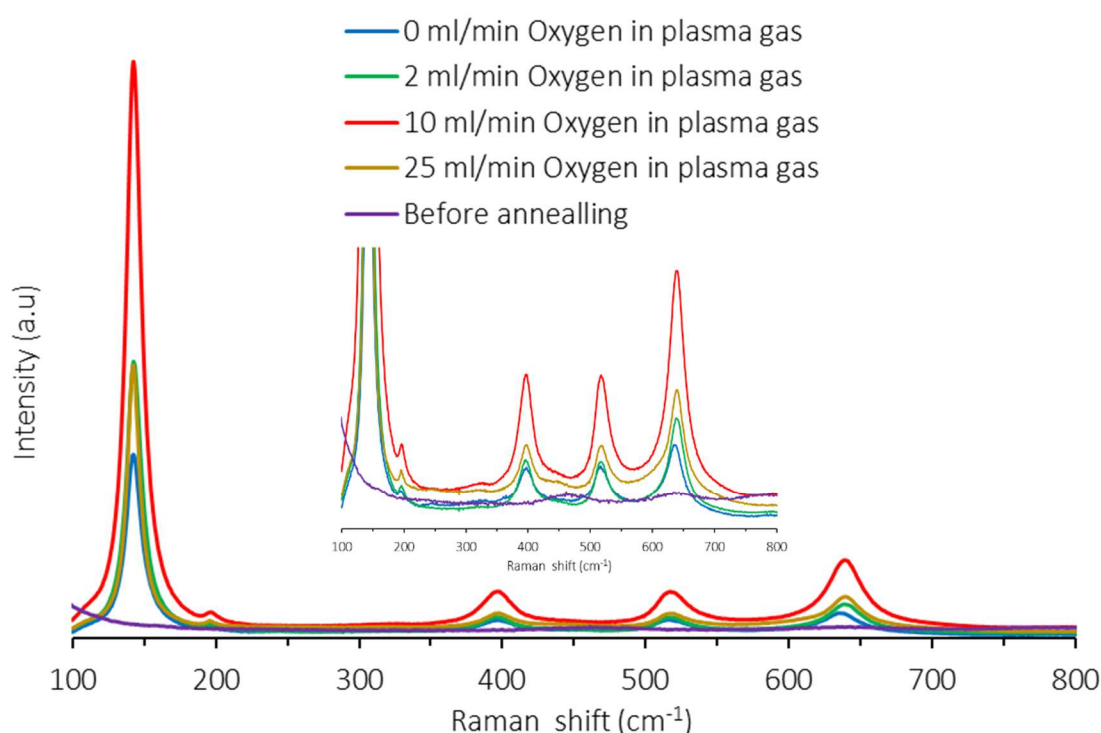


Figure 45. Raman spectra of TiO_2 deposited films on glass beads with different oxygen flux in plasma gas during 60 min.

3.1.2. X-ray diffraction (XRD)

To further compare the crystallinity of TiO_2 films on glass beads, an X-ray diffraction (XRD) analysis was performed. The XRD patterns for the TiO_2 samples are presented in figure 46. As shown, the results have introduced the crystalline structure of deposited films with the different ratios of O_2 flux as reactive gas. All the observed XRD patterns of all TiO_2 films were in good agreement with the standard of anatase tetragonal structure that is indicated with the black line in figure 49. The films also contained the rutile phase of TiO_2 because several

small peaks corresponded to the rutile phase. We observed the apparition of the rutile phase with increasing oxygen in plasma gas. The peaks at $2\theta = 27.4, 36.1, 41.2,$ and 54.3° correspond to the rutile lattice. The peak at 27.4° was related to the rutile phase and its intensity increased with increasing oxygen content inside the plasma reactor chamber. At the same time, two additional peaks were characteristic for rutile ($2\theta = 36.1^\circ$ and 41.2°) and they appeared to be less sensitive to the oxygen flow.

The intensity of the peak at $2\theta = 27^\circ$ corresponding to the rutile phase increased with the concentration of oxygen in plasma gas while the intensity of the anatase peak at $2\theta = 25^\circ$ decreased confirming that the crystalline phase changed from anatase to rutile with increasing oxygen in plasma gas. Most of the peaks in the diffractogram of the TiO_2 films could be identified as the anatase phase. The peaks at $2\theta = 25.3, 38.2, 48.2, 55.02,$ and 62.7° corresponded to (1 0 1), (0 0 4), (1 1 2), (2 0 0), and (2 1 1) plans of the anatase phase of titanium dioxide, respectively (186-188). Our TiO_2 films contained the strongest anatase peak at $2\theta = 25.3^\circ$ and other peaks had less intensity that was similar to the TiO_2 films reported in many other works (99, 189). The intensity of anatase phase peaks became weak as oxygen flux raised. In addition, by increasing O_2 in plasma discharge deposited TiO_2 films were performed in a polycrystalline structure (56).

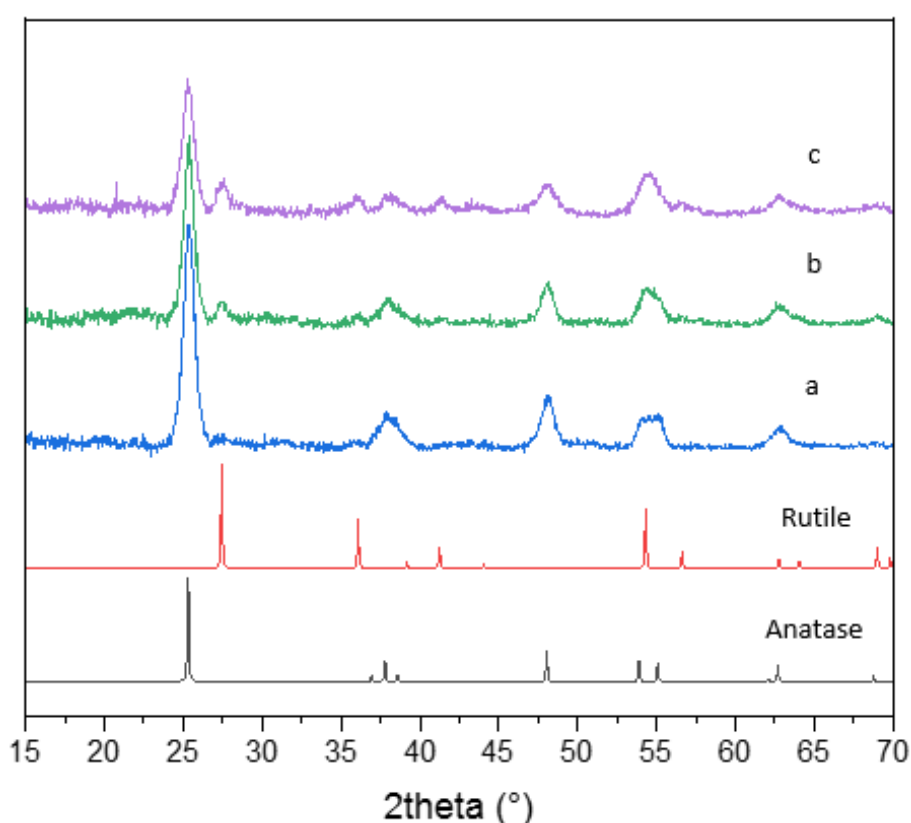


Figure 46. XRD patterns of TiO_2 deposited films on glass beads with a) 0 ml/min, b) 2 ml/min, and c) 10 ml/min oxygen flow in plasma gas.

The crystal size was derived from the full width at half maximum (FWHM) value according to the Debby-Scherrer formula ($D = K\lambda / \beta \cos(\theta)$). The phase quantification was estimated from the Grazing Incidence XRD (GIXRD) patterns with rutile/anatase ratio calculated from the respective (110) and (101) peak intensities via equation $f = \left(1 + 1.265 \frac{I_R}{I_A}\right)^{-1}$ (174). Table 7 summarizes the crystal size of the anatase and rutile phases of the TiO₂ films. By increasing oxygen flow from 0 to 10 ml/min, the anatase phase crystal size was similar of 9 ± 1 nm. The same size of the rutile phase of TiO₂ films for two flow rates of oxygen (2 and 10 ml/min) was calculated by Scherrer relation. The rutile phase content in polycrystalline films was 16 and 27 in mol% for TiO₂ layers prepared in the presence of 2 and 10 ml/min oxygen flow in plasma discharge, respectively.

Table 7. Nano particles' size measurement with Scherrer equation and XRD patterns.

Catalyst	O ₂ flux in plasma gas (ml/min)	Crystallites size (nm)		Rutile content (mol%)
		Anatase	Rutile	
TiO ₂	0	9.3	-	0
TiO ₂	2	9.6	8.1	16
TiO ₂	10	8.7	8.5	27

3.1.3. X-ray photoelectron microscopy (XPS)

X-ray photoelectron spectroscopy (XPS) was used to check the chemical states on the surface of TiO₂ photocatalysts. The experiments have been done in Institut Lavoisier de Versailles at Université de Versailles Saint-Quentin-en-Yvelines. Five samples were analyzed by the XPS technique, the plasma deposition parameters of these TiO₂ layers are presented in table 8.

The XPS spectra of TiO₂ films coated on the plate with 0 ml/min of oxygen flow rate in plasma discharge are shown in figure 47. The XPS survey spectra showed that five samples displayed similar features. All samples had the same oxygen, titanium, and carbon core-level XPS spectra which centered around 529, 458, and 284 eV, respectively.

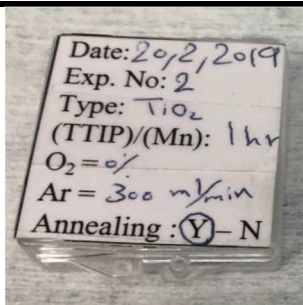
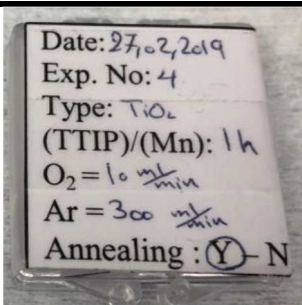
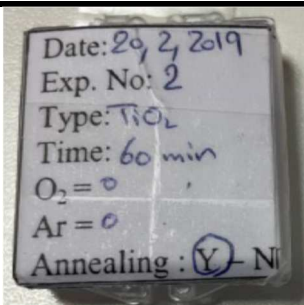
The Ti2p core level peaks (23.3 at. %) with binding energies of 458.9 eV (2p_{3/2}) and 464.6 eV (2p_{1/2}) and the satellite peak related to surface plasmon at 472.2 eV are characteristic of Ti⁴⁺ cation in TiO₂ (190). As reported in the literature, the Ti2p spectra suggest the presence of Ti under Ti⁴⁺ state that confirms the stoichiometry of TiO₂ in the plasma deposited samples. No significant signal of partially reduced Tiⁿ⁺ (n<4) to the lower energies from the principal Ti2p_{3/2} peak (191) have been observed in our spectra. However, a weak Ti2p_{3/2} contribution suggested a minor (~2 at. %) appearance of suboxide Ti³⁺ at 457.4 eV, which nature will be discussed below. The O1s spectra were de-convoluted into three peaks at 530.2 eV (46.3 at %), 531.2 eV (3.4 at%), and 532 eV (8.9 at%). The lower energy one originated from Ti–O–Ti bonds, while the less intense one at higher binding energy was attributed to the physisorbed

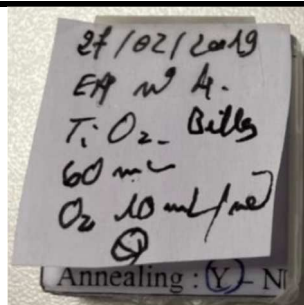
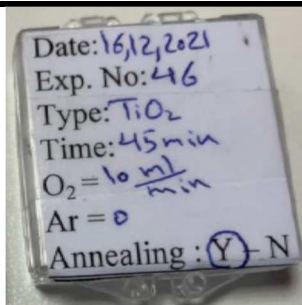


species (O_{phs}), typically oxidised carbonaceous species, supported by observation of four C1s contributions in the vicinity of 285 eV with the total content between 15.5 and 18.7 at% in two samples with 0 and 10 ml/min oxygen in plasma gas, respectively. In addition, the O1s spectra at 530 eV confirmed the presence of TiO_2 in the films that corresponded to the O-Ti bonds and matched for stoichiometric TiO_2 (192, 193). The shoulder at 531.8 eV attributed to the O in cross-linking bonding Ti–O–Si (190, 194, 195). The peak position for Ti and O signals agreed well with literature values for TiO_2 (180, 193).

We notice that a weak peak associated with Si–O–Si bonds at about 533.0 eV could not be identified in the intense spectrum of O1s because of the screening of pure silica substrate by TiO_2 coating. This O1s analysis might indicate $\text{O}=\text{Ti}-\text{O}-\text{Si}=\text{O}$ bonds formed between the coating and substrate. However, Ti–O–H bonds (190) could also contribute at this energy that may compromise the assignment. The Si2p spectra were therefore recorded to verify this point. The interval between two peaks ($\text{Ti}2p_{3/2}$ and $\text{Ti}2p_{1/2}$) is around 5.7 eV (spin-orbit splitting energy) that related to the oxidation state of TiO_2 (196). This ration demonstrated the stoichiometric TiO_2 films were obtained after heat treatment (185, 197). The complementary suboxide Ti^{3+} (457.4 eV) was observed in Ti2p spectrum (191).

The C1s spectra of carbon in both TiO_2 films showed the carbon content was similar and was less than 20 percent. It can be explained by residual amount from the titanium precursor or by adsorption of species from the air atmosphere after deposition (180, 185). The XPS peaks occurred at 283, and 288 eV may be assigned to the C–C, and C=O, respectively (198, 199).

Table 8. Properties of XPS analysis samples.

Deposition	Experiment No. 02	Experiment No. 04	Experiment No. 02
Photo of sample			
Deposition parameters	TTIP/Isopropanol: 50/50 O ₂ : 0 ml/min Ar carrier: 300 ml/min Deposition time: 60 min Annealing: Yes	TTIP/Isopropanol: 50/50 O ₂ : 10 ml/min Ar carrier: 300 ml/min Deposition time: 60 min Annealing: Yes	TTIP/Isopropanol: 50/50 O ₂ : 0 ml/min Ar carrier: 300 ml/min Deposition time: 60 min Annealing: Yes
Type of substrate	Plate	Plate	Plate
Date of XPS analysis	2019 / 07 / 06	2019 / 07 / 06	2022/ 07 / 27

Deposition	Experiment No. 04	Experiment No. 46	
Photo of sample			
Deposition parameters	TTIP/Isopropanol: 50/50 O ₂ : 10 ml/min Ar carrier: 300 ml/min Deposition time: 60 min Annealing: Yes	TTIP/Isopropanol: 30/50 O ₂ : 10 ml/min Ar carrier: 300 ml/min Deposition time: 45 min Annealing: Yes	
Type of substrate	Glass bead	Plate	
Date of XPS analysis	2022/ 07 / 27	2022/ 07 / 27	

The Si2p spectrum with the maximum at 102.3 eV and full-width at half maximum $\Delta E_{1/2}=1.8$ eV (figure 47) evidenced Si³⁺ suboxide (200), which chemical shift of 1.05 eV per oxidation state of Siⁿ⁺ has been earlier established (201). This signal was significantly weaker compared to that of Ti2p and O1s indicating the screening effect of the film. Furthermore, the signal of Si⁴⁺ at 103.8 eV characteristic of silica was not observed which was expected to come from the silica substrate. We noticed in this respect that the peak at ~102-103 eV was a common feature of silicon exposed to plasmas and according to Cardinaud et al. (202) could only be indicative of the Siⁿ⁺ oxidation state and belong to an ultrathin surface SiO₂ layer. Although Si–O–Si moieties made the surface non-reactive, their thermal activation was expected to break Si–O + Si forming point defects Si³⁺, which promoted the film adherence (see e.g. (203, 204)).

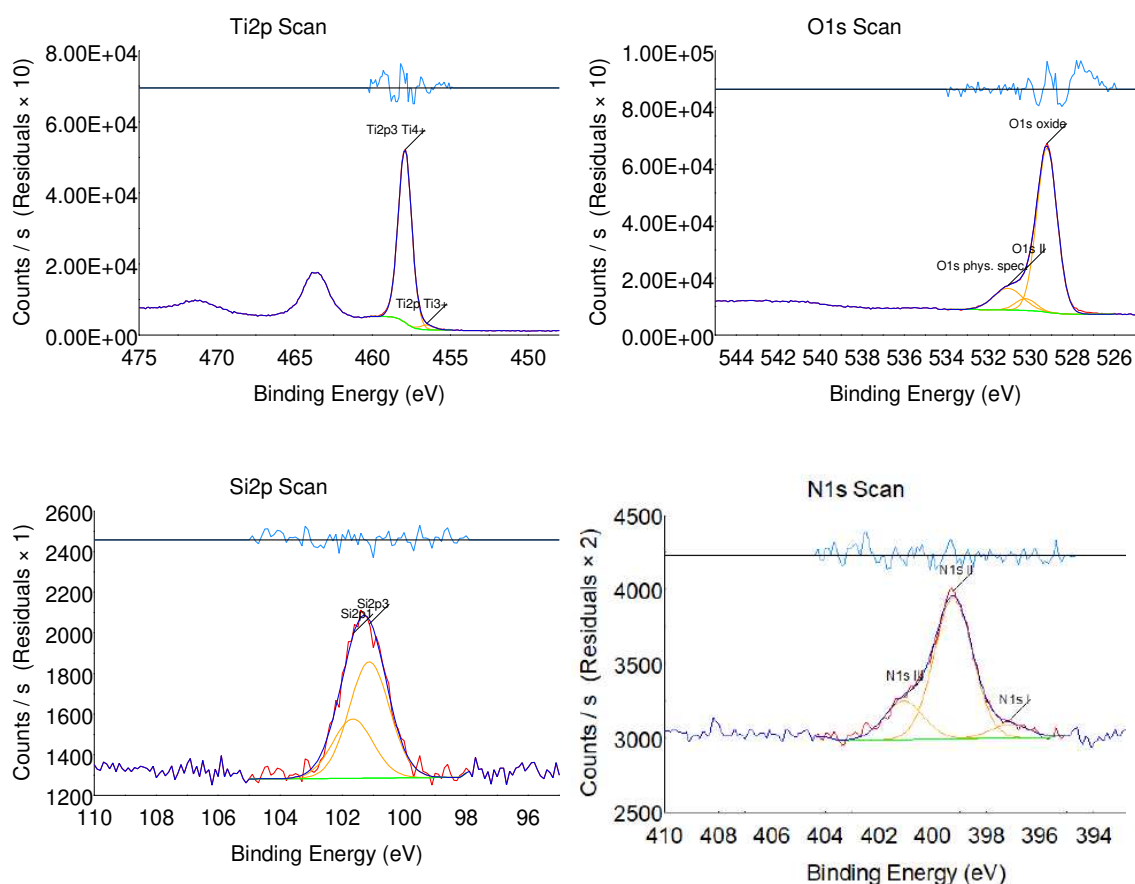


Figure 47. XPS analysis of TiO₂ film coated with 0 ml/min oxygen flux in plasma gas during 60 min.

Considering the weak Si³⁺ and Ti³⁺ signals assigned to the suboxide cations, one could assume participation of asymmetric O≡Si–Ti≡O bonds between the titania film and silica substrate. We noticed in this connection that annealing at 300 °C promoted the formation of Ti–Si bonds in the Ti/O/Si system with a thin oxidized layer (205) and plasma environment could activate the formation of Ti–Si bonds in our experiments. Furthermore, another solution could be proposed involving the formation of O≡Si–O–Ti≡O bonds. In fact, examination of the Ti

coordination number changed in the $(\text{TiO}_2)_x(\text{SiO}_2)_{1-x}$ layer has been undertaken by Gaultois and Grosvenor (206), who had shown that Ti2p and Si2p XPS band energies significantly decreased with Ti content increase due to nearest-neighbor and next-nearest-neighbor effects. In particular, the Si2p energy has decreased by 0.74 eV as x increased from 0 to 0.33. Therefore, somewhat large x-value in the interface region could explain the Si2p band position measured in our study. Although we could not prefer one solution, both $\text{O}=\text{Si}-\text{Ti}=\text{O}$ and $\text{O}=\text{Si}-\text{O}-\text{Ti}=\text{O}$ covalent bonds assured strong adherence to the prepared nanocomposite coatings.

The spectra of oxygen, titanium, and carbon were the major constituents of the films while N and Si have lower spectra with small atomic percentages. In table 9 and 10, the atomic percentage of all elements of two kind of films are listed. The ratio of O/Ti was found 2 and 2.008 for 0 and 10 ml/min oxygen in the plasma deposition process. The presence of carbon is related to the low quantities of oxygen in plasma gas. The presence of nitrogen is due to the presence of leaks or residual nitrogen in our devices.

Table 9. XPS analysis of TiO_2 films deposited with 0 ml/min O_2 in plasma gas.

Name	Peak BE	FWHM eV	Area (P) CPS.eV	Atomic %
O1s oxide	529.23	1.11	171452.07	46.32
Ti2p3 Ti4+	458.01	1.02	134219.99	23.16
N1s	401.08	1.69	471.17	1.1
C1s	284.32	1.16	11518.49	20.5

The carbon comes from the precursor, as the table 8 presents, 10 ml/min oxygen in plasma discharge was not sufficient to oxidize all C to CO_2 . So, carbon as nanofilm or graphene were visible by Raman spectroscopy analytical method on our deposits which presented in figure 44.

Table 10. XPS analysis of TiO_2 films deposited with 10 ml/min O_2 in plasma gas.

Name	Peak BE	FWHM eV	Area (P) CPS.eV	Atomic %
O1s oxide	529.31	1.1	161436.07	41.28
Ti2p3 Ti4+	458.01	1.01	125826.49	20.55
C1s C-C	284.25	1.16	24491.84	16.89
O1s phys. spec.	531	1.94	37033.41	9.48
C1s C-O / C-N	285.56	1.45	5061.36	3.49
C1s COO	287.96	1.75	4353.77	3
O1s II	530.24	1.1	6759.09	1.73
C1s Ph	283.53	1.16	1675.62	1.16
N1s II	399.34	1.75	2073.22	0.88
Si2p3	101.08	1.46	728.66	0.81
Ti2p Ti3+	456.67	1.01	4102.22	0.46

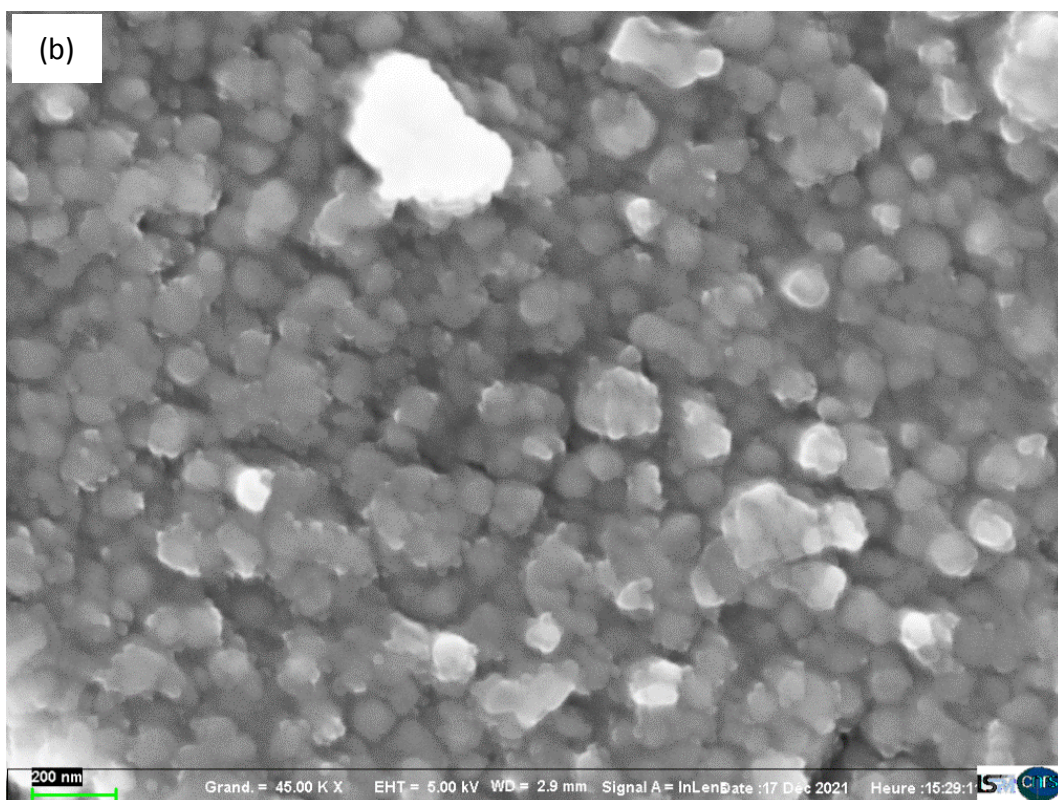
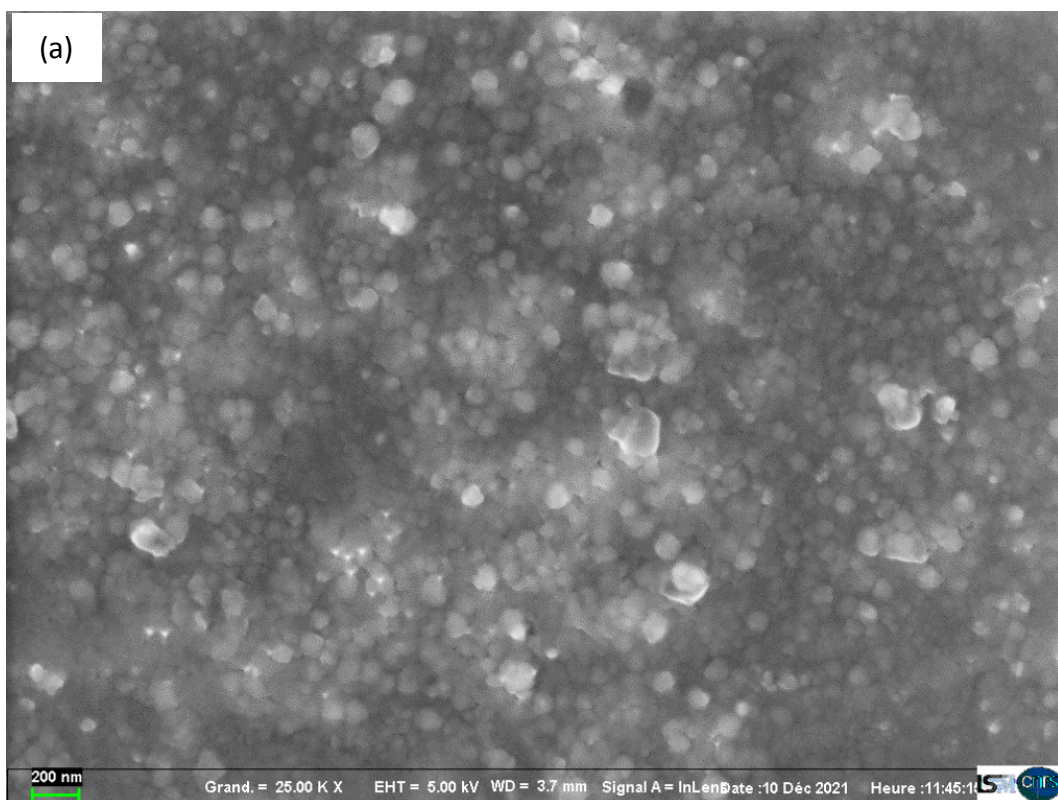
N1s III	401.27	1.75	489.35	0.21
N1s I	397.18	1.75	175.1	0.07

XPS analysis was performed on three more samples which are indicated in table 6. The homogeneity of the chemical environment was verified. The analysis reports thanks to the Institute Lavoisier of Versaille (ILV) are presented in annex I.

3.1.4. Scanning electron microscopy (SEM)

The surface morphology of TiO₂ films coated on the glass beads with various oxygen flow rates after heat treatment at 450 °C, is illustrated in figure 50. The scanning electron microscopy (SEM) micrographs indicated that the films have fully covered the substrate's surface. The granular nanostructure of the crystallites in all films was observed without any cracks or effects and continuous. In figure 48 (a, b, c, and d) as the oxygen flow rate increased from 0 to 25 ml/min, the film uniformity was the same. SEM observations showed no obvious difference in the morphology of TiO₂ films on glass beads with various oxygen content in the plasma discharge. As can be seen, the surface was rough and sphere-liked. In addition, the whole morphology of the surface seems to be homogenous and the size of nano-particles was found to be less than 100 nm.

As reported in a study by Mauchauffé et al. (197) who used atmospheric pressure plasma for the preparation of TiO₂ deposits on silicon wafers, the influence of oxygen in the plasma gas was studied on the morphology of deposited films in the case of O₂/He/TTIP discharges. They reported coatings depositions at low and high power were homogenous and dense. However, at high power in the presence of additional oxygen, they observed the formation of the higher amount of aggregates.



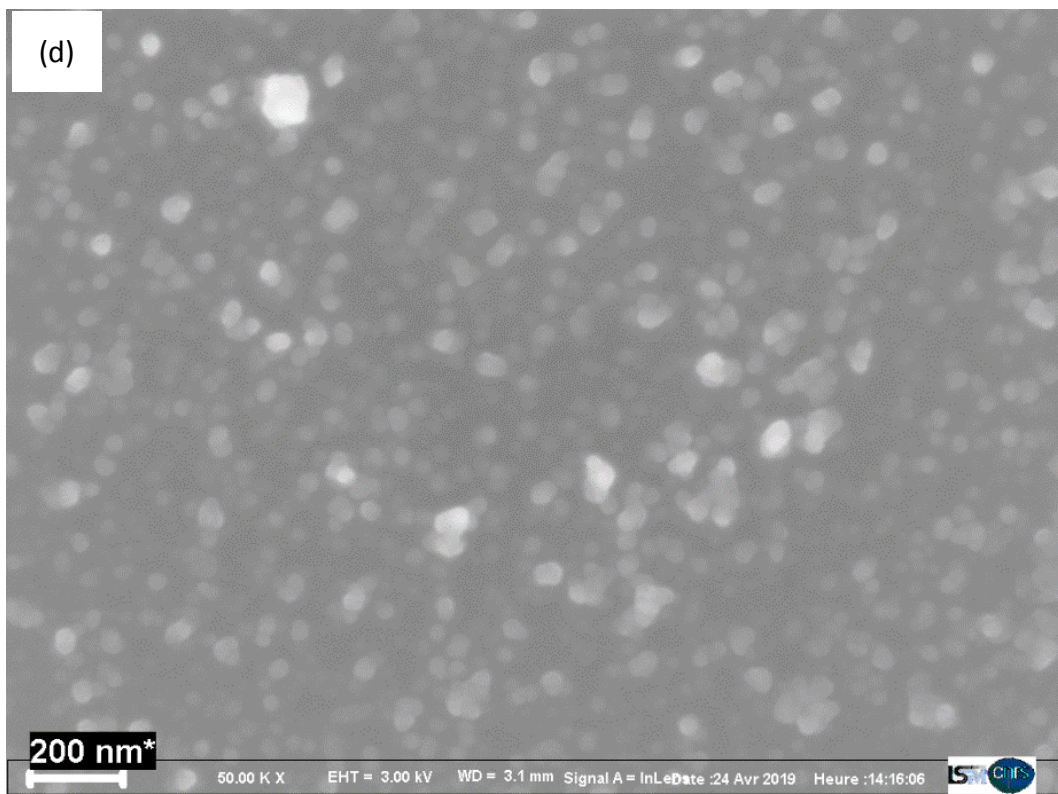
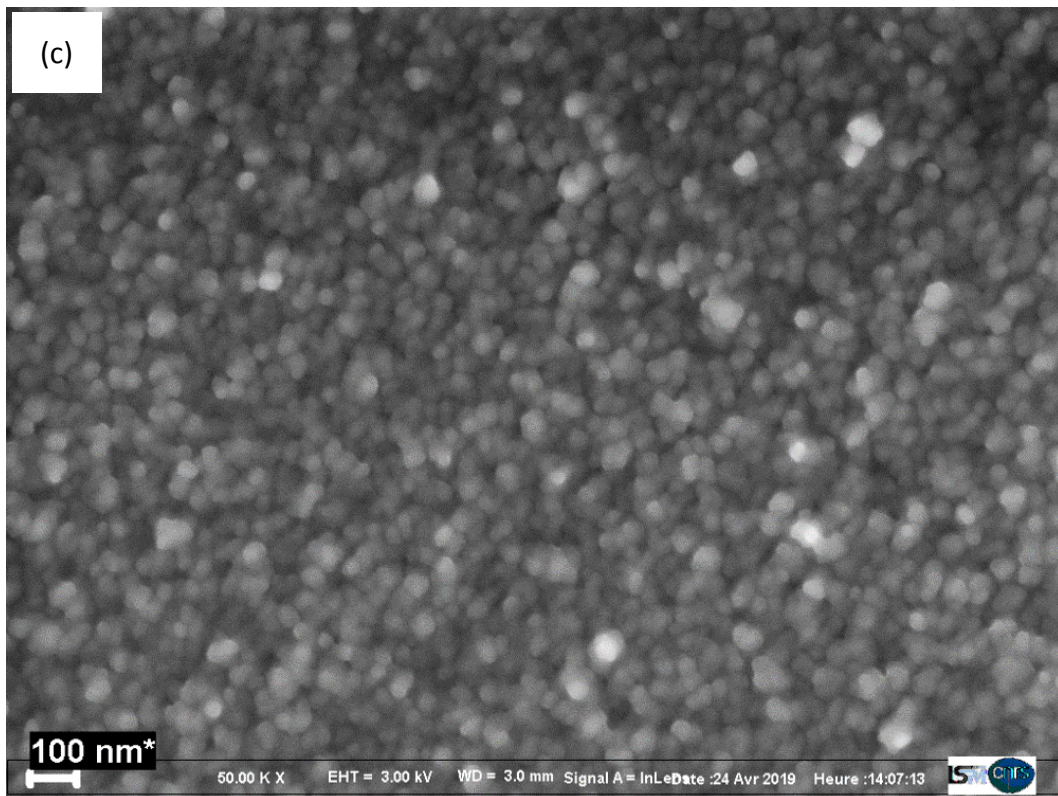


Figure 48. SEM images and histogram graphs of TiO_2 films on glass beads with (a) 0 ml/min, (b) 2 ml/min, (c) 10 ml/min, and (d) 25 ml/min oxygen flux in plasma gas during 60 min.

3.1.5. Transmission electron microscopy (TEM)

To extensively characterize the nano-structure of TiO_2 films on glass beads, transmission electron microscopy (TEM) was applied to observe the crystal structure of TiO_2 coatings. The samples were prepared by crushing TiO_2 on the surface of beads using a diamond pencil then the particles were collected in a droplet of ethanol before observation.

The images of TEM analysis on samples performed with 0, 2, 10 and 25 ml/min O_2 in their deposition are shown in figures 49-51. As images showed atomic spaces were in different directions and lattice rows clearly indicated the crystallized area of nano-sized titania. It was evident from micrographs that nanocrystals particles size was uniform and small with good dispersion. In TiO_2 films with 2 and 10 ml/min of the oxygen content, crystals were highly crystalline on the whole surface. The titanium dioxide's size determined from TEM analysis was in good agreement with values obtained from XRD results with the mean grain size of about 10 nm. The high magnification of TEM images showed the lattice space between two parallel was about 0.32 and 0.35 nm. Results of films on glass beads confirming TiO_2 depositions were successfully prepared by TTIP precursor in fluidized bed plasma device. The d-spacing of TiO_2 with 0.35 nm and 0.32 nm agreed well with anatase (101 plane) and rutile crystalline phases (79, 207, 208).

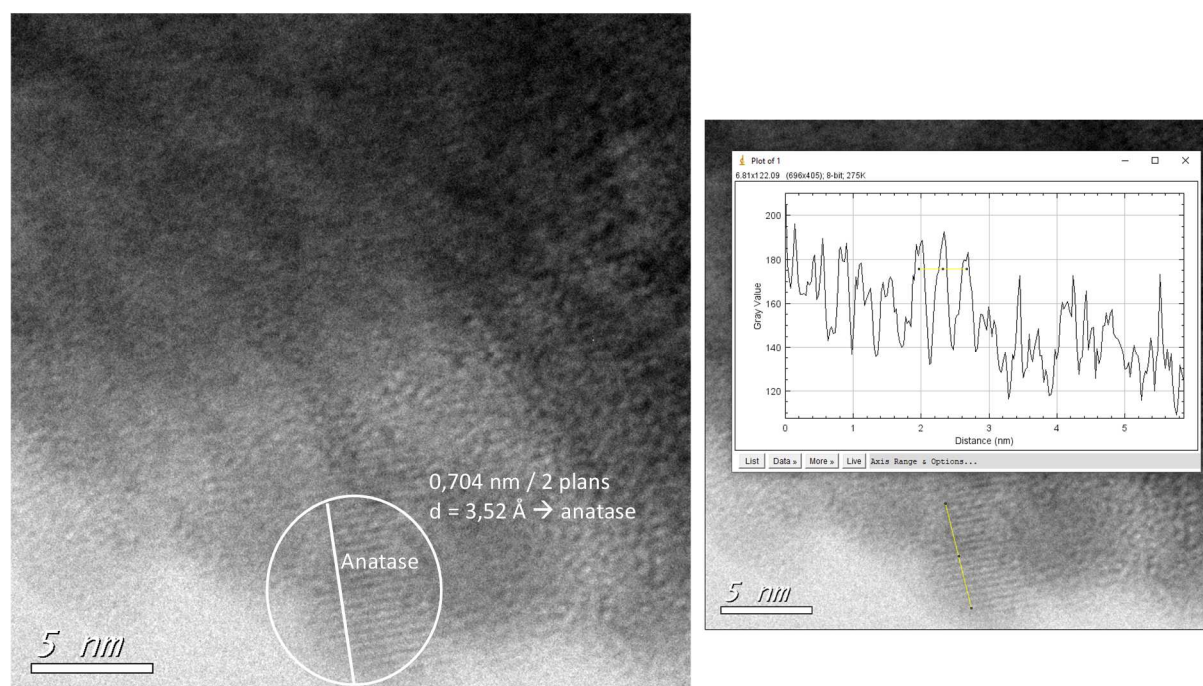
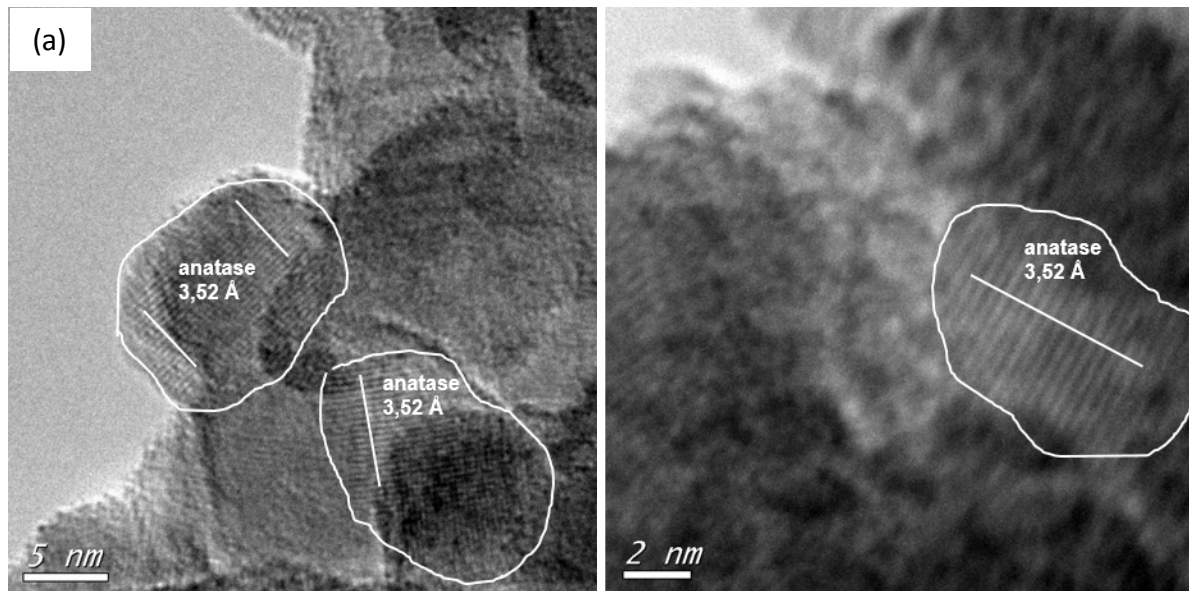


Figure 49. TEM images of TiO_2 films deposited on glass beads with 0 ml/min O_2 in plasma gas during 60 min. The photo on the right represents the profile of light intensity that permitted to measure the inter-reticular distance with a high accuracy (Image J free software (209)).

TEM analysis presented the multi-crystalline structure of TiO_2 , it was evident enhancing the oxygen flux could aid to perform rutile phase even at lower annealing temperature like 450

°C because more studies (210, 211) indicated for rutile phase appearance calcination temperature should be higher than 500 °C. While in the plasma deposition method used in this study, the multi-crystalline phase could obtain. The appearance of the rutile phase after heat treatment at 450 °C was unexpected. In fact, previous studies (210, 212) have shown that rutile appeared in single TiO₂ nanoparticles of size larger than 14 nm and in agglomerated nano-powders at temperatures above 550 °C (t=4 h) (210, 211). The new phase in nano-powders nucleates in the contact area, which required lower activation energy compared to that at the surface or in the bulk (213); concerning anatase-rutile phase transformation, it was initiated more favorably at the twin 112 anatase interface (214). On the other hand, the mixed anatase and rutile phase composition has been reported in films deposited with pulsed micro-plasma cluster source (215). A variation of the stoichiometry has been disregarded in these experiments because of the homogeneous elemental condition O:Ti = 2:1 reported in the XPS analysis performed on our films.



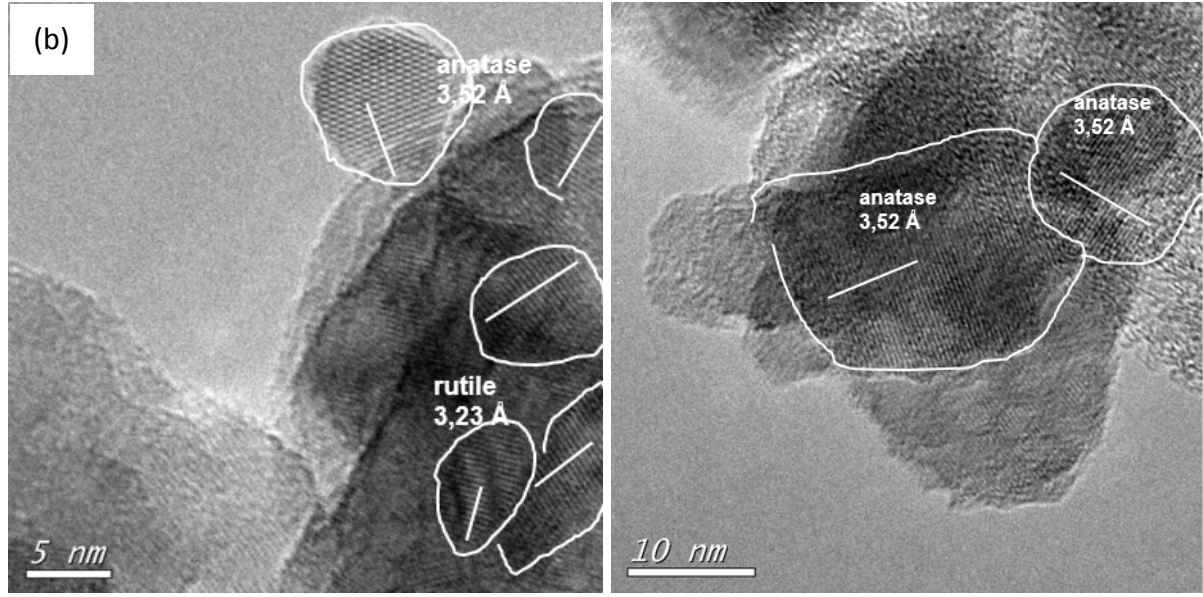


Figure 50. TEM images of TiO₂ films deposited on glass beads with (a) 2 ml/min, and (b) 10 ml/min O₂ in plasma gas during 60 min.

An interesting observation is, however, the formation of similar sizes of anatase and rutile crystallites evidenced by GIXRD and TEM data. This makes the proposed cluster size effect on TiO₂ polymorph formation doubtful (215), since smaller clusters and bigger nanoparticles are not expected to result in the same size entities after crystallization. We believe that the surface state is responsible for the appearance of the rutile phase. In fact, the standard free energy change is expressed by eq. 28:

$$\Delta G^0 = \Delta_f G^0(T)_2 - \Delta_f G^0(T)_1 + A_2 \gamma_2 - A_1 \gamma_1 \quad 28$$

where $\Delta_f G^0$ is the standard free energy of the formation of the two phases and A and γ are respectively the surface area and surface free energy of the particles. The condition of $\Delta G^0 = 0$ enables the phase transformation 1→2 (anatase → rutile) and it obviously depends on the surface state and size of the particle and temperature T (212). Low pressure plasmas, under which the layers were elaborated, are known as thermodynamically non-equilibrium media. It is noteworthy that in these conditions, oxygen molecules undergo dissociative reactions leading to generation of reactive oxygen radicals (163, 216). The exothermic recombination reactions, particularly those of oxygen radicals on the surface of deposit, could also enhance local temperature leading to the rutile phase formation on some sites while the surroundings remain cold. More oxygen radicals are produced in plasma, more recombination reactions take place and, consequently, more rutile crystallites could be produced, in accordance with the correlation between the rutile contents and oxygen gas flow observed in our experiment (Table 7).

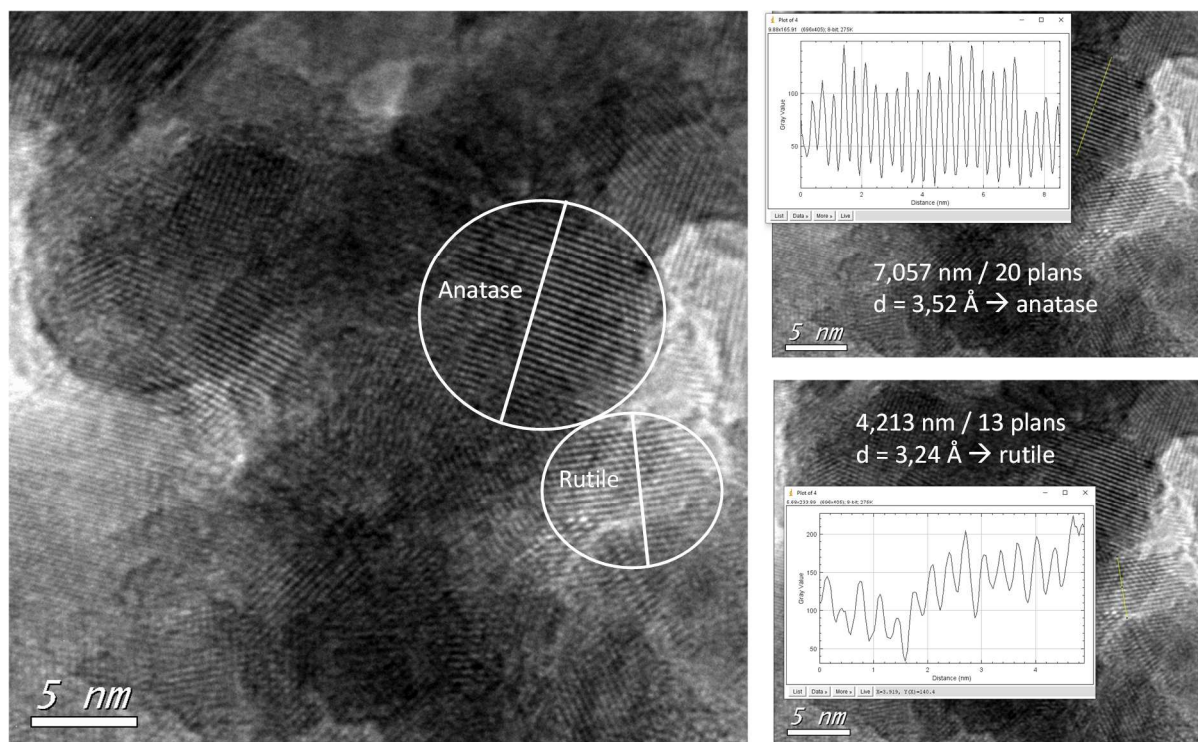


Figure 51. TEM images of TiO_2 films deposited on glass beads with 25 ml/min O_2 in plasma gas during 60 min (left) and analysis of interplane distances of anatase and rutile phases by Image J (right).

3.1.6. Atomic force microscopy

The surface morphology and the roughness were characterized by atomic force microscopy (AFM) measurements to take data about the crystal growth of post-annealed TiO_2 films on glass beads. The images of the AFM technique are presented in figures 52, 53, and 54 for TiO_2 samples deposited with the oxygen flow rate of 0, 10, and 25 ml/min, respectively. It was seen in the figures that all the titanium dioxide films were deposited in continuous mode and exhibited columnar structure. The amount of oxygen in plasma gas had a substantial effect on film morphology during the preparation process. The higher flow rate of oxygen affected the roughness of the surface, with 25 ml/min of oxygen gas, the roughness of films grew with sharper edges of crystalline in the deposition method. As well as, the distribution of the sharper columns was uniform. The surface of the TiO_2 films with sharper edges like mountains and thin protrusions that might aid to have a more specific surface area.

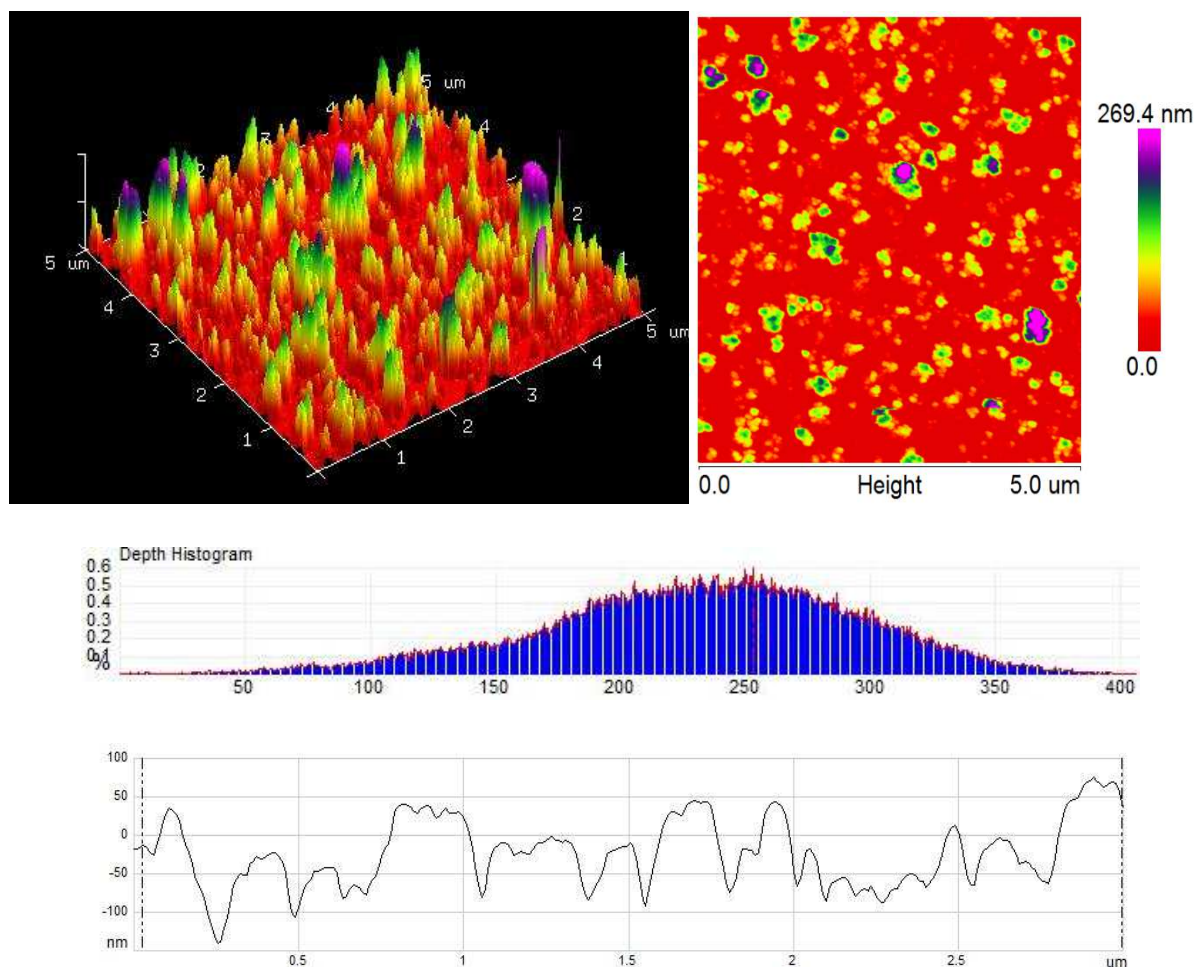


Figure 52. AFM images, depth histogram and the value of root mean square roughness (RMS) of TiO₂ films on glass beads with 0 ml/min oxygen flux in plasma gas during 60 min.

The depth histogram of all TiO₂ photocatalysts was also presented in figures. The values of the graph varied in the range of 0 and 400 nm for 0 ml/min O₂ in sample deposition and it was measured lower than 70 nm for TiO₂ prepared under 10 ml/min O₂ in plasma gas. As well as, the histogram of particle depth in the TiO₂ sample deposited under 25 ml/min O₂ presented values less than 40 nm.

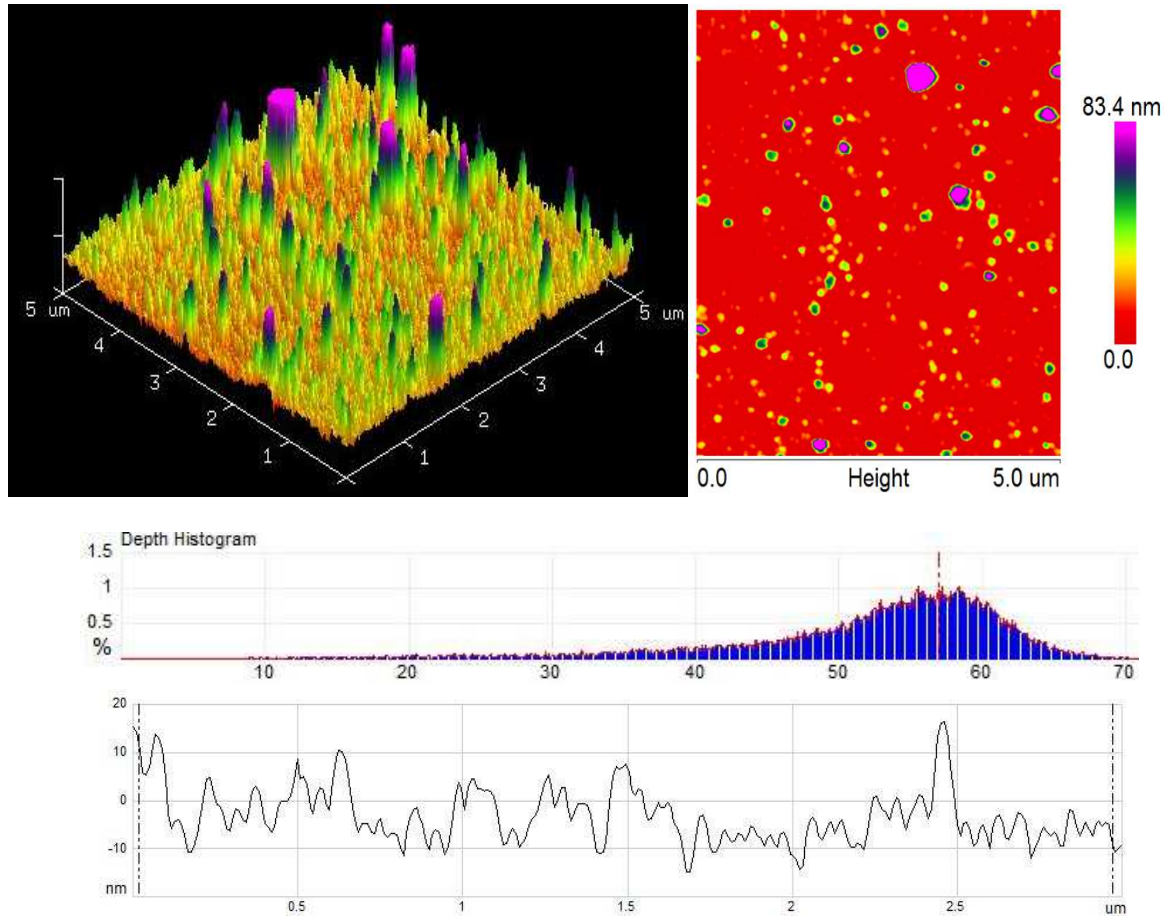


Figure 53. AFM images, depth histogram and the value of root mean square roughness (RMS) of TiO_2 films on glass beads with 10 ml/min oxygen flux in plasma gas during 60 min.

The 3D image suggested that the thickness of TiO_2 films (calculated from AFM images) were 270, 80, and 45 nm for TiO_2 films deposited at 0, 10, and 25 ml/min oxygen concentrations in plasma gas, respectively.

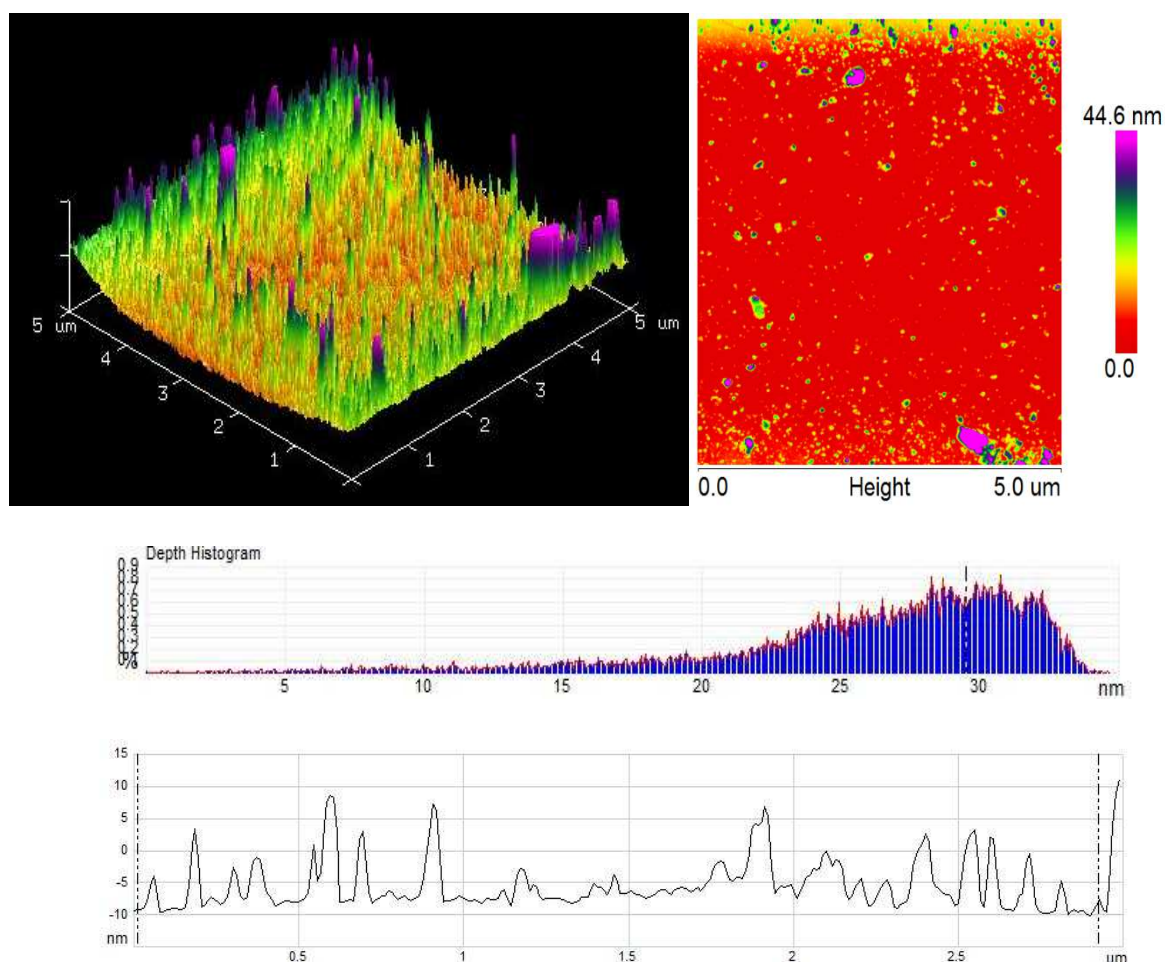


Figure 54. AFM images, depth histogram and the value of root mean square roughness (RMS) of TiO₂ films on glass beads with 25 ml/min oxygen flux in plasma gas during 60 min.

An analysis of the images allowed us to assess the surface roughness as well as the Root Mean Square (RMS). The values of R_a and RMS parameters are presented in table 11. The surface roughness values, in terms of RMS, were measured at 43.6, 5.8, and 3.7 nm for TiO₂ samples deposited with 0, 10, and 25 ml/min oxygen in plasma gas over a measured area of $5 \times 5 \mu\text{m}^2$, respectively.

Table 11. Roughness parameters of TiO₂ films deposited with 0, 10, and 25 ml/min O₂ in plasma gas during 60 min.

Roughness parameter	0 ml/min O ₂	10 ml/min O ₂	25 ml/min O ₂
RMS (nm)	43.6	5.8	3.7
R_a (nm)	35.9	4.2	2.8

We estimated that TiO₂ films deposited in the presence of oxygen have a larger surface area than without the oxygen sample which can influence photocatalytic activity. It was evident

from the XRD measurements that the crystal size decreased when the surface roughness increased which implied the significant effect of oxygen on surface morphologies. Thereby, yielding more surface sites for photocatalytic properties. The highest photocatalytic efficiency of anatase/rutile TiO_2 films was suggested due to the large surface area that originated from the large surface roughness of films on glass beads.

The wider protrusion was obtained for TiO_2 films obtained without oxygen. Both parameters (RMS and R_a) were higher in the case of the films deposited using 0 ml/min O_2 flow rate in the fluidized bed plasma device. While they obtained $R_a = 4.2$ and 2.8 nm, RMS = 5.8 and 3.7 nm for the oxygen flux of 10 ml/min and 25 ml/min in the plasma discharge.

The images of AFM analysis of TiO_2 series II are presented in figures 55, 56, and 57. In this series, three TiO_2 samples deposited under 2, 10, and 25 ml/min O_2 in plasma gas during 45 min with lower TTIP concentration ($C_{\text{Ti}} = 1.002$ mol/L) were analyzed by AFM technique. The surface of TiO_2 film was rougher in 2 ml/min oxygen flow rate in plasma gas than in other samples. Plus, its length and height distribution differed throughout the film.

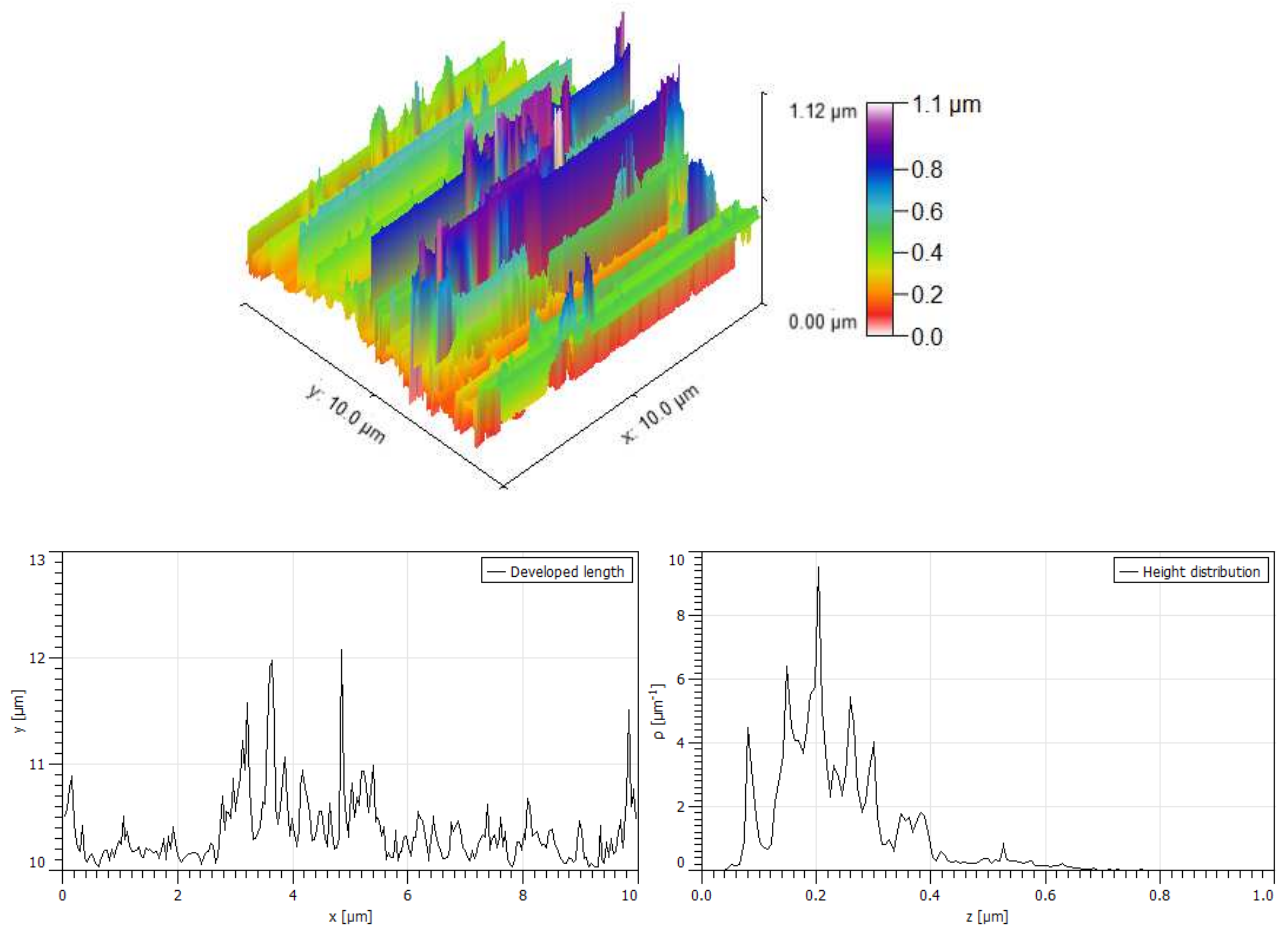


Figure 55. AFM image, developed length and height distribution of TiO_2 films on glass beads with 2 ml/min oxygen flux in plasma gas during 45 min.

In the TiO_2 sample under 10 ml/min oxygen, the developed length and height distribution became higher as the oxygen flow rate increased from 2 to 10 ml/min O_2 . The film morphology also was not similar over a measured area of $20 \times 20 \mu\text{m}^2$. The roughness distribution was not homogenous in this area.

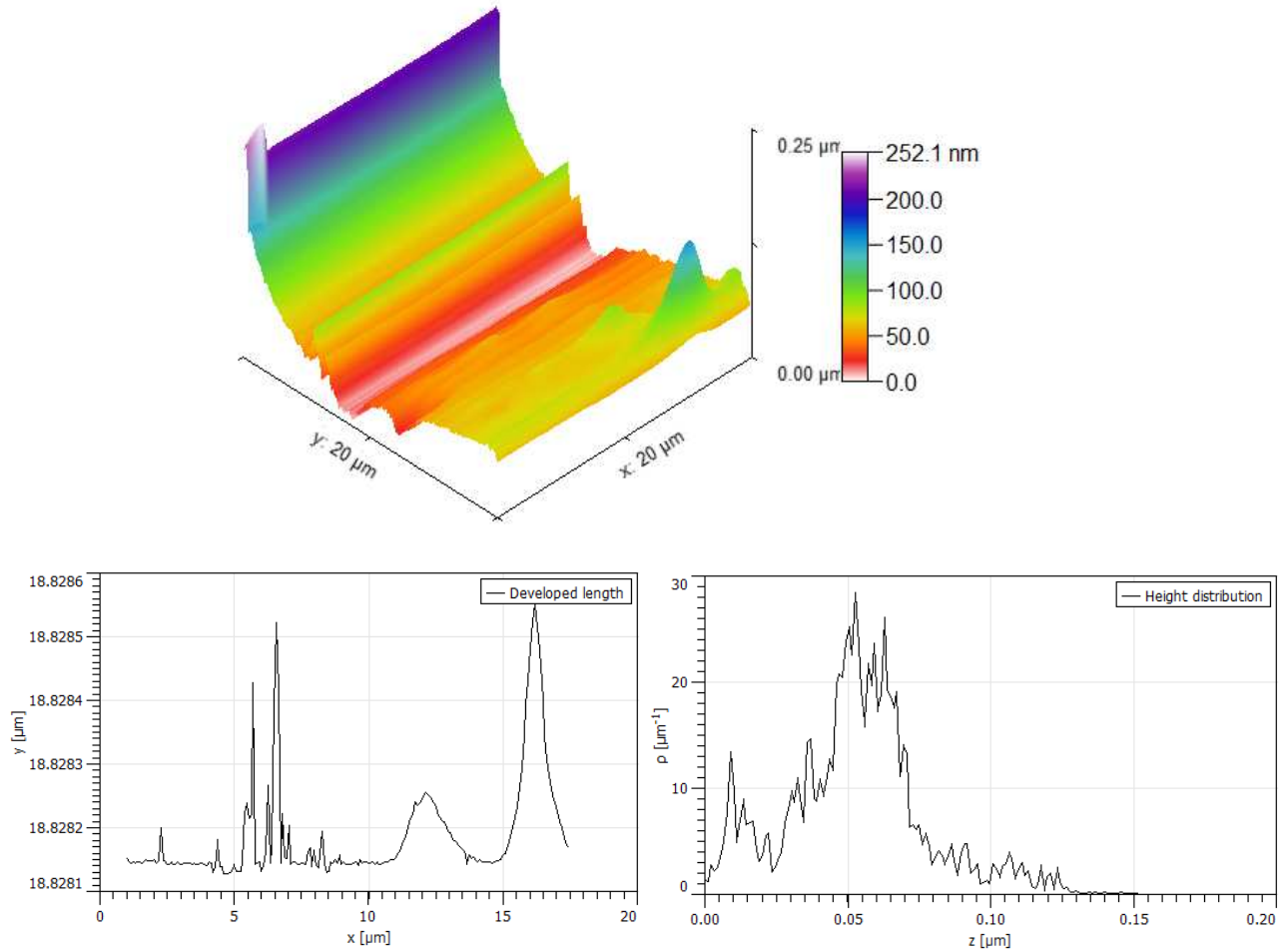


Figure 56. AFM image, developed length and height distribution of TiO_2 films on glass beads with 10 ml/min oxygen flux in plasma gas during 45 min.

As the oxygen increased to 25 ml/min, a few columns were prepared on the surface of glass beads while a great number of films were covered uniformly. The length of columns was higher than samples deposited in 2 and 10 ml/min O_2 in plasma gas. This sample's surface and morphology were not similar.

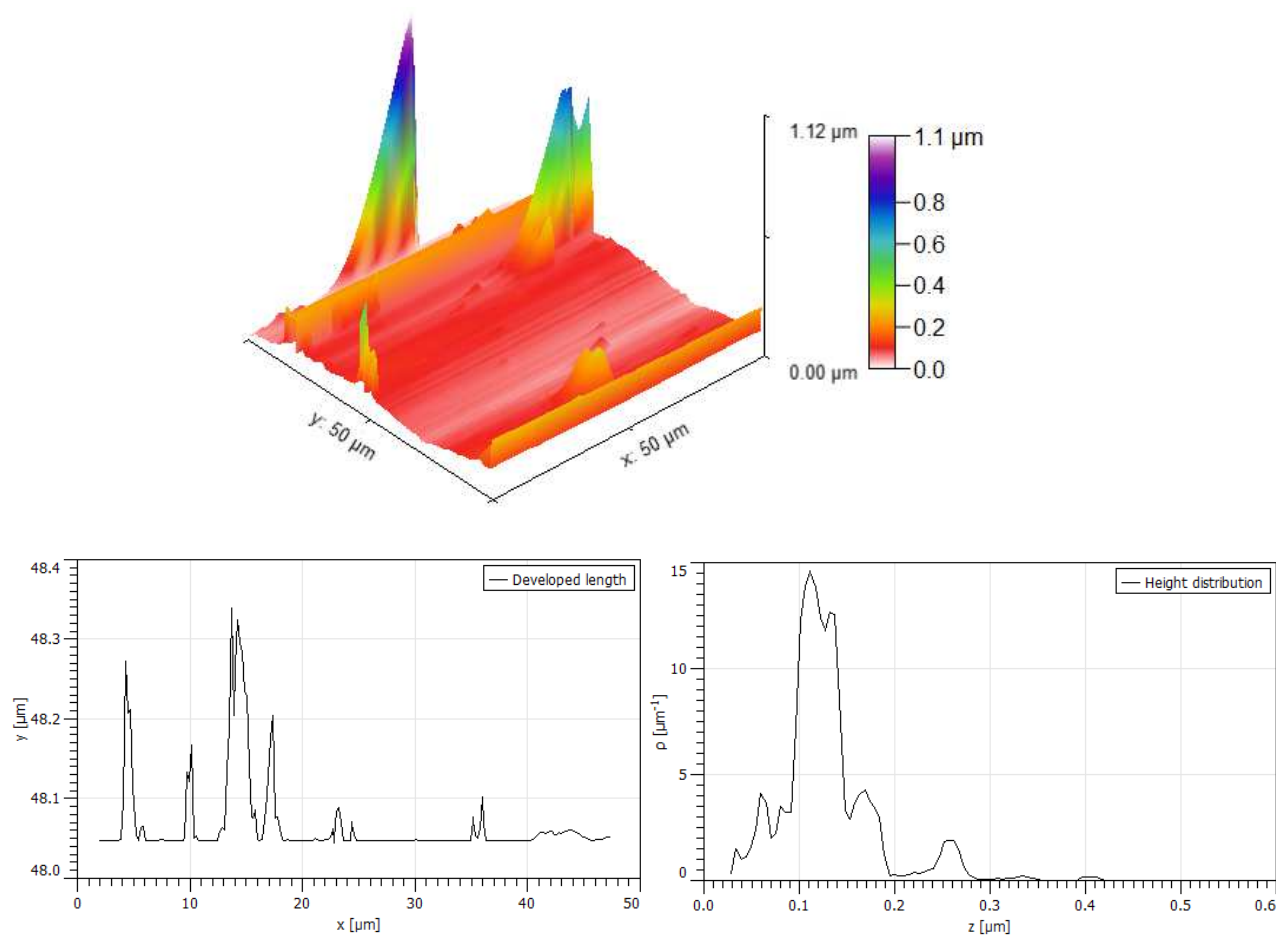


Figure 57. AFM image, developed length and height distribution of TiO_2 films on glass beads with 25 ml/min oxygen flux in plasma gas during 45 min.

The roughness parameters of TiO_2 series II are listed in table 12. The RMS values were determined at about 56.8, 3.04, and 43.8 nm for TiO_2 films deposited with 2, 10, and 25 ml/min oxygen flow rate in plasma gas during 45 min, respectively. the higher RMS and R_a values were obtained for TiO_2 ample deposited under 2 ml/min O_2 with 56.8 and 39.6 nm values, while the lower values were obtained for samples deposited under 10 ml/min O_2 in plasma gas.

Table 12. Roughness parameters of TiO_2 films deposited with 2, 10, and 25 ml/min O_2 in plasma gas during 45 min.

Roughness parameter	2 ml/min O_2	10 ml/min O_2	25 ml/min O_2
RMS (nm)	56.8	3.04	43.8
R_a (nm)	39.6	1.8	22.8

In conclusion, it must be noted that the oxygen flux, deposition time, and TTIP concentration in plasma deposition parameters can affect the surface morphology. Oxygen flow rate plays an important role in the roughness of the surface. Deposition time and TTIP precursor concentration can influence the thickness of films coated on glass beads. The TTIP concentration in precursor solution has affected the growth rate of films on the surface of glass beads, in the high-level concentration, the substrate surface was covered homogenously. While less amount of TTIP concentration in precursor indicated the layer's growth rate was not similar on the whole substrate's surface and in several points the particles growth rate was higher. In addition, higher deposition time and TTIP concentration can increase the photocatalytic activity of TiO_2 samples by about 15-20% (see 2.1.1 and 2.1.3 in part 4).

3.2. Characterization of deposited $\text{Mn}_x\text{Ti}_{1-x}\text{O}_2$ films on glass beads

In the next step, metal doping in the TiO_2 lattice was studied. For Mn-doped TiO_2 films different Mn acetate content in methanol between 0.1281 and 1.284 g were solved. The Mn-doped TiO_2 layers were generated using the fluidized bed plasma reactor. The two precursor solutions were prepared, a titanium tetraisopropoxide (TTIP, 98%, Sigma-Aldrich) precursor in isopropanol (99.5%, Sigma Aldrich) and manganese acetate ($\text{C}_4\text{H}_6\text{MnO}_4$, Aldrich) in methanol (99%, Aldrich). The titanium precursor concentration in the solution volume was $C_{\text{Ti}} = 1.67 \text{ M}$ for these depositions. The precursor solutions were prepared and the droplets were separately injected into the plasma chamber. Three types of $\text{Mn}_x\text{Ti}_{1-x}\text{O}_2$ ($0.003 \leq x \leq 0.02$) layers were coated on glass beads (4 mm diameter). The 100 g of glass beads were used in $\text{Mn}_x\text{Ti}_{1-x}\text{O}_2$ samples. Firstly, two samples with $x = 0.003$ of Mn percentage solved in methanol were deposited under 10 and 25 ml/min of oxygen flow rate in plasma gas for 35 min, then other samples with $x = 0.01$ and 0.02 of dopant concentration solved in methanol were deposited only in the presence of 10 ml/min O_2 in the plasma discharge. So, four kinds of MnTiO_2 photocatalysts were deposited on glass beads to study dopant influence on characteristic properties. The plasma parameters for Mn-doped TiO_2 deposits are listed in table 13.

Table 13. Plasma deposition conditions of $\text{Mn}_x\text{Ti}_{1-x}\text{O}_2$ layers coated on glass beads with different deposition times.

Deposition conditions	Value
Oxygen plasma gas	10 and 25 ml/min
Precursor TTIP carrier gas	300 ml/min
Concentration of TTIP in solution	1.67 mol/L (50:50 V% TTIP: isopropanol)
Precursor Mn carrier gas	150 ml/min
Concentration of Mn in methanol	$0.128 \leq m \leq 1.284 \text{ g}$
Duration of each experiment	35 min
Quantity of glass beads 4 mm in diameter	90-100

Figure 58 presents the photos of deposited films on glass beads at different plasma conditions before and after post-annealing at 450 °C. Before annealing (figure 58(a)), coated films on the beads' surface were brown which might be related to the carbon or other species of two precursor solutions. As mentioned previously in section 1.1, Raman spectra of black color on coatings related to the graphene-based materials. The coated glass beads with pure and Mn-doped TiO_2 were annealed at the furnace during 240 min at 450 °C. Visually pure TiO_2 displays a remarkable white color, which changed to a light brown color according to the Mn doping that can be seen in figure 58 (b). In other words, Mn-doping could change the appearance of the film's color which might mean Mn atoms were placed in the TiO_2 structure.

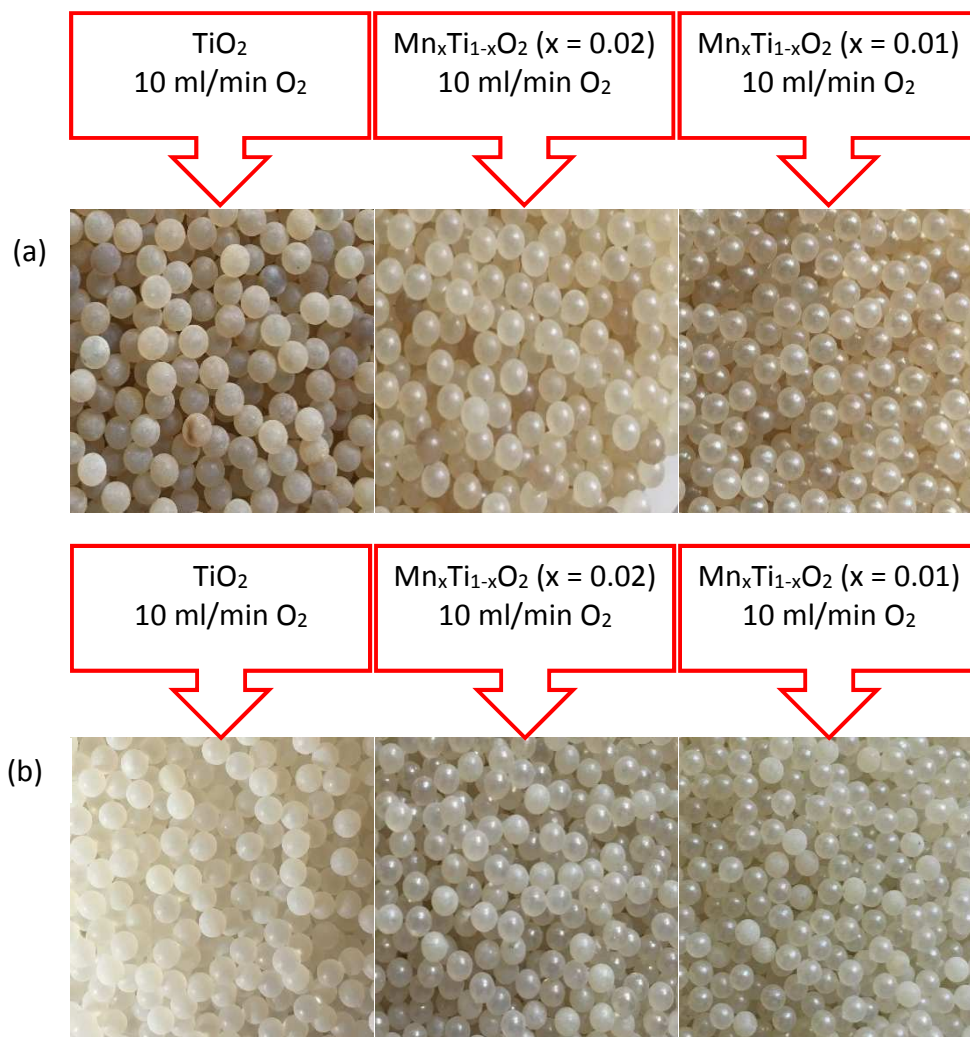


Figure 58. Photos of deposited TiO_2 and $\text{Mn}_x\text{Ti}_{1-x}\text{O}_2$ ($x = 0.01$ and $x = 0.02$) films on glass beads with 10 ml/min oxygen flux in plasma gas (a) before annealing and (b) after annealing at $T = 450$ °C in 4 h.

3.2.1. Raman spectroscopy

Raman spectra of plasma deposited TiO_2 and MnTiO_2 films on glass beads with different manganese concentrations in the region of 100 to 800 cm^{-1} is presented in figure 59. Here, all five Raman active bands were known well, the Raman modes at 145, 198, 399, 515, and 640 cm^{-1} which assigned to the E_g , B_{1g} , A_{1g} , and E_g modes respectively (183-185). These modes confirmed the characteristic mode of the anatase phase of TiO_2 . These results were consistent with the observed XRD results, confirming the anatase phase of TiO_2 films. Raman modes of Mn-doped TiO_2 became wider and the band intensity decreased. The highest Raman peak at 144 cm^{-1} corresponded to the symmetrical stretching of O-Ti-O bonds. As the Mn was added in the deposition process, the vibration frequency was changed, this change indicated the symmetry change in the TiO_2 crystal structure (77). Because the laser signal of Raman analysis depended on vibrational modes, variation of the lattice through the solid formation and associated peak shift were expected.

With inserting the Mn in the TiO_2 lattice a slight shift was detected in the modes since the TiO_2 lattice was sensitive to adding Mn. This shift was strong evidence for the incorporation of Mn^{2+} ion into TiO_2 lattice (112). The Raman shift spectra could be the result of oxygen vacancies (217) and distorting in Ti-O band after Mn incorporation (117).

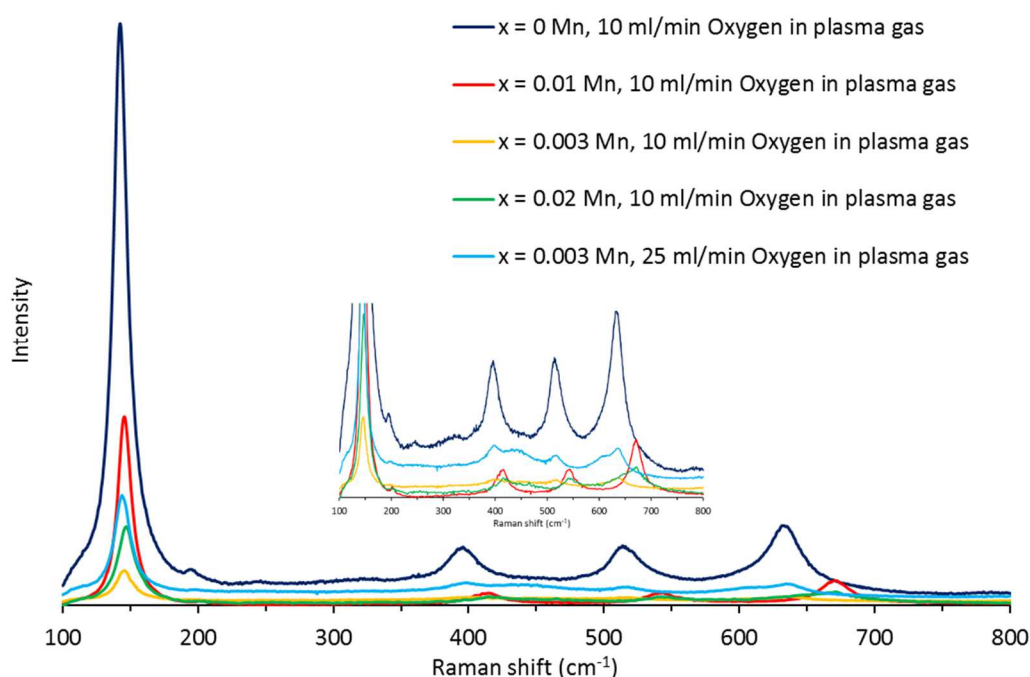


Figure 59. Raman spectra of TiO_2 and $\text{Mn}_x\text{Ti}_{1-x}\text{O}_2$ ($x = 0.003, 0.01$, and 0.02) deposited films on glass beads with 10 and 25 ml/min oxygen flux in plasma gas during 35 min.

3.2.2. X-ray diffraction (XRD)

The XRD patterns of TiO_2 , $\text{Mn}_x\text{Ti}_{1-x}\text{O}_2$ ($x = 0.01$), and $\text{Mn}_x\text{Ti}_{1-x}\text{O}_2$ ($x = 0.02$) films deposited on glass beads with 10 ml/min O_2 in plasma gas are shown in figure 60. The existence of both rutile and anatase phases was confirmed by reference patterns (COD–ID 9015929) and rutile (COD–ID 9015662) (218). These patterns had different peak intensities and widths. As mentioned above plasma deposited films with the multi-crystalline phase had the anatase peaks at 2θ of 25.3, 37.8, 38.6, 48.2, 53.8, 62.6, and 68.7° while the diffraction peaks of the rutile phase were found at 27.4, 54.3, and 62.7°. We found 13 mol% of rutile fraction in $\text{Mn}_x\text{Ti}_{1-x}\text{O}_2$ at $x = 0.02$ composition. When Mn concentration was higher the peak intensity was stronger than the pure TiO_2 indicating higher Mn concentration helped the increase of the particles size (219).

When the Mn content increased in TiO_2 as host lattice, a phase transformation occurred. With $x = 0.02$ mol% Mn-doped in TiO_2 , rutile peaks appeared. As the graph shows, the intensity of $2\theta = 27.4^\circ$ was increased which evidently confirmed the transformation from anatase to rutile due to the generation of oxygen vacancies originating from the imbalanced charge distribution (73, 113). In the case of $x = 0.01$ mol% Mn dopant, rutile phase did not observe when 10 ml/min O_2 was injected into the reaction chamber. It can be described by the fact that doping might inhibit the rearrangement of the TiO_6^{2-} octahedra (220).

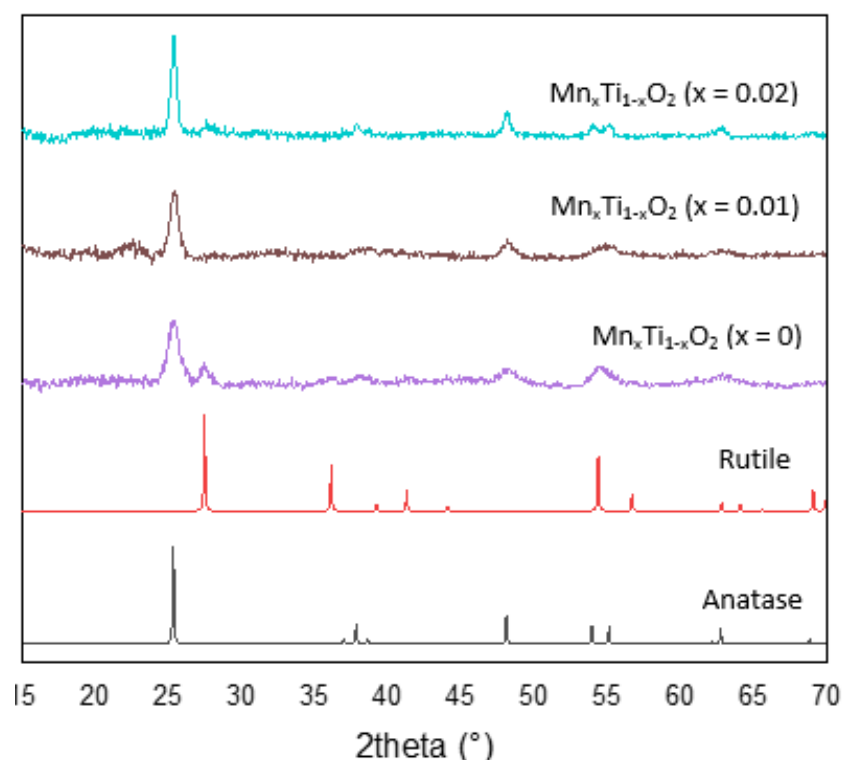


Figure 60. XRD patterns of TiO_2 and $\text{Mn}_x\text{Ti}_{1-x}\text{O}_2$ ($x = 0.01$ and $x = 0.02$) deposited films on glass beads with 10 ml/min oxygen flux in plasma gas during 45 min.

No significant change was observed in the position of peaks when Mn was doped in the TiO₂ structure. The same kind of behavior was obtained in the literature (75) when Mn ions incident inside TiO₂ films. In addition to this, no characteristic peaks were identified for metal oxides in XRD patterns due to low dopant content which did not make the formation of distinct impurity phases and the Mn ion appeared to have been investigated in the basic lattice of TiO₂ (77, 221).

The crystalline size of anatase and rutile phases was calculated by considering the FWHM values of (1 0 1) and (1 1 0) peaks, respectively (112, 173, 219). The calculated crystallite size of TiO₂ and Mn-doped TiO₂ nanofilms are presented in table 14.

Table 14. Nano particles' size measurement with Scherrer equation and XRD patterns.

Catalyst	Mn _x Ti _{1-x} O ₂ (x)	Crystallites size (nm)		Rutile content (%)
		Anatase	Rutile	
TiO ₂	0	8.7	8.5	27
MnTiO ₂	0.01	11.38	-	-
MnTiO ₂	0.02	19.86	7.25	13

The D values for the anatase phase of TiO₂, Mn_xTi_{1-x}O₂ (x = 0.01), and Mn_xTi_{1-x}O₂ (x = 0.02) were found at 9 ± 1 nm, 12 ± 1 nm, and 20 ± 1 nm, respectively. The observed crystallite size revealed that with increasing doping concentration the average size of crystallite increased. It was evident from the decrease of full width at half maxima in diffraction patterns. In the obtained rutile fraction with increased Mn content in the plasma chamber, the value of crystallite size for Mn_xTi_{1-x}O₂ (x = 0.02) was found to be 7 ± 1 nm for rutile. Generally, anatase to rutile phase transformation was considered as a nucleation growth process within the anatase phase (110). In addition, metal ions with valency less than +4 and higher ionic radius promoted oxygen vacancy. In Mn doping TiO₂, high Mn might assist the agglomeration of particles. The increase in crystal size might be due to distortion of the TiO₂ lattice (113, 222). This indicated the incorporation of dopant substituted the Ti⁴⁺ ions from the TiO₂ lattice. Mn was in +2 oxidation state within ionic radii of 0.83 Å which could replace the Ti⁴⁺ ion and charge compensation was achieved by the formation of oxygen vacancies (73, 113). The higher valence of (Mn⁴⁺) had a lower ionic radius and shifted the XRD peaks to a higher angle (62). So, at lower Mn concentration the induced oxygen vacancies might not be sufficient to phase transformation.

As per reported in literature, Devi et al. (110) obtained the crystal structure of mixture phases TiO₂ with metal dopants. Phase transformation occurred after the transition of metal dopants. Bharat et al. (219) observed a mixed phase of anatase and rutile with Mn doping. In contrast to our results, Li and Cao (75) reported a stable anatase phase with increasing Mn concentration up to 10%.

3.2.3. Transmission electron microscopy (TEM)

The morphology of the Mn-doped TiO_2 ($x = 0.003$) photocatalyst was investigated by the TEM technique. Figure 61 shows the TEM images of $\text{Mn}_{0.003}\text{Ti}_{0.997}\text{O}_2$ films deposited on glass beads with $x = 0.003$ mol% of Mn under 10 ml/min O_2 flow rate for 35 min. The crystal structure of MnTiO_2 was observed in micrographs. These photos also showed the TiO_2 crystallite films formed a porous network and that the nanoparticles were not well-defined separate crystallites. In comparison to undoped TiO_2 with the same oxygen flow rate, doping of Mn in TiO_2 lattice displayed different results which suggested that doping might have caused clustering and disfiguring structure of TiO_2 (74).

High-resolution TEM images of the MnTiO_2 sample with $x = 0.003$ mol% Mn exhibited lattice fringes around 0.32 and 0.35 nm corresponding to the rutile and anatase phases, respectively. Therefore, their results confirmed both the purity of the deposited TiO_2 films and the effectiveness of the Mn substitution in their lattice.

The observed value of the energy dispersive analysis spectrum of the Mn-doped TiO_2 sample indicated that Mn ions have been integrated into TiO_2 films. However, the atomic ratio of Mn-doped TiO_2 was found lower than the nominal concentration in the precursor solution. As a result of EDS analysis, Ti, O, and Mn peaks with high intensity were obtained and no other structure was found. The atomic percentage suggested that the Mn was not homogeneously dispersed in TiO_2 films.

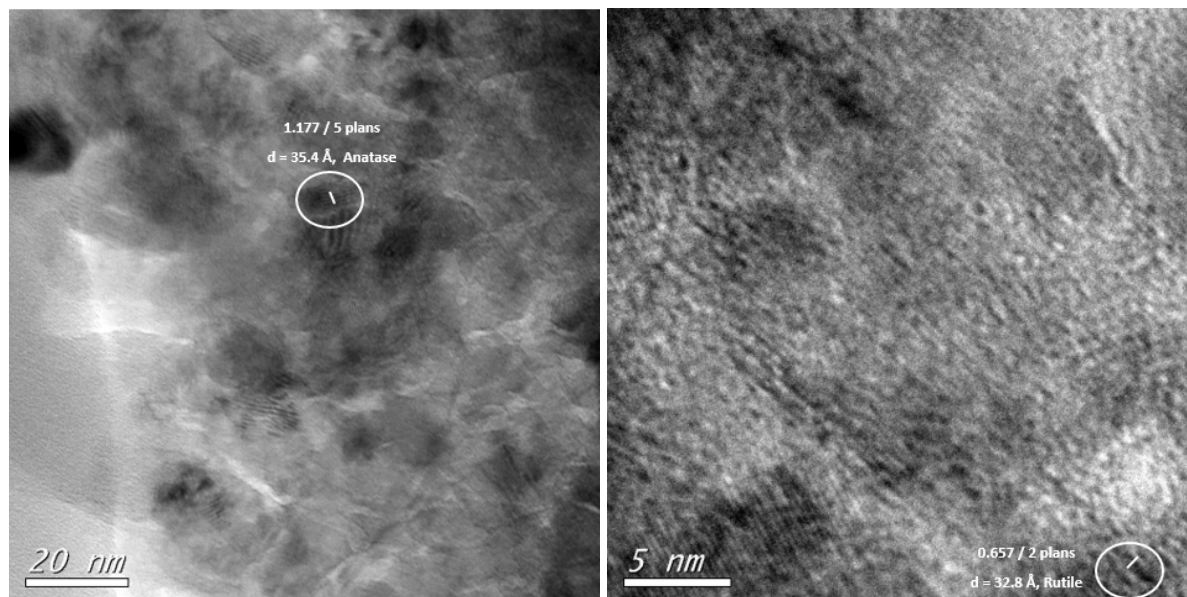


Figure 61. TEM images of $\text{Mn}_x\text{Ti}_{1-x}\text{O}_2$ ($x = 0.1$) films deposited on glass beads with 10 ml/min oxygen flux in plasma gas during 45 min.

Conclusion

- The TiO_2 films coated on glass beads were deposited by the low-pressure fluidized bed plasma device under different oxygen fluxes with 0 ml/min, 2 ml/min, 10 ml/min, and 25 ml/min.
- The TiO_2 photocatalysts were found in the amorphous phase before annealing and crystallized by heat treatment at $T = 450\text{ }^\circ\text{C}$ for 240 min under atmospheric conditions.
- The Raman spectra of as deposited indicated the presence of the rutile phase, while the anatase phase of TiO_2 is observed after annealing. In addition, SEM and AFM images presented the nano-size of films on the surface of glass beads.
- The XRD, RAMAN, and TEM analytical methods presented a mixture of anatase and rutile phases, these results displayed that as the oxygen flux in plasma discharge increased from 2 to 10 ml/min, the rutile phase appeared and its fraction was determined about 16 and 27 mol% with 2 and 10 ml/min O_2 in plasma gas, respectively. While the pure anatase phase was obtained in the absence of O_2 in plasma gas.
- The stoichiometric ratio of TiO_2 was obtained for all samples on the basis of XPS results. Chemical bonds between TiO_2 films and glass beads are shown by XPS analysis.
- The Mn-doped TiO_2 photocatalytic films were deposited on glass beads with three content of manganese acetate (0.128, 0.313, and 1.284 g) solution in methanol which was injected separately inside the fluidized bed plasma chamber.
- The ICP technique exhibited that the atomic ratio of $\text{Mn}_x\text{Ti}_{1-x}\text{O}_2$ was obtained about 0.01, 0.003, and 0.02 for 0.128, 0.313, and 1.284 g Mn acetate in methanol.
- The XRD patterns and TEM images confirmed the presence of anatase and rutile phases in $\text{Mn}_x\text{Ti}_{1-x}\text{O}_2$ samples after annealing for four hours at $T = 450\text{ }^\circ\text{C}$.

Notations

ICP-OES	Inductively coupled plasma-optical emission spectroscopy
XRD	X-ray Diffraction
XPS	X-ray Photoelectron Spectroscopy
SEM	Scanning Electron Microscopy
TEM	Transmission Electron Microscopy
AFM	Atomic Force Microscopy
ZnO	Zinc oxide
CuO	Copper oxide
PECVD	Plasma Enhanced Chemical Vapor Deposition
TiO ₂	Titanium dioxide
Mn	Manganese
Zr	Zirconium
V	Vanadium
mm	Millimeter
MFC	Mass Flow Meter
Pa	Pascal (unit of pressure)
TTIP	titanium tetraisopropoxide
g/mol	gram per mole
C _{Ti}	Titanium concentration
mol/L	Mole per liter
Ar	Argon
P	Power (W)
W	Watt
t	Time (s)
T	Temperature (°C or K)
ml/min	Milli liter per minute
M	Molar concentration (mol/L)
mol	Mole
Mn	Manganese
X	composition of dopant content compared to concentration of precursor
ppm	Part per million
mmol/L	Milli mole per liter
°C/min	Centigrade degree per minute
h	Hour
H	Hydrolysis ratio
C _w	Water concentration
C _v	Vanadium concentration
Re	Reynolds number
m/s	Meter per second
min	Minute

λ	Wavelength (nm)
d	Interplanar distance between planes
θ	Angle
D	Crystallite size (nm)
B	Full width at half maximum
K	Shape factor
I_A	X-ray intensity of peak corresponding to anatase phase
I_R	X-ray intensities of peak corresponding to rutile phases
EDS	X-ray Detector
He	Helium
$\Delta_f G^0$	Standard free energy
A	Surface area and
γ	Surface free energy
RMS	Root Mean Square

PART 4. PHOTOCATALYTIC ACTIVITY OF TiO_2 FILMS

This chapter will explain the photocatalytic activity of different catalysts under natural and artificial irradiation. The photo-reactor pilots used for the photocatalytic activity of different photocatalysts will be presented. Photo-degradation of cefixime in an aqueous solution with all samples will permit us to compare the activity of our photocatalysts. The results also will report the optimum preparation conditions of TiO₂-based films coated on glass beads. Then the regeneration methods will be expressed and their performance on our photocatalysts will describe.

Chapter 1. Experimental setups

The photocatalysis experiments allowed us to determine the conditions and study the activity of TiO₂ films coated on glass beads and consequently, know the influence the fluidized bed plasma parameters of deposited films compared to those photocatalysts obtained by Sol-Gel method. The photocatalysis experiments were performed in two pilot-scale photoreactors with different radiation sources: sunlight and an artificial light (UV lamp).

1.1. The solar photo-reactor

The solar photolytic and photocatalytic activity of different catalysts were carried out in a compound parabolic concentrator (CPC) solar pilot which was installed on the roof of the Chemical Engineering Department of the Faculty of Engineering, University of Isfahan, Iran. It was mounted on a fixed platform facing south tilted 33° (latitude: 32.65, longitude: 51.66) to collect maximum solar energy.

The designed solar photoreactor for solar photocatalytic applications consists of several parts: concentrators or collectors, an absorber pipe, a peristaltic pump, a recirculation tank, and light meters measuring the light intensity of sun. The schematic of the solar pilot is presented in figure 62.

The solar collectors were manufactured with highly reflective aluminum; the CPC used for this work has been described in part 2 (see chapter 4). It has a concentration factor ($CR = \frac{1}{\sin \theta_a} = \frac{A}{2\pi r}$) equal to 1 and an acceptance angle (θ_c) of 90°. This structure aids to collect and focus both direct and diffuse solar radiation onto a transparent Pyrex pipe. It was placed around the tube in the east-west orientation. The Pyrex tube (inner diameter of 46.8 mm, length of 500 mm, and thickness of 1.6 mm) aligned in the same orientation.

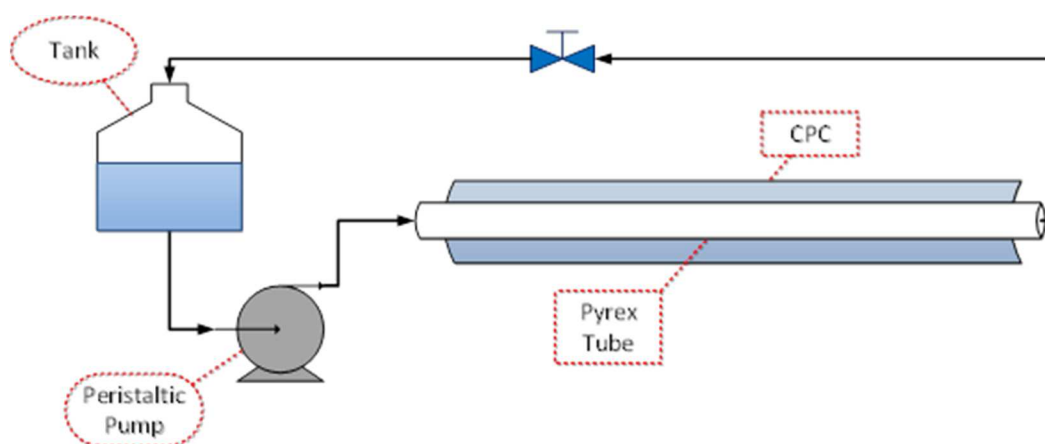


Figure 62. Schematic of the CPC photo-reactor installed at the University of Isfahan, Iran.

It operates in continuous batch mode with a fixed volume of wastewater which was recirculated continuously through the system employing the peristaltic pump.

The total irradiated surface and total CPC surface are around 735 and 1120 cm², respectively. The vessel of the reactor was covered with aluminum foil to avoid solar radiation to enter the tank from all directions. Experiments were done during the central hours of days due to receiving maximum solar radiation.

1.1.1. Photocatalysis experiments by natural irradiation in the CPC solar photo-reactor

Degradation of cefixime with differently prepared photocatalysts was performed in parallel or on successive days at about the same time from 10:00 to 16:00 at local time in Isfahan during spring, summer, and autumn with the CPC solar photo-reactor shown in figure 63. Experiments started at local noon for maximum solar radiation, which was measured with Solar Power Meter (Datalogging, TES 132) on the average 1000 W/m².

In a typical solar test, a specific amount of photocatalyst beads were loaded inside the Pyrex tube. The photo-reactor was connected to a reservoir with a capacity of 2 L. Antibiotic aqueous solution with 10 mg/L of cefixime concentration was prepared in distilled water. The pH of the solution was not adjusted (natural solution pH) and the temperature was not controlled, it varied from 20 to 45 °C during experiments. Experiments were performed in batch mode and the synthetic antibiotic solution was initially added to the reactor in the dark until complete filling before uncovering the CPC photo-reactor. Experiments began by uncovering the CPC solar pilot, the ratio of irradiated water (0.86 L) to total water (2 L) is 43% with a CPC of 0.112 m². The treated samples were at different times took from the tank and kept in the dark at room temperature to analyze the residual cefixime concentration.

The adsorption of cefixime was investigated by performing blank experiments in the CPC reactor but without light (photo-reactor was covered), and under the same experimental

conditions as a photodegradation experiment. Cefixime was always used at a concentration of 10 mg/L.



Figure 63. Photos of the CPC solar photo-reactor with its measurement equipment installed at the University of Isfahan, Iran.

1.2. The lab scale photo-reactor

Experiments using artificial light were performed in a lab-made photocatalytic reactor which was made in the Process and Material Sciences Laboratory (LSPM, UPR3407) at the University of Sorbonne Paris-Nord, France, as shown in figure 64. In the lab-scale photoreactor, there are two cylindrical quartz tubes with 34 and 50 mm (thickness = 2 mm) of outer diameter in the same vertical axis (height = 400 mm) around the irradiation light. As illustrated in the schematic, coated glass beads (diameter = 4 mm) were loaded between these quartz tubes. In the interval space (6 mm) only one row of beads can be located and there was not any passive location. A lamp was inserted in the inner quartz tube located at the center of the reactor as a source of radiation that the radiations emitted reached the catalyst surface to start photocatalysis reactions. The outer quartz tube was wrapped in aluminum foil to reflect radiation into the reactor. A peristaltic pump recirculated the contaminated water from a

glass bottle, acting like a recirculation tank, to the reactor with the desired flow rate. The reactor temperature was maintained constant using a water-cooling circuit to keep the temperature at 25 °C.

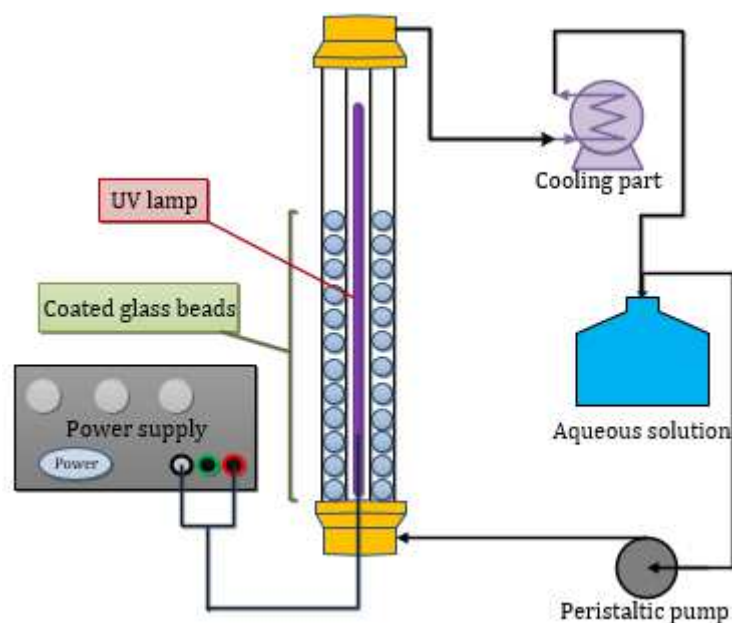


Figure 64. Schematic of the lab-scale photo-reactor using UV lamp.

1.2.1. Photocatalysis experiments by an artificial irradiation in the lab-scale photo-reactor

To examine the photocatalytic treatment efficiency of cefixime solution, a series of photocatalyst experiments on various TiO₂ samples were carried out under artificial light. A UV lamp emitting at $\lambda = 370$ nm was employed in all experiments (see figure 65).

In a typical run, the reactor was filled with 100 g of coated glass beads as the photocatalyst with 500 mL of contaminated solution with cefixime at the concentration of 10 mg/L. The cefixime powder was added to distilled water and stirred by a magnetic stirrer for complete dissolving. A peristaltic pump was used to make a continuous flow between the reactor tube and storage vessel. The solution was recycled for 240 minutes, samples were taken every 30 min period from the reservoir. Throughout the experimental procedure, the temperature was controlled (25 °C) with the use of a thermostatic bath. After one cycle, the photocatalyst washed with deionized water, then was put in an oven at 80 °C to dry. The recovered beads used for the next photocatalytic run.



Figure 65. Photos of the lab-scale photoreactor with an artificial light installed at LSPM, France.

1.3. Characterization methods

1.3.1. UV-Visible spectrophotometric technique

UV/Vis spectroscopy was used to determine the concentration of the pollutant in a solution. According to Beer-Lambert law (eq. 29-30), the solution receives radiation of intensity I_0 at a given wavelength, I is the transmitted intensity and L is the path length through the sample. A is the measured absorbance:

$$A = \log \frac{I_0}{I} = -\log (T) ; T: \text{transmittance} \quad 29$$

The absorbance A measured by a spectroscope follows Beer Lambert's law:

$$A = \epsilon c L \quad 30$$

where ϵ is the molar extinction coefficient in L/mol.cm, C is the concentration of the absorbing substance in mol/L, L is the width of the spectroscopy cell in cm, and A is absorbance without unit.

During photocatalysis experiments, the variation in the cefixime concentration was observed from its characteristic absorption band at 286 nm using a UV-Visible spectrophotometer (JASCO, Model; V-570, Japan) with a 1 cm optic pathway quartz cell.

1.3.1.1. Calibration curve

The cefixime was used as an antibiotic molecule model to study the degradation efficiency with our photocatalysts using lab-scale and solar pilot reactors. Cefixime trihydrate [(6R,7R,E)-7-(2-(2-aminothiazol-4-yl)-2-(carboxymethoxyimino) acetamido) -8-oxo-3-vinyl-5-thia-1-azabicyclo [4.2.0]oct-2-ene-2-carboxylic acid] with molecular weight of 507.50 g/mol was

obtained from Daana pharmaceutical company, Iran. Its structure formula and some chemical characteristics are presented in figure 66.

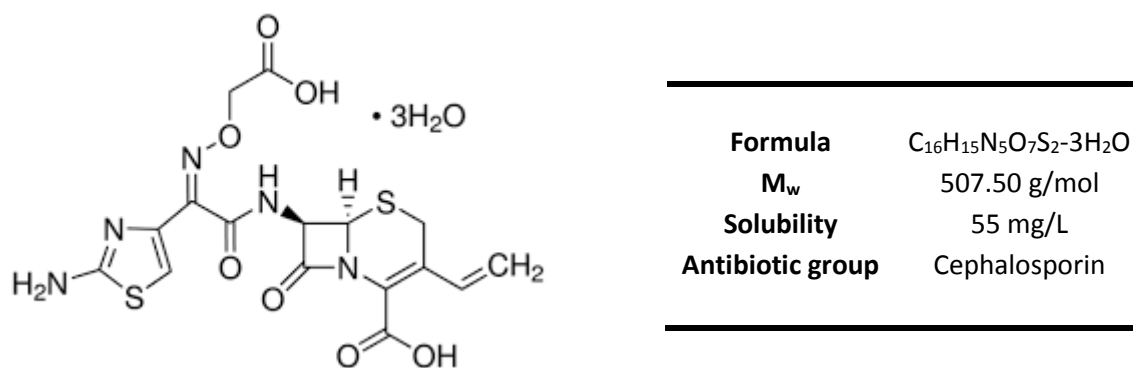
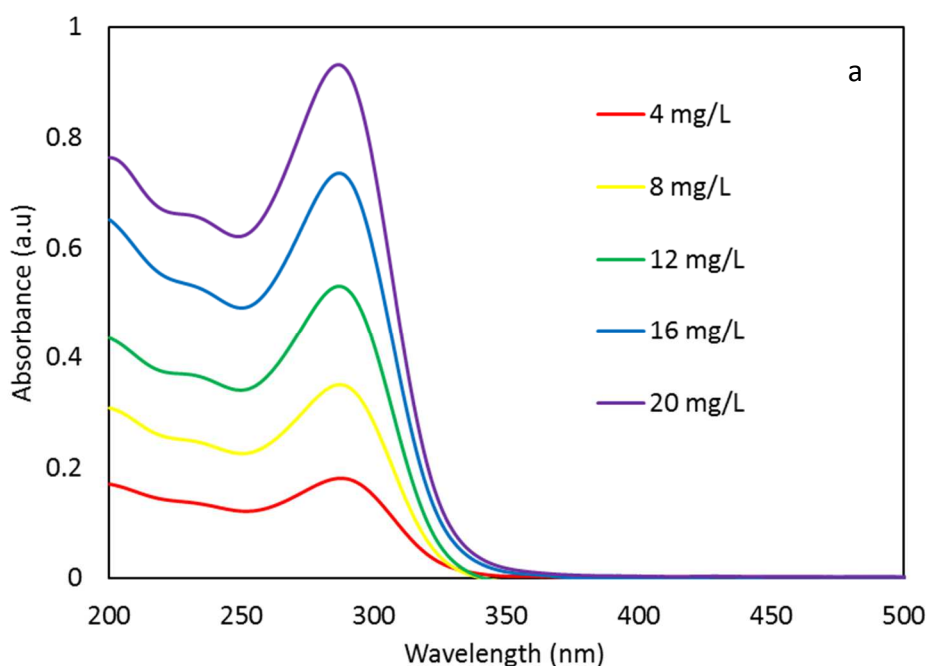


Figure 66. Cefixime trihydrate chemical structure and characteristics.

For obtaining calibration curve, firstly, five concentrations of cefixime were prepared with distilled water, the 4, 8, 12, 16, and 20 mg of cefixime powder were dissolved in distilled water by a magnetic stirrer under laboratory conditions. The preparation procedure was in the dark condition which means the volumetric flask was covered with an aluminum foil to avoid any light penetration inside the solutions. Then their absorbance was obtained by the UV-vis spectrophotometer. As seen in figure 67 (a) the maximum absorbance was observed at the wavelength of 286 nm for all cefixime concentrations. Figure 67 (b) presents a linear dependence between the concentration of cefixime and the absorption at 286 nm. The concentration of cefixime was determined with the calibration equation at this wavelength during the photocatalytic experimental process.



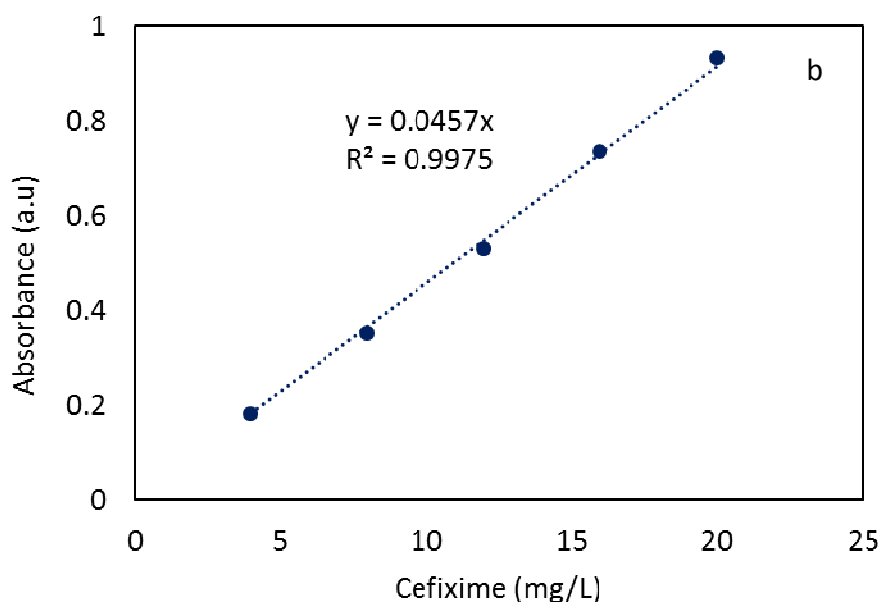


Figure 67. a) Absorbance graphs of different cefixime concentrations, and b) calibration graph and equation of cefixime.

1.3.2. Liquid chromatography–mass spectrometry

Liquid Chromatography-Mass Spectrometry (LC-MS) is an analytical chemistry technique that is a combination of Liquid Chromatography (or HPLC) and Mass Spectrometry (MS). The pump, sample injector, column, detectors, and recorded mass spectrometry are the main parts of an LC-MS device. As shown in figure 68, the LC physically separates the components of mixtures by passing through a chromatographic column. The unknown separated components are identified by mass spectrometry.

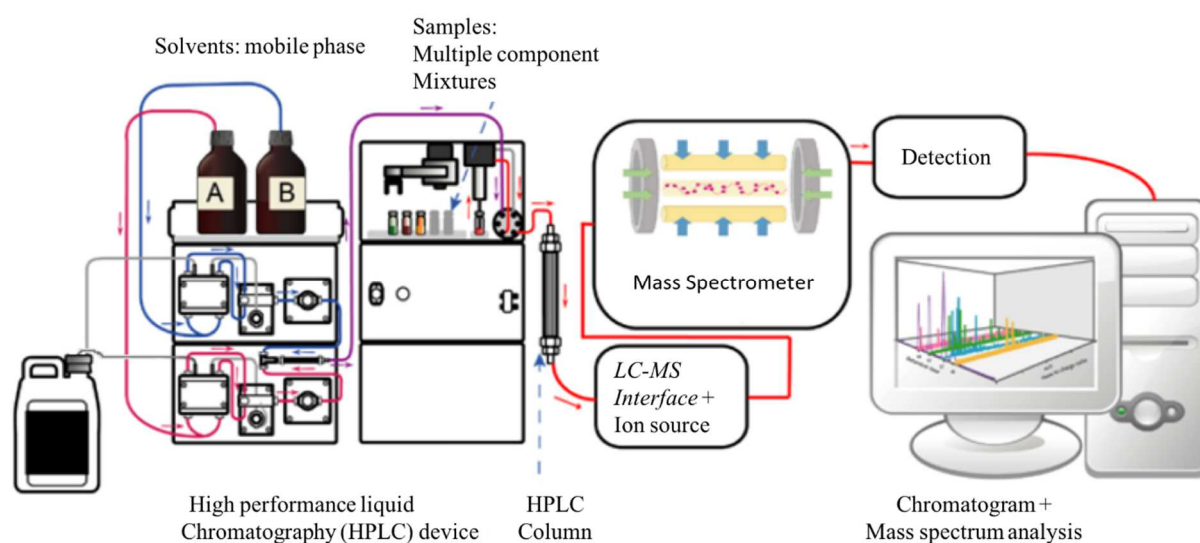


Figure 68. Schematic of a LC-MS analytical device.

Liquid Chromatography (LC) is a high-performance liquid chromatography in which the separation of components of the mixture can be carried out by using liquid mobile and solid stationary phases. In common applications, the mobile phase is a mixture of water and other polar solvents (e.g., methanol, isopropanol, and acetonitrile), and the stationary matrix is prepared by attaching long-chain alkyl groups. Typically, the sample is injected into the mobile phase stream delivered by a high-pressure pump. The mobile phase containing the analytes permeates through the stationary phase bed in a definite direction. The components of the mixture are separated depending on their chemical affinity with the mobile and stationary phases. The separation occurs after repeated sorption and desorption steps occurring when the liquid interacts with the stationary bed. The liquid solvent (mobile phase) is delivered under high pressure (up to 400 bar or 300.000 torr) into a packed column containing the stationary phase. Depending on the partitioning between the mobile and stationary phases, the components of the sample will flow out of the column at different times. While the mobile phase in an LC system is a pressurized liquid, the MS analyzers commonly operate under high vacuum. Thus, the column must withstand the high pressure of the liquid.

Mass Spectrometry is an analytical technique based on the measurement of the mass-to-charge ratio of ionic species related to the analyte under investigation. There are many different kinds of mass spectrometers, and all of them make use of electric or magnetic fields to manipulate the motion of ions produced from an analyte of interest and determine their m/z . The basic components of a mass spectrometer are the ion source, the mass analyzer, the detector, and the data and vacuum systems. After ionization, the ions are transferred into a mass analyzer where the separation of ions is done according to their mass-to-charge (m/z) ratio (223).

The intermediates of the cefixime during solar photocatalysis degradation were identified by a Water Alliance 2695 coupled to a Micromass Quattro micro API mass spectrometer (ESI) operating in positive mode. The analytical LC-MS system used for intermediates identification was equipped with a C18 column (2.1 mm x 150 mm) at 35 °C. The mobile phase was made up of 60/40% acetonitrile/ultra-pure water + 0.1% formic acid. The injection volume was 5 µL at a flow of 0.2 mL/min. Mass spectra were accomplished under the following conditions: Mode, ESI+; Capillary Volt, 4 kV; Gas nebulizer, N₂ (grade 5); Flow rate, 350 L/h; Source temperature, 120 °C; Desolvation temperature, 300 °C.

1.3.3. Solar energy measurements

In general, the weather of Isfahan is warm and dry, so most of the year has high solar radiation which makes it a favorable region for use of solar photochemistry techniques (139). As expected, the incident UV irradiance varied almost every minute and from day to day. The incident UV energy was monitored (in the UV-A and UV-B regions) by employing a Lutron UV LIGHT METER (UV-340A) in the spectral range from 290 nm to 390 nm. This device also was mounted and fixed on any surface of the platform at the same latitude as the sun. For each experiment, the intensity of UV radiation was measured by the UV light meter over the time

of the experiments which were carried out on different days. In addition, the solar total intensity was measured by a Solar Power Meter (Datalogging, TES 132) in the spectral range of 400-1000 nm (see figure 69).



Figure 69. UV light meter (left) and solar power meter (right) devices.

A typical UV radiation was measured during a day in summer at the University of Isfahan, Iran which is presented in figure 70. A variation of average solar UV energy from 20 to 50 W/m² was identified during a day between 10:00 and 13:00.

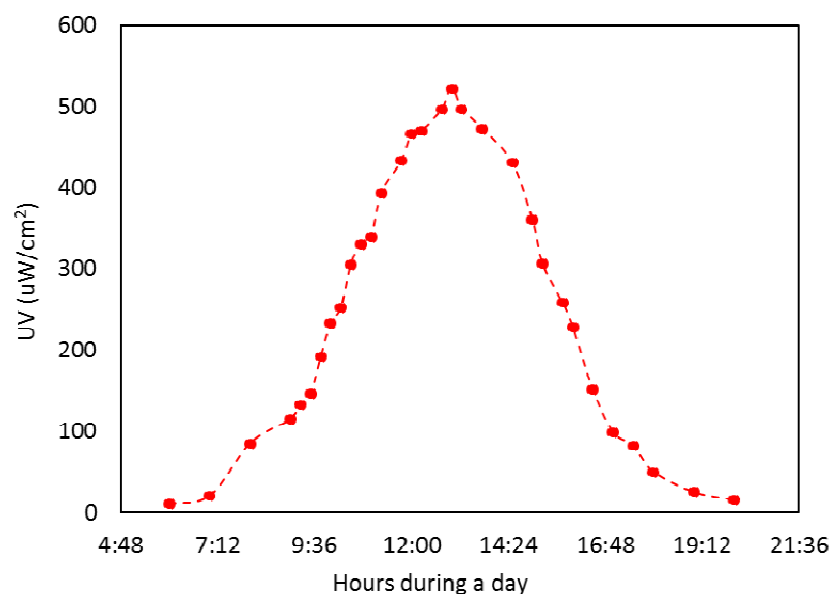


Figure 70. Typical UV radiation (wave length) during a day in summer at the University of Isfahan, Iran.

1.3.3.1. Cefixime degradation kinetic study

It should be noted, the efficiency of photodegradation of natural radiation depends on the UV radiation power. As the irradiation conditions changed during the experiments, concentration changes were reported and discussed against the accumulated energy, Q_{UV} (kJ/L), rather than the irradiation time. As mentioned earlier in part 2 (chapter 4), for comparison between experiments that were carried out on parallel or consecutive days in terms of treatment time, the accumulated energy per volume was needed to reach the degradation efficiency. This accumulated solar UV energy was calculated with the following equation 31;

$$Q_{UV,n} = Q_{UV,n-1} + \Delta t_n \overline{UV_{G,n}} \frac{S}{1000 \times V_t}; \quad \Delta t_n = t_n - t_{n-1} \quad 31$$

Where t_n is the experimental time for each sample (S), V_t is the total volume of wastewater at n water sample (L), A_r is illuminated collector surface area (m^2), $Q_{UV,n}$ is the accumulated energy (per unit of volume in kJ/L), and $UV_{G,n}$ is the average solar UV radiation during Δt_n (W/m^2) (144).

The accumulated UV energy was used as the independent variable instead of time in this kinetic analysis due to the variety of sun radiation. The average solar accumulated UV energy for four hours under cloudy conditions was calculated at $20 W/m^2$ and under sunny conditions was calculated at about $35 W/m^2$.

The kinetic of the first order reaction rate can be calculated with the equation 32 which used accumulated UV energy instead of reaction time (143):

$$\ln \frac{C}{C_0} = -kQ_{UV} \quad 32$$

C_0 is the initial concentration, C is the concentration at time of drawl, and k is the rate constant (L/kJ).

Chapter 2. Experimental results of cefixime degradation

2.1. Photocatalysis study of plasma deposited TiO_2 catalysts under natural and artificial light

As was seen previously the physical characteristics and stoichiometry of TiO_2 films elaborated depend on the plasma conditions. In this chapter, we present the role of oxygen plasma gas and doping with Mn on photocatalytic performances of TiO_2 layers deposited on the surface of 4 mm in diameter glass beads. Several lots of TiO_2 samples were prepared under various oxygen flow rates and deposition times. The oxygen flow was adjusted from 0 ml/min to 25 ml/min in 300 ml of argon as plasma gas. The deposition time was fixed at 30 min, 45 min, and 60 min. The Mn-doped TiO_2 photocatalysts also were deposited with manganese acetate concentration between 1 and 10% (mol%) in the precursor liquid in methanol. All TiO_2 and

$\text{Mn}_x\text{Ti}_{1-x}\text{O}_2$ photocatalysts were annealed at 450 °C for 240 minutes and then used in the photocatalytic experiments. To assess the photocatalytic activity of different TiO_2 films that were elaborated under the above-mentioned conditions with the fluidized bed plasma device, photocatalysis degradation of cefixime as a pharmaceutical molecule model was analyzed under natural and artificial irradiation. The aqueous solution of cefixime was used as contaminated water and treated in the presence of each catalyst with both kinds of photo-reactors: a lab-scale photo-reactor operating with a UV lamp, and a CPC photo-reactor using natural solar irradiation.

2.1.1. Photocatalytic activity of TiO_2 samples deposited with different oxygen flux in plasma gas under solar irradiation

Synthetic contaminated water (2 L) with 10 mg/L of cefixime concentration was filled in a tank that fed the CPC solar reactor by a peristaltic pump in a closed loop. The solar experiments were carried out in the CPC photo-reactor tilted at 33° for 240 minutes. Degradation of contaminant was studied at neutral pH and ambient pressure and temperature. In each test 100 g of catalyst beads lining the lower cut of the Pyrex tube were used. A previously calibrated UV-vis spectrophotometer (Jasco-Japan) was used to follow the degradation rate of cefixime during each run. The calibration was done with known solutions (concentrations varied from 4 to 20 mg/L) of pure cefixime in distilled water at the maximum absorbance of 286 nm. In UV-vis spectrophotometry of treated solution, the absorbance of cefixime solution is known to correlate directly to the cefixime concentration.

Firstly, the blank runs were performed in the dark with all TiO_2 samples inside the solar photo-reactor previously to solar experiments. In dark experiments, cefixime solution was in contact with the catalyst without any irradiation. The adsorption capacities of cefixime are shown in figure 71. It can be seen that cefixime adsorbed on the surface of the beads or experimental setup. The cefixime molecules adsorption were 3, 8, 5, and 7% for TiO_2 films deposited on glass beads with 0, 2, 10, and 25 ml/min oxygen concentration in plasma gas, respectively. In graphs several points did not follow the straight line, it might be due to the adsorption and desorption phenomena of molecules from the surface of the films or parts of the solar pilot. These results were obtained for 100 g of coated glass beads for 4 h considering that the decrease of cefixime concentration during photocatalytic activity is not any more affected by adsorption phenomena. The maximum adsorption capacity of TiO_2 -coated films indicated less than 10% of molecules could adsorb on the surface of photocatalysts or other parts. In addition, we suggested these molecules that were adsorbed on the film's surface could degrade during photocatalysis reactions under light illumination.

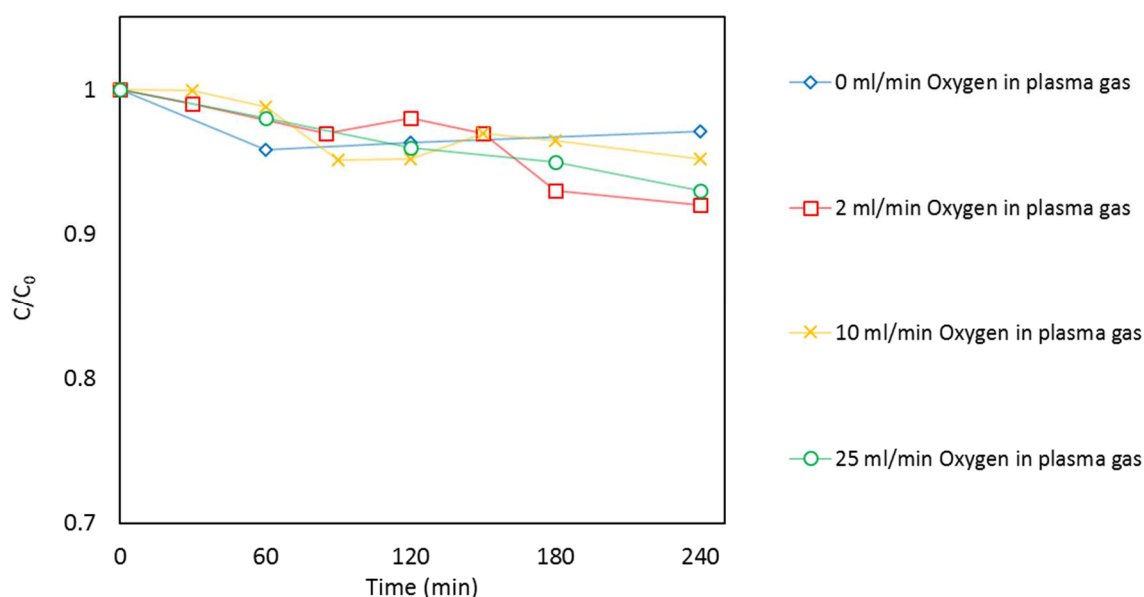


Figure 71. Blank experiment of cefixime with TiO_2 films deposited with different oxygen flux in plasma gas during 60 min.

Figure 72 illustrates the photolytic and photocatalytic degradation of cefixime solution as a function of solar irradiation time. In all of these experiments, the catalysts were in contact with the solution in dark for 4 hours which permitted us to isolate the effect of adsorption from the photocatalytic effect. First, the evolution of cefixime concentration by photolysis under solar irradiation in the absence of any catalyst was studied as a function of time. During the first 60 min, the decrease in cefixime concentration was low about 2 – 3%, then we observed a sharp decrease after one hour to reach 7.8%. This increase in photolysis activity might be due to an increase in solar radiation intensity after 10:00 a.m. just one hour after the beginning of the run. The sunlight intensity increases from 20 W/m^2 to 45 W/m^2 between 10 and 12 h. Then, after the exposition to the solar light for 240 min, the cefixime solution concentration decreased about 29%. These results underline the importance of sunlight intensity on photolytic effects under our conditions.

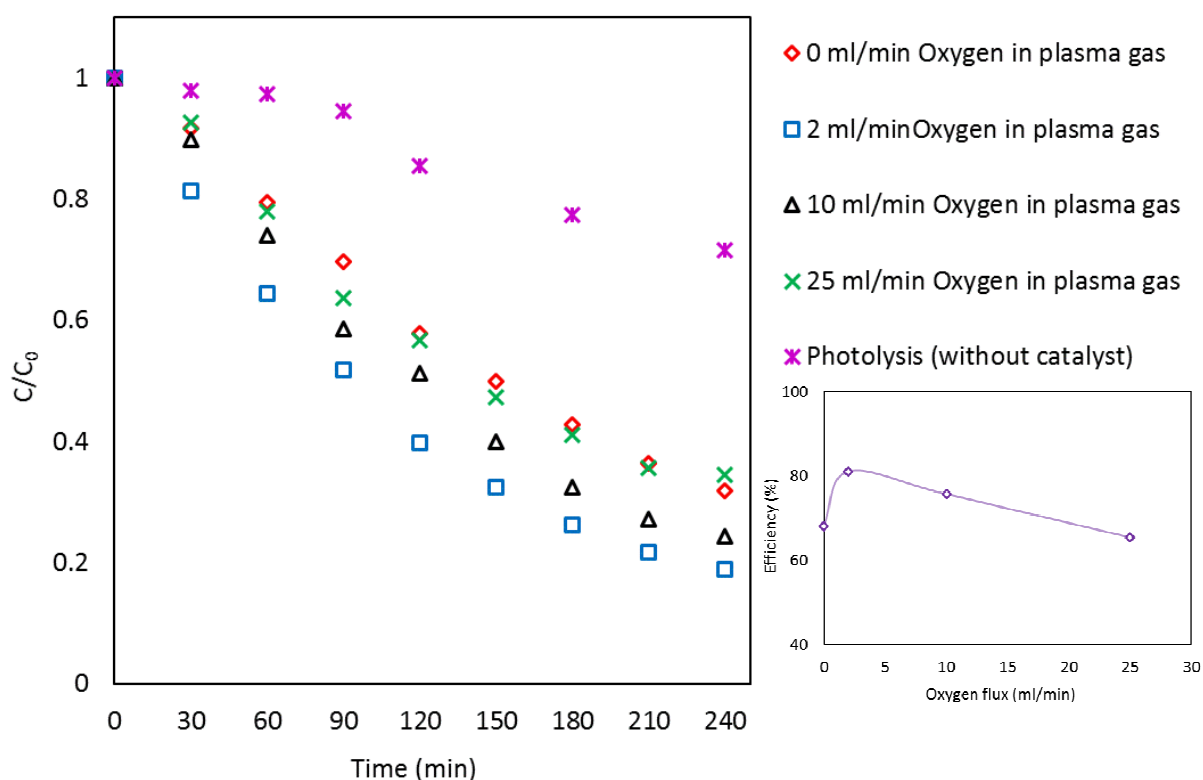


Figure 72. Cefixime degradation with TiO₂ films deposited with different oxygen flux in plasma gas during 60 min. The graph inset depicts the efficiency of TiO₂ catalysts elaborated in plasma vs rutile fraction.

All TiO₂ samples displayed a good photocatalytic performance. The antibiotic concentration was below 4 mg/L after 240 minutes of solar radiation for all samples. The cefixime reduction for TiO₂ films elaborated with 0, 2, 10, and 25 ml/min O₂ flux in plasma gas are shown in table 15:

Table 15. Cefixime degradation efficiency with TiO₂ samples deposited under various oxygen flux in plasma gas during 60 min.

Photocatalyst	Oxygen flux (ml/min)	Deposition time (min)	Efficinecy (%)
TiO ₂	0	60	68 ± 5
TiO ₂	2	60	81 ± 5
TiO ₂	10	60	75 ± 5
TiO ₂	25	60	65 ± 5

With an increase in the oxygen flow rate of plasma discharge, the photocatalytic activity first increased and then decreased. The best photocatalytic activity of TiO₂ films (efficiency 85%) has been obtained for the sample prepared with 2 ml/min of the reactive gas in the plasma

deposition parameter. The cefixime solution presented the lowest degradation efficiency in the presence of TiO₂ films deposited with 25 ml/min O₂ in plasma gas.

As previously presented and explained in chapter 3 of part 3, the XRD and TEM analysis techniques confirmed the existence of the multi-phase crystallite structure of TiO₂ layers coated on glass beads. Briefly, the sample deposited without any oxygen in plasma gas presented a single anatase phase while other TiO₂ samples prepared in O₂/Ar plasma discharge contained anatase and rutile complex structure. Based on published papers (21, 70) there was a relation between TiO₂ crystalline structure and photocatalytic activity. In addition, the commercial TiO₂ Degussa P25 demonstrated high photocatalytic activity due to its complex structure of anatase and rutile. It has been reported in (21, 70) that the complex crystalline composition (anatase/rutile) showed high photoactivity because of its lower e⁻/h⁺ recombination ratio (21, 70, 146).

The TiO₂ (2 ml/min O₂) that contained 16 mol% of the rutile phase exhibited better photocatalytic properties than other deposits due to a mixed crystal phase and lower rutile content with anatase/rutile ratio 19%. In fact, it has been reported (146) that the photochemical stability of the TiO₂ catalyst is related to the anatase/rutile ratio since rutile is the thermodynamically stable phase while anatase is the most photoactive phase. Mixture crystallite structure with a wider band energy gap than anatase (3.2 eV) indicated significant photo-activity (224). The smaller band gap of rutile (3.02 eV) catches the photons generating e⁻/h⁺ pairs. Electrons are transferred from the rutile conduction band to electron traps in the anatase phase. Recombination is thus inhibited allowing the hole to move to the surface of the particle and react. Since the P25 Degussa exhibited the highest overall activity for the degradation of the pollutants with the best ratio reported in the bibliography (80% anatase and 20% rutile) (21, 70, 225, 226).

The lowest photocatalytic activity for TiO₂ prepared with the high flux of oxygen in plasma deposition could be partially referred to as the increase in the weight of the rutile phase fraction. However, other phenomena may enhance the decrease in lower photocatalytic activity that was observed. According to published experimental results (227), as shown in figure 73, with high oxygen content in plasma discharge the oxygen species fluxes (O, O₂⁺) increase with the O₂ fraction while that of Ar⁺ decreases over the entire range investigated. And the ratio of oxygen flux (Γ_O) over the total positive flux (Γ₊) as a function of the O₂ fraction increased (see figure 73 (c)), this nearly linear increase is due to the fact that the O flux and the small O₂⁺ flux have similar evolutions with the O₂ fraction while at the same time the Ar⁺ flux decreased. As discussed in part 3 section 3.1.5, the increase of oxygen species could increase exothermic recombination reactions which leading to form the rutile phase. The high photoactivity of the films with a mixture of the anatase/rutile at low oxygen flow was in agreement with previously reported results (228).

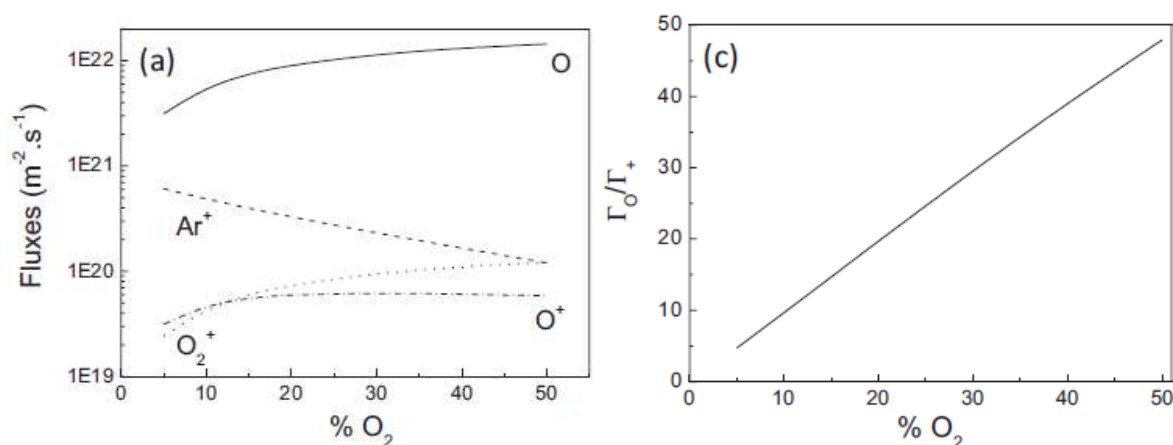


Figure 73. a) Evolution of the species fluxes as a function of O_2 fraction at 30 mTorr. c) Evolution of the ratio of the O flux and the total positive ion flux as a function of O_2 fraction at 30 mTorr. The power is 400 W (227).

Thus, the oxygen concentration in plasma gas played an important role in TiO_2 composition, crystallite phase, and photocatalytic activity. In our results, the anatase/rutile structure of plasma deposited films on glass beads was formed and a lower fraction of rutile in the compound showed better photocatalysis performance in comparison with others. Additionally, the single anatase phase of TiO_2 was deposited in the absence of oxygen gas in the plasma discharge but the photocatalytic activity lowered with this sample. On the basis of these results we believe that small amounts of rutile phase (here 16 mol%) together with anatase (84 mol%) gives the optimal photocatalytic activity of TiO_2 in our experimental conditions.

The photocatalyst samples were activated under solar irradiation to photocatalytic degradation of cefixime, under solar irradiation from 10:00 a.m to 2:00 p.m for each experiment. Therefore, to compare the influence of solar irradiation during photocatalysis experiments over several days, the normalized solar intensity was needed for yield comparison of experiments. The accumulated UV energy during interval time was used instead of time. This parameter was calculated by the equation ($Q_{\text{UV},n} = Q_{\text{UV},n-1} + \Delta t_n \overline{UV_{G,n}} \frac{s}{1000 \times V_t}$). The kinetic plots for cefixime degradation are illustrated in figure 74 by plotting the $-\ln(C/C_0)$ versus accumulated UV energy (kJ/L). As seen in the figure, the average incident UV radiation on the concentrator surface was 30 kJ/L for 240 min in these experiments.

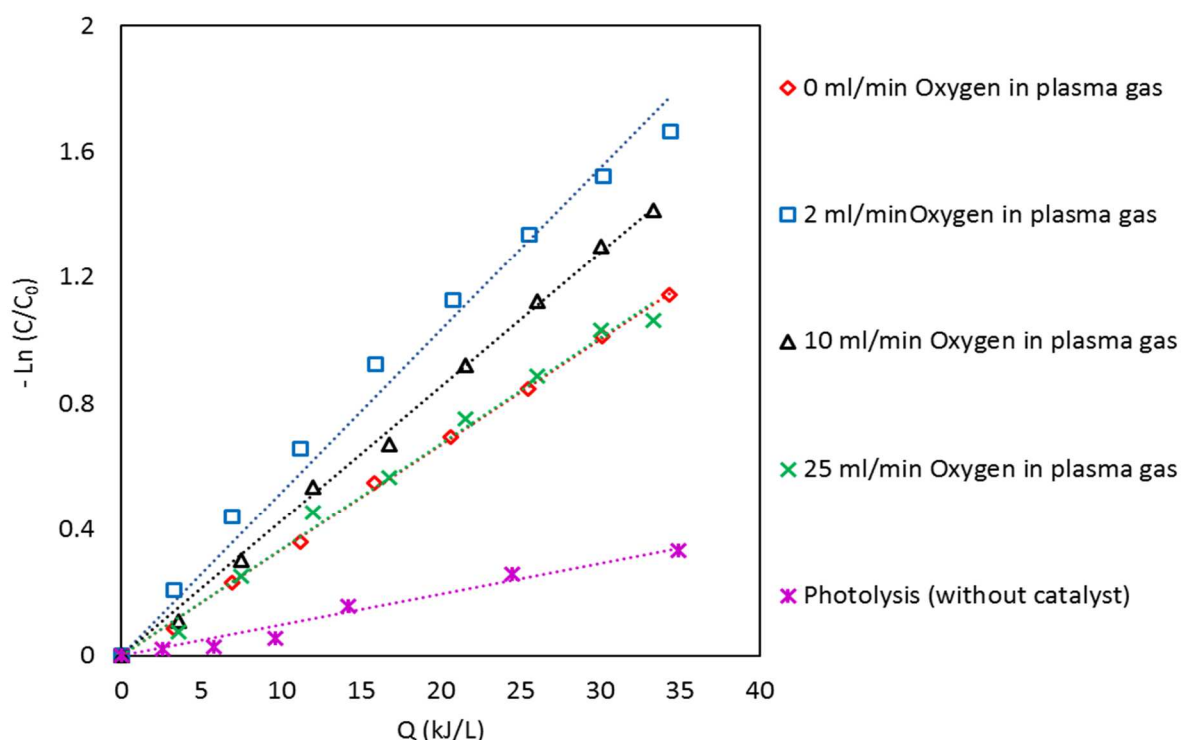


Figure 74. Kinetic plots of cefixime degradation with TiO₂ films deposited with different oxygen flux in plasma gas during 60 min.

The k values were measured from slopes of the regression curves representing $-\ln(C/C_0)$ Vs. Q (kJ/L). The first-order kinetic model was able to fit the degradation results of cefixime. The values of k and correlation coefficient (R^2) are indicated in table 16. After 240 min solar irradiation, the kinetic efficiency of cefixime in photolysis was about 29% and the kinetic constant was 9.7×10^{-3} L/kJ. The kinetic constant for photocatalysis only decreased when the O₂ flux increased more than 2 ml/L in the preparation method. The photocatalytic activity rate for TiO₂ deposited by using 0 and 25 ml/min of oxygen flow, were almost similar and their constants were 33.4×10^{-3} and 33.6×10^{-3} L/kJ, respectively. The TiO₂ photocatalyst deposited with 2 ml/min O₂ had a higher rate constant value than the other TiO₂ samples; it was 1.54, 1.21, and 1.53 times higher than the rate constants belonging to TiO₂ layers obtained with 0, 10, and 25 ml/min O₂ in plasma gas, respectively.

Table 16. The rate constant of cefixime degradation with TiO₂ films deposited with different O₂ in plasma gas during 60 min under solar irradiation.

Photocatalyst	Oxygen flux (ml/min)	Deposition time (min)	$k \times 10^{-3}$ (L/kJ)	R^2
TiO ₂	0	60	33.4	0.99
TiO ₂	2	60	51.6	0.98
TiO ₂	10	60	42.6	0.99
TiO ₂	25	60	33.6	0.99
Without catalyst	-	-	9.7	0.97

Shaniba et al. studied cefixime degradation by several TiO_2 nanoparticles under natural solar irradiation, after 60 min (2.62 kWh = 1368 kJ) they obtained about 60% degradation efficiency for antibiotic at 25 mg/L concentration with 0.05 g of nano-powder TiO_2 photocatalyst in 100 ml solution (229). In comparison with the present work, the initial cefixime content was destructed about 60% after 30 kJ of accumulated UV energy per liter of solution. In the paper of Shaniba et al. photocatalyst was used in slurry batch mode that needed filtration technique so fixed films on substrates in continuous flow have advantages like the elimination of separation step.

2.1.2. Photocatalytic activity of TiO_2 samples deposited with different oxygen flux in plasma gas under artificial irradiation

Photocatalytic activity of TiO_2 samples on cefixime destruction was examined in the lab-scale photo-reactor using a UV lamp emitting at 370 nm (power = 8 W). As seen in figure 75, the coated glass beads with TiO_2 films were placed between two quartz tubes, and the UV lamp was located in the center of the inner tube. The glass beads were coated in the plasma reactor using 0, 2 ml/min, 10 ml/min, and 25 ml/min oxygen flow rates in the fluidized bed plasma device.

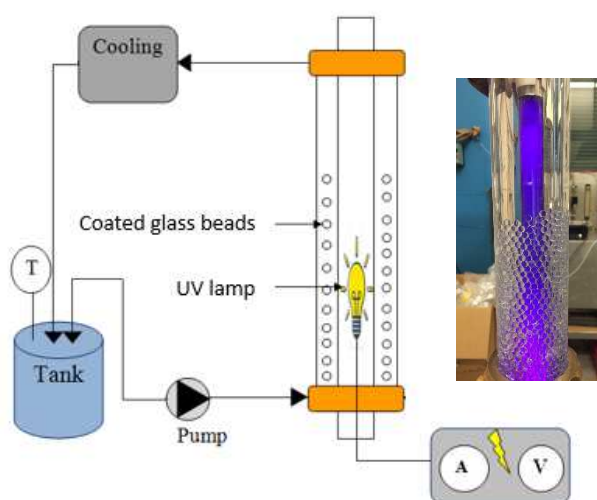


Figure 75. Schematic of the lab-scale photo-reactor.

The photocatalytic degradation of cefixime in water was performed by circulating each solution through the lab-scale photoreactor under UV irradiation. In these experiments, 500 ml of contaminated solution was treated using 100 g coated glass beads at an initial cefixime concentration of close to 10 mg/L and neutral pH for 4 hours.

The photocatalytic activity of various films is illustrated in figure 76. The photolysis degradation of cefixime under UV was observed at about 20% after 240 min. Under UV light, the photocatalytic activity levels of TiO_2 photocatalysts were in the order of TiO_2 (25 ml/min O_2) > TiO_2 (10 ml/min O_2) > TiO_2 (2 ml/min O_2) > TiO_2 (0 ml/min O_2) with degradation efficiency

of 97, 93, 91, and 55% \pm 5%, respectively. The degradation efficiencies were similar for TiO₂ samples deposited with 2, 10, and 25 ml/min oxygen in plasma gas while the lowest efficiency was obtained for the TiO₂ sample deposited in the absence of oxygen in the plasma discharge.

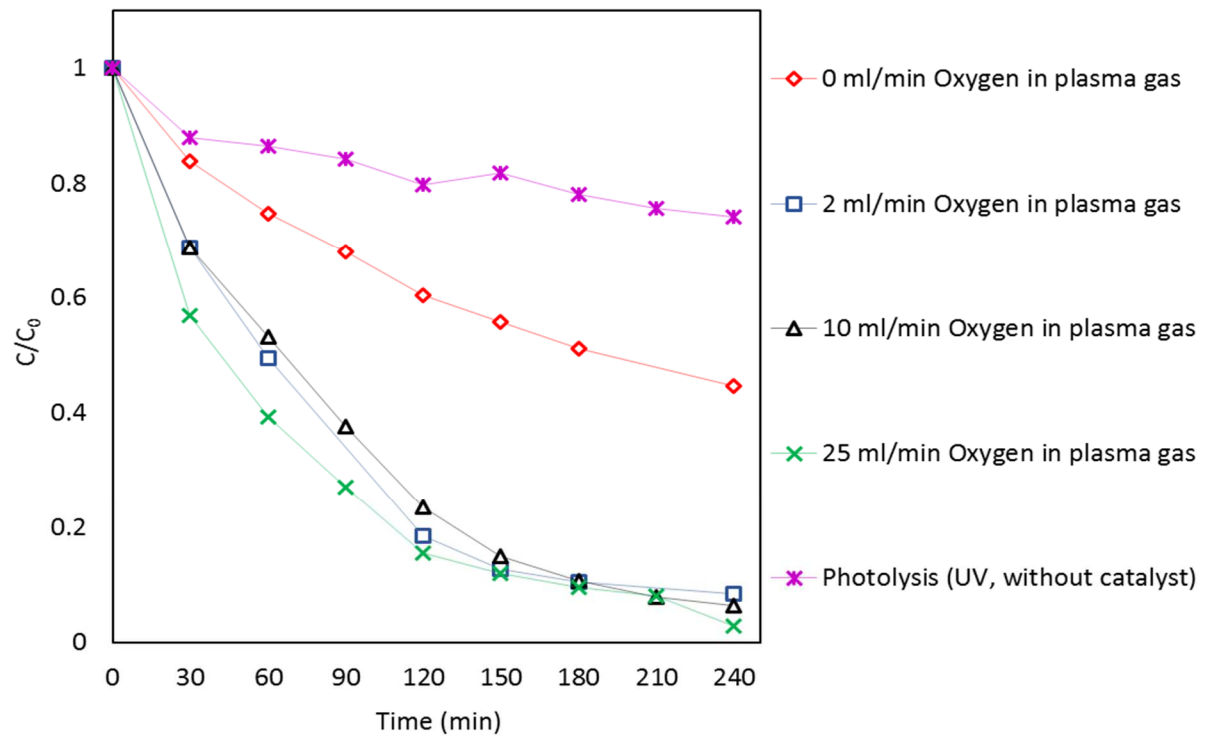


Figure 76. Cefixime degradation with TiO₂ films deposited with different oxygen flux in plasma gas (deposition time 60 min) under UV 370 nm irradiation.

To compare these results with other studies, as reported by Sahraeian et al. (230) who indicated degradation efficiency higher than 90% for a 20 mg/L cefixime solution after 90 min UV irradiation using 1 mg/L of commercial TiO₂ (EMSURE) suspension and a UV intensity (125 W) used in a lab-scale reactor. The adsorption of cefixime and photolysis of cefixime was measured at around 25 and 10% for 210 min. They employed a suspension equipped with a powerful lamp with a UV intensity 15.6 times higher than our radiation source in a lab-scale photo-reactor.

The first-order kinetics of cefixime degradation had been computed by linear regression between $-\ln(C/C_0)$ and time (min). The accumulated UV energy of the UV lamp with a power of 8 watts could be calculated from the equation 33 as follows:

$$I_0 = 3.01 \times 10^{-5} \times \lambda_{\max} \times P_{\text{out}} \quad 33$$

The I_0 in Einstein.h⁻¹, λ_{\max} is the maximum wavelength of emitted from the UV lamp in nm, and P_{out} is the output power of the UV lamp in W. One Einstein is 6,022x10²³ photons and the energy of each photon is equal to 5.37x10⁻¹⁹ J, consequently, one Einstein is equal to 35.5x10⁴ J. With $P_{\text{out}} = 1.3$ W and $\lambda_{\max} = 370$ nm, the UV lamp delivers 0,014 Einstein/h which means

that at 370 nm it delivers 5.1 kJ per hour. For the 0,5 L solution, it corresponded to 10.2 kJ/hL and after 4 h treatment, the accumulated energy was calculated as 40,8 kJ/L. The plot of C/C_0 versus the accumulated UV energy for different TiO_2 films deposited with an oxygen flow rate between 0 and 25 ml/min for 60 min in plasma gas is presented in figure 77.

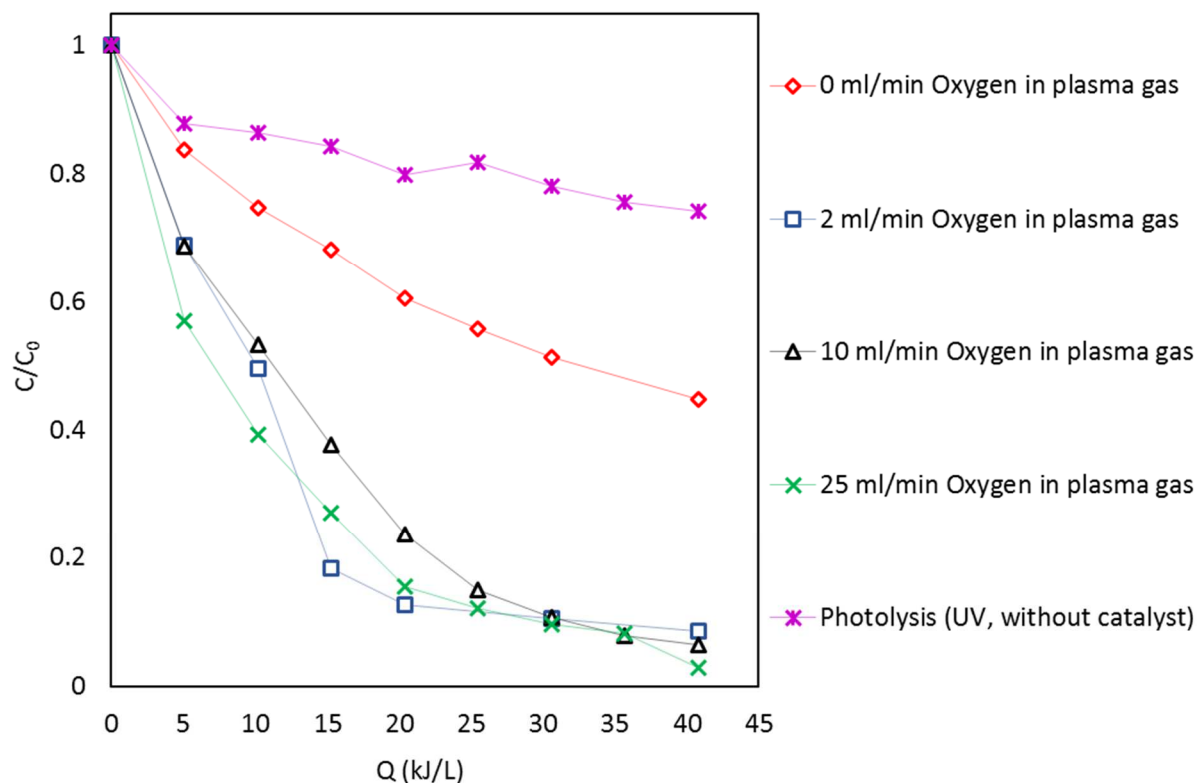


Figure 77. Cefixime degradation with TiO_2 films deposited with different oxygen flux in plasma gas (deposition time 60 min) versus accumulated energy of UV lamp irradiation.

The rate constants for each type of TiO_2 catalysts are reported in table 17. The highest rate constant was calculated for the sample obtained under the highest oxygen flow rate (25 ml/min) in the deposition method. The TiO_2 photocatalyst with the pure anatase phase exhibited lower degradation efficiency and k value. A similar rate constant was achieved for the samples prepared with 2 and 10 ml/min oxygen flow rate in plasma gas and it was calculated at 73.1 and 70.2 (L/kJ), respectively.

Table 17. The rate constant of cefixime degradation with TiO₂ films deposited with different O₂ in plasma gas during 60 min under artificial irradiation.

Photocatalyst	Oxygen flux (ml/min)	Deposition time (min)	$k \times 10^{-3}$ (min ⁻¹)	$k \times 10^{-3}$ (L/kJ)
TiO ₂	0	60	3.7	21.9
TiO ₂	2	60	11.9	73.1
TiO ₂	10	60	11.9	70.2
TiO ₂	25	60	13.8	81.8
Without catalyst	-	-	1	6.1

Comparing the degradation percentage of cefixime plotted in figure 72 obtained under solar irradiation and figure 77 obtained under UV irradiation, it can be noted that the degradation efficiencies of cefixime in the CPC reactor were higher than the lab-scale photo-reactor because the total volume of solution. In the CPC photo-reactor, 2 liters of cefixime contaminated solution was treated with 100 g of coated glass beads, while in the lab-scale photo-reactor 0.5 liters of cefixime contaminated solution was treated with 100 g of coated glass beads. Actually, photocatalysis experiments were done with the same weight of coated glass beads in both photo-reactors but the solution volumes were different.

At the lab-scale reactor, the power of the lamp was 8 W with 40.8 kJ/L of accumulated energy for the duration of 4 h, while at the solar photoreactor, the average UV radiation was 30 kJ/L for 4 h.

Even if degradation profiles were similar in photolysis under artificial and solar light, photolysis of cefixime under sunlight showed that there was a better conversion due to more distribution of diffuse radiation on the solar collector and its ability to photolyze more molecules and by-products (231). In direct photolysis of cefixime, the mineralization was very low due to the absence of reactive species of photocatalysis (231, 232).

In applying TiO₂ deposited in 0 ml/min O₂ flux, when the lab-scale reactor was used, about 49% ± 5% removal was obtained for 30 kJ/L of accumulated UV energy. Under solar light, about 64% ± 5% of degradation was achieved in the same accumulated UV energy. The difference could be related to the kind of radiation. Natural sunlight contains energy from UV to IR regions which can make an impression on pollutants or intermediates (231). As previously noted (147), solar radiation contains two kinds of radiation namely direct and diffuse. Direct radiation reaches the surface of the photocatalyst while diffuse radiation reaches all sides of the photocatalyst. In solar radiation, the highest incident diffuse radiation could increase photon absorption therefore could enhance the generation of e⁻/h⁺ pairs, consequently increasing the photodegradation. Besides, one of the main benefits of a solar reactor was the light reflection inside the Pyrex tube which had quantum and optical efficiencies (233). On other hand, the aluminum collector could reflect around 89% of incident radiation on the surface (234). In the lab scale reactor only one side of the beads was exposed

to the light direction while in the CPC photo-reactor both sides are exposed to solar irradiation. However, one side was exposed to direct and the other side was exposed to diffuse light.

2.1.3. Reproducibility of TiO₂ deposited films on glass beads with fluidized bed plasma device

Reproducibility is an important criterion to assess the fluidized bed plasma reactor performance. In the present work, the second series of TiO₂ films coated on glass beads were deposited under different plasma conditions. Several conditions like TTIP concentration in the precursor solution, deposition time, and oxygen flux changed in the fluidized bed plasma technique. The precursor solution was prepared with the concentration of $C_{Ti} = 1.002$ M of TTIP in series II (deposition time = 45 min) while in series I $C_{Ti} = 1.67$ M (deposition time = 60 min) was used in the precursor solution. Plasma gas with the different fluxes of oxygen was adjusted between 0 and 10 ml/min in series II. These photocatalysts with 0, 1, 2, 3, 4, and 10 ml/min of O₂ in plasma discharge were prepared. The second series of TiO₂ films on glass beads were annealed at 450 °C for 240 min.

The photocatalysis degradation of cefixime was studied with series II of TiO₂ depositions under natural solar light. Each deposition contained 100 g of coated glass beads which were loaded inside the CPC photo-reactor. Solar photocatalysis experiments were carried out with 10 mg/L of cefixime concentration in 2 liters of distilled water. These solar tests were done in the middle of the day for the duration of 4 hours.

Cefixime adsorption studies were performed for all TiO₂ films deposited on glass beads. As figure 78 displays, during the dark experiments, up to 6% of cefixime was adsorbed on the surface of TiO₂ films deposited with different oxygen flow rates in plasma gas.

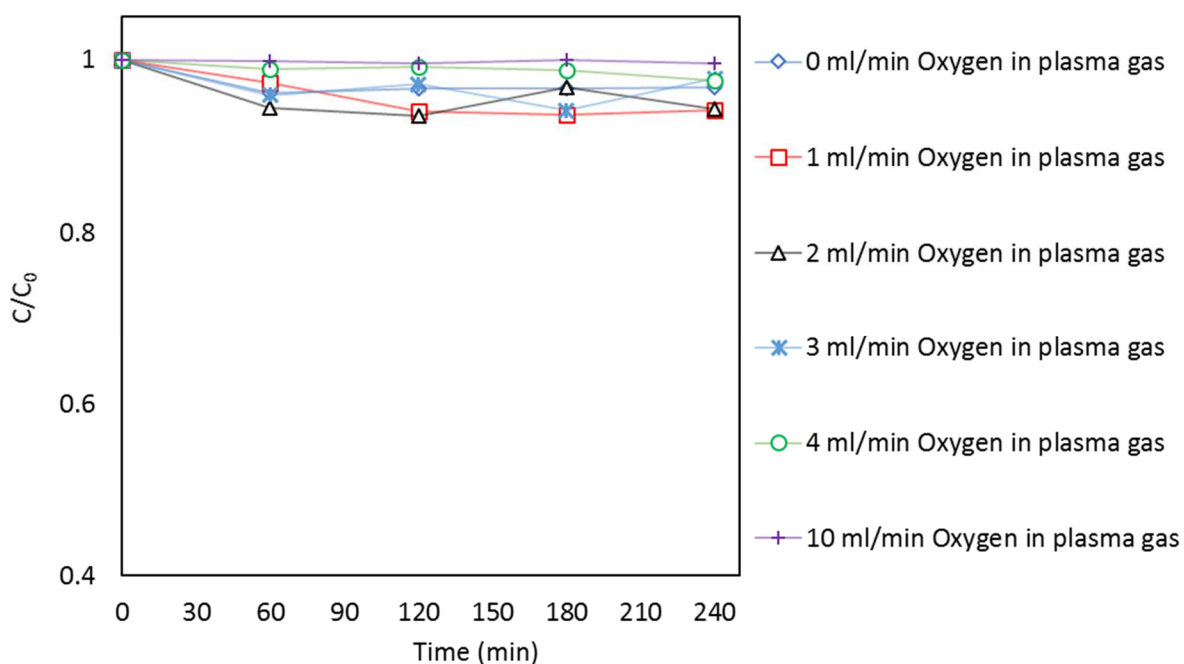


Figure 78. Cefixime adsorption on TiO₂ films coated on glass beads with different oxygen flow rates (from 0 to 10 ml/min) during 45 min.

After dark experiments, solar photocatalyst experiments were done in the CPC photo-reactor under natural solar irradiation. The results of cefixime degradation as a function of accumulated UV energy are shown in figure 79. At a time of 240 min, for all samples, the increase in photocatalytic activities are presented in the following order TiO₂ (4 ml/min O₂) < TiO₂ (0 ml/min O₂) < TiO₂ (10 ml/min O₂) < TiO₂ (1 ml/min O₂) < TiO₂ (3 ml/min O₂) < TiO₂ (2 ml/min O₂) . The key parameter namely accumulated energy must consider for better comparison because solar radiation differs in experiments, it is obvious after 25 kJ/L of accumulated UV energy, TiO₂ films deposited with 0 ml/min of O₂ in plasma gas could decompose 50% of initial cefixime concentration by solar photocatalysis process. This result was similar to the sample deposited under 1 ml/min of oxygen in the plasma discharge.

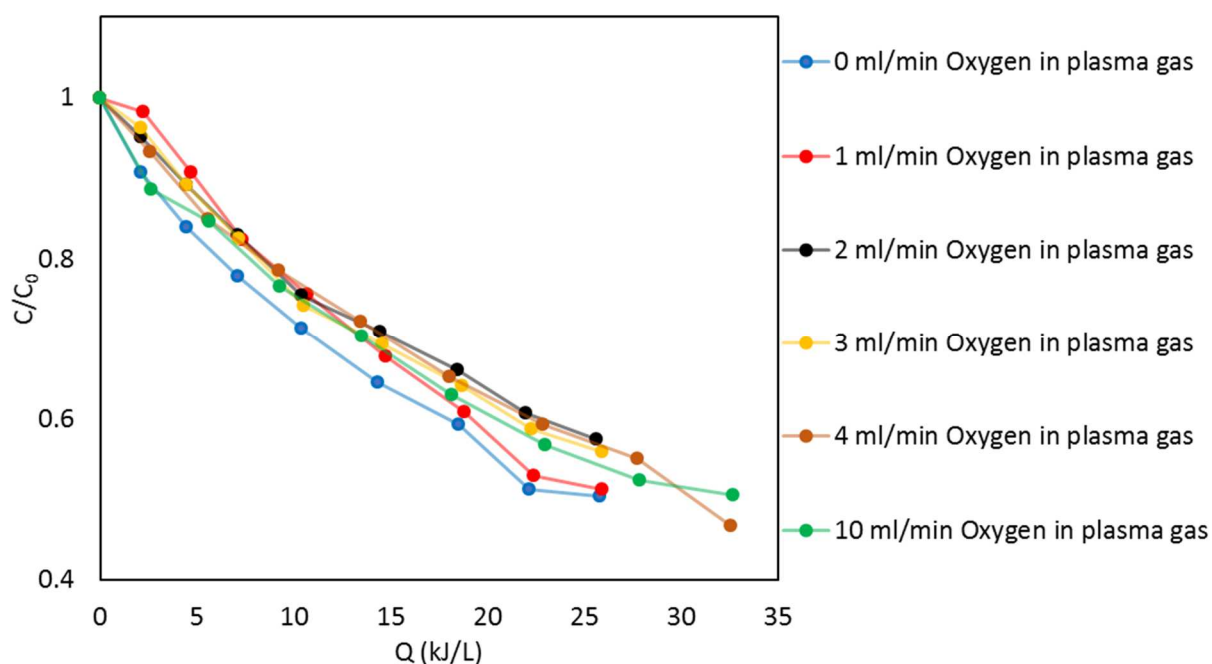


Figure 79. Cefixime degradation with TiO_2 films deposited with different oxygen flux in plasma gas during 45 min.

The $-\ln(C/C_0)$ vs Q (kJ/L) was prepared to obtain the corresponding rate constant from the slope of the fitting curve. The plasma deposition conditions and rate constants of the TiO_2 films are present in table 18. Considering the first run, the rate constant calculated 29×10^{-3} , 26.6×10^{-3} , 22.8×10^{-3} , 23.8×10^{-3} , 23×10^{-3} , and 23.4×10^{-3} L/kJ for TiO_2 films in the presence of 0, 1, 2, 3, 4, and 10 ml/min oxygen in plasma gas, respectively.

Table 18. The rate constant of cefixime degradation efficiency after 240 min with TiO_2 films deposited with different oxygen flux in plasma gas during 45 min.

Catalyst	O_2 flux (ml/min)	Deposition time (min)	$k \times 10^{-3}$ (L/kJ)	R^2	Efficiency (%)
TiO_2	0	45	29	0.97	49.58 ± 5
TiO_2	1	45	26.6	0.99	48.84 ± 5
TiO_2	2	45	22.8	0.99	42.58 ± 5
TiO_2	3	45	23.8	0.98	44.05 ± 5
TiO_2	4	45	23	0.99	53.26 ± 5
TiO_2	10	45	23.4	0.96	49.45 ± 5
Photolysis	-	-	-	-	29 ± 5

Photocatalytic activity of the first and second series of TiO₂ films deposited with different plasma conditions like concentration of TTIP in the precursor solution, deposition time, and oxygen flow rate in plasma gas was compared. In two series of TiO₂ deposited layers, we used the same oxygen flux (0, 2, and 10 ml/min) during the elaboration in the plasma process. However, in series I the ratio TTIP/ Isopropanol was fixed at 50% and the deposition time was fixed at 60 min while in series II the ration TTIP/isopropanol and deposition time were fixed respectively at 30% and 45 min. These two parameters lead to a lower amount of TiO₂ in the series II photocatalysts. For comparison, the reaction rate constants of 0, 2, and 10 ml/min oxygen flux in the two series are depicted in figure 80. As a result, the degradation rate of the first series (series I) of TiO₂ with 0, 2, and 10 ml/min were 1.15, 2.56, and 1.82 times higher than the second series (series II). This finding pointed out the synergetic effect of the TTIP's concentration in precursor solution and the deposition time. We believe that the lower TTIP concentration might influence the nanoparticle's total mass deposited that in turn influences the photodegradation efficiency of TiO₂ catalysts. In addition, shorter deposition time also decrease the amount of deposited TiO₂ particles on the surface of the glass beads.

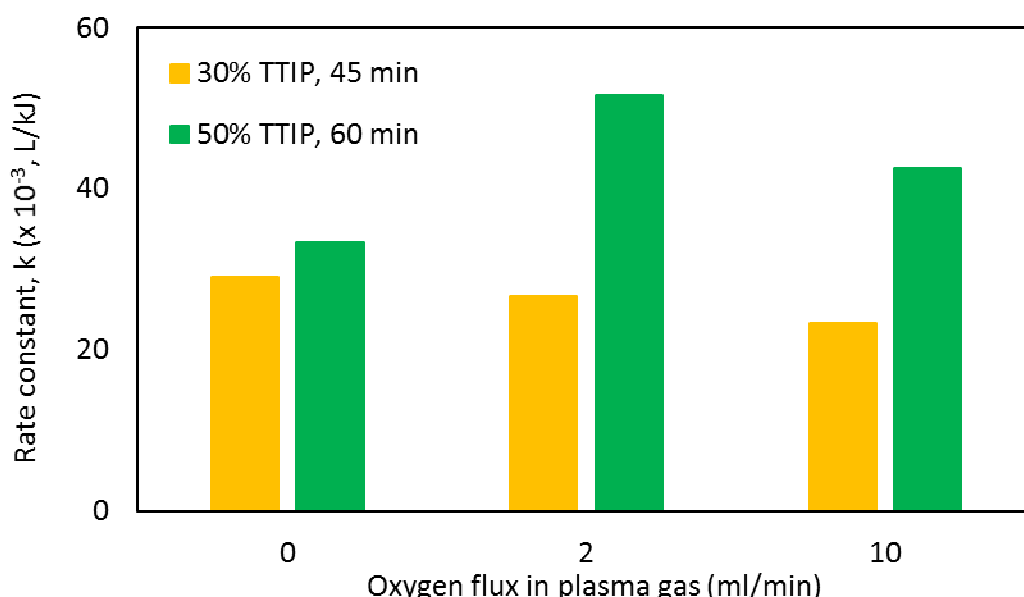


Figure 80. Rate constant comparison of cefixime degradation with TiO₂ films deposited under 30 and 50% of TTIP precursor concentration during 45 and 60 min with different oxygen flux in plasma gas.

2.1.4. Photocatalytic activity, under solar irradiation, of TiO₂ samples deposited with two deposition times in plasma gas influencing the quantity of coating on beads surface

The photocatalytic degradation of aqueous cefixime was also examined by different TiO₂ films prepared with two deposition times in the plasma method. The 30 min of deposition duration was also used to implement TiO₂ films on glass beads with 10 ml/min of oxygen flow rate in plasma gas, the TTIP concentration was fixed at C_{Ti} = 1.67 mol/L in isopropanol (50:50 volume

ratio). These experiments were performed with 100 g of coated glass beads in the CPC photo-reactor under sunlight.

Figure 81 illustrates the degradation efficiency of cefixime with these photocatalysts under 240 min solar irradiation ($Q \approx 30$ kJ/L). A deposition time of 60 min with 10 ml/min O_2 seems better where 75% of cefixime degradation efficiency was obtained. And near 62% of cefixime was lost in 240 min with 30 min deposition time and 10 ml/min O_2 in plasma gas.

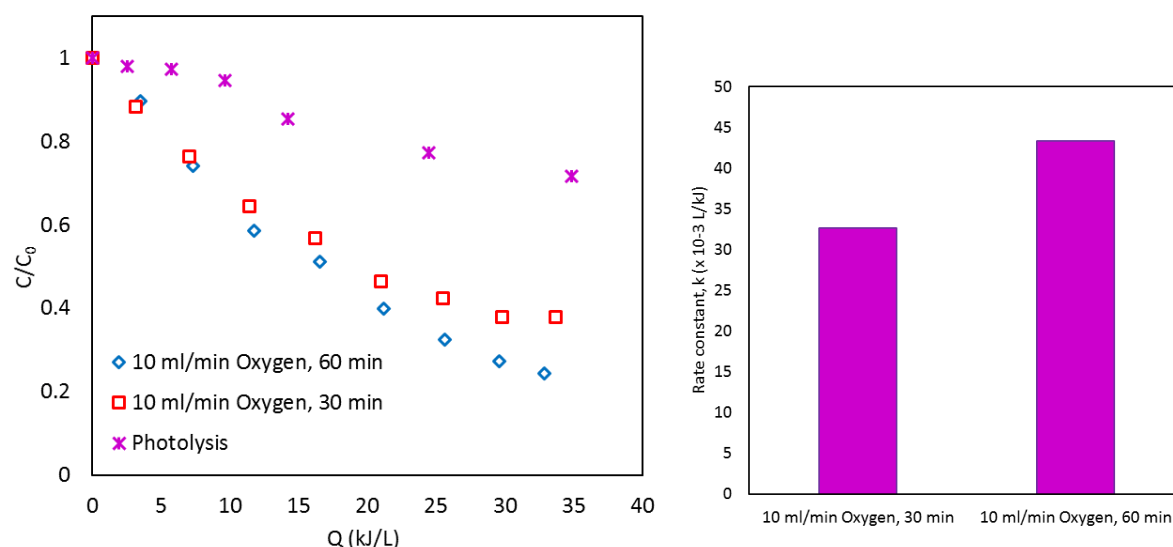


Figure 81. Photo-degradation (left) and rate constant (right) of cefixime with TiO_2 films deposited with 10 ml/min oxygen flux in plasma gas during 30 and 60 min.

The rate constant for two samples was calculated by using the slope of the curves of $-\ln(C/C_0)$ vs Q (kJ/L) and depicted in figure 81 (right). The rate constant of first-order reaction kinetics was 32.6×10^{-3} , and $43.3 \times 10^{-3} \text{ L/kJ}$ for 10 ml/min of O_2 during 30 and 60 min of deposition time, respectively. The higher k value belongs to the better photocatalyst. Thus, high losses of cefixime in the solar experiments were obtained for TiO_2 deposited with 10 ml/min O_2 for 60 min. It was observed in the figure that the apparent rate constant k increased with increasing deposition time to 60 min in 10 ml/min O_2 flux. In conclusion, the time of deposition played an important role in the degradation efficiency which showed the highest deposition time had the best performance.

In conclusion, the TiO_2 layers were deposited under different plasma conditions. The oxygen flux changed from 0 to 25 ml/min in plasma gas for the duration of 30, 45, and 60 min with two TTIP concentrations in the precursor solution. At first, four kinds of TiO_2 layers were coated on glass beads under 0, 2, 10, and 25 ml/min of oxygen flow rates with the titanium concentration of 1.67 M in the precursor for 60 min in the plasma discharge. In the second section, the TiO_2 samples were prepared with 0, 1, 2, 3, 4, and 10 ml/min of O_2 flux in plasma

gas for 45 min, in these deposits the TTIP concentration was $C_{Ti} = 1.002$ M in isopropanol. The last sample was deposited with 1.67 M of Ti in precursor under 10 ml/min O_2 for 30 min. The results indicated, there were two principal parameters to explain the obtained results. First, the anatase/rutile ratio depended on the concentration of oxygen in plasma gas during the elaboration step. Second, the thickness of the layers could be controlled by two factors: deposition time and TTIP/isopropanol ratio. There was certainly an optimum layer below which the thickness was too low to cover all of the substrate surfaces, and over which the thickness was too high leading to charge recombination.

2.1.5. Effect of net weight of coated glass beads

We supposed the weight of coated glass beads had an effect in the pollutant decomposition. The photocatalytic degradation of cefixime was performed with different weight of TiO_2 coated glass beads such as 100, 200, 300, 400, and 500 g. These photocatalysis experiments carried out with TiO_2 sample prepared in plasma device under 2 ml/min of oxygen flow rate. Typically, similar cefixime solutions was used at a specific time of the day. When 100 g of coated beads were used, they regenerated with hot water and used again in the next experiment. As seen from figure 82, the degradation efficiency of cefixime increased with using more amount of TiO_2 coated glass beads. The cefixime degradation efficiency increased from 43 to 74% after 240 min solar irradiation when substrates net weight increased from 100 to 500 g, respectively.

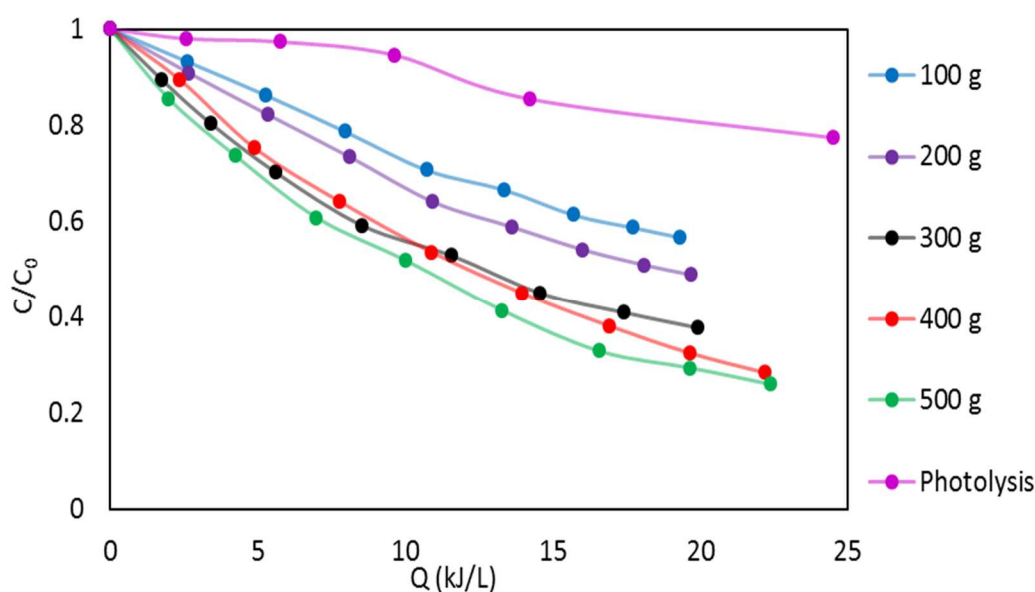


Figure 82. Cefixime degradation with TiO_2 photocatalyst (2 ml/min O_2 , 45 min) with different net weight of coated glass beads under solar light.

For each solar experiment, the rate constant was computed. The k values were 30.3, 37.9, 52.7, 57.1, and 63.8 L/kJ for 100, 200, 300, 400, and 500 g of TiO_2 coated beads with 2 ml/min O_2 in the plasma discharge. The highest efficiency and maximum k value were obtained for

500 g of the photocatalyst. This enhancement was clearly linked to the higher activated surface area of TiO₂ films which increased photocatalytic reaction since the fraction of incident radiation absorbed by films increased and photogenerated oxidative species increased. Figure 83 shows the plot of the rate constant of cefixime degradation as a function of the photocatalyst's net weight loading. It presented there was a linear relationship between the kinetic of cefixime degradation and the net weight of TiO₂ coated glass beads. This important result underline the fact that the number of active sites is increasing linearly with the number of beads involving in the degradation of cefixime.

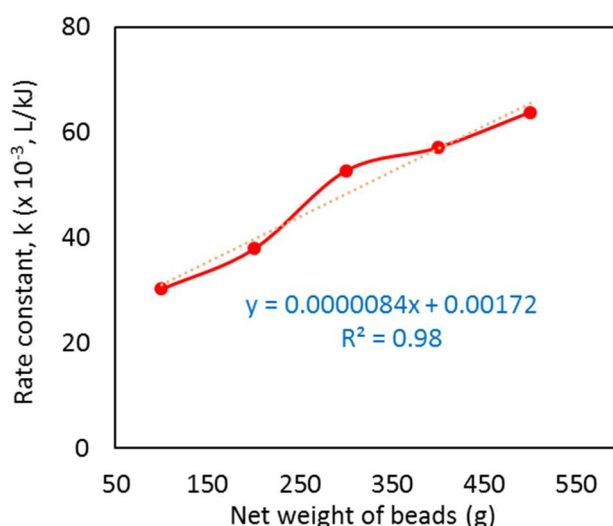


Figure 83. Linear regression between rate constant of cefixime degradation and net weight of TiO₂ (2 ml/min O₂, 45 min) coated glass beads.

Therefore, the reaction rate of cefixime degradation can be rewritten as the following expressions (eq. 34-35):

$$r = -KC \quad 34$$

$$K = f(W) \quad 35$$

r is the reaction rate, K is the rate constant as a function of net weight of coated glass beads (W in g), and C is the concentration (in mol/L).

2.2. Influence of doping in TiO₂ photocatalytic activity

The controversial influence of doping has been reported during the last decade. On the one hand, the modification of the band gap of TiO₂ by doping elements is expected to use a larger spectrum of solar radiation that in turn may enhance the efficiency of TiO₂ in photocatalytic reactions (46, 104, 106, 111). On the other hand, the presence of other elements in the lattice may enhance the charge recombination leading to a reduction in charge separation and a reduction in the efficiency of TiO₂ (115). In this work, we report our experiments on the influence of two known doping elements manganese and Vanadium. Mn-doped TiO₂ particles were elaborated in the fluidized bed plasma reactor while V-doped TiO₂ particles were

elaborated on the surface of glass beads by the sol-gel method both described in the previous chapter.

2.2.1. Photocatalytic activity of Mn-doped TiO₂ samples deposited with the plasma method under solar irradiation

The photocatalytic activity of Mn-doped TiO₂ nanomaterials was evaluated for cefixime degradation under sunlight irradiation. The contaminated solution containing 10 mg/L cefixime concentration was treated in presence of Mn_xTi_{1-x}O₂ samples ($x = 0.01, 0.003$, and 0.02 mol% Mn) at natural pH and ambient temperature. The Mn-doped TiO₂ films were coated on glass beads under 10 ml/min of oxygen flow rate in plasma gas for 35 min, and TTIP concentration was 1.67 M in isopropanol. The deposited Mn_xTi_{1-x}O₂ photocatalysts were annealed at 450 °C for 240 min to crystalize.

The photocatalytic activity of annealed Mn_xTi_{1-x}O₂ samples with different dopant concentrations (Mn: 0.01, 0.003, 0.02 at mol%) displays in figure 84. As shown in the figure, after 240 min of solar radiation about 75, 51, and 50% \pm 5% of cefixime degraded with TiO₂, Mn_{0.003}Ti_{0.997}O₂, Mn_{0.02}Ti_{0.98}O₂, and Mn_{0.01}Ti_{0.99}O₂ (10 ml/min O₂), respectively. The degradation efficiency of all Mn-doped catalysts clearly presented a small difference during 2 h (25 kJ/L of accumulated UV energy) solar exposition. The obtained results indicated that undoped TiO₂ samples provided the maximum degradation efficiency. The high photocatalytic activity of undoped TiO₂ can be attributed to the polymorphic nature that introduced the possibility of heterojunction formation which prevents the recombination of photogenerated e⁻/h⁺ pairs (110). The coexistence of anatase/rutile phases of TiO₂ films has been confirmed by XRD results (see section 1.1.3, chapter 4). The photocatalytic activity of films also was affected probably by the size of particles. The XRD analysis equipped with Scherrer measurements showed a higher crystallite size of Mn-doped TiO₂ in comparison with pure TiO₂. This synergetic effect was also reported by the literature (112). In $x = 0.01$ and $x = 0.02$ Mn concentrations, the degradation efficiencies were similar and less than Mn at $x = 0.003$ mol%. Therefore, the photocatalytic activity of Mn_xTi_{1-x}O₂ samples was low. As a result, the photocatalytic performance of films did not improve with doping Mn, it might be due to the lattice distortion. In the work of others (44, 74), who investigated the effect of doping on lattice distortion and photocatalytic activity, they reported adding dopants hindered grain growth and caused agglomeration of films. The interaction between Ti and Mn ions created a plurality of surface defects which increased the e⁻/h⁺ pairs recombination rate. As well as, this may be caused by the metal covering the surface of titanium films (235). There is a valence difference between Mn²⁺ and Ti⁴⁺ which causes oxygen vacancies. This reduction also can be explained by the fact that Mn ions in the TiO₂ structure act as a recombination center for e⁻/h⁺ which was reported by previously published papers (236-238). Several studies dealing with Mn ion on photocatalytic efficiency of TiO₂ were reported while the results were disputable and a wide range of explanations was presented because photocatalytic activity was related to many factors (44). In another study, Chang et al. (237) reported in Mn-doped

TiO_2 , $\text{Mn}^{3+}/^{4+}$ ions could trap electrons and holes and destroy the trapped carriers through inter-atomic relaxation.

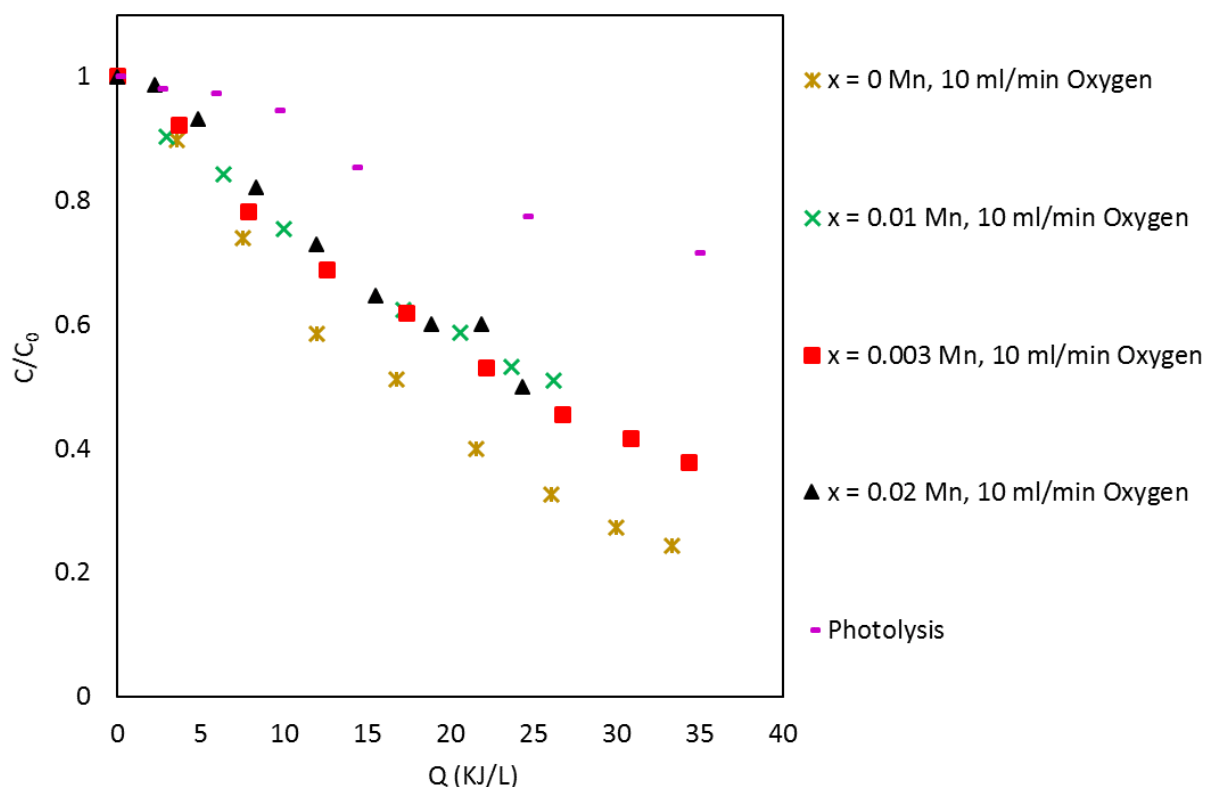


Figure 84. Cefixime degradation of TiO_2 and $\text{Mn}_x\text{Ti}_{1-x}\text{O}_2$ ($x = 0.003, 0.01$, and 0.02 at mol% Mn) deposited films on glass beads with 10 ml/min oxygen flow in plasma gas during 35 min.

The experimental data were fitted to the first-order kinetic model by the linear regression described by $-\ln(C/C_0)$ versus accumulated UV energy during 240 min of irradiation. The values of rate constants and coefficient of determination (R^2) are given in table 19. The k values for $\text{Mn}_{0.01}\text{Ti}_{0.99}\text{O}_2$, $\text{Mn}_{0.003}\text{Ti}_{0.997}\text{O}_2$, and $\text{Mn}_{0.02}\text{Ti}_{0.98}\text{O}_2$ were 26.4×10^{-3} , 28.6×10^{-3} , and 26.3×10^{-3} L/kJ, respectively. It can be seen the degradation rate of cefixime in presence of $\text{Mn}_x\text{Ti}_{1-x}\text{O}_2$ decreased from 1.62 to 1.49 times by comparison with undoped TiO_2 . These results were confirmed in experiments where $\text{Mn}_x\text{Ti}_{1-x}\text{O}_2$ ($x = 0.003$ mol%) layer was elaborated by using 25 ml/min oxygen flux in plasma gas.

In conclusion, doping TiO_2 with Mn in our experimental conditions led to a reduction of photocatalytic activity of TiO_2 may be because of recombination processes in presence of Mn in the TiO_2 lattice.

Table 19. The rate constant of cefixime degradation with TiO₂ and Mn_xTi_{1-x}O₂ (x = 0.01, 0.003, and 0.02 mol% Mn) deposited films on glass beads with 10 ml/min oxygen flow in plasma gas for 35 min.

Photocatalyst	O ₂ flux (ml/min)	Deposition time (min)	Mn (mol%)	K × 10 ⁻³ (L/kJ)	R ²
TiO ₂	10	60	0	42.6	0.99
MnTiO ₂	10	35	0.01	26.4	0.99
MnTiO ₂	10	35	0.003	28.6	0.99
MnTiO ₂	10	35	0.02	26.3	0.97
Photolysis	-	-		9.7	0.97

2.3. Photocatalytic activity of TiO₂ coatings on glass beads prepared with sol-gel method

In this study, the photocatalytic properties of TiO₂ coatings on glass beads with the sol-gel technique were compared to the properties of TiO₂ coating with the radiofrequency fluidized bed plasma method. The TiO₂ nanoparticles were coated on glass beads using a micro-mixing sol-gel reactor. Several types of TiO₂ and metal-doped (Zirconium and vanadium) TiO₂ were synthesized under various sol-gel conditions described in previous studies (171, 239-241). In these studies, the prepared TiO₂, ZrTiO₂, and VTiO₂ photocatalysts firstly were used for photocatalytic degradation of methylene blue and amoxicillin pollutants under artificial and solar irradiation (166, 239).

In each solar experiment with the synthetic cefixime solution, 350 g of coated glass beads were placed inside the chamber of the solar pilot. The 2 liters of cefixime solution with a concentration of 10 mg/L was circulated for 240 min. The adsorption of cefixime on coated glass beads was studied by passing cefixime solution under dark conditions. After 240 min, it was observed a decrease in cefixime concentration between 1.5 and 12% that was due to the adsorption of cefixime molecules on the surface of glass beads or other parts of photo-reactor.

Solar photocatalytic degradation of cefixime was carried out in presence of sol-gel catalysts in the middle of the day for 4 hours. Figure 85 shows plots of cefixime decomposition as a function of accumulated UV energy (kJ/L), for all TiO₂, V, and Zr doped TiO₂. From the experimental results, degradation of cefixime after 22 kJ/L of accumulated solar UV energy were 43.3, 44, 45.5, 41.2, 33.08 and 32.9% ± 5% for TiO₂, V_xTi_{1-x}O₂ (x = 2 mol%), V_xTi_{1-x}O₂ (x = 3 mol%), V_xTi_{1-x}O₂ (x = 5 mol%), V_xTi_{1-x}O₂ (x = 10 mol%) and V_xTi_{1-x}O₂ (x = 20 mol%), respectively. The best performance related to the V_xTi_{1-x}O₂ (x = 3 mol%) sample which was in agreement with previous results of methylene blue photocatalytic degradation experiments in the lab-scale photoreactor equipped with a UV lamp (239). The degradation efficiency for used TiO₂ and Zr_{0.05}Ti_{0.95}O₂ in amoxicillin removal achieved 59.6 and 36.3% ± 5%, respectively.

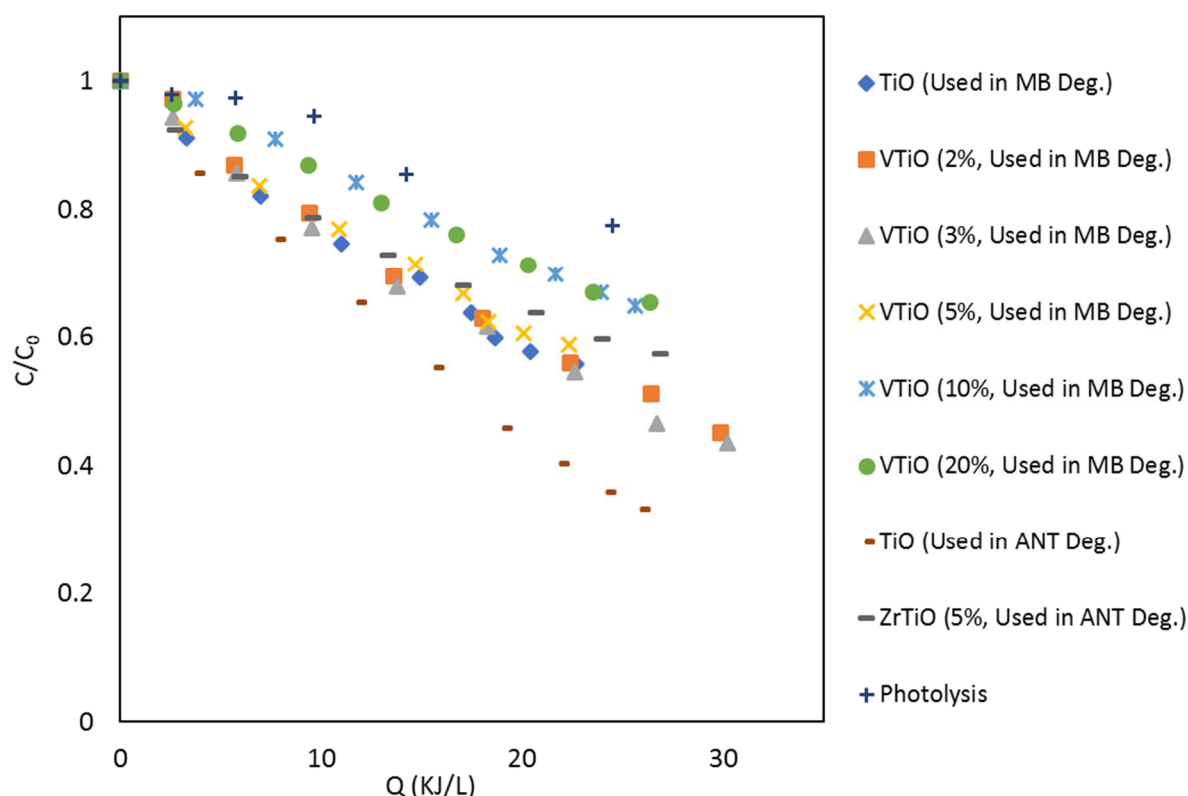


Figure 85. Cefixime degradation with used TiO_2 , $\text{V}_x\text{Ti}_{1-x}\text{O}_2$ ($x = 2, 3, 5, 10$ and 20 mol% V) and $\text{Zr}_x\text{Ti}_{1-x}\text{O}_2$ ($x = 5$ mol%) nano-powder coated on glass beads with sol-gel method. MB refers to methylene blue, ANT refers to amoxicillin antibiotic, and Deg refers to degradation.

These results indicated that the decomposition of cefixime via the photocatalytic reaction in the presence of the used catalysts approximated a first-order reaction model. The rate constant was determined from the slopes of linear regression, the all rate constants of the sol-gel used catalysts are demonstrated in table 20. The calculated rate constants varied from 15×10^{-3} to 41×10^{-3} L/kJ for the first usage of catalysts in the CPC photo-reactor. The highest degradation rate belonged to the pure TiO_2 that was used in amoxicillin degradation tests. The $\text{V}_x\text{Ti}_{1-x}\text{O}_2$ samples with $x = 2, 3$, and 5 mol% to higher reactivity than $\text{V}_x\text{Ti}_{1-x}\text{O}_2$ with $x = 10$ and 20% of vanadium dopant concentration in their structure.

Table 20. The rate constant of cefixime degradation with TiO_2 , $\text{Zr}_{0.05}\text{Ti}_{0.95}\text{O}_2$ and $\text{V}_x\text{Ti}_{1-x}\text{O}_2$ ($x = 2, 3, 5, 10$, and 20 mol% V) nanoparticles coated on glass beads used in CPC photo-reactor. MB refers to methylene blue, AMX refers to amoxicillin, and Deg refers to degradation.

Catalyst	Dopant concentration (mol%)	$K \times 10^{-3} \text{ (L/kJ)}$	R^2
TiO_2 (used in AMX Deg.)	-	41	0.99
ZrTiO_2 (used in AMX Deg.)	Zr = 5%	21.9	0.98
TiO_2 (used in MB Deg.)	-	26.3	0.99
VTiO_2 (used in MB Deg.)	V = 2%	25.9	0.99
VTiO_2 (used in MB Deg.)	V = 3%	27.6	0.99
VTiO_2 (used in MB Deg.)	V = 5%	24.3	0.99
VTiO_2 (used in MB Deg.)	V = 10%	16.4	0.98
VTiO_2 (used in MB Deg.)	V = 20%	16.4	0.99

The photocatalytic performance of plasma deposited and sol-gel synthesized photocatalysts were compared on cefixime degradation. The highest cefixime degradation efficiencies were observed for plasma deposited samples ranging from 65 to 80% under four hours solar irradiation in the CPC phot-reactor. In addition, photo-degradation of plasma deposited samples were obtained using 100 g of coated glass beads while 350 g of sol-gel coated glass beads were used in photocatalysis experiments. These results indicated photocatalytic activity of plasma deposited TiO_2 based samples was higher than sol-gel synthesized TiO_2 based samples.

Chapter 3. Regeneration of photocatalysts

This chapter will present the regeneration methods to recover the photocatalytic activity of used TiO_2 samples. The results of regenerated photocatalysts used for cefixime degradation will explain and compare.

3.1. Regeneration of photocatalysts

All the deposited films on glass beads were used more than two times in the lab-scale or solar photo-reactor pilot. Therefore, their photocatalytic activity was reduced because of the occupation of active sites by photo-degradation products or cefixime molecules. In the present work, the regeneration study of deactivated catalysts was performed with three regeneration methods. The hot water washing, heat treatment, and alkaline solution washing techniques were applied to study the recovery of active sites on the surface of photocatalysts.

As the deactivation of photocatalysts by molecules is of great concern, chapter 3 will be dedicated to the regeneration methods and their influence on photocatalyst's efficiency.

As shown in figure 86, for the hot water washing procedure, 100 ml of deionized water was used to regenerate the catalyst in a beaker by heating at $T = 80\text{ }^\circ\text{C}$ for 60 minutes. On other hand, the deactivated samples were heated in water from the ambient temperature to $80\text{ }^\circ\text{C}$, then maintained at the constant temperature for one hour. Finally, the sample was dried in an oven overnight at $80\text{ }^\circ\text{C}$. The regenerated sample was applied in the solar photo-reactor for photocatalytic degradation of cefixime under natural irradiation for four hours.



Figure 86. Hot water regeneration process.

For the heat treatment recovery method, the used photocatalyst was discharged from the photocatalysis reactor and washed with distilled water, after that the sample was thermally

treated in the air at 450 °C for 240 min in Nabertherm 3000 furnace. The thermal regeneration conditions were the same for all TiO₂, Mn-TiO₂, and V-TiO₂ catalysts.

In a typical alkaline washing regeneration technique, the net weight (from 100 to 500 g coated glass beads) of the sample was loaded in 100 ml of 1 M NaOH aqueous solution for 30 min. After alkaline treatment, glass beads were washed in distilled water until the pH of the solution was adjusted to the natural pH of water. Subsequently, dried in an oven at 80 °C over a night.

In order to check the efficiency these regeneration methods, the regenerated catalysts were used for the photocatalytic degradation of cefixime, following the same procedure which was described above. To compare the performance of regenerated techniques, the total cefixime degradation efficiency within the accumulated UV energy was calculated. The comparison between the photocatalytic activity of the fresh photocatalyst and regenerated photocatalyst can be revealed the regeneration efficacy of each technique.

3.2. Reusability of plasma deposited TiO₂ and MnTiO₂ films on glass beads

The reusability was a critical issue for the practical application of photocatalysts prepared in our study with the fluidized bed plasma technique. The reusability experiments were done in the same operating and radiation conditions in the solar pilot. After the first run, the photocatalyst beads were collected from the reactor and washed with distilled water, and dried at 80 °C. The recollected catalyst was used again for another photo-degradation run. The fresh cefixime solution was prepared and recirculated in the CPC photo-reactor for 240 min under natural irradiation. The solar photocatalysis degradation of cefixime was repeated with 100 g of coated glass beads with TiO₂ and MnTiO₂ layers. The photocatalytic degradation kinetics of cefixime in the second usage of catalysts was investigated by plotting $-\ln(C/C_0)$ versus the accumulated UV energy of solar irradiation. The rate constants (k) were obtained from the slope of curves. In figure 87, the calculated k values of all photocatalysts in two cycles are depicted.

A decrease in reaction rate between the first and second runs was observed. The rate constant of degradation efficiency of cefixime after the second run decreased from 51.6×10^{-3} to 44.7×10^{-3} L/kJ for the best TiO₂ photocatalyst that was deposited with 2 ml/min oxygen in plasma gas for 60 min.

In photocatalytic experiments with TiO₂ sample deposited with 25 ml/min O₂ in plasma gas for 60 min deposition duration, the rate constant seems higher but this corresponded to an experimental error.

Other photocatalysts exhibited a reduction in their rate constant after two solar photocatalytic degradations. This reduction could be attributed to the adsorbed molecules or by-products of photo-degradation on the active sites of the catalyst. This observation was in agreement with previous study which proved that Norfloxacin molecules were adsorbed on catalyst surface along with reaction by-products thus decreasing the photocatalytic activity of

TiO₂ composited films on the PET polymer (64). The results of reused catalysts exhibited good photocatalytic degradation of the pharmaceutical pollutant model but it was necessary to recover or regenerate the deactivated photocatalysts to obtain the activity. In practical application, it was not economic to synthesize TiO₂ films just for one usage, but to recover the catalysts by an appropriate method.

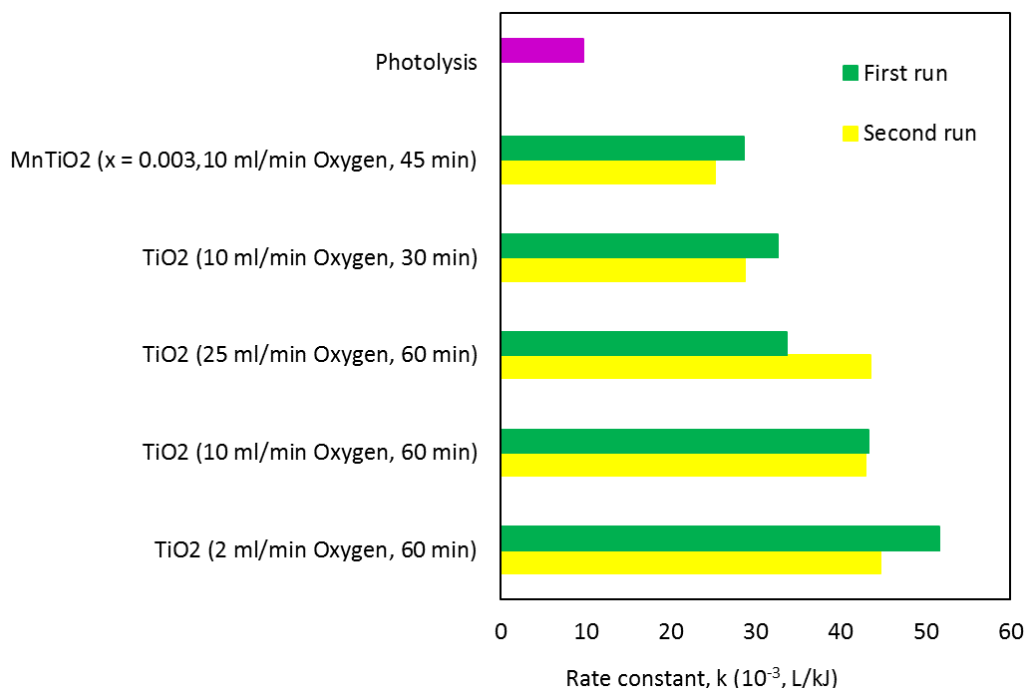


Figure 87. Comparison of cefixime degradation's reaction rate constant with different plasma deposited TiO₂ films on glass beads in solar photo-reactor.

The crystalline structure of TiO₂ films on glass beads before and after photocatalysis was characterized by the Raman spectroscopy method. A glass bead was taken as a sample before and after catalyst usage in the treatment method. Figure 88 shows the Raman modes of the photocatalyst before and after a photocatalytic degradation of the pollutant. It can be observed that there was no difference in Raman spectra results between the fresh and used catalyst. All peaks in the two curves were related to the anatase phase of the TiO₂ crystalline structure. As well as, no other peaks appeared in the Raman spectra in the range of 100 and 1000 cm⁻¹. The modes did not change or shift which suggested that the presence of cefixime or by-products did not induce a significant change in the TiO₂ composition and crystallinity during the photocatalysis degradation process.

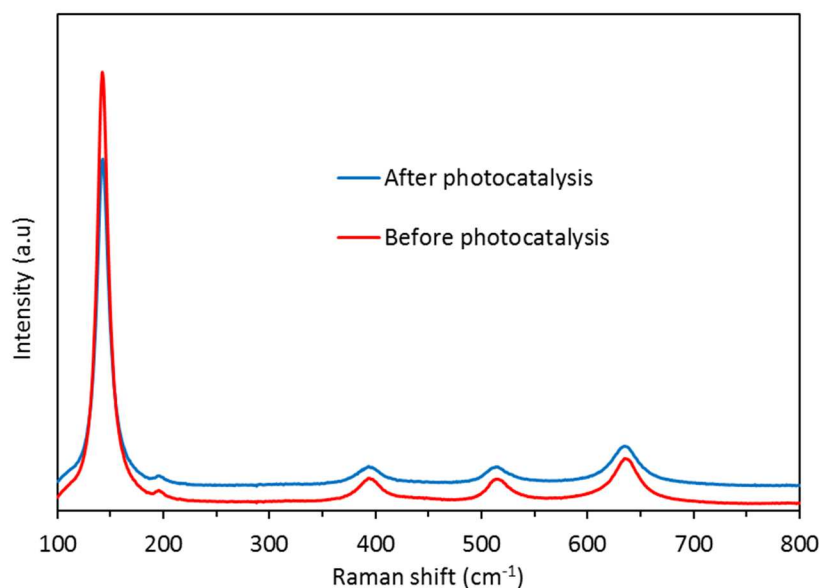


Figure 88. Raman spectra of TiO₂ films deposited on glass beads before and after photocatalysis experiment.

3.3. Photocatalysts regeneration methods

In the previous section, we reported the photocatalytic activity of different TiO₂-based samples on cefixime degradation. Actually, we proposed the products of photocatalysis reactions partially adsorbed on the surface of TiO₂ films and decreased their activity due to the occupation of active sites. This adsorption might limit the surface charge carrier transportation and cefixime adsorption. Therefore, the recovery of active sites on the surface of films should be considered.

Several regeneration methods were discussed in the literature (156, 158, 160, 242, 243), in this work three regeneration methods were studied to recover the photocatalytic activity of TiO₂-based samples. A comparative study of the three regeneration techniques including hot water, heat treatment in the air atmosphere at 450 °C, and treatment with the alkaline solution were performed. The evolution of the performance of regenerated TiO₂ films coated on glass beads was measured on the elimination of cefixime with solar radiation in the CPC photo-reactor. Solar photocatalytic experiments carried out with 100 g of recovered catalysts, the initial concentration of cefixime was around 10 mg/L at neutral pH and ambient temperature. In a typical experiment, 2 L of cefixime solution was treated under solar irradiation for a period of four hours.

3.3.1. Hot water regeneration method

In this case, two types of photocatalysts were examined to regenerate with hot the water method. The TiO₂ coated films deposited with 2 and 25 ml/min O₂ flow rate in plasma gas for 60 min were recovered in hot water. In this method, the photocatalysts beads in a container

with distilled water were heated up to 80 °C and remained at constant temperature for 60 min. After that photocatalysts were dried at 80 °C over a night in an oven.

Photocatalytic activity of regenerated catalysts was tested for cefixime degradation. Figure 89 shows the cefixime concentration reduction under similar solar UV that was received on the reactor. In the case of TiO₂ deposited under 2 ml/min oxygen in plasma gas, the C/C_0 values achieved in the order of 0.26 > 0.22 > 0.26 for the first run, regenerated run, and second run after regeneration under 26 kJ/L of accumulated UV energy, respectively. For the first regeneration cycle, the activity of TiO₂ completely recovered as cefixime degradation was increased from 74 to 78%. The regenerated (washing by 80 °C water) TiO₂ (2 ml/min O₂, 60 min) in the second cycle after regeneration showed the same activity as the fresh catalyst indicating nearly complete regeneration of the catalyst.

The TiO₂ (25 ml/min O₂, 60 min) catalytic activity also was recovered with hot water and cefixime degradation efficiency increased from 51 to 71%. Plus, in the second cycle after regeneration, it gave 70% removal of cefixime after 240 min. Based on these results, we suggested that the hot water was a powerful method for regeneration of the deactivated samples prepared with the fluidized bed plasma technique. During the hot water recovery method, no visually detectable particles were leached into the water. According to the results of the XPS analysis technique (see 3.1.3 in part 3) there was a strong adhesion between TiO₂ films and the surface of glass beads because during experiments we did not observe the peeling during cefixime decomposition under solar irradiation even though TiO₂ films soaked in liquids for 4 h. These results confirmed that the adhesion of films on substrates was strong.

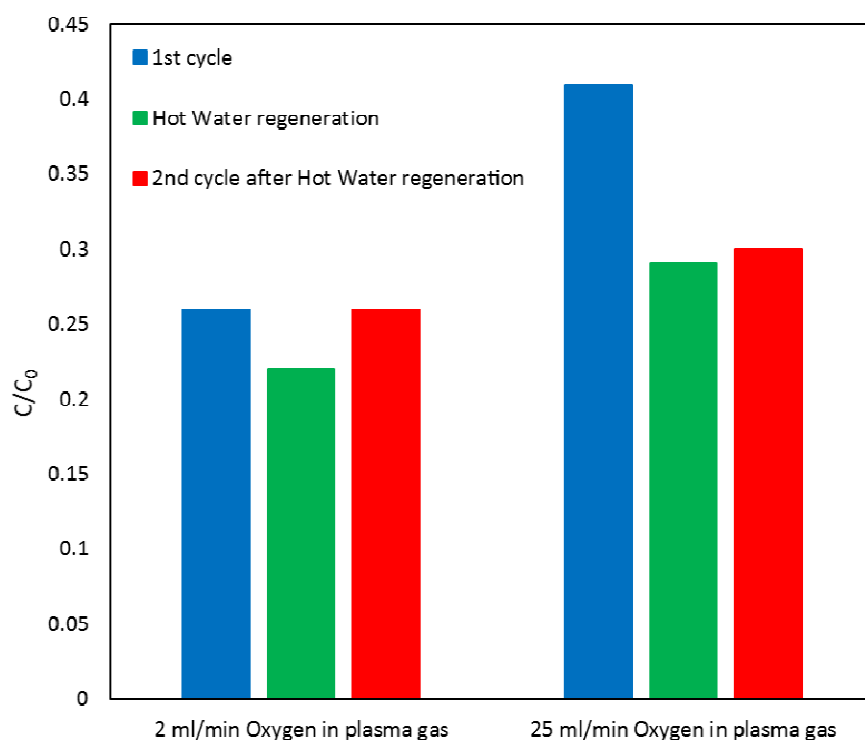


Figure 89. Cefixime concentration reduction after hot water regenerated TiO_2 (2 and 25 ml/min O_2 in plasma gas at 60 min of deposition time) photocatalysts.

Photocatalysis tests were continued in the presence of the regenerated TiO_2 sample (2 ml/min O_2 in plasma gas) for four consecutive cycles. The reduction of cefixime concentration was plotted vs accumulated energy in four solar photocatalytic experiments. The performance slightly decreased during four cycles up to 10% of loss in its photocatalytic activity looking figure 90. The degradation rate of the first curve (first cycle) did not fit well with the first order and the best fit was observed in the second order. While in other runs the kinetic of cefixime degradation followed first order. The value of the rate constant for cefixime degradation was computed from the slopes of the linear regression between $-\ln(C/C_0)$ and accumulated UV energy (kJ/L). The k values were calculated at 55.5, 50.3, and 51.4 L/kJ for the second, third and fourth cycles, respectively. These observations presented that the photo-activity of coated TiO_2 films on glass beads slightly decreased.

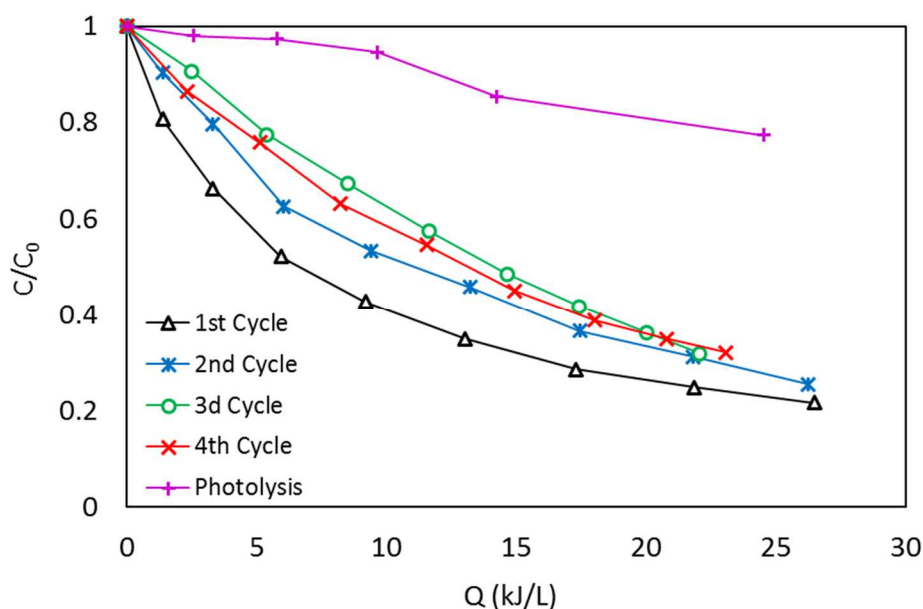


Figure 90. Cefixime concentration reduction after hot water regenerated TiO_2 (2 ml/min O_2 in plasma gas at 60 min of deposition time) during four consecutive cycles.

This regeneration method also was applied for the second series of TiO_2 depositions prepared with dilute precursor solution ($C_{\text{Ti}} = 1.002$ mol/L, 30:70 Vol.% of TTIP: Isopropanol) under various oxygen flow rates between 0 and 10 ml/min for 45 min in the plasma reactor. In the first usage of these TiO_2 photocatalysts in the solar pilot, the first order kinetic was evaluated to describe photocatalytic cefixime degradation. After the first run, photocatalysts were recovered with hot water for 60 min, and were used one more time in the solar photo-reactor. The rate constant of cefixime photo-degradation with fresh and hot water regenerated photocatalysts were plotted in figure 91.

It was observed that in the case of TiO_2 (0 ml/min O_2), the photocatalytic activity of the hot water regenerated TiO_2 greatly increased when compared with the first usage. The obtained cefixime degradation efficiency was 15% higher than the fresh sample. The photocatalytic activity of TiO_2 films deposited with 1, 3, and 4 ml/min O_2 in plasma gas was slightly increased after regeneration.

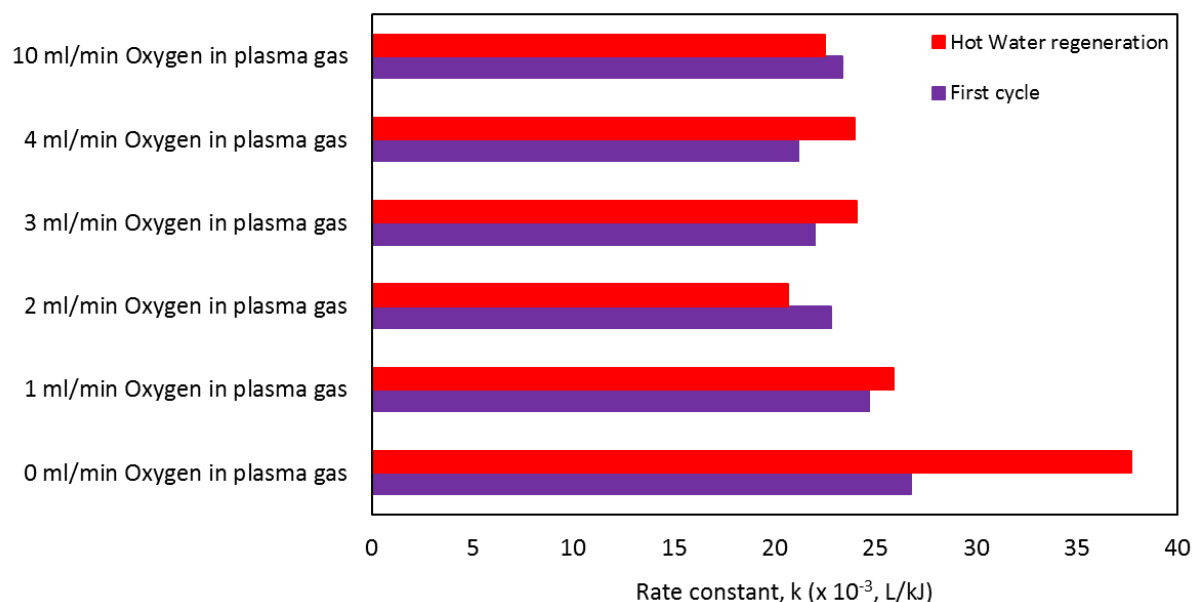


Figure 91. Rate constant of cefixime degradation with TiO_2 ($C_{\text{Ti}} = 1.002$ mol/L, 45 min) films in first usage and after hot water regenerated photocatalyst usage.

This enhancement might be due to removing adsorbed particles from active sites of films coated on glass beads during hot water recovery at 80 °C.

3.3.1.1. Study the cefixime degradation under longer solar irradiation time

To achieve a more efficient degradation of cefixime or complete degradation, a longer reaction time or some other improvements in the process are required. Two photocatalysts TiO_2 (2 and 25 ml/min O_2 , 60 min) were regenerated and used for cefixime degradation under solar irradiation to study the long-time effect. These experiments were done during (7 hours) in the day from 10:00 am to 5:00 pm local time. The photodegradation of cefixime in the CPC reactor with two TiO_2 samples is depicted in figure 92. For longer solar irradiation times, cefixime degradation follow first-order kinetics as a function of accumulated energy for 360 or 420 min, the degradation curve varies after 270 min ($Q = 30$ kJ/L). We observed a kinetic variation for times up to 7 h, followed by a reduction of the slopes that corresponded. To explain the slowing down of degradation kinetics, occupation of catalyst's active sites by the cefixime by-product was one of the causes. Because in photocatalysis reactions, adsorption and desorption of pollutants from the photocatalyst surface were the main reactions, therefore, for a long time the degradation by-products competed with cefixime molecules.

From the results, it appeared the reaction rate was too slow and the degradation was incomplete after such long solar radiation.

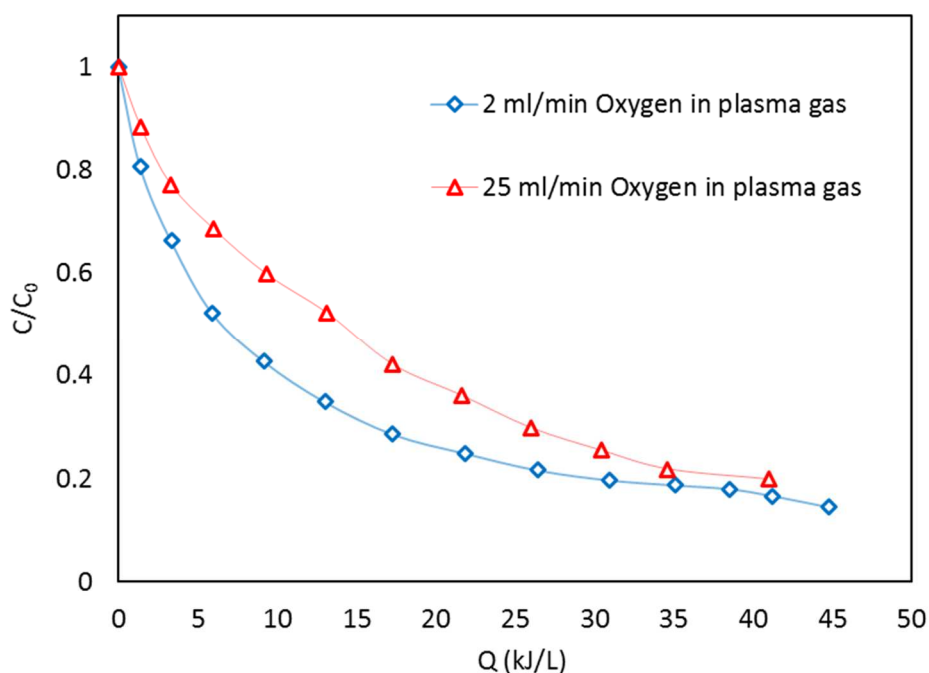


Figure 92. Cefixime degradation of two TiO_2 films (2 and 25 ml/min O_2 flux, 60 min) at longer time of solar irradiation.

3.3.2. Heat treatment regeneration method

Thermal treatment was employed as well to regenerate the deactivated catalyst since carbonaceous deposits could remove at high temperatures under the oxygen atmosphere. The $\text{Mn}_x\text{Ti}_{1-x}\text{O}_2$ photocatalysts which were deposited with two Mn percentages ($x = 0.01$ and 0.02 mol%) in precursor solution and 10 ml/min oxygen flux were used to examine the heat treatment regeneration technique. After heat treatment at 450°C in air for 4 h, the value of the rate constant with photocatalyst and the regenerated photocatalyst was obtained from the reaction rate curves, where the evolution of the initial concentration with time was followed for 240 min. Results of the photocatalytic activity with recovered $\text{Mn}_x\text{Ti}_{1-x}\text{O}_2$ samples are illustrated in figure 93.

Firstly, the hot water recovery technique was studied, as the result, obtained rate constants demonstrated hot water could partially remove adsorbed species from film's surface. The $\text{Mn}_x\text{Ti}_{1-x}\text{O}_2$ catalysts regenerated by thermal treatment displayed slower degradation efficiency of cefixime after 240 min solar irradiation, the 41.5 and 59.8% of cefixime initial concentration removed with $\text{Mn}_x\text{Ti}_{1-x}\text{O}_2$ ($x = 0.01$ mol%) and $\text{Mn}_x\text{Ti}_{1-x}\text{O}_2$ ($x = 0.02$ mol%), respectively. The $\text{Mn}_x\text{Ti}_{1-x}\text{O}_2$ deposited with higher dopant concentration exhibited better performance under heat treatment recovery. As seen in figure 92, the hot water washing improved the degradation efficiency as compared to heat treatment which indicated the

photocatalyst could partially recover and the surface of the photocatalysts was not free of adsorbed species.

Compared with the hot water method, heat treatment was less effective and time-consuming for the regeneration of the deactivated $\text{Mn}_x\text{Ti}_{1-x}\text{O}_2$ catalyst. Heat treatment may cause agglomeration of $\text{Mn}_x\text{Ti}_{1-x}\text{O}_2$ particles which was not favorable for the photo-activity (150). On other hand, catalyst calcination could be detrimental to the photocatalytic properties of the $\text{Mn}_x\text{Ti}_{1-x}\text{O}_2$ samples.

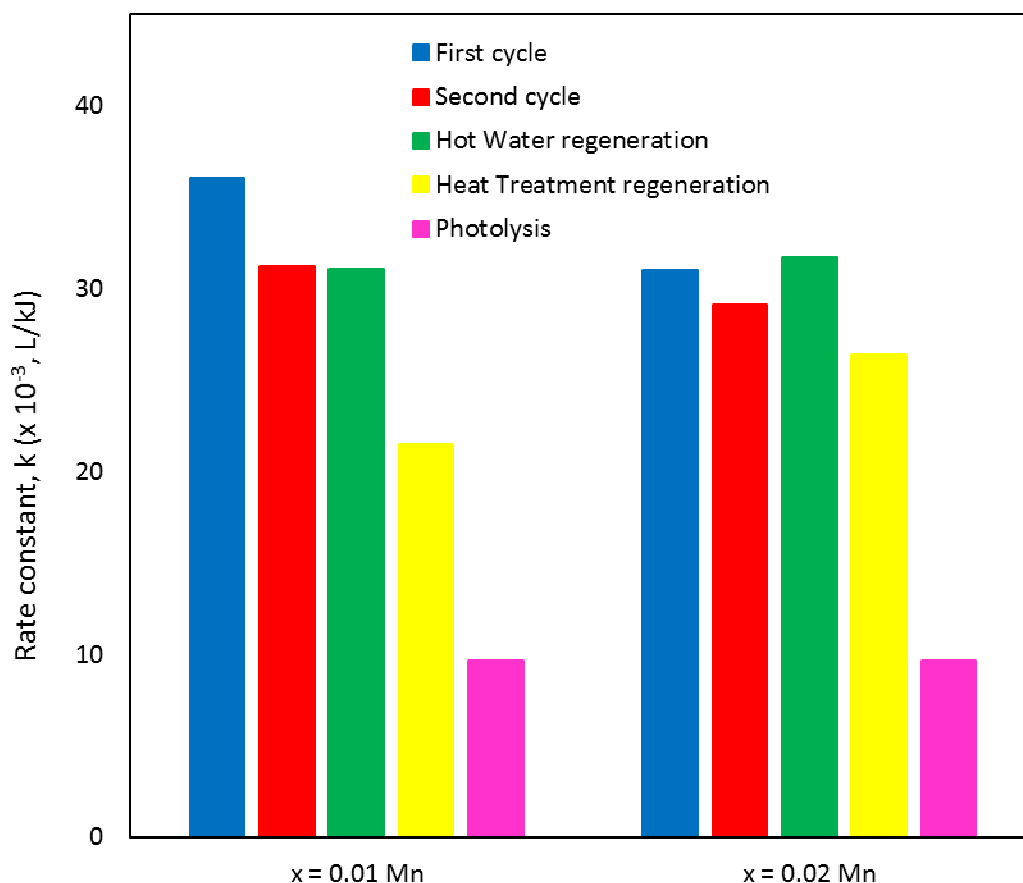


Figure 93. Rate constant comparison of $\text{Mn}_x\text{Ti}_{1-x}\text{O}_2$ ($x = 0.01$ and 0.02 mol% Mn, 10 ml/min O_2) films regenerated with hot water and heat treatment (annealed at 450°C , 4 h) methods.

As the result, heat treatment might agglomerate and calcinate the nanoparticles of TiO_2 at 450°C for 4 h and consequently decrease photocatalytic activity.

3.3.3. Alkaline solution regeneration

The last recovery method was washing with an alkaline solution at $\text{pH} = 11$ for 30 min. All three recovery methods were applied for $\text{Mn}_x\text{Ti}_{1-x}\text{O}_2$ ($x = 0.01$ mol%) photocatalyst. At first, the catalyst was regenerated in hot water and used in the CPC reactor, then it was washed and annealed for 240 min at $T = 450^\circ\text{C}$ to remove adsorbed cefixime degradation by-products. Another solar test was carried out after heat treatment. In the next step, the coated films on

glass beads were washed with hot water another time. As shown in figure 94, after washing the photocatalyst in an alkaline solution, the regeneration rate constant increased from 22.8 to 25.2 L/kJ. It found that treatment in NaOH solution with pH 11 cannot remove completely toxic particles at 30 min treating time. The regeneration performance became slightly lower than the hot water method. The photodegradation products or intermediates adsorbed on the titania active sites could be removed by NaOH washing. Poisoning of the surface were responsible for inhibition of O_2 for producing active oxygen species (158).

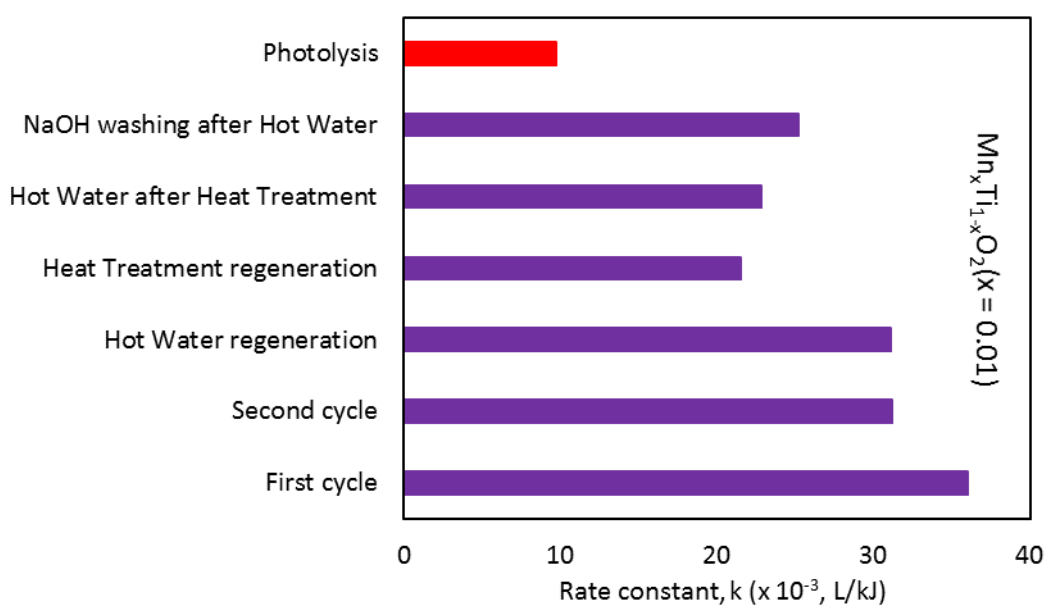


Figure 94. Comparison of different regeneration methods used for $Mn_xTi_{1-x}O_2$ ($x = 0.01$ mol%, 10 ml/min O_2) photocatalyst coated on glass beads.

In conclusion, the higher degradation efficiency with TiO_2 as well as $Mn_xTi_{1-x}O_2$ catalysts indicated that hot water regeneration was the best technique. And the catalysts could not completely regenerate by heat treatment and alkaline solution washing techniques.

In comparison with previous studies (154), the thermal treatment and washing with solvent (methanol and water) indicated poor regeneration activity for catalyst P25 Degussa during photocatalysis of phthalic acid which was in agreement with our results. While in another published paper, Yang et al. (160) reported that alkaline washing and thermal treatment were effective methods to regenerate the TiO_2 photocatalyst that was deactivated by humic acid degradation intermediates. They concluded the critical factor in recovery methods related to the chemicals that adsorbed on active sites. It was concluded that the by-product species adsorbed on active sites deactivate the photocatalytic sites that constitute a critical factor for industrial applications.

Additionally, a comparative study examined four kinds of regeneration methods on sulfate poisoning of TiO_2 surface. Different regeneration methods including hot water washing, sulfuric acid washing, sodium hydroxide washing, and thermal treatment were investigated

for the regeneration performance of TiO_2 . The efficiency of the NaOH treatment was higher than other methods while the regeneration efficiency significantly decreased as the number of cycles increased due to the loss of catalyst particles. Hot water washing was the effectiveness and simplest process in photocatalytic recovery. The thermal treatment showed good reusability in removing surface compounds from the active sites of TiO_2 . In addition, acid washing displayed a negative effect on the regeneration (149).

3.3.4. Regeneration stability of plasma deposited photocatalysts

Regeneration stability was the number of cycles that we could regenerate our deposited photocatalysts. Good repeatability and stability of photocatalysts were beneficial to decrease water treatment costs. The stability of TiO_2 films deposited on glass beads was evaluated by using times in solar tests.

For this subject, we used a TiO_2 (25 ml/min O_2 , 60 min) sample to study its reusability stability. Photocatalyst beads after each solar photocatalysis test were regenerated by the hot water method and used in the solar photo-reactor with fresh cefixime solution for another run.

The regeneration stability of the TiO_2 photocatalyst is shown in figure 95. The efficiency decreased from 65% for the first regeneration step to 51% for the fourth regeneration step. The efficiency decreased to about 14% after the deactivated catalyst was recovered by the hot water four times. We found that the deactivated TiO_2 films during cefixime decomposition could be regenerate easily by removing adsorbed species using the hot water method without making an impression on TiO_2 films. After several times usage, the results presented that TiO_2 supported on glass beads showed well photocatalytic efficiencies after more than several experiments. This result was also obtained by Chekir et al. who reported that TiO_2 supported on fiber cellulose presented good stability and high yield after several uses (244). So, plasma deposited TiO_2 films could effectively applied and regenerated in photocatalysis experiments without destroying layers.

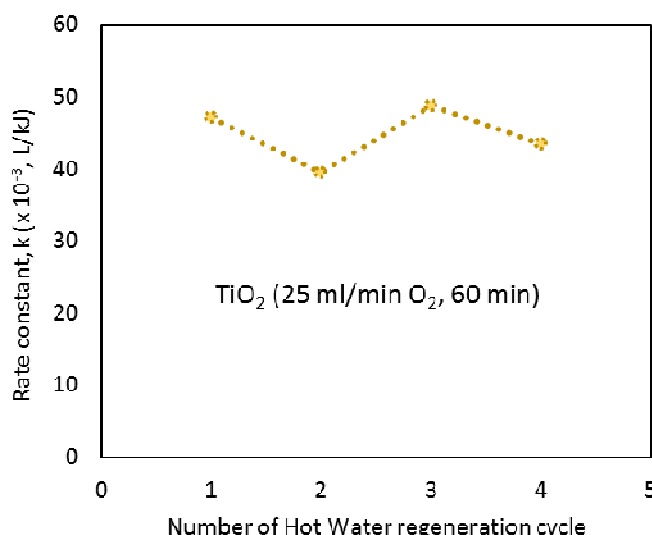


Figure 95. Regeneration stability of hot water regenerated TiO₂ (25 ml/min O₂, 60 min) sample coated on glass beads.

3.3.5. Regeneration of sol-gel prepared photocatalysts

Recovering ability was one of the important parameters in the photocatalytic process, to assess the regeneration ability of the sol-gel prepared TiO₂ coated particles, two regeneration methods were applied. As mentioned previously, the hot water recovery method showed the best performance in different plasma deposited catalysts, so the hot water regeneration method was used on all sol-gel synthesized samples after the first cycle. The rate constant of cefixime degradation under 240 min solar irradiation with regenerated photocatalysts are presented in figure 96. After the hot water washing, cefixime degradation increased just for Zr_{0.05}Ti_{0.95}O₂, VTiO₂(10 mol%), and VTiO₂(20 mol%) samples. In VTiO₂ catalysts, this improvement could be attributed to the methylene blue removal from the surface of glass beads because their activity increased about 11.2 and 4.5% for 10 and 20 mol% vanadium after 21 kJ/L of accumulated energy, respectively. In the Zr_{0.05}Ti_{0.95}O₂ sample, enhancement related to the regenerating active sites of TiO₂ films due to higher cefixime degradation efficiency after regenerating the catalyst. The rate constant became 1.8 times higher than the first usage.

To compare the hot water and the heat treatment method, the used TiO₂ sample in antibiotic degradation was selected. The rate constant reached 41, 28.2, and 19.2 L/kJ for the first run, after hot water regenerated photocatalyst run and heat treatment regenerated photocatalyst run, respectively. As shown in figure 96, hot water recovery was the best method also in sol-gel synthesized photocatalysts.

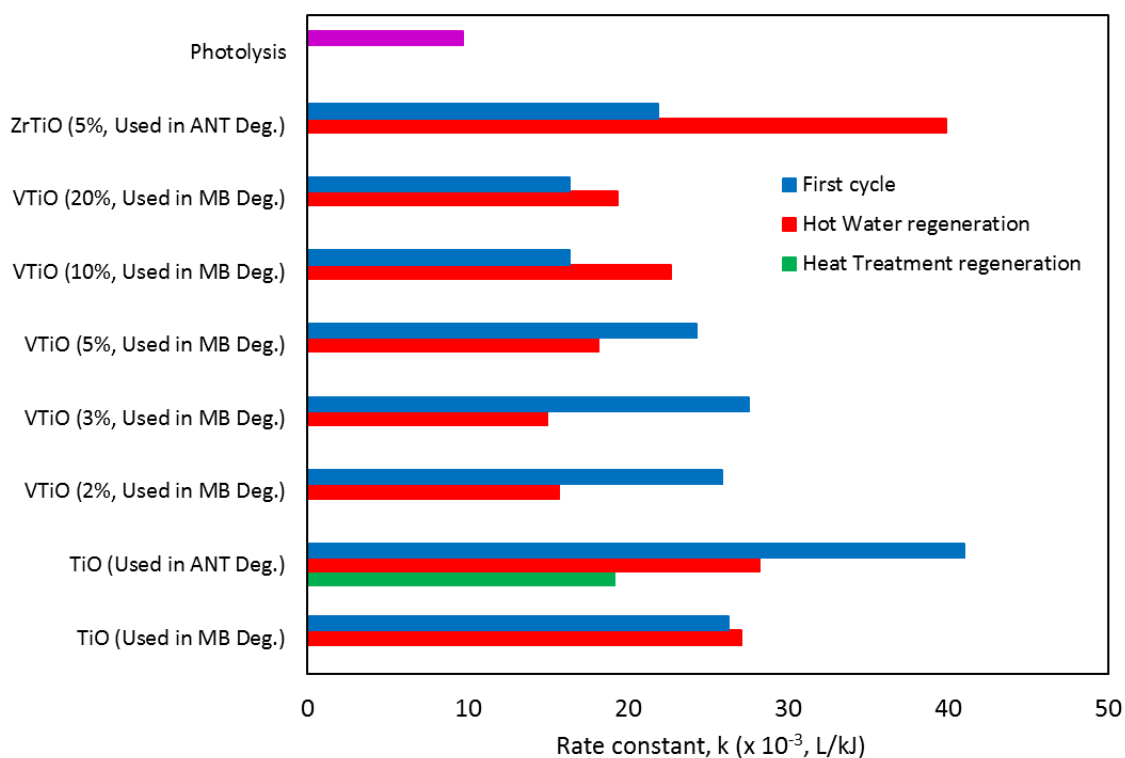


Figure 96. The rate constant of cefixime degradation with used TiO₂, VTiO₂ (2, 3, 5, 10 and 20 mol% V) and ZrTiO₂ (5 mol%) beads before and after two regeneration methods.

3.3.5.1. Regeneration of the fresh TiO₂ and VTiO₂ (3 mol%) prepared with sol-gel method

As explained before TiO₂ and VTiO₂ (3 mol%) sol-gel synthesized photocatalysts indicated better photocatalytic performance on cefixime degradation under solar irradiation. So, two fresh samples were prepared by the micro-mixing reactor and used in the solar pilot for cefixime degradation. The TiO₂ and VTiO₂ (3%) catalysts synthesized by the sol-gel method were used to study their recyclability by hot water and heat treatment regeneration techniques. Figure 97 illustrates the rate constant of cefixime degradation with TiO₂ and VTiO₂ (3%) photocatalysts in different conditions of catalyst. The hot water regeneration method only could recover and increase the photo-activity of pure TiO₂, while VTiO₂ (3%) did not lose adsorbed species from the surface of nano-particles coated on glass beads. The rate constant

of cefixime degradation was computed at 21.1 and 21.5 L/kJ for TiO₂ regenerated by the hot water and heat treatment methods, respectively.

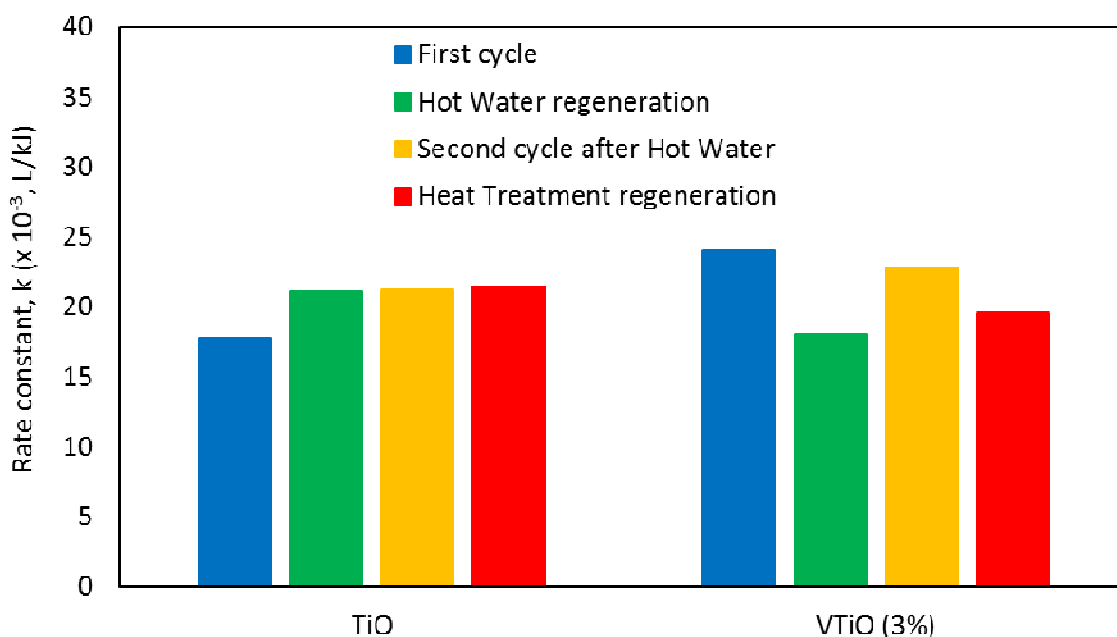


Figure 97. Rate constant comparison of the fresh and regenerated TiO₂ and VTiO₂ (3%) beads prepared by sol-gel, with hot water and heat treatment regeneration methods.

As well as, in the second cycle after the hot water recovery, the rate constant obtained 21.2 which was similar to other experiments.

In the case of VTiO₂ (3%), the heat treatment method showed a higher rate constant in comparison with hot water regenerated catalysts and it was calculated at 18 and 19.6 L/kJ, respectively.

In conclusion, the regeneration studies with three methods on plasma deposited and sol-gel synthesized films on glass beads indicated that hot water recovery was the most effective technique. This regeneration method was simple and cost-effective without the requirement of high energy demand or materials.

Chapter 4. Mechanism of cefixime photocatalytic degradation under solar irradiation

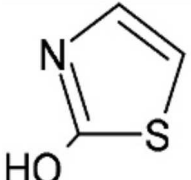
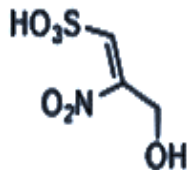
4.1. Analysis of treated cefixime solution by LC-MS technique

In the presented thesis we focused our efforts to elaborate TiO₂ photocatalysts in low-pressure plasma reactor and study the influence of oxygen concentration in plasma gas on the structure and composition of TiO₂ deposits. As comparison point, we used TiO₂ elaborated by sol-gel technique. We focused also our attention on the photocatalytic activity of the so

elaborated TiO₂ particles. We used a pharmaceutical molecule model as cefixime to check the efficiency of the deposits. A chemical pathway study needs more time and materials. Particularly it needs to develop liquid chromatography associated with mass detector. In order to have an idea of the composition of cefixime degradation we asked an independent private laboratory (Mahamax Laboratory, Tehran, Iran) to perform tests on two samples of water with cefixime after degradation in the CPC solar pilot reactor containing TiO₂ deposited by plasma on glass beads using 2 ml/min of oxygen.

After 4 h of photocatalysis, cefixime degradation products were analyzed by the LC-MS technique through the solar photocatalysis process under natural irradiation for 240 min. Two samples were selected with the efficiency of 40% and 85% cefixime degradation in order to determine the remaining by-products. In the case of 45% degradation efficiency under 240 min solar irradiation in the CPC photoreactor, two main intermediate compounds were identified according to the total ion chromatogram and mass spectra. The chemical structure and its fragments are listed in the table 21. The characteristic ions (m/z) of the intermediates were identified at 101, 105, 115, 121, 146, 162, and 183.

Table 21. Identified products of cefixime degradation by solar photocatalytic process (Experimental conditions: initial cefixime concentration = 10 mg/L, reaction time = 240 min, catalyst = TiO₂)

No	Chemical formula	R _t (min)	Characteristic Ions (m/z)	Proposed Structure
1	C ₃ H ₃ NOS	1.4	101	
2	C ₃ H ₅ NO ₆ S	1.5	183	

Apparently, the dominant peaks were seen at m/z = 80, 142, and 183 for the degradation of cefixime with 85% efficiency. The other peaks appeared at 64, 74, 79, 105, 115, 121, 141, 146, 162, and 193.

Erim et al. (106) predicted four cefixime degradation by-products using the photocatalysis process under 3 h UV-A irradiation. They identified intermediates like thiazol-2-ol, N-(dihydroxymethyl)-2-(2-hydroxythiazol-4-yl)acetamide, (S)-N-(2-amino-1-hydroxy-2-oxoethyl)-2-(2-hydroxythiazol-4-yl), and 2-(2-hydroxythiazol-4-yl)-N-((2R,3R)-2-mercapto-4-oxoazetidin-3-yl)acetamide.

It is difficult to determine the exact mechanism of cefixime degradation during the photocatalytic process. In a published paper (12), the cefixime removal was studied by the

sono-electro-Fenton method They proposed a cefixime degradation pathway by identification of intermediates with an LC-MS analytical technique which is presented in the figure 98.

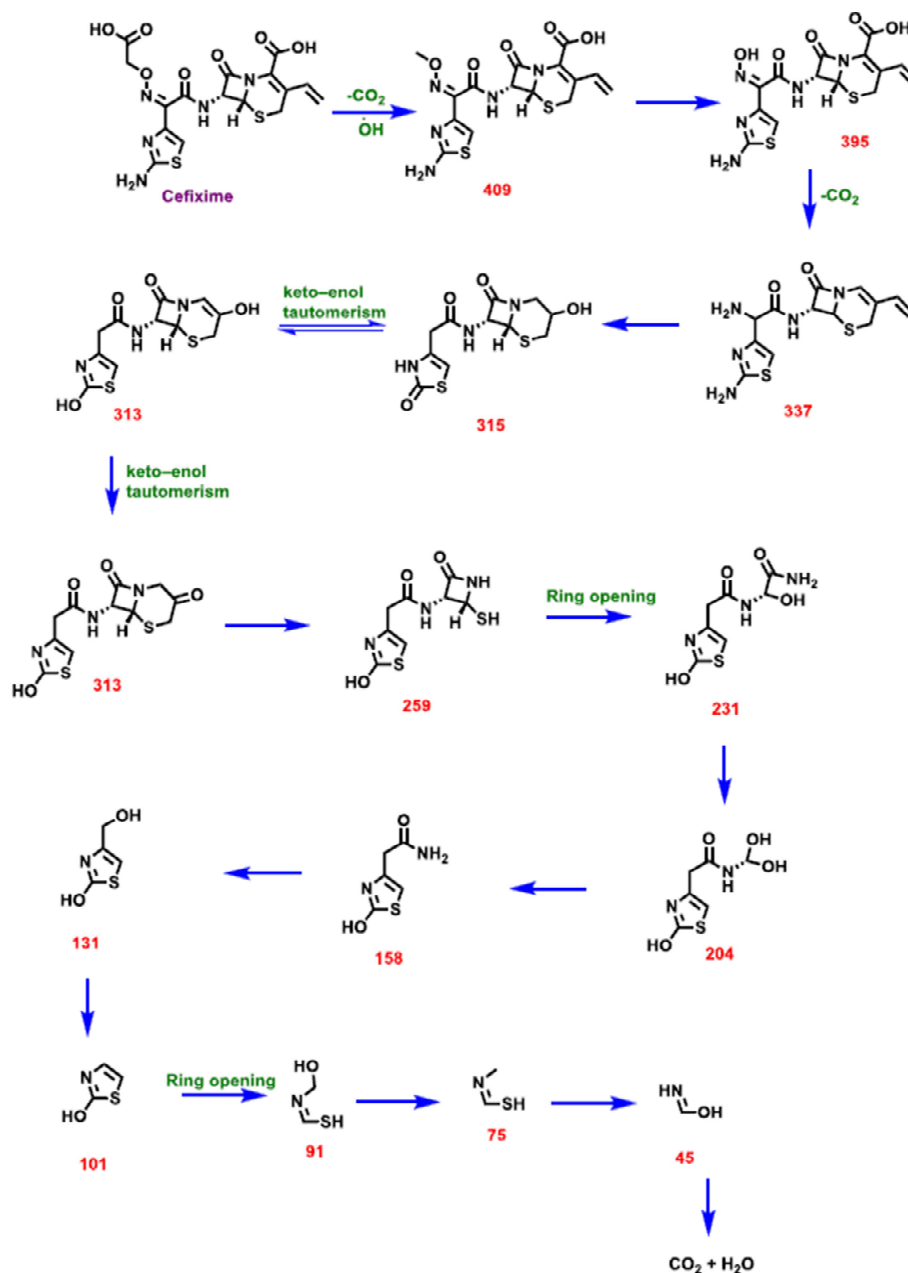


Figure 98. Proposed pathway for degradation of Cefixime antibiotic by the sono-electro-Fenton process (12).

Referring to the literature, firstly the thiazol side was decomposed then the β -lactam was degraded to small molecule structures and further, the intermediates continued to decompose through the oxidation process products such as SO_4^{2-} , NO_3^- , CO_2 and H_2O (12, 52, 106, 245).

The finding showed that cefixime molecules were fractured into smaller fragmented molecules. Production of these intermediates during solar photocatalysis approved the effective degradation of cefixime.

Conclusions

The TiO₂ and Mn-doped TiO₂ films were successfully deposited on the surface of glass beads via the low-pressure fluidized bed plasma method. The plasma deposition technique allowed to control of photocatalysts composition by plasma parameters such as oxygen flux, deposition time, and TTIP concentration in the precursor. Also, it permitted to attachment of photocatalyst layers with chemical bonds between TiO₂ and the glass beads' surface evidenced by the XPS analytical technique. Oxygen flux in plasma gas leads to the apparition of the rutile phase beside the anatase grains. The rutile fraction increased as the oxygen flux increased in the plasma discharge.

Cefixime degradation in the presence of a photocatalyst was studied under a UV lamp ($\lambda = 370$ nm, 8 W) and solar irradiation. The accumulated UV energy of the lamp was calculated at about 40 kJ/L over 4 hours while the accumulated UV of solar energy was determined around 35 kJ/L over 4 hours on a sunny day. The cefixime degradation efficiency was obtained at 90 and 80% under the artificial lamp and natural solar irradiation, respectively.

The best performance of photocatalytic activity was obtained for TiO₂ photocatalyst deposited under 2 ml/min oxygen flow rate in plasma gas with 80% cefixime degradation efficiency due to its rutile/anatase ratio of 19% which has the same anatase/rutile ratio of P25 Degussa. Under 35 kJ/L solar radiation, as the rutile fraction increased in the TiO₂ polymorph structure, the photocatalysis performance decreased.

Kinetic cefixime photodegradation was obtained in the first order for all kinds of TiO₂ samples. The rate constant of kinetic was calculated from the slope of $-\ln(C/C_0)$ versus accumulated UV energy (kJ/L). These values were determined at 33.4, 51.6, 42.6, and 33.6 $\times 10^{-3}$ L/kJ for TiO₂ films containing 0, 16, 27, and 31 mol% of rutile fractions in their structure. It means the plasma condition of O₂ flux can influence the photocatalytic performance of TiO₂ films by creation of rutile phase beside anatase phase.

The deposition time and TTIP concentration in the precursor also affected the photocatalytic activity of TiO₂ films. These parameters can influence the number of active sites. Higher deposition time (60 min) and TTIP concentration in precursor solution ($C = 1.67$ mol/L) resulted in higher photocatalytic activity because of the higher growth rate of TiO₂ films and homogeneity of films.

The net weight of coated glass beads also affected the cefixime degradation rate, as the net weight of photocatalysts increased from 100 to 500 g, the degradation efficiency of cefixime increased under similar solar irradiation. In addition, there was a linear relation between the kinetic constant and the net weight of coated glass beads. This enhancement is due to an increasing number of photocatalytic active sites.

The three types of Mn-doped TiO₂ plasma deposited samples were used in the solar pilot, photocatalysis results with Mn_xTi_{1-x}O₂ ($x = 0.01, 0.003, \text{ and } 0.02$) illustrated that doping with manganese did not enhance the photocatalytic performance of TiO₂. It might be due to the

rutile fraction in TiO_2 crystal or distortion of TiO_2 as the host lattice. In the higher Mn dopant concentration, the rutile phase appeared and its fraction was determined around 13 mol% while in two other samples anatase phase was obtained. Based on XRD measurements, nano-particles size increased as Mn was doped in the TiO_2 lattice. Moreover, the deposition time in Mn-doped samples was 35 min which emphasized the catalyst's composition, thickness, and photocatalytic activity. As well, the Mn presence in TiO_2 crystalline lattice might assist as the recombination center of electrons and holes (e^-/h^+).

To compare the preparation techniques of TiO_2 and doped- TiO_2 on photocatalytic activity, the different sol-gel synthesized photocatalysts were also prepared and applied in the CPC solar pilot on cefixime removal in the same conditions. The TiO_2 , $\text{V}_x\text{Ti}_{1-x}\text{O}_2$ ($x = 2, 3, 5, 10$, and 20 mol%), and $\text{Zr}_x\text{Ti}_{1-x}\text{O}_2$ ($x = 5$ mol%) were coated on the glass beads by a micro-mixing reactor. Results presented that TiO_2 and VTiO_2 (3 mol%) had better cefixime degradation efficiency in comparison with other sol-gel prepared catalysts. But, plasma-deposited TiO_2 samples showed higher photocatalytic activity than our sol-gel prepared samples. In the other words, the plasma-deposited sample increased the photocatalytic activity by about 40% and its rate constant was 1.3 times higher than the sol-gel sample. It can be explained by the film's thickness and TiO_2 composition, because plasma deposited TiO_2 film has polymorph (anatase/rutile) crystal structure and higher film thickness with good adherence.

Finally, the regeneration of deactivated photocatalysts was investigated. Hot water washing, heat treatment, and washing in alkaline solution methods were used to remove adsorbed degradation by-products or cefixime molecules from the surface of films coated on glass beads. Solar photocatalysis tests with regenerated catalysts showed hot water technique can effectively recover the active sites without detachment of the particles. The heat treatment regeneration method partially recovered the active sites, which might be for the agglomeration or calcination of particles. The alkaline solution regeneration efficiency also was lower than the hot water technique. Results of various experiments indicated hot water regeneration technique is simple, economic, and effective for recovering poisoned active sites of TiO_2 photocatalysts without destroying and leaching nano-particles.

Notations

TiO ₂	Titanium dioxide
UV	Ultraviolet
CPC	Compound Parabolic Concentrator
CR	Concentration factor
θ_c	Acceptance angle
A	Surface (m ²)
mm	Millimeter
cm ²	Square centimeter
W/m ²	Watt per square meter
L	Liter
mg	Milligram
°C	Centigrade degree
m ²	Square meter
λ	Wavelength (nm)
nm	Nano meter
mL	Milliliter
g	Gram
mg/L	Milligram per liter
min	Minute
UV/vis	Ultraviolet visible
I_0	Incident intensity (W/m ²)
I	Intensity (W/m ²)
L	length (m)
A	Absorbance (unitless)
T	Transmittance
E	Molar extinction coefficient (L/mol.cm)
C	Concentration (mol/L)
g/mol	Gram per mole
M _w	Molecular weight
LC-MS	Liquid Chromatography-Mass Spectrometry
bar	bar (unit of pressure)
torr	Torr (unit of pressure)
m/z	Mass-to-charge
kV	Kilo volt
L/h	Liter per hour
μL	Micro liter
mL/min	Milliliter per minute
kJ/L	Kilo joule per liter
t _n	Time (s)
V _t	Total volume (L)

A_r	Collector surface area (m^2)
$Q_{UV,n}$	Accumulated energy (kJ/L)
$UV_{G,n}$	UV radiation (W/m^2)
K	Rate constant (L/kJ)
XRD	X-ray Diffraction
O_2	Oxygen
Ar	Argon
e^-	Electron (negative charge)
h^+	Hole (positive charge)
eV	Electron volt
Γ_o	Oxygen flux
Γ_+	Positive flux
mTorr	Milli torr (unit of pressure)
R^2	Correlation coefficient
L/kJ	Liter per kilo joule
kWh	Kilo watt hour
kJ	Kilo joule
W	watt
I_o	Intensity (Einstein/h)
P_{out}	Power (W)
J	Joule
kJ/hL	Kilo joule per hour liter
TTIP	Titanium tetraisopropoxide
C_{Ti}	Titanium concentration (mol/L)
r	Reaction rate
K	Rate constant
$Mn_xTi_{1-x}O_2$	Manganese doped titanium dioxide
Mn	Manganese
$ZrTiO_2$	Zirconium doped titanium dioxide
$VTiO_2$	Vanadium doped titanium dioxide
MB	Methylene blue
AMX	Amoxicillin
Deg	Degradation
T	Temperature ($^{\circ}C$ or K)
R_t	Retention time (s)
XPS	X-ray Photoelectron Spectroscopy

Part 5. Multiphysics modeling by COMSOL

Chapter 1. Introduction

The solar photocatalytic process is considered a growing method to solve environmental effects related to water pollution. One of the main issues in photocatalytic reactors is the photoreactor engineering scale-up. The behavior of light inside the solution in contact with the photocatalyst still remains a complicated subject. It is necessary to consider that the photocatalytic performance relates to the light irradiation and distribution inside the reactor volume. A full-scale application would require the development of a model that can use solar UV photons to increase the degradation kinetic for the practical process. In addition, it is necessary to use simple geometry.

Modeling is an effective tool to understand the reaction between the physical and chemical reactions to determine the key parameters in the process. The mathematical modeling investigates the impacts of the parameter on its performance. It aids to design the future reactor and scale-up. A useful model can describe and predict the process under various conditions that are close to the real situation.

Several experimental and modeling studies have been investigated to analyze photocatalytic performance in various types of photo-reactors (246, 247).

Avila-Lopez et al. (248) studied experimentally and numerically photocatalytic degradation of CO_2 with a different configuration of CuO-based photocatalyst. They found the CuO coating on the glass fiber mesh exhibited the highest production of CH_4 . A mathematical model was built using COMSOL on hydrodynamics and mass transfer modules. Combining the experimental and simulated results indicated that the numerical model fitted well.

In another study, Malayeri et al. (249) reported the study on kinetic modeling of methyl ethyl ketone photodegradation using TiO_2 coated on silica fiber felts. They studied six kinetic rate equations in two mathematical models, ideal plug flow and axially dispersed plug flow. The light intensity distribution on the photocatalyst surface was simulated using COMSOL Multiphysics method and validated with the experimental data. The experiments were carried out in a bench-scale continuous flow reactor at different initial concentrations of pollutant (0.1–1 ppm), relative humidities (17–67%), flow rates (10–30 L/min), and light intensities (7–23.5 W/m^2). The results of the kinetic study indicated that the dispersion mode combined with the unimolecular Langmuir-Hinshelwood model can be chosen as the best-fitting model. Evaluation of mass transfer concluded that the mass transfer effect on the photocatalytic oxidation process was not dominating step; consequently, the photocatalytic reaction was the rate-limiting process.

Zhao et al. (250) investigated experimentally modeling of LED radiation on the light distribution inside the fixed bed TiO_2 nanotubes on mesh layers (see figure 1). They concluded the data numerically calculated was applicable and that the attenuation I_a of light distribution in the water body was related to several factors like incident illuminated area, the total

incident intensity, the space between photocatalysts layers, and the size of the reactor system.

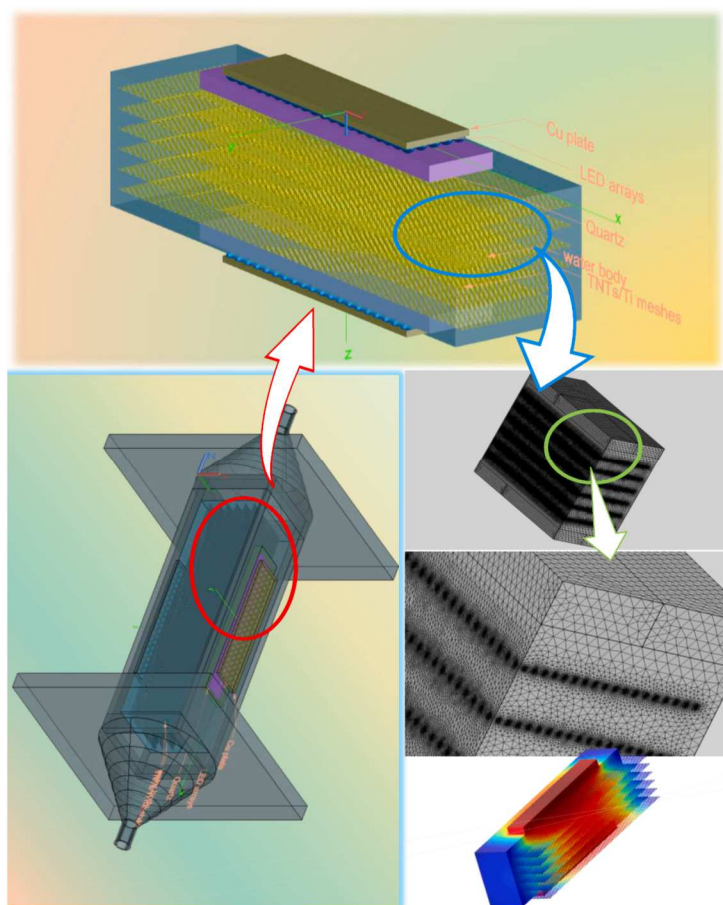


Figure 99. Schematic and geometry of photocatalytic reactor with fixed TiO_2 beds on mesh layers (250).

Several studies discussed the production of photocatalytic TiO_2 films and their use in pollutant removal under various irradiations in microstructure reactors (251-253). They focused on mathematical simulation of process optimization parameters like radiation and light distribution phenomena inside the fixed bed reactor (250, 254), kinetic modeling of photocatalytic degradation in the plug flow model (249), and mass transfer role in photocatalytic oxidation (247).

Previously published papers concluded that mathematical modeling was a useful technique in simulating photocatalytic reactors. Photoreactor configuration, experimental conditions, catalyst preparation method and mode (slurry or fixed bed), radiation type, and intensity were the main issues in COMSOL modeling (253, 255-257).

Chapter 2. Multiphysics modeling

The modeling of the CPC photoreactor for contaminated water treatment has been performed using COMSOL Multiphysics version 6.1. This software utilizes the finite element method to obtain the numerical solution of model equations.

2.1. Geometry of the solar photoreactor

The figure 100 shows the corresponding schematic illustration of a CPC-based photocatalytic reactor for pollutant removal degradation installed at the University of Isfahan, Iran. The CPC collector was fabricated with a 50 cm-long horizontal Pyrex tube. The highly polished semi-involute aluminum reflector is located at the bottom of the reactor tube. The solar pilot is static and faces the sun at an angle that maximizes the absorption of solar light both direct and diffuse irradiation that reflects on the water flow inside the tube. The inlet and outlet of the solar photo-reactor are connected to a recirculation tank where the cefixime solution was stored inside. The cefixime water solution was used for kinetic studies in a solar pilot with accumulated solar radiation that was monitored with a UV light meter (290-390 nm). The average solar and UV light intensity on the collector aperture are 900 and 40 W/m² on a typical summer day, respectively. The model was designed as a batch mode operation where the outlet stream was recirculated back into the inlet.

The photoreactor dimensions are also shown in figure 100. The diameter of the solution inlet and outlet is 10 mm and they were located below and above the tube's center, respectively. The synthetic antibiotic solution (2 L) enters the reactor at a constant flow rate of 20 ml/s. The number of coated glass beads with photocatalytic films was about 1100 and each glass sphere has a 4 mm diameter.

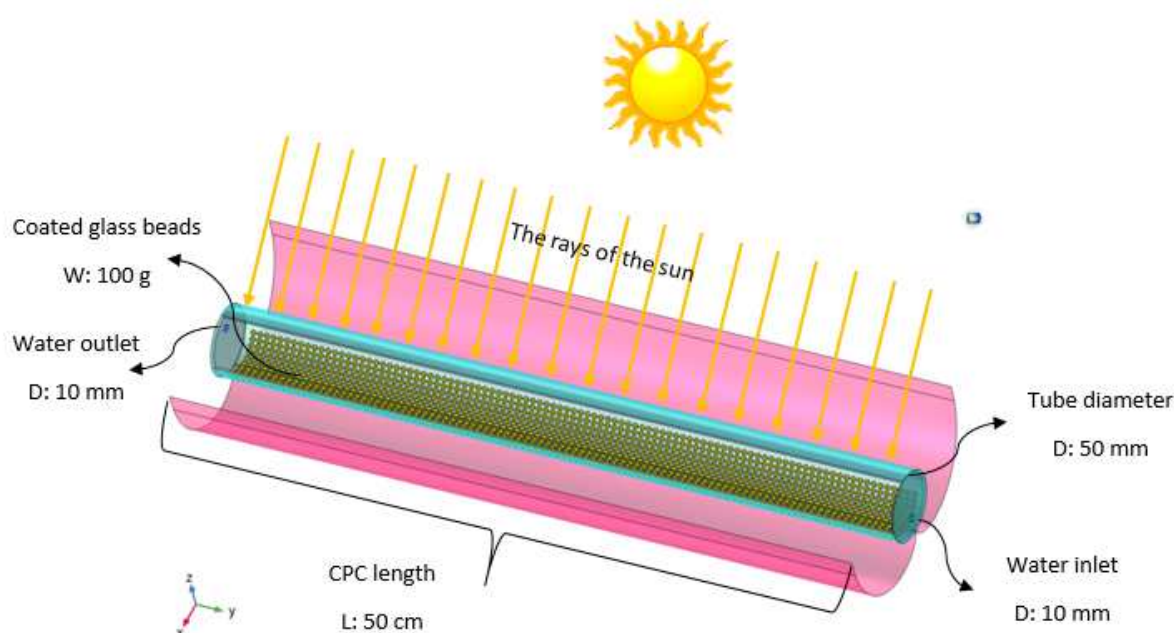


Figure 100. Dimensions of the CPC photoreactor contained coated glass beads.

2.2. Optical modeling

The Geometrical Optics interface solves for the position and wave vector of individual rays. It also allows them to interact with boundaries that intersect their paths. For optic simulations, ray tracing is a useful tool in COMSOL software. The “Ray Optics Module” for tracing solar rays and optical analysis was used. The Ray Optics Module is a computational tool for modeling the propagation of light and other electromagnetic radiation with a ray tracing approach. The rays can propagate through the model geometry while being reflected, refracted, or absorbed at boundaries.

In optical physics, default nodes are **Medium Properties**, **Material Discontinuity**, and **Ray Properties**. Other nodes, for example, light sources or boundary conditions, add from the Physics toolbar.

The **Medium Properties** node to specify the refractive index of the medium including all of the selected domains for the physics interface. For the region outside the geometry and for any domains not included in the physics interface selection, the refractive index is instead controlled by the Optical dispersion model in the physics interface Material Properties of Exterior and Unmeshed Domains section. A dispersion model for the refractive index of air can be used in exterior and unmeshed domains. The Edlen (258) air model gives the refractive index of air as a function of wavelength, temperature, and pressure that presents in the equation 36:

$$n_{\text{air}}(\lambda_0, T, P) = \frac{n_{\text{air,STP}}(\lambda_0) - 1}{1 + 3.4785 \times 10^{-3}(T - T_{\text{std}})} \frac{P}{P_{\text{std}}} \quad 36$$

where T is the temperature (K) and P is the pressure (Pa). The refractive index of air at T= 15 °C and P_{std} = 101.325 kPa, is given by equation 37:

$$n_{\text{air,STP}}(\lambda_0) = 1 + 10^{-8} \times \left(6,432.8 + \frac{2,949,810(\lambda_0^2)}{146\lambda_0^2 - 1} + \frac{25,540\lambda_0^2}{41\lambda_0^2 - 1} \right) \quad 37$$

The **Material Discontinuity** node is the default feature on all boundaries. The Geometrical Optics interface always applies reflection and refraction at boundaries between different media using a deterministic ray splitting approach. The direction of the refracted ray is computed using Snell’s law, based on the refractive index on either side. Snell’s law describes the relationship between the angles of incidence and refraction, when light passes from one medium to another. It states that the ratio of the sine of the angle of incidence to the sine of the angle of refraction is equal to the ratio of the velocity of light in the first medium to the velocity of light in the second medium.

First the angle of incident θ_i is computed by the following equation (eq. 38):

$$\theta_i = \arccos\left(\frac{n_i \cdot n_s}{|n_i||n_s|}\right) \quad 38$$

where n_i is a unit vector in the direction of the incident ray and n_s is a unit vector normal to the material discontinuity.

At a boundary between two isotropic, nonabsorbing media with the normal direction of n_1 and n_2 , the refracted ray propagates in the direction n_t given by the following relations (eq. 39-42):

$$n_t = \eta n_i + \gamma n_s \quad 39$$

$$\eta = \frac{n_1}{n_2} \quad 40$$

$$\gamma = -\eta \cos \theta_i + \cos \theta_t \quad 41$$

$$\theta_t = \text{asin}(\eta \sin \theta_i) \quad 42$$

where the ray propagates from the medium with refractive index n_1 into the medium with refractive index n_2 . Because the two media are nonabsorbing, the quantities n_1 , n_2 , θ_i , and θ_t are real-valued. If the media are weakly absorbing, the real parts of n_1 and n_2 , are used. If the media are strongly absorbing, several corrections to Snell's law and the Fresnel equations must be made (259).

The reflected ray is also released at the material discontinuity with the initial direction of n_r (eq. 43):

$$n_r = n_i - 2 \cos \theta_i n_s \quad 43$$

If the ray intensity or power is solved for in the model, the **Material Discontinuity** feature computes the new values of these variables for the reflected and refracted rays. This reinitialization uses the Fresnel Equations while accounting for the incident ray polarization.

Fresnel equations (eq. 44-47) are used to find the ray directions and its incident angles inside the system (260, 261).

$$r_p = \frac{n_2 \cos \theta_i - n_1 \cos \theta_t}{n_2 \cos \theta_i + n_1 \cos \theta_t} \quad 44$$

$$r_s = \frac{n_1 \cos \theta_i - n_2 \cos \theta_t}{n_1 \cos \theta_i + n_2 \cos \theta_t} \quad 45$$

$$t_p = \frac{2n_1 \cos \theta_i}{n_2 \cos \theta_i + n_1 \cos \theta_t} \quad 46$$

$$t_s = \frac{2n_1 \cos \theta_i}{n_1 \cos \theta_i + n_2 \cos \theta_t} \quad 47$$

r is the reflection coefficient, t is the transmission coefficient, s subscripts the s-polarized ray, and p denotes the p-polarized ray (259, 262). The incident ray is assumed to move from a region of refractive index n_1 toward a region of refractive index n_2 . The angles θ_i and θ_t are the angle of incidence and angle of refraction, respectively.

The intensities of the transmitted (I_t) and reflected (I_r) rays are related to the intensity of the incident ray (I_i) by the following equations (eq. 48-51) for p-polarized rays (259, 260, 262):

$$I_r = I_i |r_p|^2 \quad 48$$

$$I_t = \frac{n_2 \cos \theta_t}{n_1 \cos \theta_i} I_i |t_p|^2 \quad 49$$

and for s-polarized rays:

$$I_r = I_i |r_s|^2 \quad 50$$

$$I_t = \frac{n_2 \cos \theta_t}{n_1 \cos \theta_i} I_i |t_s|^2 \quad 51$$

The **Ray Properties** node defines the equations for ray propagation and may also include inputs for some ray properties.

In geometrical optics light source and surface boundary conditions were applied. Three main parts of the system as surface boundary condition are illustrated in figure 101. When the sun's rays are received on the surface of the pilot, a portion is absorbed by the CPC, and most parts of them are reflected inside the absorber pipe. It also concentrates rays on the heating walls of the absorber pipe. Then reflected rays are incident on the outer surface of the Pyrex tube, and absorption and refraction of rays occur in it. The Pyrex pipe transmits solar irradiation to the water solution. The third part of the optical components is the coated glass beads as reactive surface that has an essential role in absorbing solar rays. For maximum optical efficiency, the absorber should have a high solar transmissivity, the collectors should have high solar reflectivity.

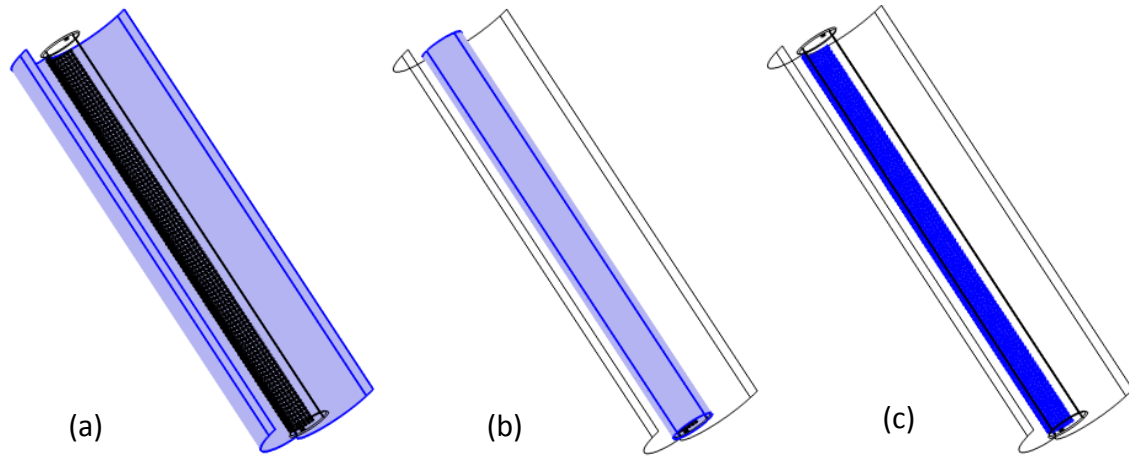


Figure 101. Three main optical parts in the system, (a) CPC, (b) Pyrex tube, and (c) reactive surfaces.

The Pyrex wall is considered a transparent wall that the solar rays pass through it with a probability of 0.9 and a little mixed diffuse scattering and absorption occurs from its surface. This option allows rays to cross the boundary unimpeded. It does not change the ray direction at a boundary between different media.

The CPC is considered a reflection surface that specularly reflects rays from its surface. The last one is reactive surfaces which are considered as diffuse scattering with reflections rays at a wall according to Lambert's cosine law.

The solar radiation data used was measured for a typical summer day in Isfahan, Iran at a latitude of 32.65 °N and a longitude of 56.6 °E. The solar rays were simulated with Release from Grid node based on space dimension for 3D components and measured solar irradiation. Figure 102 shows the coordinate preview of radiation rays on the CPC photo-reactor in -z direction which was similar to real situation. The initial of radiation was inserted based on the real values of solar radiation which we measured during the experiment.

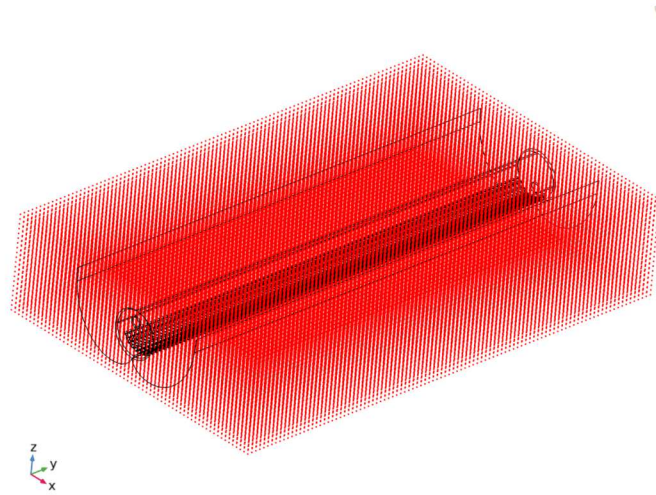


Figure 102. The coordinate preview of the simulated solar radiation with Release from Grids node.

The Geometrical Optics interface always solves for the ray position q (m) and wave vector k (rad/m). Generally, the ray tracing based on a non-sequential ray tracing with a deterministic ray splitting algorithm at boundaries. In other words, rays can interact with any surfaces in the model geometry that they hit, without the order of ray-boundary interactions having to be specified a priori. At boundaries between different media, each incident ray can be split into a reflected ray and a refracted ray.

In this type of ray-tracing methodology approach, the instantaneous ray position and wave vectors, q and k , respectively, can be computed by solving a set of coupled first-order equations. These equations (eq. 52-53) are given by the following expressions (263):

$$\frac{dq}{dt} = \frac{\partial \omega}{\partial k} \quad 52$$

$$\frac{dk}{dt} = -\frac{\partial \omega}{\partial q} \quad 53$$

where q is the ray position, k is the wave vector, and ω is the angular frequency. Angular frequency and wave vector are related by the expression 54 (263):

$$\omega = \frac{c|k|}{n(q)} \quad 54$$

where c is the speed of light, and $n(q)$ is the refractive index of the medium. The refractive index, real part, n (dimensionless) may be expressed as a function of wavelength using an

optical dispersion model. In addition to the ray trajectories within the system, the power conveyed by rays and incidents on the surfaces are calculated.

The total solar energy power at any time is solved by the equation 55:

$$P(t) = I(t) \times A_c \quad 55$$

where I is the global irradiation intensity at time t (W/m^2) and A_c is the aperture area of the collector (m^2).

2.2.1. Results of optical modeling

At the given geometry, the geometrical optics module was used to predict the irradiance distribution inside the reactor for the photocatalytic experiments.

The ray's trajectory, departing from the solar simulated on the surface of the CPC photoreactor is illustrated in figure 103. The figure shows that the reflected rays are homogenously distributed at each component of the reactor. In addition, all sides of the tube received solar rays with varied power and intensity.

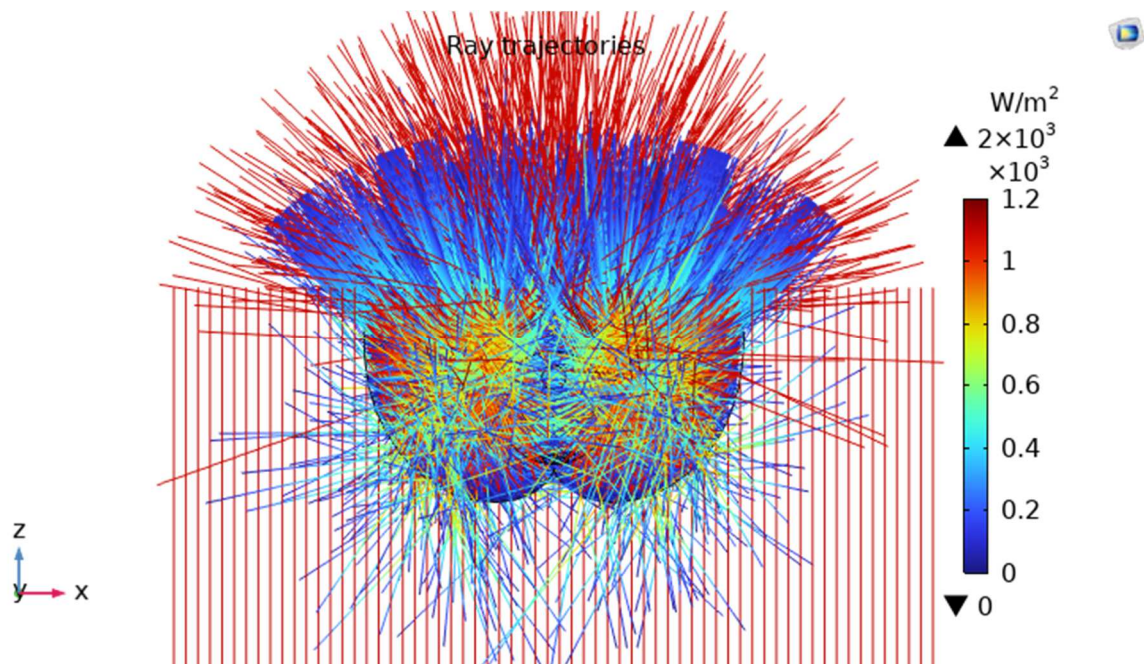


Figure 103. Schematic of ray trajectory on the CPC photoreactor.

The vertical red lines in z direction are the incident rays as solar rays received on the surface of solar pilot. The initial solar intensity was measured about $1.2 \text{ W}/\text{m}^2$ in the middle hour of a sunny day in summer that the radiation angle with the surface of collector was 90° . As the legend shows in the right side, the reflected rays intensity varied between zero to $2000 \text{ W}/\text{m}^2$ as the minimum and maximum intensity, respectively. The radiation field model provided valuable insights into irradiance distribution, which was difficult to measure with a conventional method like spectrometry.

The **Deposited Ray Power** sub-node was inserted to the surface boundaries which computes the total incident energy flux on a surface based on the power of incident rays. The total amount of heat absorbed by CPC, tube, and reactive surfaces is illustrated in figure 104.

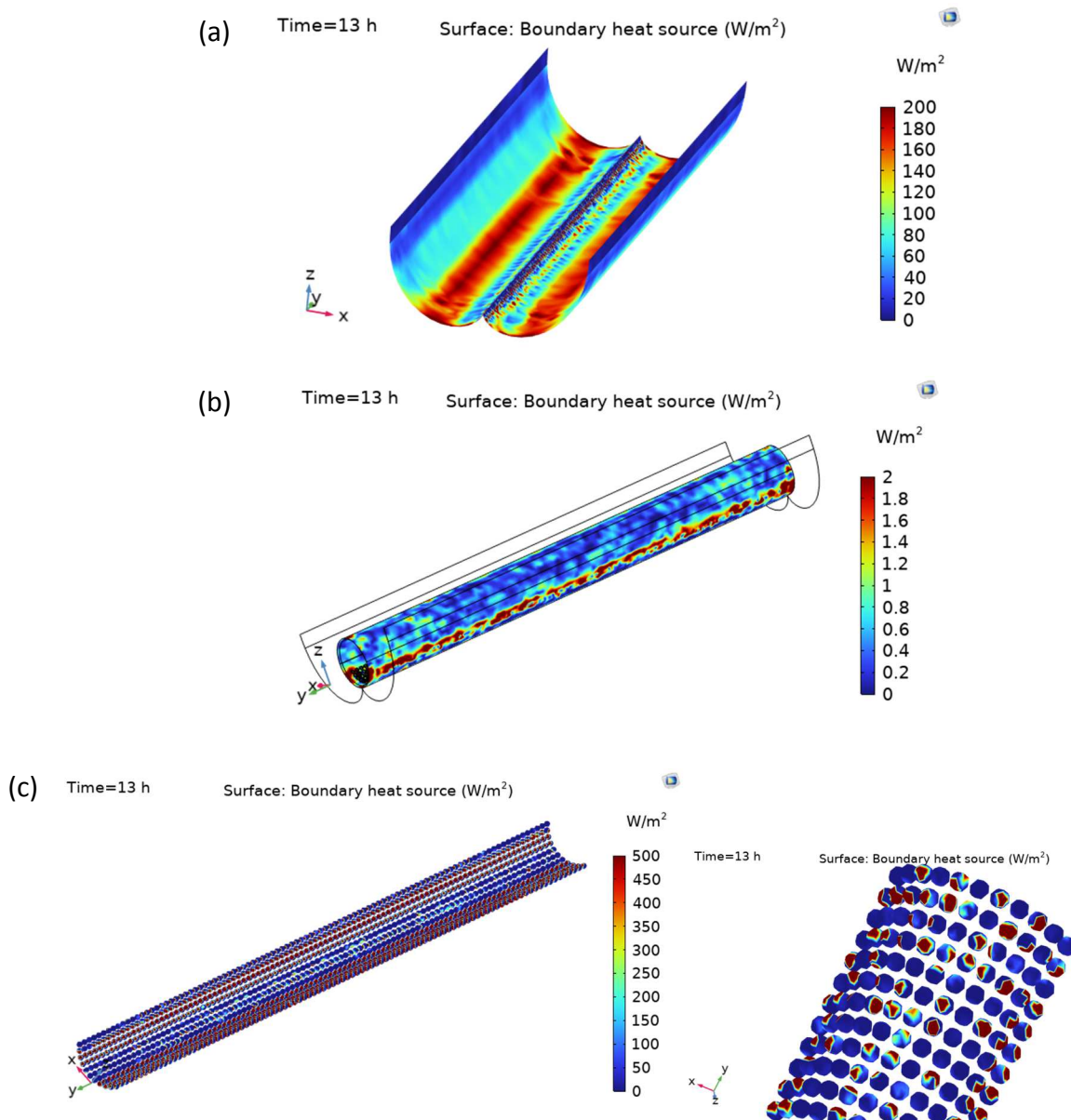


Figure 104. The distribution of solar flux on the surface of a) CPC, b) exterior wall of Pyrex tube, and c) coated glass beads with TiO₂ photocatalyst.

The solar flux distribution on the surface of the collector was different due to its configuration. The higher heat flux belonged to the compound section which received more reflection of the rays. The reflected solar heat flux distribution is more intense at the bottom of the tube than in other areas. The catalytic surfaces received non-uniform irradiance for all coatings.

2.3. Thermal modeling

Based on the physics involved in the CPC pilot, the Heat Transfer in Solids and Fluids module was selected. The governing heat transfer equations for coupled conduction in the solid domains and convection in the fluid domain are derived as follows (eq. 56-61) (264, 265):

$$\text{Heat transfer in solids: } \rho C_p \frac{\partial T}{\partial t} + \rho C_p u \cdot \nabla T + \nabla \cdot q = Q + Q_{ted} \quad 56$$

$$q = -k \nabla T \quad 57$$

$$Q_{ted} = -\alpha T : \frac{dS}{dt} \quad 58$$

ρ (kg/m³) is the solid density, C_p (J/(kg.K)) is the solid heat capacity at constant pressure, u (m/s) is the velocity field, q (W/m²) is the heat flux by conduction, k (W/(m.K)) is the solid thermal conductivity (a scalar or a tensor if the thermal conductivity is anisotropic), Q (W/m³) is the heat source, and Q_{ted} is the thermoelastic damping and accounts for thermoelastic effects in solids. The thermal conductivity k describes the relationship between the heat flux vector q and the temperature gradient ∇T in $q = -k \nabla T$, which is Fourier's law of heat conduction. In third equation, α (1/K) is the coefficient of thermal expansion, T (K) is the absolute temperature, S is the second Piola-Kirchhoff stress tensor (Pa).

$$\text{Heat transfer in fluid: } \rho C_p u \cdot \nabla T + \nabla \cdot q = Q + Q_p + Q_{vd} \quad 59$$

$$Q_p = \alpha_p T \left(\frac{\partial p}{\partial t} + u \cdot \nabla p \right) \quad 60$$

$$Q_{vd} = \tau : \nabla u \quad 61$$

ρ (kg/m³) is the density, C_p (J/(kg.K)) is the fluid heat capacity at constant pressure, u (m/s) is the fluid velocity field, q (W/m²) is the heat flux by conduction, k (W/(m.K)) is the fluid thermal conductivity (a scalar or a tensor if the thermal conductivity is anisotropic), and Q (W/m³) is the heat source. The Q_p is the work done by pressure changes and is the result of heating under adiabatic compression as well as some thermoacoustic effects, α_p is the coefficient of thermal expansion (1/K), T (K) is the absolute temperature, u (m/s) is the velocity field, and P (Pa) is the pressure. Q_{vd} represents viscous dissipation in the fluid, τ (Pa) is the viscous stress tensor.

For thermal modeling, the appropriate boundary conditions need to identify. The inlet temperature was used for water and at the outlet of the reactor pipe (eq. 62), the outflow boundary condition is used. That is a suitable boundary condition for convection-dominated heat transfer at outlet boundaries (eq. 63).

$$T = T_0 \quad 62$$

$$-n \cdot q = q_0 = 0 \quad 63$$

n is the normal vector on the boundary, q (W/m^2) is the convective heat flux vector. The special case $q_0 = 0$ is called thermal insulation. This boundary condition means that there is no heat flux across the boundary and the temperature gradient across the boundary is zero.

The heating wall of the reactor pipe was considered as heat flux on surface boundary condition which came from optical modeling. The heat flux on the external wall of the pipe was estimated from the equations 64-65:

$$-n \cdot q = q_0 \quad 64$$

$$q_0 = h(T_{\text{ext}} - T) \quad 65$$

h $W/(m^2.K)$ is the heat transfer coefficient ($h = 5$ for air) and T_{ext} is the ambient temperature. In this model, only convection heat transfer occurs across the tube wall boundaries to the air. Regarding the boundary conditions for thermal modeling, the inlet temperature was also used for the air stream. And last boundary condition was derived as equation 66:

$$-n \cdot q = Q_b \quad 66$$

Q_b is the boundary heat source that calculates from the Ray Optic module.

The velocity of water inside the absorber for thermal modeling was obtained from the fluid flow modeling that will present in the next section. In addition, the heat flux on the heating wall of the reactor pipe was obtained by the Ray Optics module. Actually, they were coupled to thermal modeling.

2.3.1. Multiphysics coupling of optical and thermal modeling

COMSOL Multiphysics offers physics interfaces for coupling computations. These interfaces have model inputs that make it possible to couple the physics.

In the optical thermal modeling of the CPC photoreactor, the **Ray Heat Source Multiphysics** was used to compute the heat source resulting from the attenuation rays. The equation 67 is used to calculate the ray heat source.

$$\frac{\partial Q_{\text{src}}}{\partial t} = - \sum_{j=1}^{N_t} \frac{\partial Q}{\partial t} \delta(\mathbf{r} - \mathbf{q}_j) \quad 67$$

δ is the Dirac delta function.

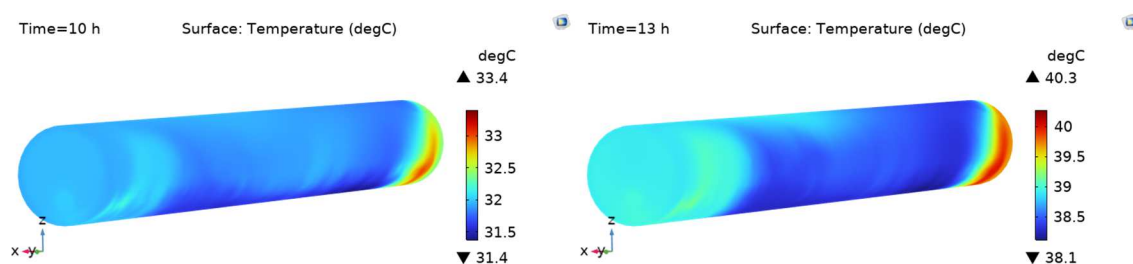
The optimal, thermal, and operational parameters used in Multiphysics modeling are presented in table 22.

Table 22. Optical and thermal parameters values and ranges in the experimental setup

Parameter	Symbol	Value
Total solar irradiation intensity	I	200-1100 W/m ²
Solar UV irradiation intensity	I_{UV}	5-50 W/m ²
Maximum number of secondary rays	-	500
Reflectance of aluminum reflector	r	0.85
Transmittance of Pyrex tube	γ	0.9
Absorptance of Pyrex tube	α	0.02
Refraction index of Pyrex tube	n	1.47
Refraction index of water	n	1.3
Initial temperature of water	T_0	25 °C

2.3.2. Results of thermal modeling

The temperature variation in the 3D domain of feed in four times of the experiment is illustrated in figure 105. As figures show, the water temperature was increased by about 2 °C from the inlet to the outlet of the photoreactor. The temperature enhancement was related to the ray heat source which coupled geometrical optic and heat transfer modules.



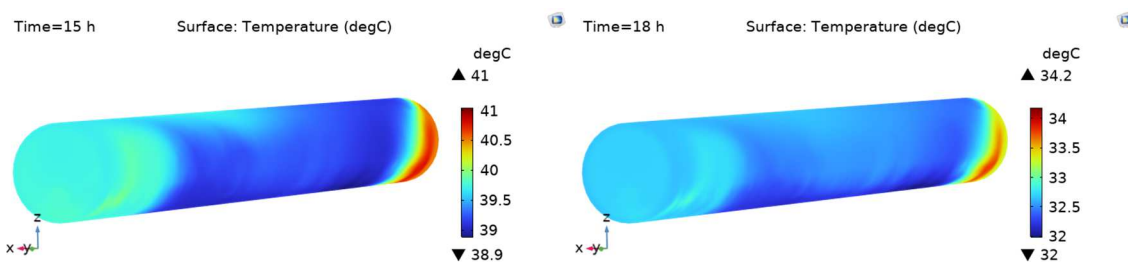


Figure 105. The temperature profiles of the feed at various times during an experiment.

The variations in water temperature at the outlet of the water from 9:00 to 19:00 are shown in figure 106. As the solar irradiation increases the temperature of the outlet water increases gradually. After 14:00 the temperature of the outlet water decreases until sunset due to less solar irradiation. Therefore, changes in the water temperature along with photocatalytic degradation relate to the amount of solar energy that is absorbed by the water or reflected by the collector and then transferred to the water.

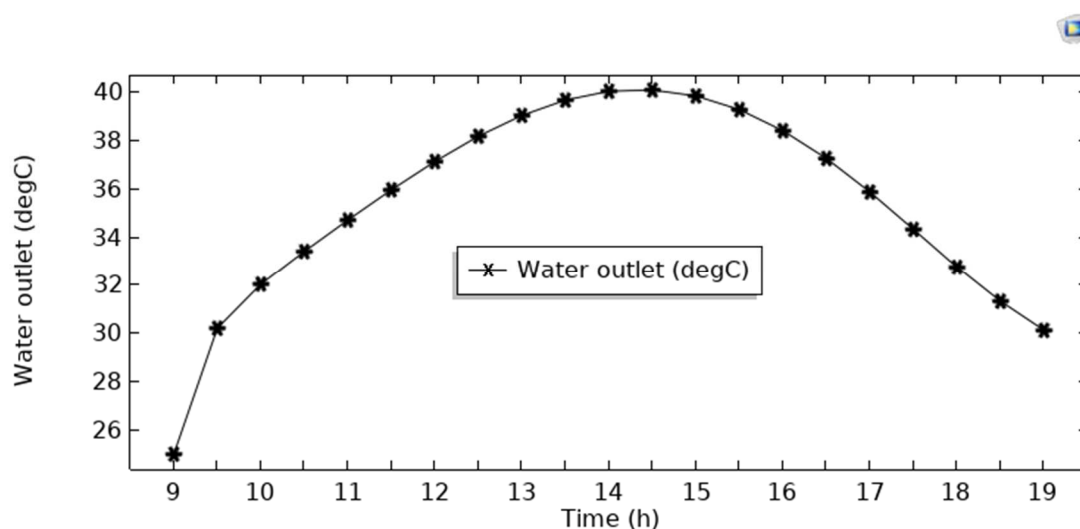


Figure 106. The variation of the average water temperature inside the CPC solar photoreactor during an experiment.

2.4. Fluid flow modeling

The solar photocatalysis reactions took place in a single-phase fluid in the laminar flow regime. The velocity and pressure profile in the reaction was modeled using the Navier-Stokes equation (266).

Several assumptions were employed in the fluid dynamics which are described as follows: 1; The flow is steady state, 2: The material properties like density and viscosity are constant during the whole process, 3: The mass flow rate of water is constant, 4; Due to the dilution of the antibiotic solution, water properties considered.

Momentum and continuity equations for water were accounted for by using the Navier-Stokes' equations for Newtonian-incompressible flow. The equations are as follows (eq. 68-70) (266, 267):

$$\rho(u \cdot \nabla)u = \nabla \cdot [-pI + K] + F + \rho g \quad 68$$

$$K = \mu(\nabla u + (\nabla u)^T) \quad 69$$

$$\rho \nabla \cdot u = 0 \quad 70$$

ρ (kg/m³) is the density, u (m/s) is the velocity vector, p (Pa) is pressure, I (unitless) is the identity matrix, K (Pa) is the viscous stress tensor, F (N/m³) is the volume force vector, g (m/s²) is the gravity, μ (kg/m.s) is the kinematic viscosity, and T is the transpose operator.

For a Newtonian fluid, there is a linear relationship between stress and strain rate. For incompressible flow, the fluid density is assumed to be constant and the density is evaluated at the reference pressure level and at the reference temperature. When gravity is considered, a volume force equal to ρg included in the momentum equation. Regarding the boundary condition for fluid flow modeling, the laminar water inlet flow is considered constant and the outlet of the reactor was set at atmospheric pressure. The initial temperature of the system is the same as the ambient temperature at the start of the simulation. And no-slip boundary conditions on the stationary wall were considered. A no-slip wall is a wall where the fluid velocity relative to the wall velocity is zero. For a stationary wall that means that $u = 0$. These equations were solved first at a steady state before coupling to other modules.

2.4.1. Multiphysics coupling of fluid flow and thermal modeling

The **Nonisothermal Flow Multiphysics** coupling node facilitates the coupling between heat transfer and fluid flow interfaces. The Nonisothermal flow module in COMSOL was applied to simulate fluid flow where the fluid properties depend on temperature. The first expression represents viscous dissipation in the fluid and F is the body force vector (N/m³) (see eq. 71-73):

$$Q_{vd} = \tau : \nabla u \quad 71$$

$$F_g = \rho_{ref}(1 - \alpha_{p,ref})(T - T_{ref})g \quad 72$$

$$\alpha_p = -\frac{1}{\rho} \left(\frac{\partial \rho}{\partial T} \right) \quad 73$$

τ is the viscous stress tensor (Pa), u is the velocity vector (m/s), α_p is the coefficient of thermal expansion (1/K), ρ is the density (kg/m³), and T is the absolute temperature (K).

2.4.2. Results of fluid flow modeling

A full 3D model of the reactor was first solved for a stationary laminar flow in absence of any reaction. The slice velocity field along the reactor axis is shown in figure 107. The flow velocity field is non-uniform in the photocatalytic reactor for an inlet flow rate of 20 ml/s. The velocity

of the solution is calculated by the volumetric flux passing from the pump into the reactor tube and the cross section of the pipe inlet. When the solution was pumped inside the tube the velocity dropped because of the cross-section difference between the inlet and tube.

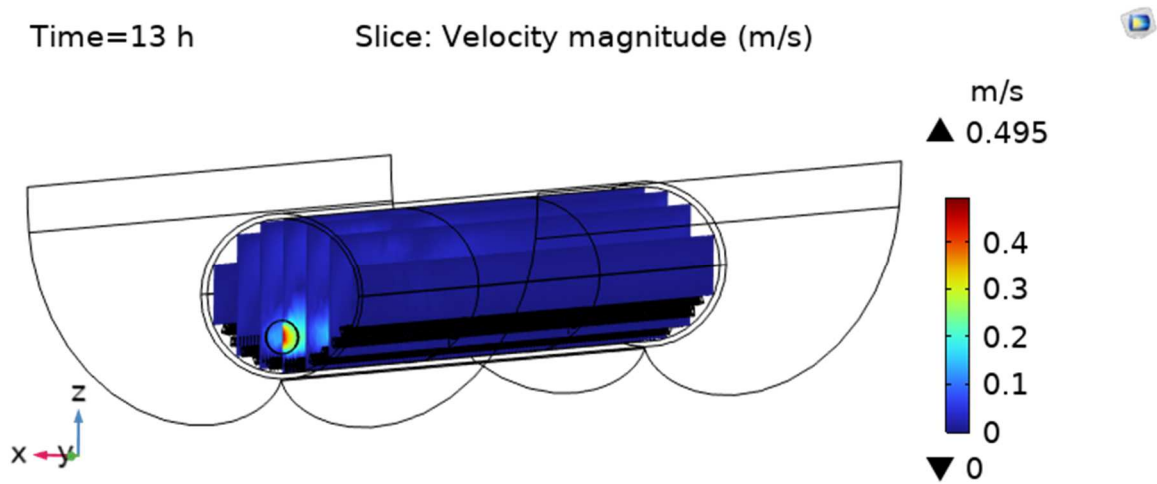


Figure 107. The slice velocity distribution in 3D domain of feed.

Figure 108 displays the velocity contours in the reactor at the flow rate of 20 ml/s. The highest velocity occurred at the second counterplot as shown in the figure (maximum velocity of 0.07 m/s). The average velocity in the reactor was estimated to be about 1.9 , 0.28 , 5.5 , and 3.3×10^{-4} m/s corresponding to the inlet, the first plane, the second plane, and outlet boundaries of 3D geometry, respectively.

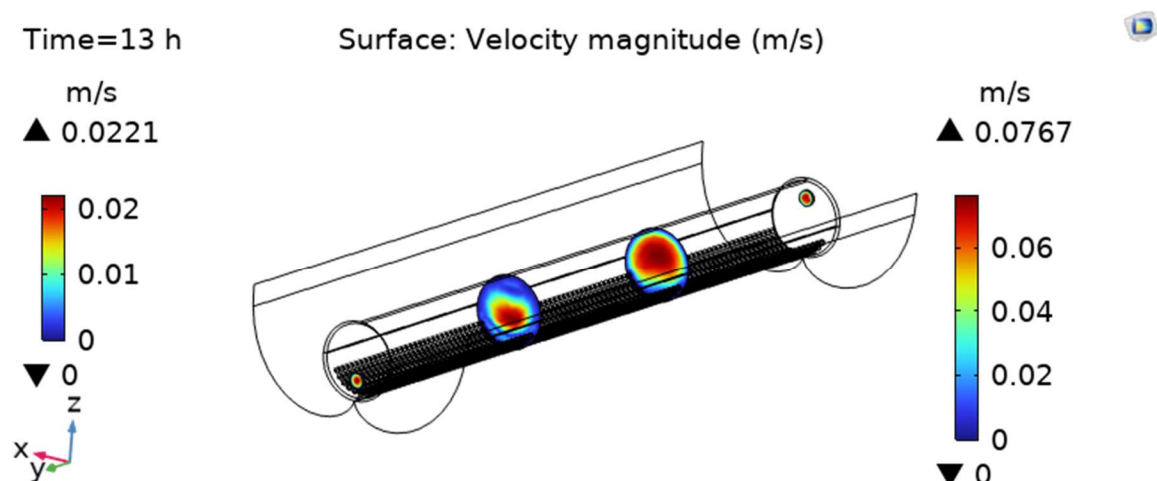


Figure 108. Velocity profile variations at the first plane (left legend column) and the second plane (right legend column) in the solar pilot with an initial flow rate of 20 ml/s.

The velocity values in the tube never exceed 0.07 m/s corresponding to a Reynolds number of 105. As shown in figure 109, the Reynolds number was varied due to the velocity difference that emphasized the laminar nature of the flow regime. The difference in the velocity and Reynolds number related to the inlet and outlet position in solar setup, the water solution was inserted from the bottom of the tube center and confronted with glass beads, then departed from the top of the tube center.

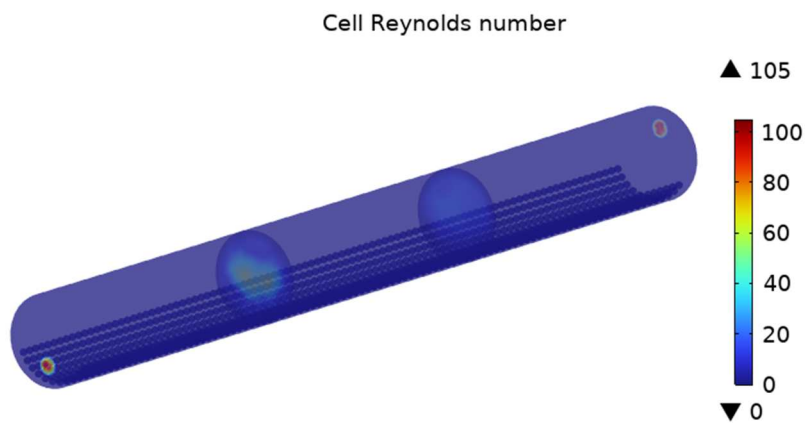


Figure 109. The contour plots of Reynolds number distribution along the tube at a flow rate of 20 ml/s in inlet.

2.5. Transport modeling

The Transport of Diluted Species Module was used for diffusion-convection mass transfer. The physics interface assumes that all species present are dilute; that is, that their concentration is low compared to a solvent fluid. Due to the dilution, mixture properties such as density and viscosity can be assumed to correspond to those of the solvent. Fick's law governs the diffusion of the solutes, dilute mixtures, or solutions. The default expression attributed to the Transport of Diluted Species interface models chemical species transport through diffusion and convection and solves the mass conservation equation 74 for one or more chemical species i :

$$\frac{\partial C_i}{\partial t} + \nabla \cdot J_i + u \cdot \nabla C_i = R_i \quad 74$$

c_i is the concentration of the species (mol/m^3), R_i is a reaction rate expression for the species ($\text{mol}/(\text{m}^3 \cdot \text{s})$), u is the mass averaged velocity vector (m/s), J_i is the mass flux diffusive flux vector ($\text{mol}/(\text{m}^2 \cdot \text{s})$). The mass flux relative to the mass averaged velocity, J_i ($\text{mol}/(\text{m}^2 \cdot \text{s})$), is associated with the mass balance equation above and used in boundary conditions and flux computations. The Transport of Diluted Species interface always includes mass transport due to molecular diffusion. In this case the mass flux J_i defines the diffusive flux vector by equation 75:

$$J_i = -D_i \nabla C_i \quad 75$$

D_i denotes the diffusion coefficient (m^2/s). The third term on the left side of equation describes the convective transport due to a velocity field u . This field can be expressed analytically or obtained from coupling the physics interface to one that solves for fluid flow, such as Laminar Flow. Note that all fluid flow interfaces solve for the mass averaged velocity.

Some boundary conditions used to solve this equation include:

- 1- This boundary condition was used on exterior boundaries in which there was no mass flux, typically solid walls where no surface reactions occur. It was used also at outlets boundary where species should be transported out of the model domain by fluid motion (eq. 76-77).

$$n \cdot D_i \nabla C_i = 0 \quad 76$$

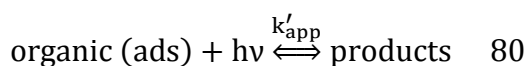
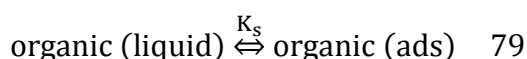
$$-n \cdot J_i = 0 \quad 77$$

- 2- One initial condition is needed to solve the bulk concentration profile. The initial value for the concentration of specie serves as an initial guess for a stationary solver or as initial conditions for a transient simulation (eq. 78).

$$C_i = C_{0,i} \quad 78$$

2.5.1. Kinetic study of photodegradation process

According to published papers (252, 257, 268), the kinetic study of photocatalytic oxidation of organic pollutant like salicylic acid, 4-chlorophenol, 4-nitrophenol in aqueous solution can be described by following reaction mechanisms (eq. 79-80):



so that a pseudo-steady state is set up. First equation is the reversible adsorption-desorption reaction rate and the second equation involves the oxidation of adsorbed organic pollutant by photogenerated surface hydroxyl radical under light irradiation. Corber et al. (252) explained the pseudo-steady state reaction occurs on the thin film of TiO_2 , this reaction strongly influenced by the transfer of reactant from the bulk toward the catalyst surface which coupled with mass transfer limitation. The reaction rate is also determined by the light intensity on the surface, the quantum efficiency of the catalyst, and the adsorption properties of the reacting components in solution (269). As it has been observed previously (86), in heterogenous catalytic surface reaction, the degradation rate of cefixime was first order and it is affected by the initial organic content. This kinetic can be commonly described in terms of a Langmuir-Hinshelwood to the chemical decomposition of cefixime at the catalytic surface which can be given by (252, 269):

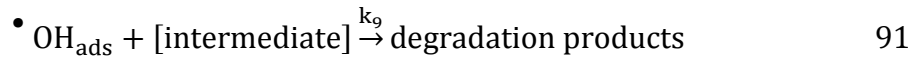
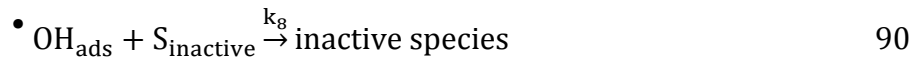
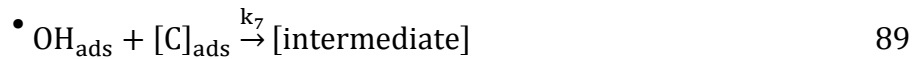
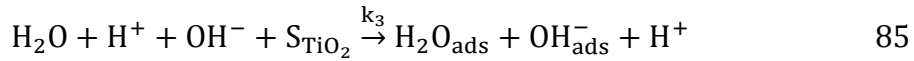
$$-r = -\frac{dC}{dt} = k_{app}C = \frac{k'_{app}K_S C}{1+K_S C_0} \quad 81$$

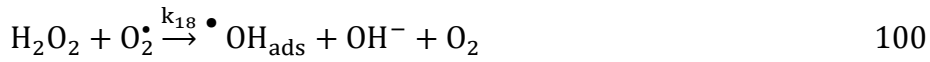
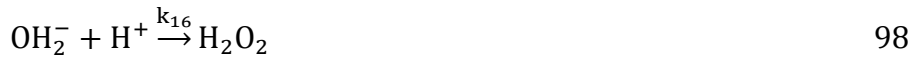
where k_{app} (1/s), k'_{app} (mol/m³.s) is the reaction rate constant, and K_S (m³/mol) is the adsorption rate constant, and C (mol/m³) is the organic concentration, and C_0 is the initial organic concentration. Therefore, the relationship between the apparent first-order rate constant and the initial content of the organic is given by equation:

$$\frac{1}{k_{app}} = \frac{1}{k'_{app}K_S} + \frac{C_0}{k'_{app}} \quad 82$$

The k'_{app} and K_S are light intensity-dependent constants, organic compound content, and absorption performance of the catalyst (269, 270).

The TiO₂ photocatalysis involves several elementary reactions which are expressed in following equations 83-101 (269):





The subscript “ads” and S_{TiO_2} refer to the adsorbed species and the surface of immobilized TiO_2 nanoparticles, respectively.

For photocatalytic kinetic modeling six assumptions are considered as follows:

- 1- Photocatalytic oxidation of organic and intermediates is mainly completed via the hydroxyl groups absorbed on the surface of the immobilized TiO_2 . This is the rate limiting step for the photocatalysis process.
- 2- The combination of $\text{H}_2\text{O}/\text{OH}^-$ with the photoinduced holes (h^+) to form hydroxyl groups and the $\bullet\text{OH}$ radicals should be mainly formed from the adsorbed H_2O molecules.
- 3- The combination rate of h^+/e^- is much more than the hydroxyl forming rate of the reaction between h^+ , H_2O , and OH^- .
- 4- The concentration of hydroxyl radicals is constant at a steady state (271).
- 5- The concentration of h^+ is constant at a steady state (271).
- 6- The hydroxyl radicals can be deactivated by de-trapping of the holes or via a reaction with surface electrons. The recombination of $\bullet\text{OH}$ radicals with surface electrons as the major pathway to explain the interdependence of the reaction rate with photon flow and the concentration of the target compound. And recombination may occur through both processes.

According to assumption (1), the photocatalytic degradation rate (r) for the decomposition of cefixime on the TiO_2 films is represented by equation 102:

$$r_0 = k_D[\bullet\text{OH}]_{\text{ads}}[\text{C}] \quad 102$$

where k_D represents the rate constants of degradation products and C is the concentration of the cefixime.

By applying assumption (5), the concentration of photoinduced holes (h^+) can be obtained by equation 103:

$$\frac{d[\text{h}^+]}{dt} = k_1\text{I} + k_{10}[\text{OH}^-]_{\text{ads}}[\text{h}^+] - k_2[\text{h}^+]^2 - k_4[\text{H}_2\text{O}][\text{h}^+] - k_5[\text{h}^+][\text{OH}^-]_{\text{ads}} \quad 103$$

According to assumption (3):

$$k_2[\text{h}^+]^2 \gg k_4[\text{h}^+][\text{H}_2\text{O}] + k_5[\text{h}^+][\text{OH}^-]_{\text{ads}} \quad 104$$

Consequently, equation 103 is became to equation 105 and h^+ can be calculated by following expression:

$$[h^+] = \left(\frac{k_1 I}{k_2}\right)^{1/2} \quad 105$$

The H₂O concentration is constant because it is solvent. According to assumption (2) equations 106 and 107 are considered:

$$k_4[h^+][H_2O] \gg k_3[OH^-]_{ads}[h^+] \quad 106$$

$$k_4[H_2O] = k'_4 \quad 107$$

Consequently, $\bullet OH_{ads}$ rate can be obtained according to the following equation:

$$\begin{aligned} \frac{d[\bullet OH]_{ads}}{dt} = & k_5[h^+][OH^-]_{ads} + k_4[h^+][H_2O] + k_2[H_2O_2][e^-] + k_{18}[H_2O_2][O_2^\bullet] + \\ & k_{19}[H_2O_2]^{1/2}[I]^{1/2} - k_7[\bullet OH]_{ads}[C]_{ads} - k_8[\bullet OH]_{ads}[S_{inactive}] - k_9[\bullet OH]_{ads}[int] - \\ & k_{10}[\bullet OH]_{ads} - k_{11}[\bullet OH]_{ads}[e^-] = 0 \end{aligned} \quad 108$$

with the following assumptions described in equations 109 and 110:

$$\begin{aligned} k_7[\bullet OH]_{ads}[C]_{ads} + k_8[\bullet OH]_{ads}[S_{inactive}] + k_9[\bullet OH]_{ads}[int] = & k_7[C_0 - S_{inactive} - int] + \\ & k_8[C_0 - C_{ads} - int] - k_9[C_0 - S_{inactive} - C_{ads}] = k_7[C]_0 - k_7[S_{inactive} - int] + k_8[C]_0 - \\ & k_8[C_{ads} - int] + k_9[C]_0 - k_9[S_{inactive} - C_{ads}] = [C]_0\{k_7 + k_8 + k_9\} - k_7[S_{inactive} - int] - \\ & k_8[C_{ads} - int] - k_9[S_{inactive} - C_{ads}] = [C]_0\{k_D\} - k_7[S_{inactive} - int] - k_8[C_{ads} - int] - \\ & k_9[S_{inactive} - C_{ads}] = [C]_0\{k_D\} \end{aligned} \quad 109$$

$$-k_7[S_{inactive} - int] - k_8[C_{ads} - int] - k_9[S_{inactive} - C_{ads}] \ll [C]_0\{k_D\} \quad 110$$

The concentration of $\bullet OH_{ads}$ for a single compound can be obtained by using expression 105 as the following equation (eq. 111):

$$[\bullet OH] = \frac{k'_4[h^+]}{k_D[C]_0 + k_{10} + k_{11}[e^-]} = \frac{k'_4(k_1/k_2)^{1/2}I^{1/2}}{k_D[C]_0 + k_{10} + k_{11}(k_1/k_2)^{1/2}I^{1/2}} \quad 111$$

Finally, the initial degradation rate is described by

$$r_0 = \frac{k_D k'_4 (k_1/k_2)^{1/2} I^{1/2} C}{k_D[C]_0 + k_{10} + k_{11}(k_1/k_2)^{1/2} I^{1/2}} \quad 112$$

The equation 112 can be transformed into equations 113 and 114:

$$k'_{app} = k'_4 (k_1/k_2)^{1/2} I^{1/2} \quad 113$$

$$K_S = \frac{k_D}{k_{10} + k_{11}(k_1/k_2)^{1/2} I^{1/2}} \quad 114$$

By assumption that $k_{10} \gg k_{11} (k_1/k_2)^{1/2} I^{1/2}$ in equation 114, k_r and $1/K_S$ should be proportional to $I^{1/2}$. So, eq 13 refers to all of the experimental dependencies of the apparent equilibrium constant and rate constant with regard to the light intensity in the liquid phase.

By dividing the numerator and the denominator of equation 112 by k_{10} , the expression 115 is found:

$$r_0 = \frac{(k_D k'_4 (k_1/k_2)^{1/2} / k_{10}) I^{1/2} C}{k_D / k_{10} [C]_0 + 1 + (k_{11} / k_{10}) (k_1/k_2)^{1/2} I^{1/2}} \quad 115$$

According to relations 82, the expression 116 is obtained:

$$r_0 = k_{app} C = \frac{\beta I^{1/2}}{1 + \alpha I^{1/2} + \eta [C]_0} C \quad 116$$

$$k_{app} = \frac{\beta I^{1/2}}{1 + \alpha I^{1/2} + \eta [C]_0} \quad 117$$

where the constants can be obtained using expressions in equations 118-120:

$$\alpha = \frac{k_{11} (k_1/k_2)^{1/2}}{k_{10}} \quad 118$$

$$\beta = \frac{k_D k'_4 (k_1/k_2)^{1/2}}{k_{10}} \quad 119$$

$$\eta = \frac{k_D}{k_{10}} \quad 120$$

2.5.2. Results of transport modeling

According to equation 82, the $1/k_{app}$ (s) was plotted versus initial cefixime concentration (C_0 , mol/m³) in figure 110 to obtain k'_{app} and K_s parameters.

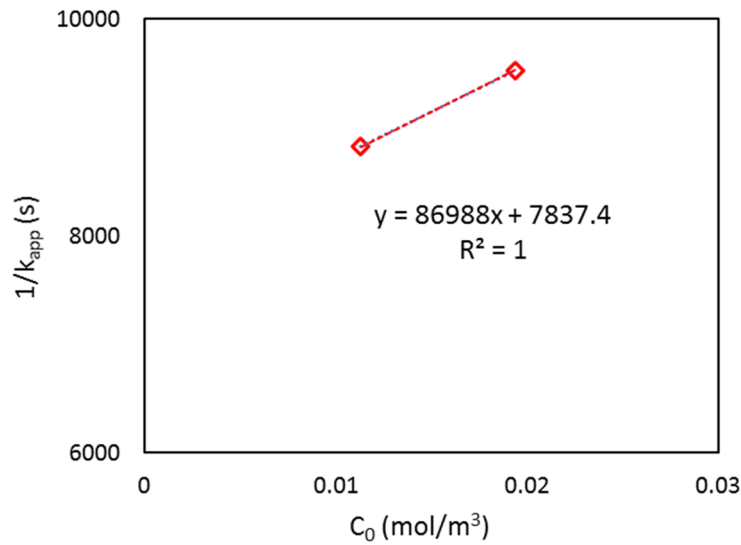


Figure 110. Relation between $1/k_{app}$ and initial cefixime concentration (C_0).

To use the model for investigating the impact of the main variables on the system's performance in terms of degradation efficiency, the proposed model must be validated. Therefore, the obtained results from the model were compared with the real data in experiments. The kinetic model of Langmuir-Hinshelwood (eq. 81) was proposed to predict the cefixime degradation through solar pilot. It should be noticed that the rate expression

used in this study was applied only for the degradation of the single compound, and it was assumed that the intermediate or byproducts did not influence the reaction rate. For an inlet concentration of $0.022 \text{ mol/m}^3 = 10 \text{ mg/L}$, the reaction rate (k'_{app}) and the adsorption rate (K_S) constants has been found and defined in equation 74. So, in mass transfer modeling the reaction rate was derived from the equation 121:

$$R = -\frac{dC}{dt} = \frac{k'_{app}K_SC}{1 + K_SC_0} = \frac{(1.15 \times 10^{-5})(11.099)C}{1 + (11.099)C}$$

R is the reaction rate ($\text{mol/m}^3.\text{s}$).

The average concentration on C_{out} was calculated by integrating the concentration on the outlet border of the domain with an average operator. In the model, the average concentrations of cefixime in the water outlet were compared with the real data at operating conditions in the solar pilot.

Figure 111 presents the comparison of experimental results to that of the model for an initial concentration of 10 mg/L .

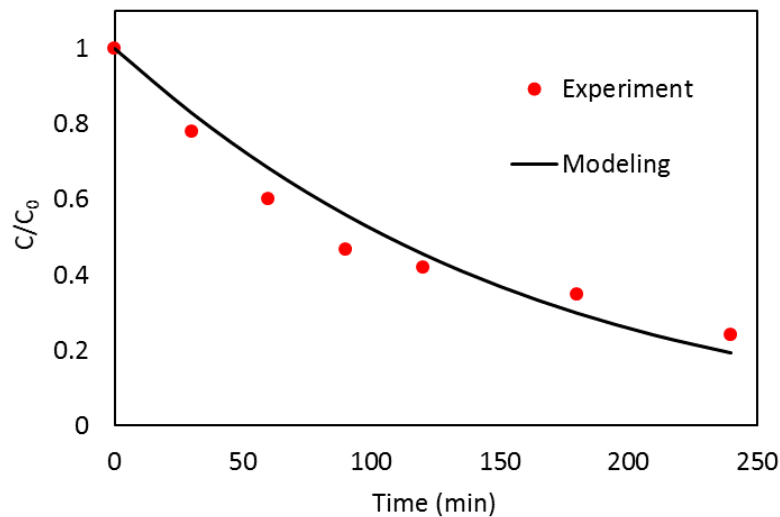


Figure 111. Comparison of experimental data and model prediction of concentration of cefixime at the outlet of solar reactor as a function of time ($C_0 = 10 \text{ mg/L}$).

Notations

T	Temperature ($^{\circ}\text{C}$ or K)
P	Pressure (Pa)
n	Refractive index
λ	Wavelength (nm)
θ	Angle
r_P	Reflection coefficient of P-polarized ray
t_P	Transmission coefficient P-polarized ray
r_S	Reflection coefficient of S-polarized ray
t_S	Transmission coefficient S-polarized ray
I_t	Intensity of the transmitted ray
I_r	Intensity of the reflected ray
I_i	Intensity of the incident ray
q	ray position (m)
k	wave vector (rad/m)
ω	Angular frequency
c	Speed of light
I	Global irradiation intensity (W/m^2)
A_c	Area of the collector (m^2)
P	Power (W)
W	Watt
ρ	Solid density (kg/m^3)
C_p	Solid heat capacity at constant pressure ($\text{J}/(\text{kg}\cdot\text{K})$)
u	Velocity field (m/s)
q	Heat flux by conduction (W/m^2),
k	Thermal conductivity ($\text{W}/(\text{m}\cdot\text{K})$)
Q	Heat source (W/m^3)
Q_{ted}	Thermoelastic heat source (W/m^3)
α	Coefficient of thermal expansion ($1/\text{K}$)
S	Second Piola-Kirchhoff stress tensor
C_p	Fluid heat capacity at constant pressure ($\text{J}/(\text{kg}\cdot\text{K})$)
Q_{vd}	Viscous dissipation in the fluid
τ	Viscous stress tensor (Pa)
h	Heat transfer coefficient ($\text{W}/(\text{m}^2\cdot\text{K})$)
T_{ext}	Ambient temperature ($^{\circ}\text{C}$ or K)
Q_b	Boundary heat source
δ	Dirac delta function
K	Viscous stress tensor (Pa)
F	Volume force vector (N/m^3)

g	Gravity (m/s^2)
ν	kinematic viscosity ($kg/m.s$)
T	Transpose operator
C_i	Initial concentration (mol/m^3)
R_i	Reaction rate ($mol/(m^3.s)$)
J_i	Mass flux diffusive flux vector ($mol/(m^2.s)$)
D_i	Diffusion coefficient (m^2/s)
k_{app}	Apparent rate constant ($1/s$)
k'_{app}	Reaction rate constant ($mol/m^3.s$)
K_S	Adsorption rate constant (m^3/mol)
C	Concentration (mol/m^3)

PART 6. GENERAL CONCLUSIONS AND PERSPECTIVES

General conclusions

Solar Photocatalysis is expected to be a promising process for the elimination of pharmaceutical contaminants in water as the energy is free. However, it remains yet many great pitfalls before industrial applications despite much progress observed over several decades. This thesis aims to contribute to the development of solar photocatalysis processes for the treatment of contaminated water with pharmaceutical chemicals. One important economic and environmental factor was to elaborate TiO_2 nanoparticles fixed on the surface of solid substrates. To reach this achievement we used glass beads as a substrate to immobilize various TiO_2 -based nano photocatalysts. Attached TiO_2 films on glass beads were investigated via the low-pressure fluidized bed plasma technique which focused on deposition conditions such as the oxygen concentration in plasma gas and deposition time on TiO_2 structure and composition. Another goal of this work was the assessment of the influence of Mn doping in TiO_2 lattice on photocatalytic performance. All deposited films were crystalized by annealing at $T = 450^\circ\text{C}$ for 4 hours because they were found amorphous.

Characteristic analysis on our deposited films demonstrated that oxygen concentration in plasma gas plays a significant role in TiO_2 formation. The pure anatase crystalline phase of TiO_2 was constructed without any oxygen flux, while a mixture of anatase/rutile crystalline phases appeared in the presence of oxygen flux in plasma gas. As well as, the rutile fraction increased as the oxygen flow rate increased in plasma discharge under our experimental conditions. The nanocrystal size ($\sim 10\text{ nm}$) of particles was observed in all photocatalytic films on the surface of glass beads with strong adherence confirmed by XPS analysis.

The solar photocatalytic treatment was performed in a pilot reactor based on compound parabolic concentrator (CPC) technology. Experiments were carried out with an initial concentration of 10 mg/L cefixime at ambient temperature and neutral pH. The cefixime degradation was assessed based on the measurement of solution absorbance by a UV-vis spectrophotometer. The results of photocatalytic degradation experiments showed that TiO_2 phase composition has a huge impact on photocatalytic activity. The TiO_2 sample deposited with a 2 ml/min oxygen flow rate in plasma gas resulted in a higher cefixime degradation than other catalysts due to its rutile/anatase ratio of 19% which was similar to P25 Degussa photocatalyst. In addition, as the oxygen flow rate increased in plasma discharge the photocatalytic activity of TiO_2 decreased due to a higher rutile fraction.

Other deposition conditions like deposition time and TTIP (titanium tetraisopropoxide) concentration in precursor also could influence the photocatalytic performance of TiO_2 films. The solar photocatalysis results indicated a lower deposition time (30 and 45 min) and lower TTIP concentration decreased photocatalytic activity because they could control the thickness of the layers.

The use of Mn in TiO_2 crystalline lattice as a dopant decreased the photo-degradation of cefixime in comparison with pure TiO_2 catalysts. This phenomenon might assist the

agglomeration of particles because XRD measurements indicated average crystal size increased by doping or might be due to distortion of the TiO_2 host lattice.

The TiO_2 , V-doped TiO_2 , and Zr-doped TiO_2 photocatalysts were synthesized by the sol-gel method in the micro-mixing reactor. These nano-particles were also coated on glass beads and used in solar CPC pilot. The solar experiments exhibited lower cefixime degradation efficiency in comparison to the plasma deposited samples. The difference may become from the thickness of the layers, but unfortunately, we couldn't estimate the exact thickness of the layers on the beads. The presence of both rutile and anatase phases in the plasma deposited layer may explain the better degradation reached with these layers.

In the next step, regeneration techniques were applied to recover active sites of films on the surface of glass beads. Because their photocatalytic activity decreased after several uses in photoreactor as the result of the occupation of active sites with degradation's by-products or by adsorbed cefixime molecules. Hot water, heat treatment, and washing in alkaline solution methods were applied and better regeneration results were observed for hot water washing at $T = 80^\circ\text{C}$.

Finally, mathematical modeling of the CPC solar photo-reactor with COMSOL Multiphysics was employed for water treatment. Ray optic, Heat transfer, Fluid Flow, and Mass Transfer modules were used. The ray trajectory and solar radiation distribution graphs were obtained by optical modeling. The results of thermal and fluid flow modeling presented the temperature gradient and velocity of solution inside the simulated CPC solar pilot. The numerical modeling indicated acceptable results, and the predicted cefixime concentrations at the outlet were in good agreement with experimental data obtained under natural solar radiation.

Perspectives

Further studies are necessary to study:

- The role of other plasma deposition parameters on TiO_2 composition and finding the optimum plasma condition.
- Using other metallic non-metallic dopants in TiO_2 lattice to increase its photocatalytic activity by decreasing band gap energy and using visible light.
- Study the industrial application of water and wastewater treatment technologies using natural solar energy.
- Study the mineralization of cefixime or characterization degradation by-products.

Publications and conferences

Publications:

1. **Moosavi, F.**, Lemarchand, A., Bazin, C., Konstantakopoulou, M., Frégnaux, M., Colbeau-Justin, C., Tavakoli Gheinani, T., Kanaev, A. and Nikravech, M.
"Photocatalytic nanocomposite anatase–rutile TiO₂ coating." **Applied Physics A** 128, no. 11 (2022): 963.
2. **Moosavi F.**, Cheng K., Tavakoli T., Traore M., Kanaev A., Nikravech M.
"Photocatalytic Destruction of Amoxicillin in a Pilot Sunlight Reactor with Supported Titania Nano-Photocatalyst ", **Chemical Engineering Transaction (CET)**, vol. 73 (2019), pages 175-180.
3. **Moosavi F.**, Cheng K., Tavakoli T., Traore M., Kanaev A., Nikravech M.
"Investigation of removal of amoxicillin antibiotic from water by photocatalyst in different operating conditions", **Journal of Natural environment**, Vol. 72, Issue 3 (2019), Pages 379-388.

Conferences:

1. **Moosavi F.**, Lemarchand A., Tavakoli T., Traore M., Kanaev A., Nikravech M.
"Effects of TiO₂ stoichiometry and oxygen defects in the photocatalytic degradation of Cefixime under solar and artificial light illuminations", **6th International Conference on Catalysis and Chemical Engineering**, San Francisco CA. USA, February 2022.
2. **Moosavi F.**, Cheng K., Tavakoli T., Traore M., Kanaev A., Nikravech M.
"Photocatalytic Destruction of Amoxicillin in a Pilot Sunlight Reactor with Supported Titania Nano-Photocatalyst ", **Conference Nine**, Naples Italy, April 2019.
3. **Moosavi F.**, Cheng K., Tavakoli T., Traore M., Kanaev A., Nikravech M.
"Effect of experimental parameters on photocatalytic activity of supported TiO₂ nano-photocatalyst on degradation of amoxicillin in a pilot sunlight reactor", **Conference EAAOP-6**, Portoroze Slovenia, June 2019.
4. **Moosavi F.**, Tavakoli T., Brinza O., Traore M., Kanaev A., Nikravech M.
"Elaboration of Supported Titania Nano-Photocatalysts in Spray Plasma reactor. Study of Photocatalytic effects on Amoxicillin in water", **Conference EAAOP-6**, Portoroze Slovenia, June 2019.

Annex

A. XPS analysis of TiO₂ Coated films on glass beads

1. XPS analysis of TiO₂ film on plate with 0 ml/min oxygen flow in plasma gas during 60 min.

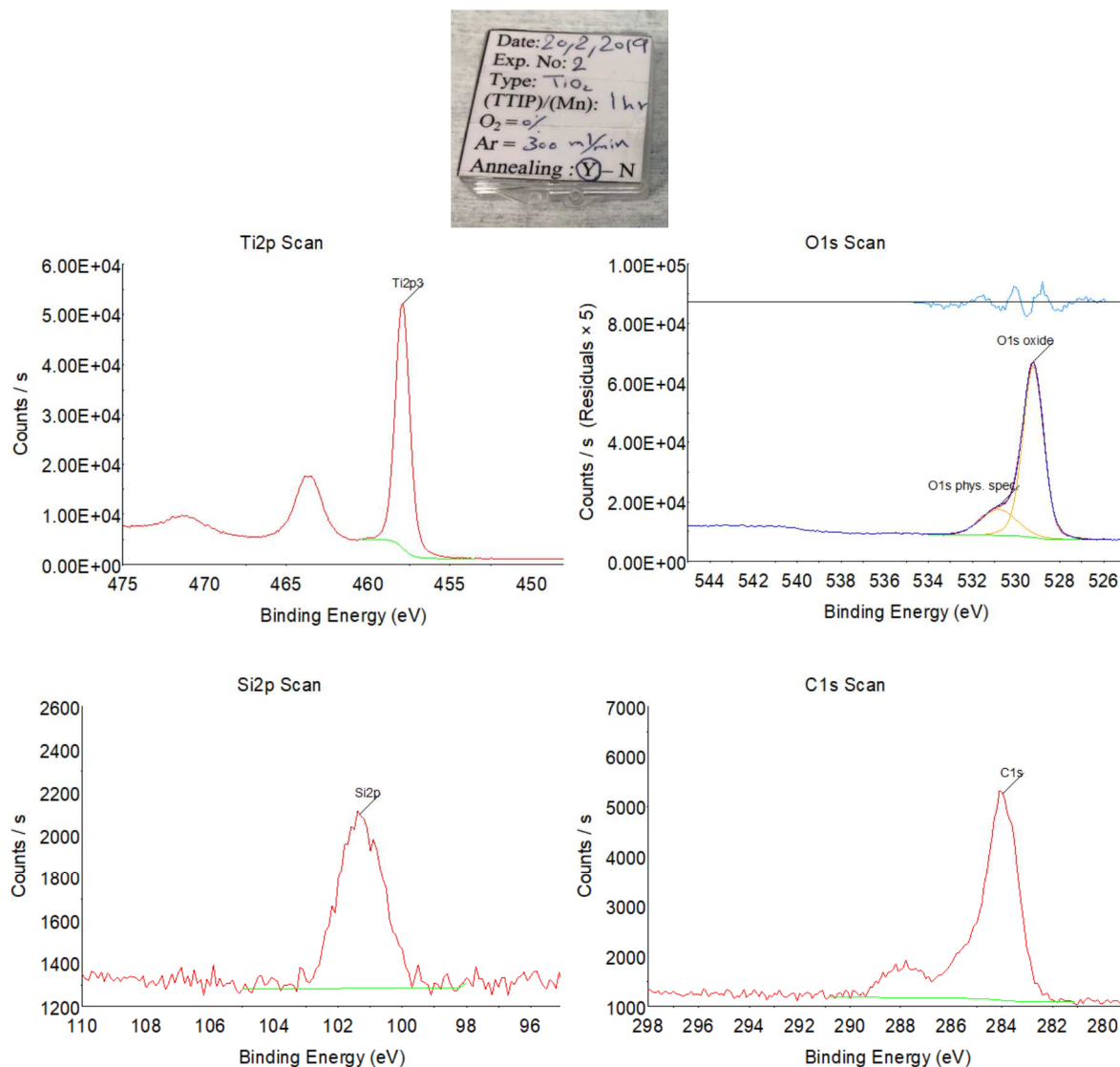


Figure 112. XPS analysis of TiO₂ film coated with 0 ml/min oxygen flux in plasma gas during 60 min.

Table 23. XPS analysis of TiO₂ films deposited with 0 ml/min O₂ in plasma gas during 60 min.

Name	PeakBE	FWHM eV	Area (P) CPS.eV	Atomic %
O1s oxide	529.22	1.11	71266.6	46.2
Ti2p3	457.91	1.01	56521.67	23.4
C1s	283.97	1.49	8913.96	15.58
O1s phys. spec.	530.79	1.93	18621.29	12.08
Si2p	101.33	1.6	1468.37	2.75

2. XPS analysis of TiO₂ film on plate with 10 ml/min oxygen flow in plasma gas during 60 min.

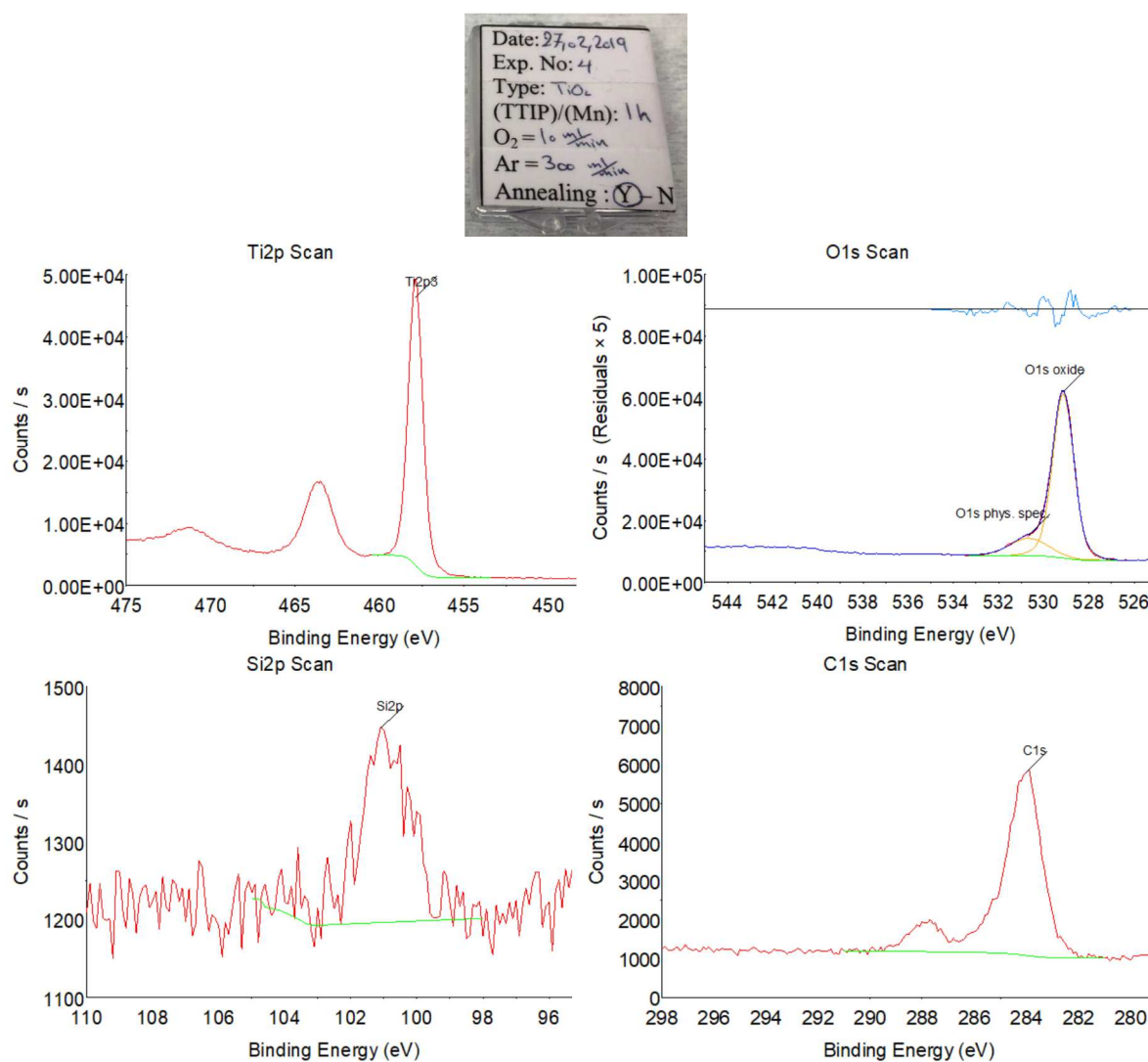


Figure 113. XPS analysis of TiO₂ film coated with 10 ml/min oxygen flux in plasma gas during 60 min.

Table 24. XPS analysis of TiO₂ films deposited with 10 ml/min O₂ in plasma gas during 60 min.

Name	Peak BE	FWHM eV	Area (P) CPS.eV	Atomic %
O1s oxide	529.14	1.1	65452.54	47.21
Ti2p3	457.88	1	51996.18	23.95
C1s	284.03	1.45	9632.97	18.74
O1s phys. spec.	530.65	1.99	12595.11	9.09
Si2p	101.08	1.19	487.52	1.02

3. XPS analysis of TiO₂ film on plate with 10 ml/min oxygen flow in plasma gas during 45 min.

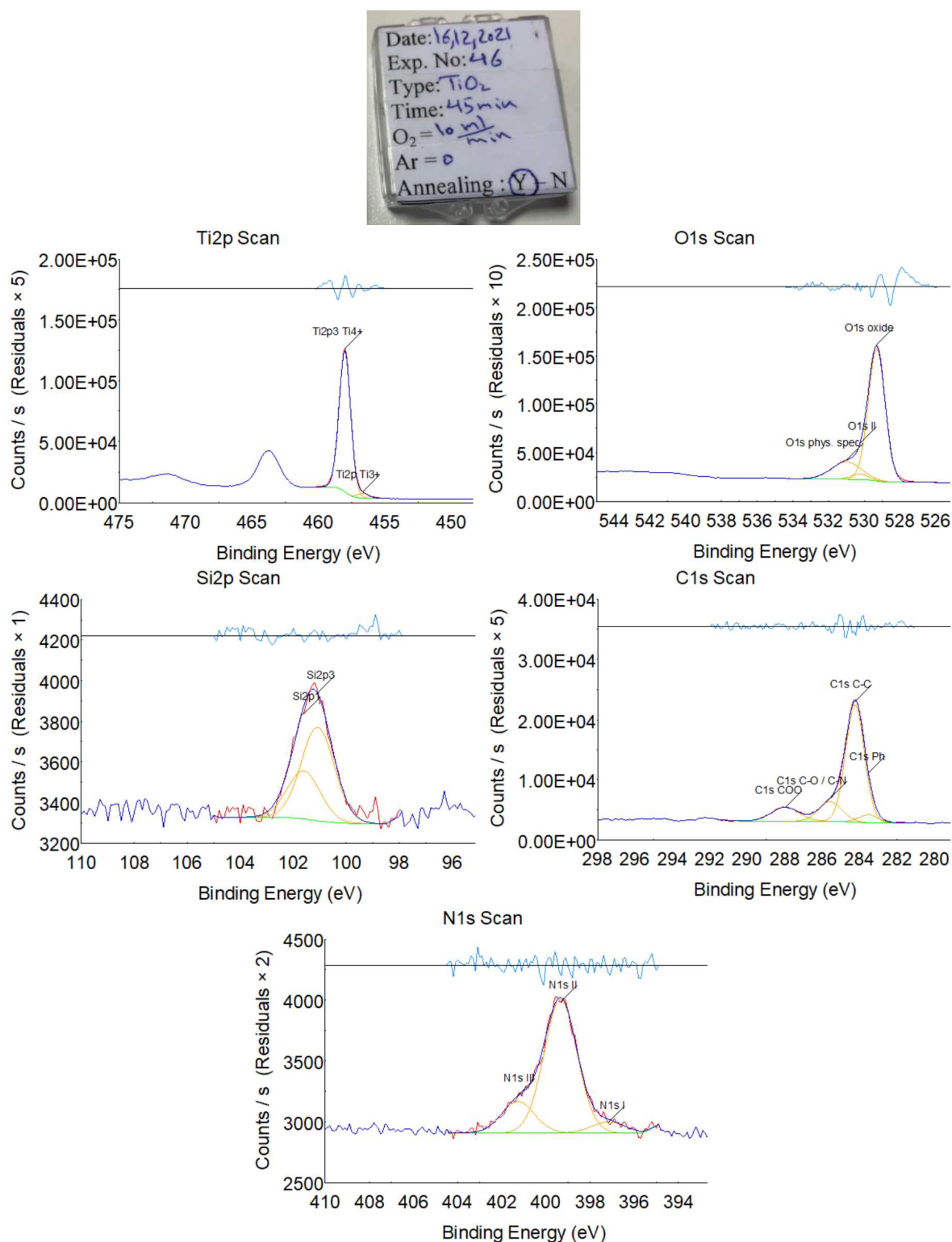


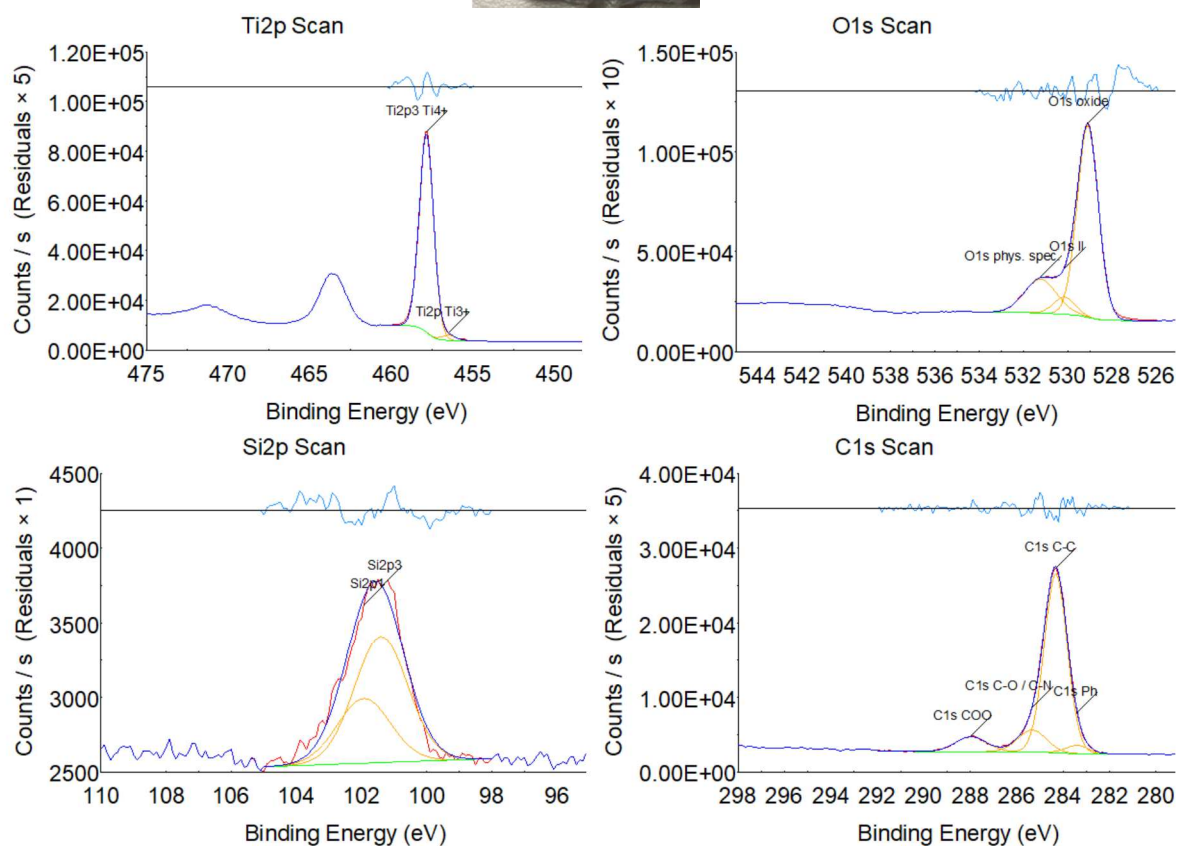
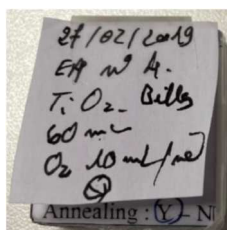
Figure 114. XPS analysis of TiO_2 film coated with 10 ml/min oxygen flux in plasma gas during 45 min.

Table 25. XPS analysis of TiO_2 films deposited with 10 ml/min O_2 in plasma gas during 45 min.

Name	Peak BE	FWHM eV	Area (P) CPS.eV	Atomic %
O1s oxide	529.31	1.1	161436.0 7	41.28

Ti2p3 Ti4+	458.01	1.01	125826.4 9	20.55
C1s C-C	284.25	1.16	24491.84	16.89
O1s phys. spec.	531	1.94	37033.41	9.48
C1s C-O / C-N	285.56	1.45	5061.36	3.49
C1s COO	287.96	1.75	4353.77	3
O1s II	530.24	1.1	6759.09	1.73
C1s Ph	283.53	1.16	1675.62	1.16
N1s II	399.34	1.75	2073.22	0.88
Si2p3	101.08	1.46	728.66	0.81
Ti2p Ti3+	456.67	1.01	4102.22	0.46
N1s III	401.27	1.75	489.35	0.21
N1s I	397.18	1.75	175.1	0.07

4. XPS analysis of TiO₂ film on glass bead with 10 ml/min oxygen flow in plasma gas during 60 min.



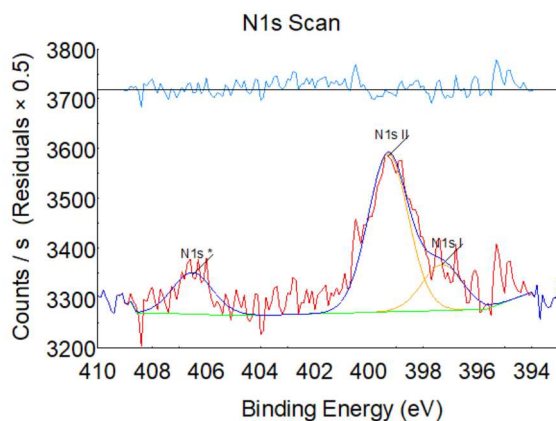


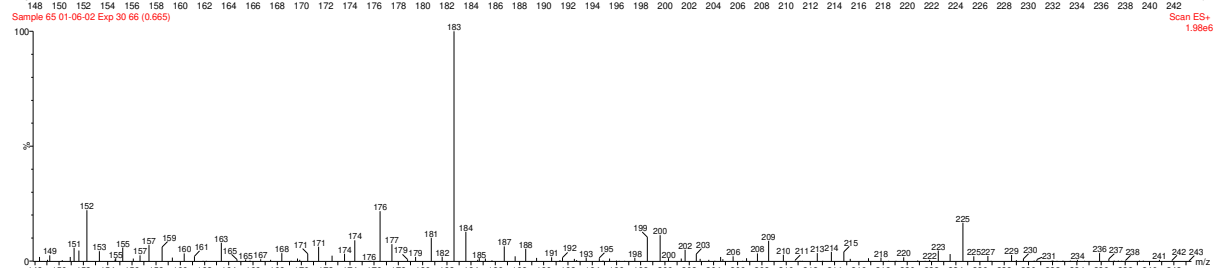
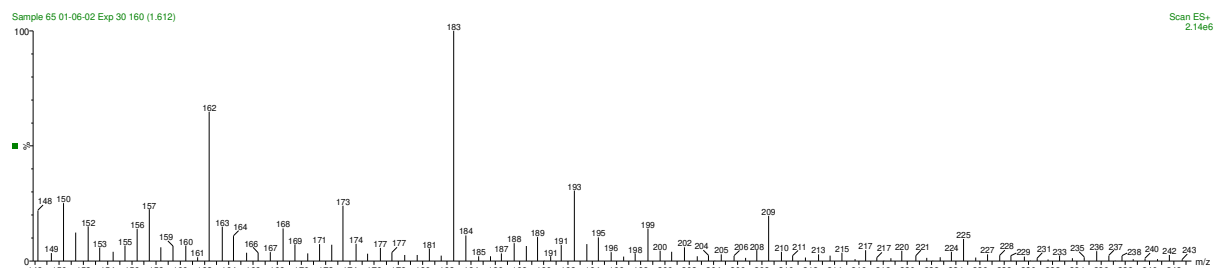
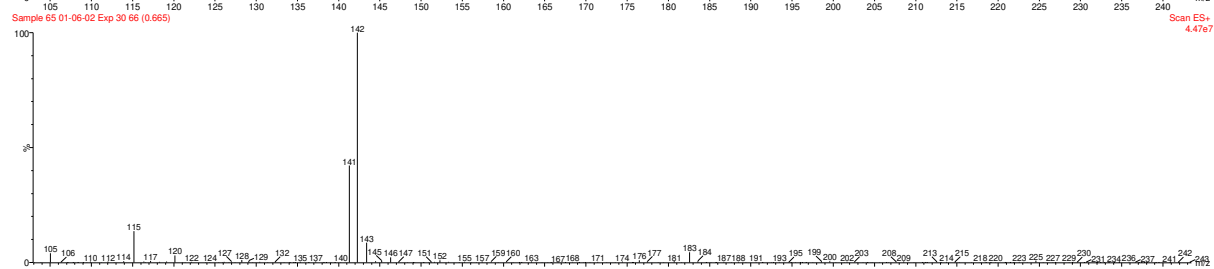
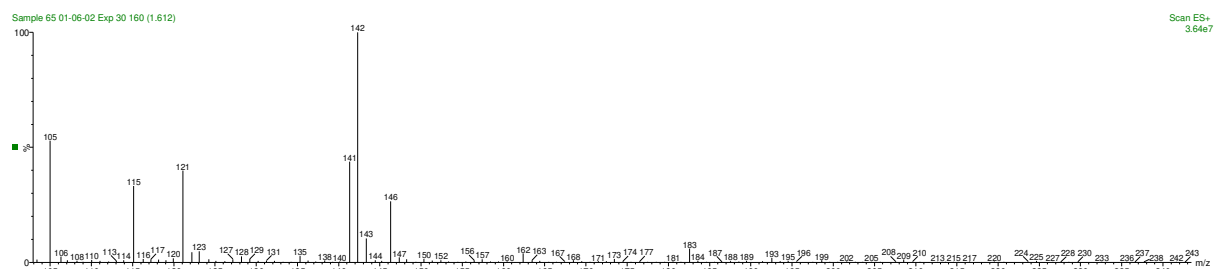
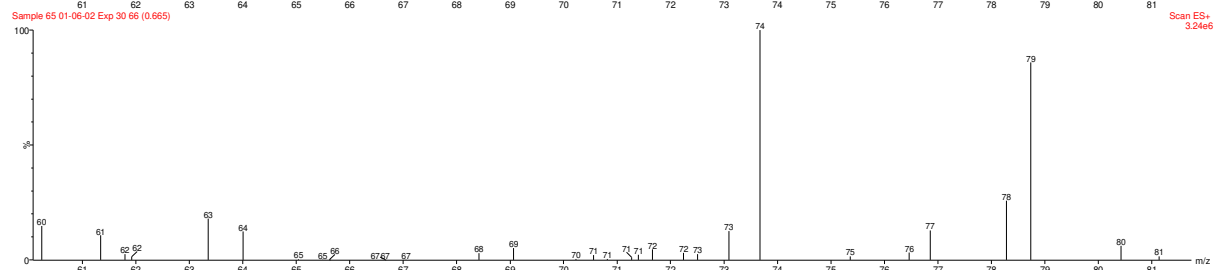
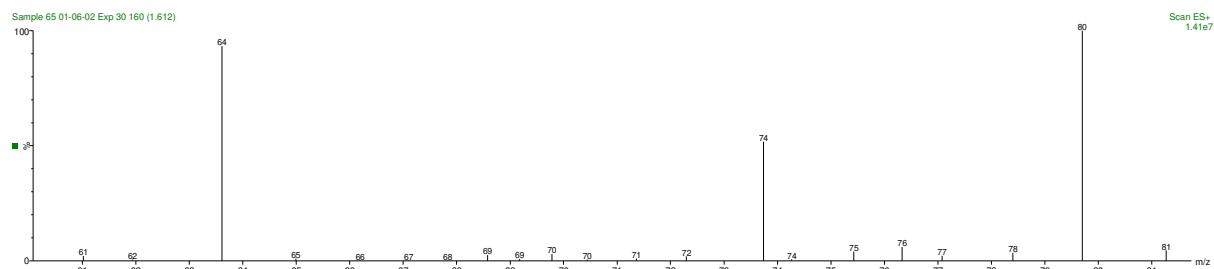
Figure 115. XPS analysis of TiO₂ film coated with 10 ml/min oxygen flux in plasma gas during 60 min.

Table 26. XPS analysis of TiO₂ film coated with 10 ml/min oxygen flux in plasma gas during 60 min.

Name	Peak BE	FWHM eV	Area (P) CPS.eV	Atomic %
O1s oxide	529.09	1.13	116140.22	35.15
C1s C-C	284.32	1.16	30122.54	24.59
Ti2p3 Ti4+	457.84	1.03	87979.31	17
O1s phys. spec.	531.23	1.7	30994.03	9.39
C1s C-O / C-N	285.34	1.45	4575.99	3.74
O1s II	530.16	1.12	10367.22	3.14
C1s COO	287.97	1.57	3405.88	2.78
Si2p3	101.4	1.93	1752.48	2.31
C1s Ph	283.4	1.16	1408.31	1.15
N1s II	399.29	1.75	596.29	0.3
Ti2p Ti3+	456.48	1.03	2249.42	0.3
N1s I	397.3	1.75	173	0.09
N1s *	406.51	1.74	157.12	0.08

B. Liquid chromatography mass spectrometry analysis (LC-MS)

1. LC-MS chromatogram and mass spectra of treated cefixime solution sample with the degradation efficiency of 85%.



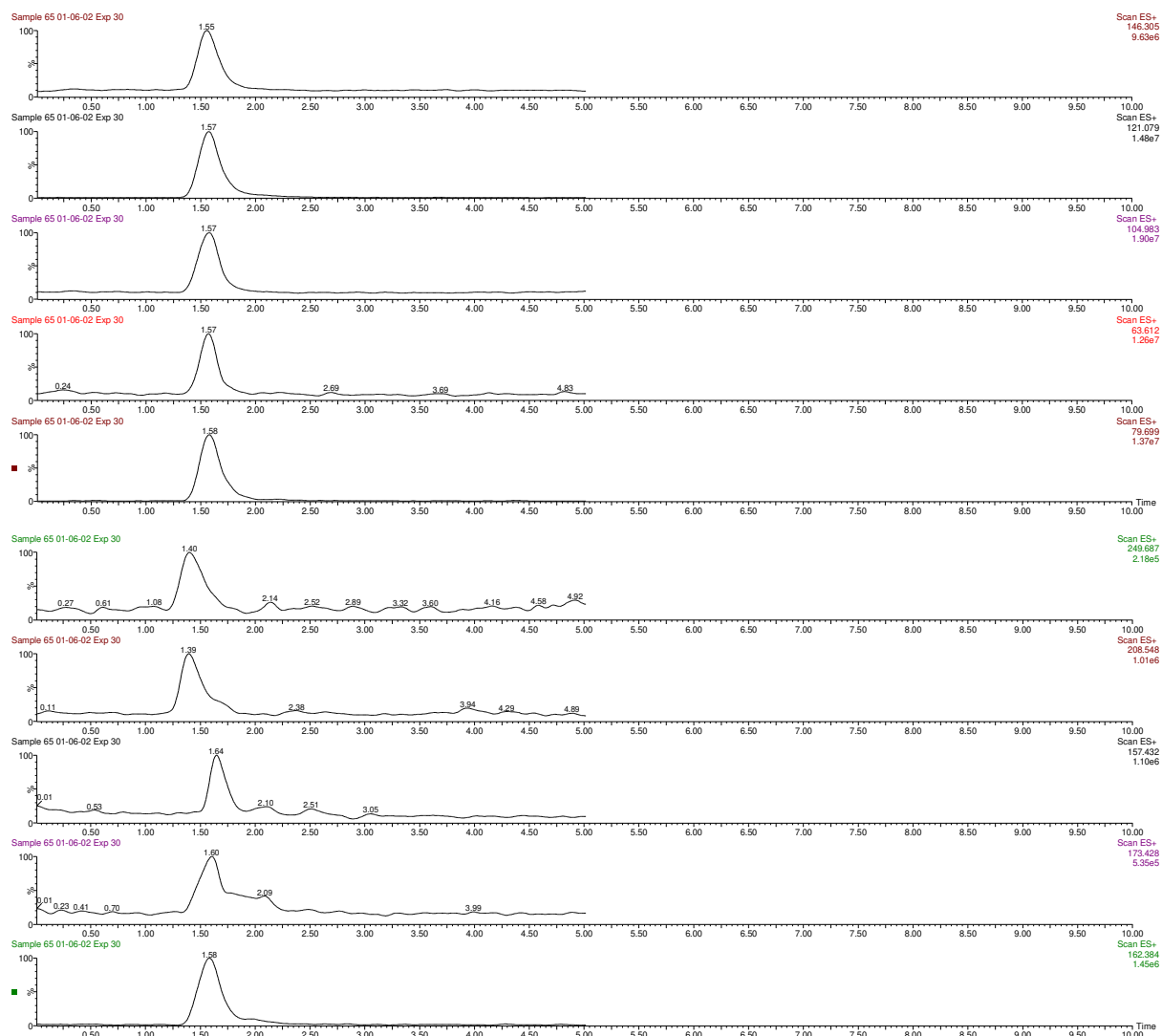


Figure 116. Mass spectra and chromatograms of treated cefixime solution sample with the degradation efficiency of 85%.

2. LC-MS chromatogram and mass spectra of treated cefixime solution sample with the degradation efficiency of 41%.

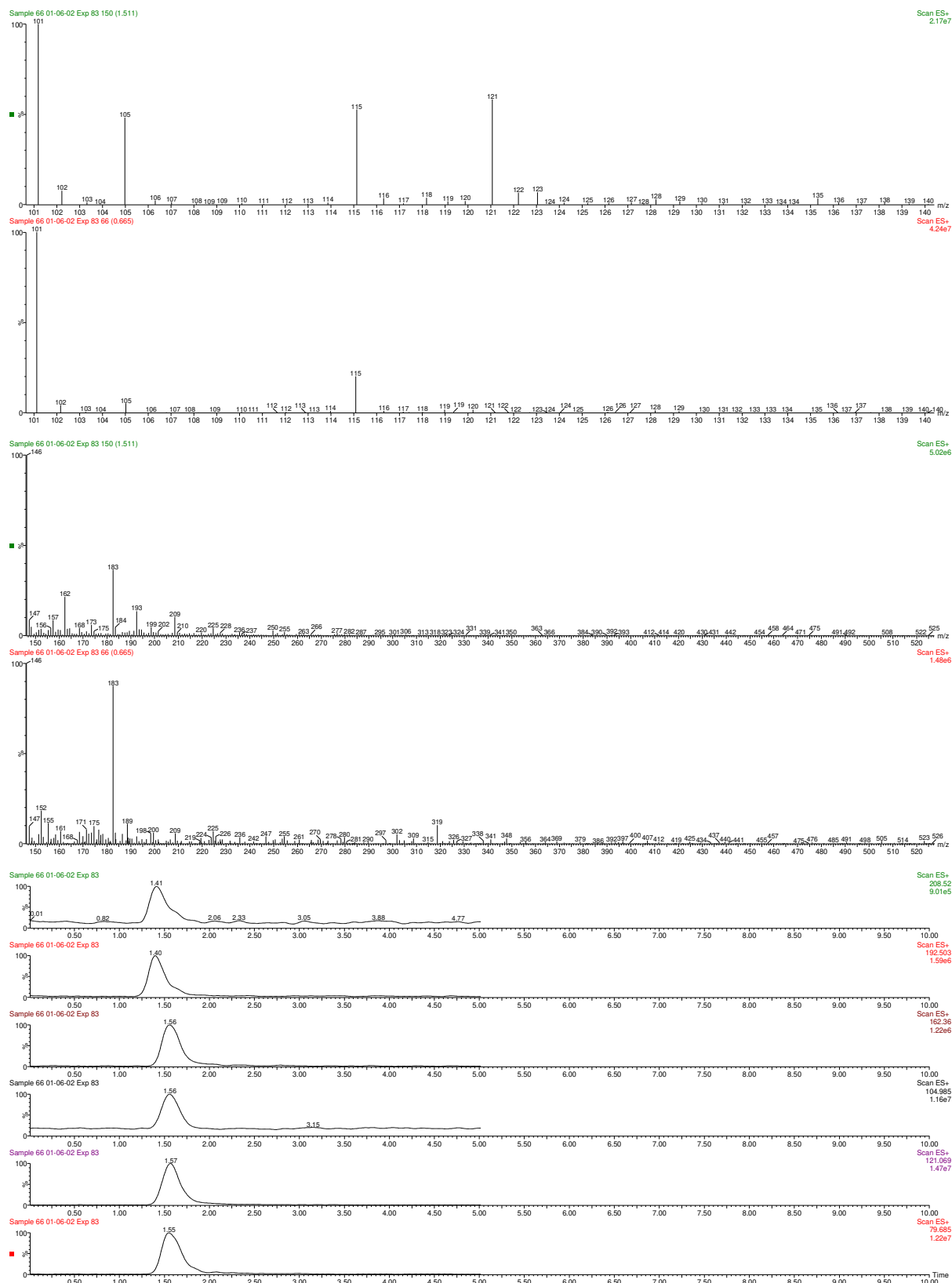


Figure 117. Mass spectra and chromatograms of treated cefixime solution sample with the degradation efficiency of 45%.

C. Heat treatment regeneration

The heat treatment method was utilized for the second series of TiO₂ films. In the second regeneration cycle, the heat treatment technique was applied for TiO₂ photocatalysts deposited with 0 and 1 ml/min oxygen in plasma gas for a period of 45 min. These regenerated photocatalysts indicated low regeneration efficiency. As shown in figure 116, the rate constants obtained 37.7, 22.6, and 18.2 x 10⁻³ L/kJ for hot water, heat treatment, and second cycle after heat treatment experiments when TiO₂ (0 ml/min O₂) was used in the solar photo reactor, respectively. These values were calculated at about 25.9, 22.9, and 22.5 x 10⁻³ L/kJ for TiO₂ which was deposited under 1 ml/min of oxygen flow in plasma gas. The main disadvantages of heat treatment were the energetic requirement and low regeneration efficiency.

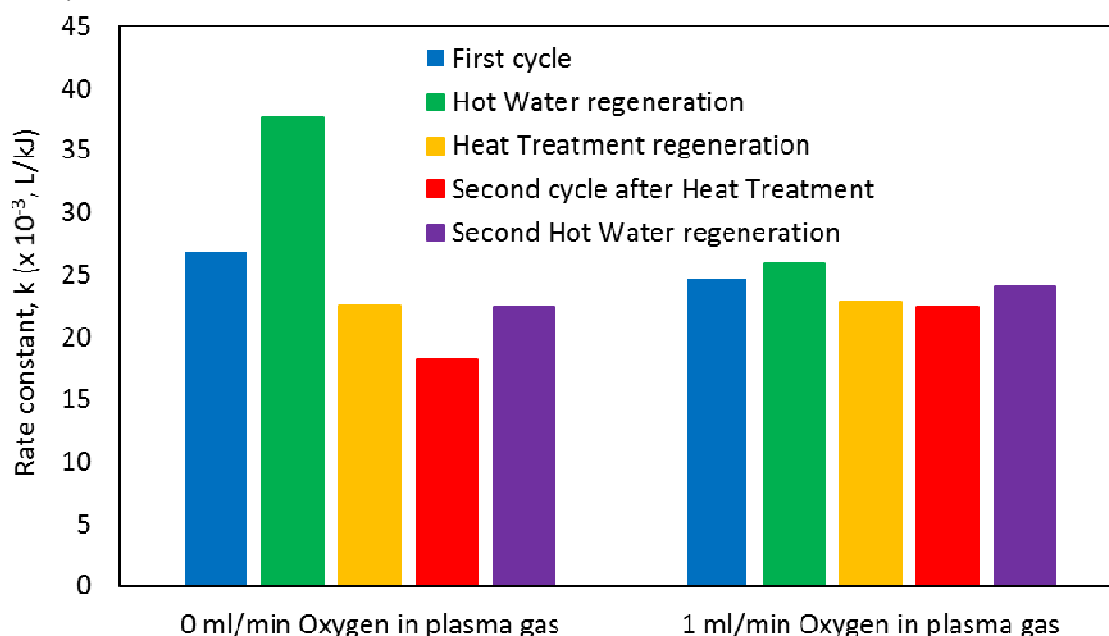


Figure 118. Rate constant comparison of TiO₂ ($C_{Ti} = 1.002$ mol/L, 0 and 1 ml/min O₂, 45 min) films regenerated with hot water and heat treatment methods.

After using the heat treatment technique, the hot water regeneration technique was used one more time on these photocatalysts. As can be seen, photocatalytic activity restored slightly from 18.2 L/kJ to 22.5 L/kJ and from 22.5 L/kJ to 24.1 x 10⁻³ L/kJ for catalysts which deposited with 0 and 1 ml/min of oxygen flow rate in plasma discharge during 45 min.

REFERENCES

1. Malato S, Blanco J, Vidal A, Alarcón D, Maldonado MI, Cáceres J, et al. Applied studies in solar photocatalytic detoxification: an overview. *Solar Energy*. 2003;75(4):329-36.
2. Li Y, Zhang L, Liu X, Ding J. Ranking and prioritizing pharmaceuticals in the aquatic environment of China. *Science of the Total Environment*. 2019;658:333-42.
3. Mirzaei A, Chen Z, Haghighat F, Yerushalmi L. Magnetic fluorinated mesoporous g-C₃N₄ for photocatalytic degradation of amoxicillin: Transformation mechanism and toxicity assessment. *Applied Catalysis B: Environmental*. 2019;242:337-48.
4. Andreozzi R, Raffaele M, Nicklas P. Pharmaceuticals in STP effluents and their solar photodegradation in aquatic environment. *Chemosphere*. 2003;50(10):1319-30.
5. Zhang Y, Wang B, Cagnetta G, Duan L, Yang J, Deng S, et al. Typical pharmaceuticals in major WWTPs in Beijing, China: Occurrence, load pattern and calculation reliability. *Water research*. 2018;140:291-300.
6. Kümmerer K. Antibiotics in the aquatic environment—a review—part I. *Chemosphere*. 2009;75(4):417-34.
7. Anjali R, Shanthakumar S. Insights on the current status of occurrence and removal of antibiotics in wastewater by advanced oxidation processes. *Journal of Environmental Management*. 2019;246:51-62.
8. Götz K, Courtier A, Stein M, Strelau L, Sunderer G, Vidaurre R, et al. Risk perception of pharmaceutical residues in the aquatic environment and precautionary measures. *Management of Emerging Public Health Issues and Risks*: Elsevier; 2019. p. 189-224.
9. Kovalakova P, Cizmas L, McDonald TJ, Marsalek B, Feng M, Sharma VK. Occurrence and toxicity of antibiotics in the aquatic environment: A review. *Chemosphere*. 2020;251:126351.
10. aus der Beek T, Weber FA, Bergmann A, Hickmann S, Ebert I, Hein A, et al. Pharmaceuticals in the environment—Global occurrences and perspectives. *Environmental toxicology and chemistry*. 2016;35(4):823-35.
11. Xiang Y, Wu H, Li L, Ren M, Qie H, Lin A. A review of distribution and risk of pharmaceuticals and personal care products in the aquatic environment in China. *Ecotoxicology and Environmental Safety*. 2021;213:112044.
12. Hasani K, Peyghami A, Moharrami A, Vosoughi M, Dargahi A. The efficacy of sono-electro-Fenton process for removal of cefixime antibiotic from aqueous solutions by response surface methodology (RSM) and evaluation of toxicity of effluent by microorganisms. *Arabian Journal of Chemistry*. 2020;13(7):6122-39.
13. Dong H, Zeng G, Tang L, Fan C, Zhang C, He X, et al. An overview on limitations of TiO₂-based particles for photocatalytic degradation of organic pollutants and the corresponding countermeasures. *Water research*. 2015;79:128-46.
14. Li WC. Occurrence, sources, and fate of pharmaceuticals in aquatic environment and soil. *Environmental pollution*. 2014;187:193-201.
15. Rosman N, Salleh W, Mohamed MA, Jaafar J, Ismail A, Harun Z. Hybrid membrane filtration-advanced oxidation processes for removal of pharmaceutical residue. *Journal of colloid and interface science*. 2018;532:236-60.
16. Ebele AJ, Abdallah MA-E, Harrad S. Pharmaceuticals and personal care products (PPCPs) in the freshwater aquatic environment. *Emerging contaminants*. 2017;3(1):1-16.

17. Felis E, Kalka J, Sochacki A, Kowalska K, Bajkacz S, Harnisz M, et al. Antimicrobial pharmaceuticals in the aquatic environment-occurrence and environmental implications. *European Journal of Pharmacology*. 2020;866:172813.
18. Rosman N, Salleh WNW, Mohamed MA, Jaafar J, Ismail AF, Harun Z. Hybrid membrane filtration-advanced oxidation processes for removal of pharmaceutical residue. *Journal of Colloid and Interface Science*. 2018;532:236-60.
19. Sharma VK, Feng M. Water depollution using metal-organic frameworks-catalyzed advanced oxidation processes: A review. *Journal of Hazardous Materials*. 2019;372:3-16.
20. Saeid S, Tolvanen P, Kumar N, Eränen K, Peltonen J, Peurla M, et al. Advanced oxidation process for the removal of ibuprofen from aqueous solution: A non-catalytic and catalytic ozonation study in a semi-batch reactor. *Applied Catalysis B: Environmental*. 2018;230:77-90.
21. Kanakaraju D, Glass BD, Oelgemöller M. Advanced oxidation process-mediated removal of pharmaceuticals from water: a review. *Journal of environmental management*. 2018;219:189-207.
22. Baaloudj O, Nasrallah N, Kebir M, Guedioura B, Amrane A, Nguyen-Tri P, et al. Artificial neural network modeling of cefixime photodegradation by synthesized CoBi₂O₄ nanoparticles. *Environmental Science and Pollution Research*. 2021;28(12):15436-52.
23. Tabatabaei FS, Asadi-Ghalhari M, Aali R, Mohammadi F, Mostafaloo R, Esmaeili R, et al. Removal of Cefixime from Water Using Rice Starch by Response Surface Methodology. *Avicenna Journal of Medical Biotechnology*. 2020;12(4):230.
24. Baaloudj O, Nasrallah N, Bouallouche R, Kenfoud H, Khezami L, Assadi AA. High efficient Cefixime removal from water by the sillenite Bi₁₂TiO₂₀: Photocatalytic mechanism and degradation pathway. *Journal of Cleaner Production*. 2022;330:129934.
25. Erim B, Cığeroğlu Z, Bayramoğlu M. Green synthesis of TiO₂/GO/chitosan by using leaf extract of *Olea europaea* as a highly efficient photocatalyst for the degradation of cefixime trihydrate under UV-A radiation exposure: An optimization study with d-optimal design. *Journal of Molecular Structure*. 2021;1234:130194.
26. Hasanzadeh V, Rahmanian O, Heidari M. Cefixime adsorption onto activated carbon prepared by dry thermochemical activation of date fruit residues. *Microchemical journal*. 2020;152:104261.
27. Binh VN, Dang N, Anh NTK, Thai PK. Antibiotics in the aquatic environment of Vietnam: sources, concentrations, risk and control strategy. *Chemosphere*. 2018;197:438-50.
28. Mirzaei R, Yunesian M, Mesdaghinia A, Nasseri S, Gholami M, Jalilzadeh E, et al. The efficiency of the conventional wastewater treatment plant in antibiotics removal and the determination of their concentration in Ekbatan and southern Tehran wastewater treatment plants: a case report. *Iranian Journal of Health and Environment*. 2018;11(3):321-36.
29. Mirzaei R, Yunesian M, Nasseri S, Gholami M, Jalilzadeh E, Shoeibi S, et al. Occurrence and fate of most prescribed antibiotics in different water environments of Tehran, Iran. *Science of the total environment*. 2018;619:446-59.
30. Mirzaei R, Mesdaghinia A, Hoseini SS, Yunesian M. Antibiotics in urban wastewater and rivers of Tehran, Iran: consumption, mass load, occurrence, and ecological risk. *Chemosphere*. 2019;221:55-66.
31. Lu Z-Y, Ma Y-L, Zhang J-T, Fan N-S, Huang B-C, Jin R-C. A critical review of antibiotic removal strategies: Performance and mechanisms. *Journal of Water Process Engineering*. 2020;38:101681.
32. Anthony ET, Ojemaye MO, Okoh AI, Okoh OO. Potentials of low-cost methods for the removal of antibiotic-resistant bacteria and their genes in low budget communities: A review. *Journal of Water Process Engineering*. 2021;40:101919.

33. de Ilurdoz MS, Sadhwani JJ, Reboso JV. Antibiotic removal processes from water & wastewater for the protection of the aquatic environment-a review. *Journal of Water Process Engineering*. 2022;45:102474.
34. Cığeroğlu Z, Küçükyıldız G, Erim B, Alp E. Easy preparation of magnetic nanoparticles-rGO-chitosan composite beads: Optimization study on cefixime removal based on RSM and ANN by using Genetic Algorithm Approach. *Journal of Molecular Structure*. 2021;1224:129182.
35. Rasoulifard MH, Ghalamch L, Aziz M, Eskandarian MR, Sehati N. Application of ultraviolet light-emitting diodes to the removal of cefixime trihydrate from aqueous solution in the presence of peroxydisulfate. *Journal of Applied Chemical Research*. 2015;9(3):61-72.
36. Zhou Z, Liu X, Sun K, Lin C, Ma J, He M, et al. Persulfate-based advanced oxidation processes (AOPs) for organic-contaminated soil remediation: A review. *Chemical Engineering Journal*. 2019;372:836-51.
37. Marcelino RBP, Queiroz MTA, Amorim CC, Leão MMD, Brites-Nóbrega FF. Solar energy for wastewater treatment: review of international technologies and their applicability in Brazil. *Environmental Science and Pollution Research*. 2015;22(2):762-73.
38. Miklos DB, Remy C, Jekel M, Linden KG, Drewes JE, Hübner U. Evaluation of advanced oxidation processes for water and wastewater treatment—A critical review. *Water research*. 2018;139:118-31.
39. Belghadr I, Shams Khorramabadi G, Godini H, Almasian M. The removal of the cefixime antibiotic from aqueous solution using an advanced oxidation process (UV/H₂O₂). *Desalination and Water Treatment*. 2015;55(4):1068-75.
40. Mostafaloo R, Asadi-Ghalhari M. Modeling and optimization of the electrochemical process for cefixime removal from water. *Analytical Bioanalytical Electrochemistry*. 2020;12(1):36-47.
41. Asadi-Ghalhari M, Mostafaloo R, Ghafouri N, Kishipour A, Usefi S, Baaloudj O. Removal of Cefixime from aqueous solutions via proxy electrocoagulation: Modeling and optimization by response surface methodology. *Reaction Kinetics, Mechanisms and Catalysis*. 2021;134(1):459-71.
42. Malato S, Fernández-Ibáñez P, Maldonado MI, Oller I, Polo-López MI, Pichat P. Solar photocatalytic pilot plants: commercially available reactors. Wiley-VCH Verlag: Weinheim, Germany; 2013.
43. Cabrera-Reina A, Martínez-Piernas AB, Bertakis Y, Xekoukoulotakis NP, Agüera A, Sánchez Pérez JA. TiO₂ photocatalysis under natural solar radiation for the degradation of the carbapenem antibiotics imipenem and meropenem in aqueous solutions at pilot plant scale. *Water Research*. 2019;166:115037.
44. El Mragui A, Zegaoui O, Daou I, Esteves da Silva JCG. Preparation, characterization, and photocatalytic activity under UV and visible light of Co, Mn, and Ni mono-doped and (P, Mo) and (P, W) co-doped TiO₂ nanoparticles: A comparative study. *Environmental Science and Pollution Research*. 2021;28(20):25130-45.
45. Tian M, Su Y, Zheng H, Pei G, Li G, Riffat S. A review on the recent research progress in the compound parabolic concentrator (CPC) for solar energy applications. *Renewable and Sustainable Energy Reviews*. 2018;82:1272-96.
46. Liu Y, Li Z, Green M, Just M, Li YY, Chen X. Titanium dioxide nanomaterials for photocatalysis. *Journal of Physics D: Applied Physics*. 2017;50(19):193003.
47. Wen J, Li X, Liu W, Fang Y, Xie J, Xu Y. Photocatalysis fundamentals and surface modification of TiO₂ nanomaterials. *Chinese Journal of Catalysis*. 2015;36(12):2049-70.

48. Ibhaddon AO, Fitzpatrick P. Heterogeneous photocatalysis: recent advances and applications. *Catalysts*. 2013;3(1):189-218.
49. Pastrana-Martínez LM, Morales-Torres S, Carabineiro SAC, Buijnsters JG, Figueiredo JL, Silva AMT, et al. Photocatalytic activity of functionalized nanodiamond-TiO₂ composites towards water pollutants degradation under UV/Vis irradiation. *Applied Surface Science*. 2018;458:839-48.
50. Boussatha N, Gilliot M, Ghoualem H, Martin J. Formation of nanogranular ZnO ultrathin films and estimation of their performance for photocatalytic degradation of amoxicillin antibiotic. *Materials Research Bulletin*. 2018;99:485-90.
51. Pourtaheri A, Nezamzadeh-Ejhieh A. Photocatalytic properties of incorporated NiO onto clinoptilolite nano-particles in the photodegradation process of aqueous solution of cefixime pharmaceutical capsule. *Chemical Engineering Research and Design*. 2015;104:835-43.
52. Zhao Y, Ji C, Wang Y, Liang X, Fan J. Green and efficient degradation of cefixime by 3D flower-like BiOBr: Performance and degradation pathway. *Colloids and Surfaces A: Physicochemical and Engineering Aspects*. 2022;635:128024.
53. Kar P, Shukla K, Jain P, Sathiyam G, Gupta RK. Semiconductor based photocatalysts for detoxification of emerging pharmaceutical pollutants from aquatic systems: A critical review. *Nano Materials Science*. 2021;3(1):25-46.
54. Kanakaraju D, Glass BD, Oelgemöller M. Titanium dioxide photocatalysis for pharmaceutical wastewater treatment. *Environmental chemistry letters*. 2014;12(1):27-47.
55. Malato S, Fernández-Ibáñez P, Maldonado M, Blanco J, Gernjak W. Decontamination and disinfection of water by solar photocatalysis: recent overview and trends. *Catalysis Today*. 2009;147(1):1-59.
56. Simionescu O-G, Romanițan C, Tutunaru O, Ion V, Buiu O, Avram A. RF magnetron sputtering deposition of TiO₂ thin films in a small continuous oxygen flow rate. *Coatings*. 2019;9(7):442.
57. Akhouri H, Arefi-Khonsari F, Jaiswal A, Pulpytel J, editors. Effect of the deposition method on silver diffusion in Ag-TiO₂ thin coatings: advantages and inconveniences for photocatalytic applications and water treatment. 22nd International Symposium on Plasma Chemistry, Antwerp, Belgium: July; 2015.
58. Varshney G, Kanel SR, Kempisty DM, Varshney V, Agrawal A, Sahle-Demessie E, et al. Nanoscale TiO₂ films and their application in remediation of organic pollutants. *Coordination Chemistry Reviews*. 2016;306:43-64.
59. Peng T, Zhang J, Ray S, Bagh FSG, Fakhouri H, Arefi-Khonsari F, et al. Optimizing one-dimensional TiO₂ for photocatalytic hydrogen production from a water-ethanol mixture and other electron donors. *Journal of Environmental Chemical Engineering*. 2019;7(1):102868.
60. Rawal S, Buer SH, Hawkins W, Sanders JR, Arce PE. Photocatalytic degradation of acetaminophen from water solutions via thin films part I: preparation, characteriation, and analysis of titanium dioxide thin films. *International Journal of Chemical Reactor Engineering*. 2022;20(1):97-112.
61. Peng T, Ray S, Veeravalli SS, Lalman JA, Arefi-Khonsari F. The role of hydrothermal conditions in determining 1D TiO₂ nanomaterials bandgap energies and crystal phases. *Materials Research Bulletin*. 2018;105:104-13.
62. Gnanasekaran L, Hemamalini R, Saravanan R, Ravichandran K, Gracia F, Gupta VK. Intermediate state created by dopant ions (Mn, Co and Zr) into TiO₂ nanoparticles for degradation of dyes under visible light. *Journal of Molecular Liquids*. 2016;223:652-9.
63. Shan AY, Ghazi TIM, Rashid SA. Immobilisation of titanium dioxide onto supporting materials in heterogeneous photocatalysis: A review. *Applied Catalysis A: General*. 2010;389(1-2):1-8.

64. Malesic-Eleftheriadou N, Evgenidou EN, Kyzas GZ, Bikiaris DN, Lambropoulou DA. Removal of antibiotics in aqueous media by using new synthesized bio-based poly(ethylene terephthalate)-TiO₂ photocatalysts. *Chemosphere*. 2019;234:746-55.
65. Lugo-Vega CS, Serrano-Rosales B, de Lasa H. Immobilized particle coating for optimum photon and TiO₂ utilization in scaled air treatment photo reactors. *Applied Catalysis B: Environmental*. 2016;198:211-23.
66. Zhang Y, Xu X. Machine learning band gaps of doped-TiO₂ photocatalysts from structural and morphological parameters. *ACS omega*. 2020;5(25):15344-52.
67. Palominos RA, Mondaca MA, Giraldo A, Peñuela G, Pérez-Moya M, Mansilla HD. Photocatalytic oxidation of the antibiotic tetracycline on TiO₂ and ZnO suspensions. *Catalysis Today*. 2009;144(1):100-5.
68. Robert D, Malato S. Solar photocatalysis: a clean process for water detoxification. *Science of the Total Environment*. 2002;291(1):85-97.
69. Moosavi FS, Tavakoli T. Amoxicillin degradation from contaminated water by solar photocatalysis using response surface methodology (RSM). *Environmental Science and Pollution Research*. 2016;23(22):23262-70.
70. Fendrich MA, Quaranta A, Orlandi M, Bettonte M, Miotello A. Solar concentration for wastewaters remediation: a review of materials and technologies. *Applied Sciences*. 2018;9(1):118.
71. Karunakaran C, Vinayagamoorthy P, Jayabharathi J. Electrical, optical and photocatalytic properties of polyethylene glycol-assisted sol-gel synthesized Mn-doped TiO₂/ZnO core-shell nanoparticles. *Superlattices and Microstructures*. 2013;64:569-80.
72. Niu X, Yan W, Zhao H, Yang J. Synthesis of Nb doped TiO₂ nanotube/reduced graphene oxide heterostructure photocatalyst with high visible light photocatalytic activity. *Applied Surface Science*. 2018;440:804-13.
73. Khan MI, Mehmood B, Mustafa GM, Humaiyoun K, Alwadai N, Almuqrin AH, et al. Effect of silver (Ag) ions irradiation on the structural, optical and photovoltaic properties of Mn doped TiO₂ thin films based dye sensitized solar cells. *Ceramics International*. 2021;47(11):15801-6.
74. Lin MZ, Chen H, Chen WF, Nakaruk A, Koshy P, Sorrell CC. Effect of single-cation doping and codoping with Mn and Fe on the photocatalytic performance of TiO₂ thin films. *International Journal of Hydrogen Energy*. 2014;39(36):21500-11.
75. Bi J, Cao X. Electrochemical Properties and Thin-Film Morphology of Mn-doped TiO₂ Thin Layer Prepared by Electrodeposition Technique and Its application as photocatalyst for Rhodamine B degradation. *INTERNATIONAL JOURNAL OF ELECTROCHEMICAL SCIENCE*. 2021;16(3).
76. Sobczyk-Guzenda A, Owczarek S, Szymanowski H, Wypych-Puszkarski A, Volesky L, Gazicki-Lipman M. Plasma enhanced chemical vapor deposition of iron doped thin dioxide films, their structure and photowetting effect. *Thin Solid Films*. 2015;589:605-12.
77. Moreira AJ, Malafatti JOD, Giraldo TR, Paris EC, Pereira EC, de Mendonça VR, et al. Prozac[®] photodegradation mediated by Mn-doped TiO₂ nanoparticles: Evaluation of by-products and mechanisms proposal. *Journal of Environmental Chemical Engineering*. 2020;8(6):104543.
78. Velardi L, Scrimieri L, Serra A, Manno D, Calcagnile L. Effect of temperature on the physical, optical and photocatalytic properties of TiO₂ nanoparticles. *SN Applied Sciences*. 2020;2(4):1-6.
79. Erdogan N, Bouziani A, Park J, Micusik M, Kim SY, Majkova E, et al. Synthesis and enhanced photocatalytic activity of nitrogen-doped triphasic TiO₂ nanoparticles. *Journal of Photochemistry and Photobiology A: Chemistry*. 2019;377:92-100.

80. Guo R, Bao Y, Kang Q, Liu C, Zhang W, Zhu Q. Solvent-controlled synthesis and photocatalytic activity of hollow TiO₂ microspheres prepared by the solvothermal method. *Colloids and Surfaces A: Physicochemical and Engineering Aspects*. 2022;633:127931.
81. Barrientos L, Allende P, Laguna-Bercero M^Á, Pastroján J, Rodríguez-Becerra J, Cáceres-Jensen L. Controlled Ag-TiO₂ heterojunction obtained by combining physical vapor deposition and bifunctional surface modifiers. *Journal of Physics and Chemistry of Solids*. 2018;119:147-56.
82. Nizard H, Kosinova ML, Fainer NI, Rumyantsev YM, Ayupov BM, Shubin YV. Deposition of titanium dioxide from TTIP by plasma enhanced and remote plasma enhanced chemical vapor deposition. *Surface and Coatings Technology*. 2008;202(17):4076-85.
83. Sobczyk-Guzenda A, Gazicki-Lipman M, Szymanowski H, Kowalski J, Wojciechowski P, Halamus T, et al. Characterization of thin TiO₂ films prepared by plasma enhanced chemical vapour deposition for optical and photocatalytic applications. *Thin Solid Films*. 2009;517(18):5409-14.
84. Melki R, Laoufi NA, Mouheb A. Effects of iron ions, doping methods and nanotubular morphology on TiO₂ solar photocatalytic performance. *Water Science and Technology*. 2021.
85. Sh S, Alipour V, Rahmanian O. High efficient degradation of Cefixime using UV/TiO₂ photocatalytic process: A comparison between photocatalytic and photolytic. *Hormozgan Medical Journal* 2017; 21 (3): 159-168. *Hormozgan Medical Journal* Vol.21:2.
86. Sheydaei M, Shiadeh HRK, Ayoubi-Feiz B, Ezzati R. Preparation of nano N-TiO₂/graphene oxide/titan grid sheets for visible light assisted photocatalytic ozonation of cefixime. *Chemical Engineering Journal*. 2018;353:138-46.
87. Nizard H, Kosinova M, Fainer N, Rumyantsev YM, Ayupov B, Shubin YV. Deposition of titanium dioxide from TTIP by plasma enhanced and remote plasma enhanced chemical vapor deposition. *Surface and Coatings Technology*. 2008;202(17):4076-85.
88. Ito Y, Sakai O, Tachibana K. Study of plasma enhanced chemical vapor deposition of ZnO films by non-thermal plasma jet at atmospheric pressure. *Thin Solid Films*. 2010;518(13):3513-6.
89. Massima Mouele ES, Tijani JO, Badmus KO, Pereao O, Babajide O, Zhang C, et al. Removal of pharmaceutical residues from water and wastewater using dielectric barrier discharge methods—A review. *International Journal of Environmental Research and Public Health*. 2021;18(4):1683.
90. Lin YB, Yang YM, Zhuang B, Huang SL, Wu LP, Huang ZG, et al. Ferromagnetism of Co-doped TiO₂ films prepared by plasma enhanced chemical vapour deposition (PECVD) method. *Journal of Physics D: Applied Physics*. 2008;41(19):195007.
91. Sobczyk-Guzenda A, Owczarek S, Batory D, Balcerzak J, Gazicki-Lipman M, Szymanowski H. The effect of thermal annealing on Fe/TiO₂ coatings deposited with the help of RF PECVD method. Part I. Chemical and phase composition. *Ceramics International*. 2017;43(5):3993-4004.
92. Anagri A, Baitukha A, Debiemme-Chouvy C, Lucas IT, Pulpytel J, Tran TM, et al. Nanocomposite coatings based on graphene and siloxane polymers deposited by atmospheric pressure plasma. Application to corrosion protection of steel. *Surface and Coatings Technology*. 2019;377:124928.
93. Yang W, Wolden CA. Plasma-enhanced chemical vapor deposition of TiO₂ thin films for dielectric applications. *Thin Solid Films*. 2006;515(4):1708-13.
94. Maeda M, Watanabe T. Evaluation of photocatalytic properties of titanium oxide films prepared by plasma-enhanced chemical vapor deposition. *Thin Solid Films*. 2005;489(1-2):320-4.
95. Srivatsa K, Chhikara D, Kumar MS. Synthesis of anatase titania nanostructures at room temperature by PECVD technique. *Journal of Materials Science & Technology*. 2011;27(8):696-700.

96. Zhou M, Roualdès S, Zhao J, Autès V, Ayrat A. Nanocrystalline TiO₂ thin film prepared by low-temperature plasma-enhanced chemical vapor deposition for photocatalytic applications. *Thin Solid Films*. 2015;589:770-7.
97. Sobczyk-Guzenda A, Pietrzyk B, Szymanowski H, Gazicki-Lipman M, Jakubowski W. Photocatalytic activity of thin TiO₂ films deposited using sol–gel and plasma enhanced chemical vapor deposition methods. *Ceramics International*. 2013;39(3):2787-94.
98. Szymanowski H, Sobczyk-Guzenda A, Rylski A, Jakubowski W, Gazicki-Lipman M, Herberth U, et al. Photo-induced properties of thin TiO₂ films deposited using the radio frequency plasma enhanced chemical vapor deposition method. *Thin Solid Films*. 2007;515(13):5275-81.
99. Sobczyk-Guzenda A, Pietrzyk B, Jakubowski W, Szymanowski H, Szymański W, Kowalski J, et al. Mechanical, photocatalytic and microbiological properties of titanium dioxide thin films synthesized with the sol–gel and low temperature plasma deposition techniques. *Materials Research Bulletin*. 2013;48(10):4022-31.
100. Kim D-J, Kang J-Y, Kim K-S. Coating of TiO₂ thin films on particles by a plasma chemical vapor deposition process. *Advanced Powder Technology*. 2010;21(2):136-40.
101. Shahmoradi B, Namratha K, Byrappa K, Soga K, Ananda S, Somashekar R. Enhancement of the photocatalytic activity of modified ZnO nanoparticles with manganese additive. *Research on Chemical Intermediates*. 2011;37(2-5):329-40.
102. Fakhouri H, Arefi-Khonsari F, Jaiswal A, Pulpytel J. Enhanced visible light photoactivity and charge separation in TiO₂/TiN bilayer thin films. *Applied Catalysis A: General*. 2015;492:83-92.
103. Fakhouri H, Pulpytel J, Smith W, Zolfaghari A, Mortaheb HR, Meshkini F, et al. Control of the visible and UV light water splitting and photocatalysis of nitrogen doped TiO₂ thin films deposited by reactive magnetron sputtering. *Applied Catalysis B: Environmental*. 2014;144:12-21.
104. Sekhar MC, Reddy BP, Vattikuti SP, Shanmugam G, Ahn C-H, Park S-H. Structural, Magnetic, and Catalytic Properties of Mn-Doped Titania Nanoparticles Synthesized by a Sol–Gel Process. *Journal of Cluster Science*. 2018;29(6):1255-67.
105. Aba-Guevara CG, Medina-Ramírez IE, Hernández-Ramírez A, Jáuregui-Rincón J, Lozano-Álvarez JA, Rodríguez-López JL. Comparison of two synthesis methods on the preparation of Fe, N-Co-doped TiO₂ materials for degradation of pharmaceutical compounds under visible light. *Ceramics International*. 2017;43(6):5068-79.
106. Erim B, Ciğeroğlu Z, Şahin S, Vasseghian Y. Photocatalytic degradation of cefixime in aqueous solutions using functionalized SWCNT/ZnO/Fe₃O₄ under UV-A irradiation. *Chemosphere*. 2022;291:132929.
107. Grabowska E, Marchelek M, Klimczuk T, Lisowski W, Zaleska-Medynska A. TiO₂/SrTiO₃ and SrTiO₃ microspheres decorated with Rh, Ru or Pt nanoparticles: Highly UV–vis responsible photoactivity and mechanism. *Journal of Catalysis*. 2017;350:159-73.
108. Song J, Xu Z, Liu W, Chang C-T. KBrO₃ and graphene as double and enhanced collaborative catalysts for the photocatalytic degradation of amoxicillin by UVA/TiO₂ nanotube processes. *Materials Science in Semiconductor Processing*. 2016;52:32-7.
109. Sayed M, Arooj A, Shah NS, Khan JA, Shah LA, Rehman F, et al. Narrowing the band gap of TiO₂ by co-doping with Mn²⁺ and Co²⁺ for efficient photocatalytic degradation of enoxacin and its additional peroxidase like activity: a mechanistic approach. *Journal of Molecular Liquids*. 2018;272:403-12.

110. Devi LG, Kottam N, Murthy BN, Kumar SG. Enhanced photocatalytic activity of transition metal ions Mn^{2+} , Ni^{2+} and Zn^{2+} doped polycrystalline titania for the degradation of Aniline Blue under UV/solar light. *Journal of Molecular Catalysis A: Chemical*. 2010;328(1):44-52.
111. Venieri D, Gounaki I, Binas V, Zachopoulos A, Kiriakidis G, Mantzavinos D. Inactivation of MS2 coliphage in sewage by solar photocatalysis using metal-doped TiO_2 . *Applied Catalysis B: Environmental*. 2015;178:54-64.
112. Benjwal P, De B, Kar KK. 1-D and 2-D morphology of metal cation co-doped (Zn, Mn) TiO_2 and investigation of their photocatalytic activity. *Applied Surface Science*. 2018;427:262-72.
113. Quan F, Hu Y, Zhang X, Wei C. Simple preparation of Mn-N-codoped TiO_2 photocatalyst and the enhanced photocatalytic activity under visible light irradiation. *Applied Surface Science*. 2014;320:120-7.
114. Li H, Wang D, Fan H, Jiang T, Li X, Xie T. Synthesis of ordered multivalent Mn- TiO_2 nanospheres with tunable size: A high performance visible-light photocatalyst. *Nano Research*. 2011;4(5):460-9.
115. Umar K, Aris A, Ahmad H, Parveen T, Jaafar J, Majid ZA, et al. Synthesis of visible light active doped TiO_2 for the degradation of organic pollutants—methylene blue and glyphosate. *Journal of Analytical Science and Technology*. 2016;7(1):29.
116. Chen Z, Li Y, Guo M, Xu F, Wang P, Du Y, et al. One-pot synthesis of Mn-doped TiO_2 grown on graphene and the mechanism for removal of Cr(VI) and Cr(III). *Journal of Hazardous Materials*. 2016;310:188-98.
117. Sudrajat H, Babel S, Ta AT, Nguyen TK. Mn-doped TiO_2 photocatalysts: Role, chemical identity, and local structure of dopant. *Journal of Physics and Chemistry of Solids*. 2020;144:109517.
118. Bunke D, Moritz S, Brack W, Herráez DL, Posthuma L, Nuss M. Developments in society and implications for emerging pollutants in the aquatic environment. *Environmental Sciences Europe*. 2019;31(1):1-17.
119. Kalogirou SA. *Solar energy engineering: processes and systems*: Academic press; 2013.
120. Shahsavari A, Akbari M. Potential of solar energy in developing countries for reducing energy-related emissions. *Renewable and Sustainable Energy Reviews*. 2018;90:275-91.
121. Kabir E, Kumar P, Kumar S, Adelodun AA, Kim K-H. Solar energy: Potential and future prospects. *Renewable and Sustainable Energy Reviews*. 2018;82:894-900.
122. Hayat MB, Ali D, Monyake KC, Alagha L, Ahmed N. Solar energy—A look into power generation, challenges, and a solar-powered future. *International Journal of Energy Research*. 2019;43(3):1049-67.
123. Rabaia MKH, Abdelkareem MA, Sayed ET, Elsaid K, Chae K-J, Wilberforce T, et al. Environmental impacts of solar energy systems: A review. *Science of The Total Environment*. 2021;754:141989.
124. Mirzabe AH, Hajiahmad A, Keyhani A. Assessment and categorization of empirical models for estimating monthly, daily, and hourly diffuse solar radiation: A case study of Iran. *Sustainable Energy Technologies and Assessments*. 2021;47:101330.
125. Naserpour S, Zolfaghari H, Firouzabadi PZ. Calibration and evaluation of sunshine-based empirical models for estimating daily solar radiation in Iran. *Sustainable Energy Technologies and Assessments*. 2020;42:100855.
126. Alamdari P, Nematollahi O, Alemrajabi AA. Solar energy potentials in Iran: A review. *Renewable and Sustainable Energy Reviews*. 2013;21:778-88.
127. Cambié D, Noël T. Solar photochemistry in flow. *Accounts on Sustainable Flow Chemistry*. 2020:1-27.

128. Rodríguez SM, Gálvez JB, Rubio MM, Ibáñez PF, Padilla DA, Pereira MC, et al. Engineering of solar photocatalytic collectors. *Solar Energy*. 2004;77(5):513-24.
129. Tanveer M, Guyer GT. Solar assisted photo degradation of wastewater by compound parabolic collectors: Review of design and operational parameters. *Renewable and Sustainable Energy Reviews*. 2013;24:534-43.
130. Malato S, Maldonado MI, Fernandez-Ibanez P, Oller I, Polo I, Sánchez-Moreno R. Decontamination and disinfection of water by solar photocatalysis: The pilot plants of the Plataforma Solar de Almeria. *Materials Science in Semiconductor Processing*. 2016;42:15-23.
131. Abdel-Maksoud Y, Imam E, Ramadan A. TiO₂ solar photocatalytic reactor systems: selection of reactor design for scale-up and commercialization—analytical review. *Catalysts*. 2016;6(9):138.
132. Spasiano D, Marotta R, Malato S, Fernandez-Ibanez P, Di Somma I. Solar photocatalysis: Materials, reactors, some commercial, and pre-industrialized applications. A comprehensive approach. *Applied Catalysis B: Environmental*. 2015;170:90-123.
133. Marcelino R, Queiroz M, Amorim C, Leão M, Brites-Nóbrega F. Solar energy for wastewater treatment: review of international technologies and their applicability in Brazil. *Environmental Science and Pollution Research*. 2015;22(2):762-73.
134. Malato S, Blanco J, Vidal A, Richter C. Photocatalysis with solar energy at a pilot-plant scale: an overview. *Applied Catalysis B: Environmental*. 2002;37(1):1-15.
135. Gálvez JB, Rodríguez SM. SOLAR PHOTOCHEMISTRY TECHNOLOGY. *Solar Energy Conversion And Photoenergy System-Volume II*. 2009;8:139.
136. Gálvez JB, Rodríguez SM. SOLAR PHOTOCHEMISTRY TECHNOLOGY. *Solar Energy Conversion And Photoenergy System-Volume II*. 2009:139.
137. Malato S, Blanco J, Alarcón DC, Maldonado MI, Fernández-Ibáñez P, Gernjak W. Photocatalytic decontamination and disinfection of water with solar collectors. *Catalysis Today*. 2007;122(1):137-49.
138. Jing D, Liu H, Zhang X, Zhao L, Guo L. Photocatalytic hydrogen production under direct solar light in a CPC based solar reactor: reactor design and preliminary results. *Energy Conversion and Management*. 2009;50(12):2919-26.
139. Avargani VM, Karimi R, Gheini TT. Mathematical modeling of an integrated system for regeneration of solid desiccants using a solar parabolic dish concentrator. *International Journal of Heat and Mass Transfer*. 2019;142:118479.
140. Blanco J, Malato S, Fernández P, Vidal A, Morales A, Trincado P, et al. Compound parabolic concentrator technology development to commercial solar detoxification applications. *Solar Energy*. 1999;67(4):317-30.
141. Pereira JH, Reis AC, Queirós D, Nunes OC, Borges MT, Vilar VJ, et al. Insights into solar TiO₂-assisted photocatalytic oxidation of two antibiotics employed in aquatic animal production, oxolinic acid and oxytetracycline. *Science of the total Environment*. 2013;463:274-83.
142. De la Cruz N, Dantas R, Giménez J, Esplugas S. Photolysis and TiO₂ photocatalysis of the pharmaceutical propranolol: solar and artificial light. *Applied Catalysis B: Environmental*. 2013;130:249-56.
143. Sousa M, Gonçalves C, Pereira JH, Vilar VJ, Boaventura RA, Alpendurada M. Photolytic and TiO₂-assisted photocatalytic oxidation of the anxiolytic drug lorazepam (Lorenin® pills) under artificial UV light and natural sunlight: A comparative and comprehensive study. *Solar energy*. 2013;87:219-28.
144. Pereira JH, Reis AC, Queirós D, Nunes OC, Borges MT, Vilar VJ, et al. Insights into solar TiO₂-assisted photocatalytic oxidation of two antibiotics employed in aquatic animal production, oxolinic acid and oxytetracycline. *Science of the Total Environment*. 2013;463:274-83.

145. Ajona J, Vidal A. The use of CPC collectors for detoxification of contaminated water: Design, construction and preliminary results. *Solar energy*. 2000;68(1):109-20.
146. Paschoalino MP, Paschoalino FC, Jardim WF, Sodré FF. An easy and cheap procedure to immobilize TiO₂ on glass surfaces using TiO₂/SiO₂ nanocomposite: Characterization and performance for the degradation of micropollutants of emerging concern in aqueous solutions. *Chemistry of the Total Environment*. 2021;1(1):9-19.
147. Maffessoni D, Grazziotin IC, Klauck CR, Benvenuti T, da Silva SW, Meneguzzi A. Heterogeneous photocatalysis of moxifloxacin at a pilot solar compound parabolic collector: Elimination of the genotoxicity. *Journal of Environmental Management*. 2021;297:113296.
148. Talwar S, Verma AK, Sangal VK, Štangar UL. Once through continuous flow removal of metronidazole by dual effect of photo-Fenton and photocatalysis in a compound parabolic concentrator at pilot plant scale. *Chemical Engineering Journal*. 2020;388:124184.
149. Wang H, Liu Q, You C. Regeneration of sulfur-deactivated TiO₂ photocatalysts. *Applied Catalysis A: General*. 2019;572:15-23.
150. Cao L, Gao Z, Suib SL, Obee TN, Hay SO, Freihaut JD. Photocatalytic oxidation of toluene on nanoscale TiO₂ catalysts: studies of deactivation and regeneration. *Journal of Catalysis*. 2000;196(2):253-61.
151. SHENG Z, Yufeng H, Jianming X, Xiaoming W, Weiping L. SO₂ poisoning and regeneration of Mn-Ce/TiO₂ catalyst for low temperature NO_x reduction with NH₃. *Journal of Rare Earths*. 2012;30(7):676-82.
152. Miranda-García N, Suárez S, Maldonado MI, Malato S, Sánchez B. Regeneration approaches for TiO₂ immobilized photocatalyst used in the elimination of emerging contaminants in water. *Catalysis Today*. 2014;230:27-34.
153. Shang J, Zhu Y, Du Y, Xu Z. Comparative studies on the deactivation and regeneration of TiO₂ nanoparticles in three photocatalytic oxidation systems: C₇H₁₆, SO₂, and C₇H₁₆–SO₂. *Journal of Solid State Chemistry*. 2002;166(2):395-9.
154. Gandhi VG, Mishra MK, Joshi PA. A study on deactivation and regeneration of titanium dioxide during photocatalytic degradation of phthalic acid. *Journal of Industrial and Engineering Chemistry*. 2012;18(6):1902-7.
155. Liqiang J, Baifu X, Fulong Y, Baiqi W, Keying S, Weimin C, et al. Deactivation and regeneration of ZnO and TiO₂ nanoparticles in the gas phase photocatalytic oxidation of n-C₇H₁₆ or SO₂. *Applied Catalysis A: General*. 2004;275(1-2):49-54.
156. Cunha DL, Kuznetsov A, Achete CA, da Hora Machado AE, Marques M. Immobilized TiO₂ on glass spheres applied to heterogeneous photocatalysis: Photoactivity, leaching and regeneration process. *PeerJ*. 2018;6:e4464.
157. Sun R-D, Nakajima A, Watanabe T, Hashimoto K. Decomposition of gas-phase octamethyltrisiloxane on TiO₂ thin film photocatalysts—catalytic activity, deactivation, and regeneration. *Journal of Photochemistry and Photobiology A: Chemistry*. 2003;154(2-3):203-9.
158. Nie L, Zhou P, Yu J, Jaroniec M. Deactivation and regeneration of Pt/TiO₂ nanosheet-type catalysts with exposed (001) facets for room temperature oxidation of formaldehyde. *Journal of Molecular Catalysis A: Chemical*. 2014;390:7-13.
159. Zhuang K, ZHANG Y-p, HUANG T-j, Bin L, Kai S. Sulfur-poisoning and thermal reduction regeneration of holmium-modified Fe-Mn/TiO₂ catalyst for low-temperature SCR. *Journal of Fuel Chemistry and Technology*. 2017;45(11):1356-64.

160. Yang X, Sun H, Li G, An T, Choi W. Fouling of TiO₂ induced by natural organic matters during photocatalytic water treatment: Mechanisms and regeneration strategy. *Applied Catalysis B: Environmental*. 2021;294:120252.
161. RAHMANI A, NIKRAVECH M. Reformage du Biogaz dans une Décharge à Barrière Diélectrique Surfactive DBDs. Influence de l'argon sur la distribution des produits liquides.
162. Rahmani A. Mise en oeuvre de procédé plasma-catalyse destiné à la valorisation du biogaz (CH₄+ CO₂) en carburants liquides. Etude expérimentale et modélisations: Sorbonne Paris Cité; 2018.
163. Baba K, Lazzaroni C, Nikravech M. Growth of ZnO thin films by spray plasma technique: Correlation between spectroscopic measurements and film properties. *Plasma Chemistry and Plasma Processing*. 2014;34(6):1433-46.
164. Martinet C, Paillard V, Gagnaire A, Joseph J. Deposition of SiO₂ and TiO₂ thin films by plasma enhanced chemical vapor deposition for antireflection coating. *Journal of Non-Crystalline Solids*. 1997;216:77-82.
165. Armstrong C, Delumeau L-V, Muñoz-Rojas D, Kursumovic A, MacManus-Driscoll J, Musselman KP. Tuning the band gap and carrier concentration of titania films grown by spatial atomic layer deposition: a precursor comparison. *Nanoscale advances*. 2021;3(20):5908-18.
166. Moosavi F, Cheng C, Gheinani T, Traore M, Kanaev A, Nikravech M. Photocatalytic destruction of amoxicillin in a pilot sunlight reactor with supported titania nano-photocatalyst. *Chemical Engineering Transactions*. 2019.
167. Fanou GD, Yao B, Cheng K, Brinza O, Traoré M, Kanaev A, et al. Elaboration of Novel Nanoparticulate TiO₂-P25@ n-TiO₂ Composite for Photocatalysis. *Int J of Advanced Applied Physics Research*. 2016;3(1):19-25.
168. Cheng K, Chhor K, Passarello JP, Colbeau-Justin C, Kanaev A. Photocatalytic Nanoparticulate Zr_xTi_{1-x}O₂ Coatings with Controlled Homogeneity of Elemental Composition. *ChemistrySelect*. 2018;3(39):11118-26.
169. Mendez MS. Elaboration of mixed metal oxide nanoparticles for applications in photocatalysis: Université Paris-Nord-Paris XIII; 2021.
170. Cheng K. Elaboration de nano-photocatalyseurs mixtes à base d'oxide de métal Zr_xTi_{1-x}O₂: Sorbonne Paris Cité; 2018.
171. Cheng K. Elaboration of mixed metal oxide Zr_xTi_{1-x}O₂ nano-photocatalysts
Elaboration de nano-photocatalyseurs mixtes à base d'oxide de métal Zr_xTi_{1-x}O₂: Université Sorbonne Paris Cité; 2018.
172. Kenney JP, Veeramani H, Alessi DS. *Analytical Geomicrobiology*: Cambridge University Press; 2019.
173. Kerkez-Kuyumcu Ö, Kibar E, Dayıoğlu K, Gedik F, Akın AN, Özkara-Aydınoğlu Ş. A comparative study for removal of different dyes over M/TiO₂ (M=Cu, Ni, Co, Fe, Mn and Cr) photocatalysts under visible light irradiation. *Journal of Photochemistry and Photobiology A: Chemistry*. 2015;311:176-85.
174. Spurr RA, Myers H. Quantitative analysis of anatase-rutile mixtures with an X-ray diffractometer. *Analytical chemistry*. 1957;29(5):760-2.
175. Triyana K, Nurwantoro P. Effect of oxygen ratio on the Electrical and optical properties of TiO₂ films deposited by DC reactive sputtering technique.
176. Rugar D, Hansma P. Atomic force microscopy. *Physics today*. 1990;43(10):23-30.
177. Malard L, Pimenta MA, Dresselhaus G, Dresselhaus M. Raman spectroscopy in graphene. *Physics reports*. 2009;473(5-6):51-87.

178. Wu J-B, Lin M-L, Cong X, Liu H-N, Tan P-H. Raman spectroscopy of graphene-based materials and its applications in related devices. *Chemical Society Reviews*. 2018;47(5):1822-73.
179. Balachandran U, Eror N. Raman spectra of titanium dioxide. *Journal of Solid State Chemistry*. 1982;42(3):276-82.
180. Birnal P, Marco de Lucas MC, Pochard I, Domenichini B, Imhoff L. Photocatalytic properties of atomic layer deposited TiO₂ inverse opals and planar films for the degradation of dyes. *Applied Surface Science*. 2020;512:145693.
181. Wu C-Y, Hong S-C, Hwang F-T, Lai L-W, Lin T-W, Liu D-S. Effect of nickel oxide seed layers on annealed-amorphous titanium oxide thin films prepared using plasma-enhanced chemical vapor deposition. *Thin Solid Films*. 2011;520(1):320-7.
182. Kim GH, Kim SD, Park SH. Plasma enhanced chemical vapor deposition of TiO₂ films on silica gel powders at atmospheric pressure in a circulating fluidized bed reactor. *Chemical Engineering and Processing: Process Intensification*. 2009;48(6):1135-9.
183. Li D, Bulou S, Gautier N, Elisabeth S, Goullet A, Richard-Plouet M, et al. Nanostructure and photocatalytic properties of TiO₂ films deposited at low temperature by pulsed PECVD. *Applied Surface Science*. 2019;466:63-9.
184. Orendorz A, Brodyanski A, Lösch J, Bai L, Chen Z, Le Y, et al. Phase transformation and particle growth in nanocrystalline anatase TiO₂ films analyzed by X-ray diffraction and Raman spectroscopy. *Surface Science*. 2007;601(18):4390-4.
185. Collette S, Hubert J, Batan A, Baert K, Raes M, Vandendael I, et al. Photocatalytic TiO₂ thin films synthesized by the post-discharge of an RF atmospheric plasma torch. *Surface and Coatings Technology*. 2016;289:172-8.
186. Li D, Carette M, Granier A, Landesman JP, Goullet A. Spectroscopic ellipsometry analysis of TiO₂ films deposited by plasma enhanced chemical vapor deposition in oxygen/titanium tetraisopropoxide plasma. *Thin Solid Films*. 2012;522:366-71.
187. Pirgholi-Givi G, Farjami-Shayesteh S, Azizian-Kalandaragh Y. The influence of irradiation intensity and stirring rate on the photocatalytic activity of titanium dioxide nanostructures prepared by the microwave-assisted method for photodegradation of MB from water. *Physica B: Condensed Matter*. 2020;578:411886.
188. Xia T, Zhang Y, Murowchick J, Chen X. Vacuum-treated titanium dioxide nanocrystals: Optical properties, surface disorder, oxygen vacancy, and photocatalytic activities. *Catalysis Today*. 2014;225:2-9.
189. Lin YB, Yang YM, Zhuang B, Huang SL, Wu LP, Huang ZG, et al. Ferromagnetism of Co-doped TiO₂ films prepared by plasma enhanced chemical vapour deposition (PECVD) method. *Journal of Physics D: Applied Physics*. 2008;41(19):195007.
190. Iatsunskiy I, Kempinski M, Nowaczyk G, Jancelewicz M, Pavlenko M, Załęski K, et al. Structural and XPS studies of PSi/TiO₂ nanocomposites prepared by ALD and Ag-assisted chemical etching. *Applied Surface Science*. 2015;347:777-83.
191. Benito N, Palacio C. Mixed Ti–O–Si oxide films formation by oxidation of titanium–silicon interfaces. *Applied surface science*. 2014;301:436-41.
192. Karches M, Morstein M, Von Rohr PR, Pozzo RL, Giombi JL, Baltanás MA. Plasma-CVD-coated glass beads as photocatalyst for water decontamination. *Catalysis Today*. 2002;72(3-4):267-79.
193. Lee C-S, Kim J, Son JY, Choi W, Kim H. Photocatalytic functional coatings of TiO₂ thin films on polymer substrate by plasma enhanced atomic layer deposition. *Applied Catalysis B: Environmental*. 2009;91(3):628-33.

194. Zhong N, Shima H, Akinaga H. Mechanism of the performance improvement of TiO₂-x-based field-effect transistor using SiO₂ as gate insulator. *AIP advances*. 2011;1(3):032167.
195. Hu E-T, Liu X-X, Cai Q-Y, Yao Y, Zang K-Y, Yu K-H, et al. Tunable optical properties of co-sputtered Ti-SiO₂ nanocomposite thin films. *Optical Materials Express*. 2017;7(7):2387-95.
196. Cao Y-Q, Zhao X-R, Chen J, Zhang W, Li M, Zhu L, et al. TiO_xNy modified TiO₂ powders prepared by plasma enhanced atomic layer deposition for highly visible light photocatalysis. *Scientific reports*. 2018;8(1):1-9.
197. Mauchauffé R, Kang S, Kim J, Kim J-H, Moon SY. Spectroscopic study of an atmospheric pressure plasma generated for the deposition of titanium dioxide thin films. *Current Applied Physics*. 2019;19(11):1296-304.
198. Tseng Y-H, Kuo C-H. Photocatalytic degradation of dye and NO_x using visible-light-responsive carbon-containing TiO₂. *Catalysis Today*. 2011;174(1):114-20.
199. Gazal Y, Dublanche-Tixier C, Chazelas C, Colas M, Carles P, Tristant P. Multi-structural TiO₂ film synthesised by an atmospheric pressure plasma-enhanced chemical vapour deposition microwave torch. *Thin Solid Films*. 2016;600:43-52.
200. Mehonic A, Buckwell M, Montesi L, Garnett L, Hudziak S, Fearn S, et al. Structural changes and conductance thresholds in metal-free intrinsic SiO_x resistive random access memory. *Journal of Applied Physics*. 2015;117(12):124505.
201. Hollinger G, Himpsel F. Probing the transition layer at the SiO₂-Si interface using core level photoemission. *Applied Physics Letters*. 1984;44(1):93-5.
202. Cardinaud C, Rhounna A, Turban G, Grolleau B. Analyse XPS des surfaces de Si et SiO₂ exposées aux plasmas de CHF₃ et CHF₃—C₂F₆. Polymérisation et gravure. *Revue de physique appliquée*. 1989;24(3):309-21.
203. Yates JT. Water interactions with silica surfaces: A big role for surface structure. *Surface science*. 2004;565(2-3):103-6.
204. Wendt S, Frerichs M, Wei T, Chen M, Kempter V, Goodman D. The interaction of water with silica thin films grown on Mo (1 1 2). *Surface science*. 2004;565(2-3):107-20.
205. Butz R, Rubloff G, Ho P. Chemical bonding and reactions at Ti/Si and Ti/oxygen/Si interfaces. *Journal of Vacuum Science & Technology A: Vacuum, Surfaces, and Films*. 1983;1(2):771-5.
206. Gaultois MW, Grosvenor AP. XANES and XPS investigations of (TiO₂)_x(SiO₂)_{1-x}: the contribution of final-state relaxation to shifts in absorption and binding energies. *Journal of Materials Chemistry*. 2011;21(6):1829-36.
207. Kadam A, Dhabbe R, Shin D-S, Garadkar K, Park J. Sunlight driven high photocatalytic activity of Sn doped N-TiO₂ nanoparticles synthesized by a microwave assisted method. *Ceramics International*. 2017;43(6):5164-72.
208. Banerjee AN, Hamnabard N, Joo SW. A comparative study of the effect of Pd-doping on the structural, optical, and photocatalytic properties of sol-gel derived anatase TiO₂ nanoparticles. *Ceramics International*. 2016;42(10):12010-26.
209. Schneider CA, Rasband WS, Eliceiri KW. NIH Image to ImageJ: 25 years of image analysis. *Nature Methods*. 2012;9(7):671-5.
210. Bouslama M, Amamra M, Jia Z, Ben Amar M, Chhor K, Brinza O, et al. Nanoparticulate TiO₂–Al₂O₃ photocatalytic media: effect of particle size and polymorphism on photocatalytic activity. *ACS Catalysis*. 2012;2(9):1884-92.

211. Zhang J, Li M, Feng Z, Chen J, Li C. UV Raman spectroscopic study on TiO₂. I. Phase transformation at the surface and in the bulk. *The Journal of Physical Chemistry B*. 2006;110(2):927-35.
212. Banfield J. Thermodynamic analysis of phase stability of nanocrystalline titania. *Journal of Materials Chemistry*. 1998;8(9):2073-6.
213. Zhang H, Banfield JF. New kinetic model for the nanocrystalline anatase-to-rutile transformation revealing rate dependence on number of particles. *American Mineralogist*. 1999;84(4):528-35.
214. Penn RL, Banfield JF. Formation of rutile nuclei at anatase {112} twin interfaces and the phase transformation mechanism in nanocrystalline titania. *American Mineralogist*. 1999;84(5-6):871-6.
215. Barborini E, Kholmanov I, Piseri P, Ducati C, Bottani CE, Milani P. Engineering the nanocrystalline structure of TiO₂ films by aerodynamically filtered cluster deposition. *Applied physics letters*. 2002;81(16):3052-4.
216. Nikravech M, Baba K, Leneindre B, Rousseau F. Role of reactive species in processing materials at laboratory temperature by spray plasma devices. *Chemical Papers*. 2012;66(5):502-10.
217. Dias JA, Freire ALF, Girotto I, Roveri CD, Mastelaro VR, Paris EC, et al. Phase evolution and optical properties of nanometric Mn-doped TiO₂ pigments. *Materials Today Communications*. 2021;27:102295.
218. Howard C, Sabine T, Dickson F. Structural and thermal parameters for rutile and anatase. *Acta Crystallographica Section B: Structural Science*. 1991;47(4):462-8.
219. Bharati B, Mishra NC, Sinha ASK, Rath C. Unusual structural transformation and photocatalytic activity of Mn doped TiO₂ nanoparticles under sunlight. *Materials Research Bulletin*. 2020;123:110710.
220. Li H, Wang D, Fan H, Jiang T, Li X, Xie T. Synthesis of ordered multivalent Mn-TiO₂ nanospheres with tunable size: A high performance visible-light photocatalyst. *Nano Research*. 2011;4(5):460-9.
221. Binas V, Stefanopoulos V, Kiriakidis G, Papagiannakopoulos P. Photocatalytic oxidation of gaseous benzene, toluene and xylene under UV and visible irradiation over Mn-doped TiO₂ nanoparticles. *Journal of Materiomics*. 2019;5(1):56-65.
222. Caligulu U, Darcan N, Kejanli H. Surface morphology and optical properties of Ca and Mn doped TiO₂ nano-structured thin films. *Engineering Science and Technology, an International Journal*. 2021;24(6):1292-300.
223. Krueve A, Rebane R, Kipper K, Oldekop M-L, Evard H, Herodes K, et al. Tutorial review on validation of liquid chromatography–mass spectrometry methods: Part I. *Analytica Chimica Acta*. 2015;870:29-44.
224. Gaya UI, Abdullah AH. Heterogeneous photocatalytic degradation of organic contaminants over titanium dioxide: A review of fundamentals, progress and problems. *Journal of Photochemistry and Photobiology C: Photochemistry Reviews*. 2008;9(1):1-12.
225. Faisal M, Abu Tariq M, Muneer M. Photocatalysed degradation of two selected dyes in UV-irradiated aqueous suspensions of titania. *Dyes and Pigments*. 2007;72(2):233-9.
226. Singh HK, Saquib M, Haque MM, Muneer M, Bahnemann DW. Titanium dioxide mediated photocatalysed degradation of phenoxyacetic acid and 2, 4, 5-trichlorophenoxyacetic acid, in aqueous suspensions. *Journal of Molecular Catalysis A: Chemical*. 2007;264(1-2):66-72.
227. Lazzaroni C, Baba K, Nikravech M, Chabert P. Model of a low-pressure radio-frequency inductive discharge in Ar/O₂ used for plasma spray deposition. *Journal of Physics D: Applied Physics*. 2012;45(48):485207.

228. Šícha J, Heřman D, Musil J, Strýhal Z, Pavlík J. High-rate low-temperature dc pulsed magnetron sputtering of photocatalytic TiO₂ films: the effect of repetition frequency. *Nanoscale Research Letters*. 2007;2(3):123-9.
229. Shaniba C, Akbar M, Ramseena K, Raveendran P, Narayanan BN, Ramakrishnan RM. Sunlight-assisted oxidative degradation of cefixime antibiotic from aqueous medium using TiO₂/nitrogen doped holey graphene nanocomposite as a high performance photocatalyst. *Journal of Environmental Chemical Engineering*. 2020;8(1):102204.
230. SAHRAEIAN S, VALIPOUR M, RAHMANIAN O. High efficient degradation of Cefixime using UV/TiO₂ photocatalytic process: A comparison between photocatalytic and photolytic. 2017.
231. Pino-Sandoval DA, Hinojosa-Reyes L, Guzmán-Mar JL, Murillo-Sierra JC, Hernández-Ramírez A. Solar photocatalysis for degradation of pharmaceuticals in hospital wastewater: Influence of the type of catalyst, aqueous matrix, and toxicity evaluation. *Water, Air, & Soil Pollution*. 2022;233(1):1-17.
232. De la Cruz N, Dantas R, Giménez J, Esplugas S. Photolysis and TiO₂ photocatalysis of the pharmaceutical propranolol: solar and artificial light. *Applied Catalysis B: Environmental*. 2013;130:249-56.
233. Martínez-Costa JI, Maldonado Rubio MI, Leyva-Ramos R. Degradation of emerging contaminants diclofenac, sulfamethoxazole, trimethoprim and carbamazepine by bentonite and vermiculite at a pilot solar compound parabolic collector. *Catalysis Today*. 2020;341:26-36.
234. Fend T, Jorgensen G, Küster H. Applicability of highly reflective aluminium coil for solar concentrators. *Solar Energy*. 2000;68(4):361-70.
235. Inturi SNR, Boningari T, Suidan M, Smirniotis PG. Visible-light-induced photodegradation of gas phase acetonitrile using aerosol-made transition metal (V, Cr, Fe, Co, Mn, Mo, Ni, Cu, Y, Ce, and Zr) doped TiO₂. *Applied Catalysis B: Environmental*. 2014;144:333-42.
236. El Mragui A, Zegaoui O, Daou I. Synthesis, characterization and photocatalytic properties under visible light of doped and co-doped TiO₂-based nanoparticles. *Materials Today: Proceedings*. 2019;13:857-65.
237. Chang S-m, Liu W-s. The roles of surface-doped metal ions (V, Mn, Fe, Cu, Ce, and W) in the interfacial behavior of TiO₂ photocatalysts. *Applied Catalysis B: Environmental*. 2014;156-157:466-75.
238. Rashad MM, Elsayed EM, Al-Kotb MS, Shalan AE. The structural, optical, magnetic and photocatalytic properties of transition metal ions doped TiO₂ nanoparticles. *Journal of Alloys and Compounds*. 2013;581:71-8.
239. Sanchez Mendez M, Lemarchand A, Traore M, Perruchot C, Sassoye C, Selmane M, et al. Photocatalytic Activity of Nanocoatings Based on Mixed Oxide V-TiO₂ Nanoparticles with Controlled Composition and Size. *Catalysts*. 2021;11(12):1457.
240. Sanchez Mendez M, Lemarchand A, Traore M, Ben Amar M, Perruchot C, Nikravech M, et al. Preparation and Photocatalytic Activity of Coatings based on Size-selective V-TiO₂ Nanoparticles. *Chemical Engineering Transactions*. 2021.
241. Sanchez Mendez M, Jia Z, Traore M, Ben Amar M, Nikravech M, Kanaev A. Nucleation and growth of mixed vanadium-titanium oxo-alkoxy nanoparticles in sol-gel synthesis. *Colloids and Surfaces A: Physicochemical and Engineering Aspects*. 2021;610:125636.
242. You YS, Chung K-H, Kim YM, Kim J-H, Seo G. Deactivation and regeneration of titania catalyst supported on glass fiber in the photocatalytic degradation of toluene. *Korean Journal of Chemical Engineering*. 2003;20(1):58-64.

243. Dalto F, Kuźniarska-Biernacka I, Pereira C, Mesquita E, Soares OSG, Pereira MFR, et al. Solar light-induced methylene blue removal over TiO₂/AC composites and photocatalytic regeneration. *Nanomaterials*. 2021;11(11):3016.
244. Chekir N, Tassalit D, Benhabiles O, Sahraoui N, Mellal M. Effective removal of paracetamol in compound parabolic collectors and fixed bed reactors under natural sunlight. *Water Science and Technology*. 2020;82(11):2460-71.
245. Zhang T, Zhou R, Wang P, Mai-Prochnow A, McConchie R, Li W, et al. Degradation of cefixime antibiotic in water by atmospheric plasma bubbles: Performance, degradation pathways and toxicity evaluation. *Chemical Engineering Journal*. 2021;421:127730.
246. Leblebici ME, Rongé J, Martens JA, Stefanidis GD, Van Gerven T. Computational modelling of a photocatalytic UV-LED reactor with internal mass and photon transfer consideration. *Chemical Engineering Journal*. 2015;264:962-70.
247. Malayeri M, Lee C-S, Haghghat F, Klimes L. Modeling of gas-phase heterogeneous photocatalytic oxidation reactor in the presence of mass transfer limitation and axial dispersion. *Chemical Engineering Journal*. 2020;386:124013.
248. Ávila-López MA, Gavrielides S, Luo X, Ojoajogwu AE, Tan JZ, Luévano-Hipólito E, et al. Comparative study of CO₂ photoreduction using different conformations of CuO photocatalyst: Powder, coating on mesh and thin film. *Journal of CO₂ Utilization*. 2021;50:101588.
249. Malayeri M, Haghghat F, Lee C-S. Kinetic modeling of the photocatalytic degradation of methyl ethyl ketone in air for a continuous-flow reactor. *Chemical Engineering Journal*. 2021;404:126602.
250. Zhao L, You H, Wang S. Design-simulation of light radiation of a novel fixed-bed photocatalytic system with LED arrays on the engineering-outlook. *Journal of Photochemistry and Photobiology A: Chemistry*. 2022;429:113889.
251. Coto M, Troughton S, Knight P, Joshi R, Francis R, Kumar R, et al. Optimization of the microstructure of TiO₂ photocatalytic surfaces created by Plasma Electrolytic Oxidation of titanium substrates. *Surface and Coatings Technology*. 2021;411:127000.
252. Corbel S, Becheikh N, Roques-Carmes T, Zahraa O. Mass transfer measurements and modeling in a microchannel photocatalytic reactor. *Chemical Engineering Research and Design*. 2014;92(4):657-62.
253. Yusuf A, Palmisano G. Three-dimensional CFD modelling of a photocatalytic parallel-channel microreactor. *Chemical Engineering Science*. 2021;229:116051.
254. Vaiano V, Sacco O, Pisano D, Sannino D, Ciambelli P. From the design to the development of a continuous fixed bed photoreactor for photocatalytic degradation of organic pollutants in wastewater. *Chemical Engineering Science*. 2015;137:152-60.
255. Rabanimehr F, Farhadian M, Solaimany Nazar AR, Behineh ES. Simulation of photocatalytic degradation of methylene blue in planar microreactor with integrated ZnO nanowires. *Journal of Applied Research in Water and Wastewater*. 2021;8(1):36-40.
256. Behineh ES, Solaimany Nazar AR, Farhadian M, Rabanimehr F. Three-dimensional simulation of microcapillary and microchannel photo reactors for organic pollutant degradation from contaminated water using computational fluid dynamics. *Advances in Environmental Technology*. 2019;5(4):229-37.
257. Rahmani E, Rahmani M, Silab HR. TiO₂: SiO₂ thin film coated annular photoreactor for degradation of oily contamination from waste water. *Journal of Water Process Engineering*. 2020;37:101374.

258. Edlén B. The dispersion of standard air. *Josa*. 1953;43(5):339-44.
259. Shurcliff WA. Polarized Light: Production and Use, Harvard Univ. Press, Cambridge, Mass. 1962.
260. Born M, Wolf E. Principles of Optics: Electromagnetic Theory of Propagation, Interference and Diffraction of Light. 7 ed. Cambridge: Cambridge University Press; 1999.
261. Yeh P. Matrix formulation for isotropic layered media. *Optical waves in layered media*. 2005;102-14.
262. Stavroudis O. The optics of rays, wavefronts, and caustics, vol. 38 of. Pure and applied physics. 1972.
263. Landau L. EM L1~ sHl~ z. The classical theory of fields. 4th revised English ed. Pergamon, New York, NY; 1975.
264. Maugin GA. The thermomechanics of nonlinear irreversible behaviours: World scientific; 1999.
265. Bird R, Stewart W, Lightfoot E. Polymeric liquids. Transport Phenomena, revised 2nd ed, John Wiley & Sons, New York. 2007:231-42.
266. Batchelor CK, Batchelor GK. An introduction to fluid dynamics: Cambridge university press; 1967.
267. Panton RL. Incompressible flow: John Wiley & Sons; 2006.
268. Mills A, Wang J, Ollis DF. Dependence of the kinetics of liquid-phase photocatalyzed reactions on oxygen concentration and light intensity. *Journal of catalysis*. 2006;243(1):1-6.
269. Khataee A, Fathinia M, Aber S. Kinetic modeling of liquid phase photocatalysis on supported TiO₂ nanoparticles in a rectangular flat-plate photoreactor. *Industrial & Engineering Chemistry Research*. 2010;49(24):12358-64.
270. Goetz V, Cambon J, Sacco D, Plantard G. Modeling aqueous heterogeneous photocatalytic degradation of organic pollutants with immobilized TiO₂. *Chemical Engineering and Processing: Process Intensification*. 2009;48(1):532-7.
271. Meng Y, Huang X, Wu Y, Wang X, Qian Y. Kinetic study and modeling on photocatalytic degradation of para-chlorobenzoate at different light intensities. *Environmental Pollution*. 2002;117(2):307-13.

Abstract

This work investigated the application of solar photocatalysis for the degradation of cefixime antibiotic using immobilized TiO_2 films on substrates. The experiments were performed in a (CPC) solar pilot reactor. The low-pressure fluidized bed plasma device was applied to prepare TiO_2 and Mn-doped TiO_2 layers on glass beads under different conditions e.g. plasma oxygen, deposition time, and precursor concentration. The SEM, TEM, AFM, and XRD techniques exhibited nanostructure morphologies of photocatalysts covering the surface of the beads. Polymorph structures of TiO_2 (anatase and rutile) formed together under low temperature ($< 450^\circ\text{C}$) conditions were revealed. The anatase and rutile crystallites sizes were calculated at around 9 ± 1 nm. Strong film adherence with stoichiometric ratio was evidenced under XPS analysis of TiO_2 films. The cefixime photo-degradation studies were performed under natural radiation and UV lamp irradiation. Under the same irradiation conditions, better degradation efficiency was observed for the TiO_2 sample containing 16 mol% of rutile phase in its crystalline structure. About 80% of the cefixime initial concentration was decomposed after 35 kJ/L of the UV accumulated energy during 4 h irradiation. Higher deposition time and titanium concentration in precursor solution resulted in higher photocatalytic activity. The TiO_2 , ZrTiO_2 , and VTiO_2 catalysts were also coated on glass beads by the sol-gel method via the micro-mixing reactor. The photocatalytic performance of coated films containing anatase and rutile phases obtained by plasma technique was higher than those of the films containing anatase phase obtained by sol-gel method. The kinetic of cefixime removal was evaluated to be a first-order reaction in all cases. In order to recover the deactivated sites, three regeneration methods like hot water, heat treatment, and washing in an alkaline solution were examined. The hot water method introduced best performances. Finally, the CPC solar photo-reactor for water treatment was modeled using COMSOL Multiphysics software.

Résumé

Ce travail est dédié à l'application de la photocatalyse solaire pour la dégradation de l'antibiotique cefixime en utilisant des films de TiO_2 immobilisés sur des billes en verre. Les expériences ont été réalisées dans un réacteur CPC solaire pilote. Un dispositif plasma à lit fluidisé basse pression a été utilisé pour élaborer des couches de TiO_2 et de TiO_2 dopé au Mn dans différentes conditions expérimentales : oxygène plasmagène, temps de dépôt et concentration du précurseur. Les techniques de caractérisation SEM, TEM, AFM et DRX révèlent la formation de films de photocatalyseurs nanostructurés couvrant la surface des billes. Des structures polymorphes de TiO_2 (anatase et rutile) ont été formées à basse température ($< 450^\circ\text{C}$). La taille des cristaux des phases anatase et rutile a été estimée à environ 9 ± 1 nm. Une forte adhérence des films de TiO_2 a été mise en évidence par l'analyse XPS. Les études de photodégradation du cefixime ont été réalisées sous rayonnement solaire et sous irradiation de lampe UV. Dans les mêmes conditions d'irradiation, une meilleure efficacité de dégradation a été observée pour l'échantillon de TiO_2 contenant 16 % molaire de phase rutile dans la structure cristalline. Environ 80 % de la concentration initiale de cefixime a été décomposée après 35 kJ/L d'énergie UV accumulée pendant 4 h d'irradiation. Un temps de dépôt plus long ou une concentration de précurseur de TiO_2 plus élevés ou une quantité plus importante de billes recouvertes de TiO_2 conduisent à une dégradation plus élevée de cefixime témoignant d'une activité photocatalytique plus élevée liées sans doute au nombre de sites actifs plus élevé. Les catalyseurs de TiO_2 , ZrTiO_2 et VTiO_2 élaborés sur des billes de verre par la méthode sol-gel dans un réacteur de micro-mélange rapide de T ont également été testés. Les performances photocatalytiques des films contenant les phases anatase et rutile obtenues par la technique plasma étaient supérieures à celles des films contenant la phase anatase seule obtenue par la méthode sol-gel. La cinétique d'élimination du cefixime a été évaluée dans tous les cas comme étant une réaction du premier ordre. Il a été constaté que les films perdent de leur activité après plusieurs cycles d'utilisation. Afin de réactiver les sites réactionnels, trois méthodes de régénération telles que le lavage à l'eau chaude, le traitement thermique et le lavage dans une solution alcaline ont été examinées. La méthode de l'eau chaude a présenté les meilleures performances. Enfin, le photoréacteur solaire CPC pour le traitement de l'eau a été modélisé à l'aide du logiciel COMSOL Multiphysics.

Keywords: TiO_2 , Photo-catalyst, CPC-Solar-reactor, plasma, cefixime.